Università degli Studi di Napoli Federico II
Facoltà di Ingegneria

Mario D'Aniello

STEEL DISSIPATIVE BRACING SYSTEMS FOR SEISMIC RETROFITTING OF EXISTING STRUCTURES: THEORY AND TESTING

Tesi di Dottorato
XX Ciclo

Il Coordinatore
Prof. Ing. Federico M. MAZZOLANI

Dottorato di Ricerca in Ingegneria delle Costruzioni

My PhD thesis is the crowning achievement of a growing and training path started when I was simply a student at the faculty of Engineering of University of Naples Federico II. In fact, the first lessons of Structural Engineering that I attended hold by Prof. Mazzolani struck a spark in my aim, thanks to his extraordinary and fascinating capacity to deliver knowledge, influencing my future choices and consequently my life. Hence, I would like to express my deep gratitude to Prof. Federico Massimo Mazzolani, who guided me during the whole doctoral activity and believed in me, offering me the possibility to improve my skill through the important research activity developed for this thesis. His wide experience, competence, determination and enthusiasm have been the reference that guided my studies and not only them.

However, my academic experience has been deeply enriched by other significant presences. In fact, attending the PhD course gave me the special opportunity to find a fundamental, solid and wise reference in the person of Prof. Raffaele Landolfo. His advices, his teachings and his esteem shaped my character and my professionalism. He opened the eyes of my mind. He gave me the tools "*to catch the perspective through the horizon*".

But I need to express a particular acknowledgement to a special friend. In fact, I got acquaintance of Dr. Gaetano Della Corte when I was a young and "insistent" student attending the course of Prof. Mazzolani. Having the fortune to get his acquaintance was one of the main contributory factors that influenced my choices. First, he was a steady, present, extremely competent professor assistant. Then, I found a friend who brotherly followed my cultural growth. Discussing with him helped me to face and deepen both scientific issues and daily matters of life.

In addition, would like to thank Prof. Bruno Calderoni for his technical and friendly support during the daily debates about technical and scientific issues and not only.

Once more I would like to thank Prof. Alberto Mandara, Prof. Gianfranco De Matteis and Dr. Beatrice Faggiano for their patience and their collaboration in the various activities carried out.

I thank my fellow Engineers (even if there are some nice and kind architect in the number) Aldo Giordano, Anna Marzo, Antonello Formisano, Costantino Giubileo, Emilia Angela Cordasco, Enrico Barecchia, Ernesto Grande, Francesco Portioli, Gianmaria Di Lorenzo, Gianpiero Lignola, Giovanni Cuomo, Giuseppe Brando, Giuseppe Brandonisio, Lucrezia Cascini, Luigi Fiorino, Manuela Brescia, Maria Guerrieri, Matteo Esposto, Oreste Mammana, Ornella Iuorio who shared with me the academic experiences during the long and, at the same time, extremely short years of my PhD course. Talking and joking with them improved the quality of my work. In particular, I thank Matteo for his patience in listening to my philosophical dissertations, sometimes extremely annoying and boring (even if extremely true and genuine, unfortunately I say).

Besides, I would like to thanks the librarian of D.A.P.S. (nowadays D.I.ST.) and friend Carmine Citro for his help in the bibliographical search, for his liking and for its sharp reflections as an expert “Homo Accademii”. Moreover, I thank all the students that I had the pleasure to keep up with. Nowadays, the most of them are valid colleagues.

I thanks to Eng. Giovanni Capasso and to Mr Massimilano De Falco for their courtesy in continuously providing the authorizations to get in ex-ILVA mill. In particular, Giovanni has been extraordinary in solving a lot logistic problems.

Thanks to my friends and to those who gave me the delight of a smile. Thus warming my engineered and hyperstatic heart.

Now, that’s it! I don’t want to compose a boring and/or honeyed panegyric of thanks, but, as above reported, the list of people who conditioned my university path is very long. I apologize if someone has been forgotten. Once more, I apologize for my windy, diffusive written speech. It was spontaneously borne, without celebratory intents.

What shall I say more? Those who fully know my heart are conscious of my actual feelings. I cannot hide my aspirations. I cherish the wish to continue this career sharing my enthusiasm and my passion for the studied matter, but the thread of my future is spun by the inexorable and ruthless “Moirae”. I don’t know what “Lachesis” will have in reserve for me. Who knows who lies ahead? Once more, I don’t know.

However, I finish with a pinch of rhetoric (useful to galvanize the melancholy spirit, particularly now that I am convulsively writing at 3:30 a.m. the last lines of this adventure) paraphrasing a famous quotation of the Italian forgotten history: “*Carri nemici irrompono spalle Ariete. Con ciò Ariete circondata. Carri Ariete combattono*”. My father well know what I mean.

Finally, let me write a few lines more. The most sweetly difficult, but the most emotionally important, I say. I have to pronounce the last but the greatest thanks. This is turned to my family for their sacrifices and for the love and encouragements proved to me during my studies. Being part of my family has been a privilege. Without them I would be nothing and no one. Unfortunately, I am not able to find a proper form to express what I feel. For this I bag their pardon.

Thanks sincerely.

Mario

Naples, November 29th 2007

To my Mother and my Father,
Their example and Their presence daily represent
the lighthouse of my life

“…**There are more things in heaven and earth, Horatio, Than are dreamt of in your philosophy**…” (W. Shakespeare, “*Hamlet*” - Act I, Scene 5)

“…**nihil sine magno labore vita dedit mortalibus**…” (Quintus Horatius Flaccus –“*Sermones*” 9, 60)

“…**Winter is coming**…” (George R. R. Martin's, “*A Song of Ice and Fire*”).

“**Con il cuore oltre l’ostacolo!**”. Motto of Italian Colonial cavalry squadron Savari e Spahis, Libya 1911-1943. These words have been victoriously and bravely cried in battle during the last heroic cavalry charge of (3°) *Savoia Cavalleria* (gold campaign medal) in August 24th of 1942 at Jsbuschenskij on Don River (Russia).

Chapter VI

NUMERICAL MODELLING AND ANALYSES OF RETROFITTED BARE RC STRUCTURES

Chapter VII

NUMERICAL MODELLING OF THE TESTED MASONRY INFILLED RC STRUCTURE EQUIPPED WITH BRBS

Chapter I

Introduction

1.1 GENERAL

Recent earthquakes have highlighted the urgency and importance of rehabilitating seismically deficient structures to achieve an acceptable level of performance. This can be achieved either reducing the load effect input to the existing structures, or improving the strength, stiffness, and/or ductility. Over the past 20 years, significant advancements have been made in the research and development of innovative materials and technologies for improving the seismic performance of existing structures through rehabilitation processes. The seismic protection of existing structures represents nowadays one of the main tasks in the field of structural engineering.

Many examples of bad and unsatisfactory structural performance, particular in case of reinforced concrete (RC) structures, have been due to several reasons such as bad quality of materials, rough execution, lack of appropriate design of local details and non-respect of code provisions. Besides, even if in very few cases, several failures have also occurred in the steel buildings during the well-known 1994 Northridge and 1995 Kobe Earthquakes, due to unexpected fragile local behaviour of connections respect to the large dissipative capacity expected by structural designers (Mazzolani, 2000). Following such experiences, research efforts have been addressed to the definition of both new proper constructional details to enhance the structural ductility (Bruneau *et al*., 1998) and to the revision of the current design procedures in seismic zones to better correlate the available plastic capacities with the actual seismic demands. As a result of these efforts, a new concept and design method has been introduced during the last years. It is represented by so-called 'Damage Tolerant Structures' approach that differs from the common seismic structural design. In fact, the latter trend is based on the well-known concept to entrust the energy dissipation role under strong earthquakes to the plastic deformation capacity of beams and columns, with a consequence damage of primary structural elements even for moderate-intensity earthquakes. The 'Damage Tolerant Structures' approach consists instead in the use of special seismic protection sacrificial devices, which modify the dynamic properties of primary structure and/or increase its dissipative capacities, controlling and reducing the dynamic response of the whole structure. The control of the dynamic response of structures can be led by passive, active and hybrid protection systems. The interest of this study is mainly turned to passive control systems, where the fundamental period and damping capacity of the structure equipped with protection devices remains constant during the seismic motion, without the intervention of any external power source, as instead happens in the active and hybrid control systems. Among several passive control systems, ductile steel bracing systems have been studied. In particular, attention has been focused on steel eccentric braces and steel buckling-restrained braces.

Use of steel bracing is an effective for the global-level strengthening and stiffening of existing buildings. Concentric or eccentric bracing schemes can be used in those selected bays of an RC frame to increase the lateral resistance of the frame. The main advantage of this method is that a rehabilitation of the foundation may not be required because steel bracings are usually installed between existing members. However, increased loading on the existing foundation is possible at the bracing locations and so the foundation still must be evaluated. In addition, the connection between the existing concrete frame and the bracing elements should be carefully treated because the connection is vulnerable during earthquakes. Several researchers have reported successful results when using steel bracing to upgrade RC structures (Bai and Hueste 2003, D’Aniello et al 2005, 2006).

1.2 MOTIVATION AND SCOPE OF THE RESEARCH

Existing reinforced concrete (RC) frame buildings with non-ductile detailing represent a considerable hazard during earthquakes. This type of building suffered severe damage and was responsible for most of the loss of life during the major Italian seismic events such as the 1981 Irpinia earthquake. Several technical solutions are currently available for the mitigation of earthquake risks, going from active to passive dissipating devices as well as base isolation. The use of steel in seismic retrofitting and upgrading of existing constructions has long been studied (Mazzolani 1992, 1996).

Systems based on steel are generally very useful in those situations characterized by the absence of purposely-designed lateral-load resisting structures. A correct design of these systems is based on the idea to eliminate/reduce the plastic deformation demand to the existing structure by adding supplemental energy dissipating devices. Among these systems, metal-based technologies are often considered as the most satisfactory technical solutions, because of the effectiveness, practicality and economy. Metal solutions mainly consist in adding new structural elements (generally in form of braces), which collaborate with the existing structure, by varying its static scheme and operating at global level as supplemental energy dissipation passive systems, thus acting as a sort of ductile hysteretic fuse.

In the last years, steel dissipative bracing systems have been widely and successfully used as complementary structural elements, and sometimes also as substitutive elements of other lateral load resisting systems under seismic actions. In fact, a number of studies proved their significant effectiveness on the structural performance under wind and seismic loads. Both eccentric braces and buckling-restrained braces are characterized by a stable and compact hysteretic response, providing large energy dissipation capacity. These dissipative bracing systems are designed to dissipate the most of the energy input by a strong earthquake and if they are damaged they make the rehabilitation easy after the earthquake, since these devices are designed to be replaceable. In eccentric braced frames (EBFs), forces are transferred to the brace members through bending and shear forces developed in the ductile steel link. The link is a beam element delimited by the braces. Links are designed to yield and dissipate energy while preventing buckling of the brace members. In RC frames, the concrete beams are incapable to perform as a ductile link for the steel bracing system that is inserted in the frame bays. Hence, the need to adopt a Y-inverted bracing configuration, with a vertical steel link, can be easily recognized. Moreover, bolted connections between the link ends are suggested, in order to facilitate replacement of dissipative zones (links) after a damaging earthquake, what reduces repair costs. In case of buckling-restrained braces (BRBs), the avoidance of global compression buckling let to solve the problem of the limited ductility of classic concentric bracings. They are made of very slender steel plates, forming the core of the BRB, which are allowed to yield both in tension and in compression. The slender plates are inserted in between steel rectangular or square hollow section profiles, which provide the restraining effect against lateral buckling. In the most classical form, the restraining tube is filled with concrete and an unbonding layer is placed at the contact surface between the core plates and the filling concrete, thus the name of this version ‘unbonded brace’. However, ‘only-steel’ solutions have been proposed, with two or more steel tubes in direct surface contact with the yielding steel plates. In the latter case, the restraining tubes can also be connected by bolted joints, thus allowing an easy inspection and maintenance during the lifetime or after a damaging earthquake.

Nowadays, many theoretical studies and experimental tests of retrofitting systems on structural elements and sub-structures are available in the technical literature. Laboratory experiences are valuable for studying the intervention techniques, but they present serious limitations, due to the difficulty to correctly reproduce actual boundary conditions and to take into account the scale effects in reduced scale models, as well as to introduce the actual RC structure defects (e.g. constructional tolerances, bad execution, reinforcing bars corrosion and/or concrete degradation). For these reasons, the opportunity to perform collapse tests on existing structures must be considered as a precious and unique unrepeatable opportunity to improve the knowledge on both design and analysis methods. Hence, the present study has an extraordinary value because it consists of both the analysis of real existing buildings and the comparison of different technologies for seismic upgrading, which are two paramount aspects in Earthquake Engineering.

In this framework, the research activity, here summarized, consisted of a series of full-scale tests on two reinforced concrete (RC) buildings, located in

Bagnoli (Naples, Italy), in the area where the plants of the previous steel mill named ILVA (former Italsider) have been destined to be demolished. Such an experimental activity was developed within a semi-voluntary project called ILVA-IDEM, whose acronym “Intelligent DEMolition” was inspired by the ongoing occurrence in the area, being coincident with the final destiny of this building itself. Afterwards new incoming supporters and partners followed and they are two research projects:

1. PROHITECH (earthquake PROtection of HIstorical buildings by reversible mixed TECHnologies), that is an international project, composed by 12 research units coordinated by Prof. F. M. Mazzolani;
2. RELUIS (REte dei Laboratori Universitari di Ingegneria Sismica), that is a national research project articulated in a group of research lines, each of them composed by a task team of research units coming from several Italian universities. The relevant research lines sustaining the current study is the line n.5 coordinated by Prof. Mazzolani (University of Naples, Federico II) and by Prof. R. Zandonini (University of Trento).

1.3 FRAMING OF THE ACTIVITY

The research activity has been addressed both to evaluate the benefits of ductile steel braces on global response of RC frames with non-ductile details and, on the other hand, to assess proper design criteria of the studied devices so that to improve their mechanical performance.

The first phase of the current study consisted in several full-scale tests on RC structural units equipped with Y-inverted eccentric braces and BRBs, respectively. In this initial stage, different design criteria have been applied in the design of the connections, thus investigating about the maximum over-strength that Y-inverted link can exhibit. On the other hand, in case of BRBs the main efforts were addressed to conceive rational details to develop an innovative only-steel device for seismic retrofitting of existing structures. To achieve these purpose, several cyclic pushover full-scale tests have been carried out. In details, three tests have been performed on EBs and three tests on BRBs. These experiences clearly showed the positive influence of ductile steel bracing on the global response of RC structure.

A second step of the research activity consisted in the numerical study in order to model and subsequently analyze the monotonic and cyclic behaviour of the retrofitted RC structures. The aim has been clearly to enlighten the key issues characterizing the inelastic behaviour of the tested steel systems and, on the other hand, to quantify the lateral capacity improvements of the RC structures without and with the retrofitting devices. In fact, the results of non-linear time history analyses showed in which terms the structures under investigation can overcome seismic events as they are and how the presence of steel ductile braces (EBs and BRBs) can improve the structural performance. The analyses showed a significant decrease of seismic demands (floor displacements, interstorey drifts and plastic rotations) was achieved.

Moreover, finite element analyses have been developed in order to investigate on the inelastic behaviour of steel links and on the evaluation of their peak inelastic strength. In fact, the key point in the design of eccentric bracing is the evaluation of the link shear over-strength, which serves for capacity design of other members and connections. Past studies have mainly been focused on the shear response in absence of significant axial forces, which is appropriate in case of links belonging to floor beams. In the current study, the tested links were subjected by axial tensile forces. Hence, it was investigated the shear response of links subjected to axial forces, either directly applied or induced by end-restraint conditions. Numerical results suggest that the peak inelastic strength may significantly vary with the level of axial force and it is strongly affected by end-restraint conditions.

The final stage of the research activity was the comparison between both the experimental and numerical results. The numerical data revealed a good agreement with the experimental results, confirming a significant increase of global ductility, strength and stiffness.

Chapter II
Steel ductile bracing systems

2.1 INTRODUCTION

The seismic retrofitting of existing buildings requires taking into account several different factors, such as architectural constraints, the cost due to the possibility to close the building (or part of it) for the duration of the retrofit work, or having to heavily reinforce existing framing due to the increased seismic demands the retrofit strategy may place on it. Referring to the structural needs, it seems that the limitation of lateral displacement in buildings under seismic action and the capacity to resist horizontal actions can be considered as the main concerns for structural designers.

Among the possible solutions to retrofit an existing structure, bracing systems are a simple and effective retrofit system, especially when story drifts need to be limited. The idea is to design systems that are strong enough to resist the seismic forces and light enough to keep the existing structural elements far from needing further reinforcement. Furthermore, if these systems could be installed quickly and eliminate the need to disrupt the occupants of existing structures, they would be even more desirable (in the context of a hospital retrofit for example). Therefore, steel braces can be considered as one of the most efficient structural systems for resisting lateral forces due to wind and earthquakes because they provide complete truss action. The common way for seismic protecting both new and existing framed structures is traditionally based on the use of concentric steel members arranged into a frame mesh (Concentrically Braced Frame – *CBF*), according to single bracing, cross bracing, chevron bracing and any other concentric bracing scheme. Even if such systems possess high lateral stiffness and strength for wind loads and moderate intensity earthquakes, some drawback have to be taken into account, concerning the unfavourable hysteretic behaviour under severe earthquake, due to buckling of the relevant members, which generally causes poor dissipation behaviour of the whole system (see Figure 2.1a).

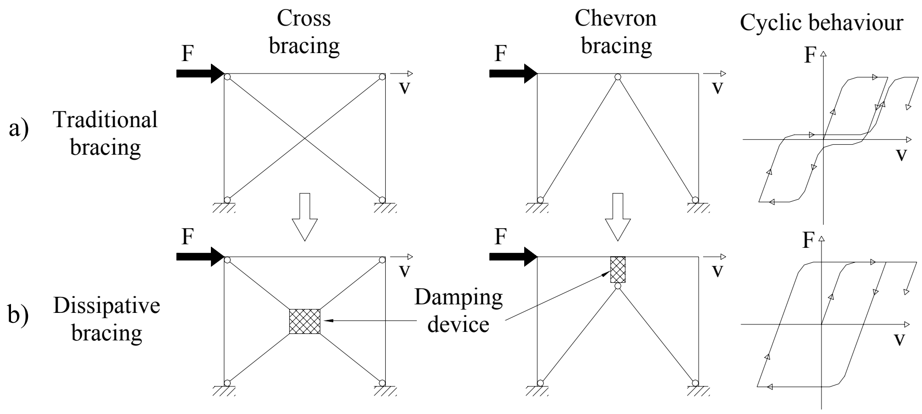

Figure 2.1. Traditional and dissipative bracing.

In case of seismic retrofitting, in addition to the strengthening of the existing frame, it is necessary to improve the global seismic performance of the structure, also in terms of dissipative capacities. Therefore, it is necessary to avoid the mentioned drawback by preventing the buckling and the premature rupture of braces. This aim can be achieved by placing in the conventional bracing system some special devices that dissipate the input energy seismic before heavy damage of the primary structure occurs. In the Figure 2.1b, some solutions to modify an ordinary bracing system in a dissipative bracing system are schematically shown. In general, steel bracing systems are a very suitable technique to retrofit existing structures, because they can get a judicious modification of the structural properties, such as lateral strength and stiffness, improving its performance in future earthquakes. Moreover, these systems reveal to have a good reversibility, because if they are damaged they make the rehabilitation easy after the earthquake, since these devices are designed to be replaceable. In particular, it is possible to design these systems to be inspected, so that it is possible to control their condition after each seismic event. Other advantages are inexpensiveness (because they are made by ordinary steel working) and easiness to be removed and assembled in a structure.

Generally speaking, beneficial dissipative and damping devices have been proposed and used worldwide. In the case of the traditional cross bracing, a simple damping system can be obtained by designing the braces in such a way plastic mechanisms due to material yielding are exploited before the buckling of the braces occurs.

Referring to a chevron bracing scheme, the transformation from traditional bracing to a dissipative scheme takes place by inserting special dissipative devices between the joint of the diagonal members and the beam (Figure 2.2a). The simplest scheme is based on the transformation of a conventional concentric brace into an eccentric brace (EB) by means of a steel link, which is fixed to the beam and pin-joined to the diagonals (see Figure 2.2b). In this way the typical Y-shaped eccentric brace behaves as a passive control device, since the inelastic cyclic behaviour of the link element allows a large amount of the input energy to be dissipated without any damage of the external framed structure. In fact, the basic design principle of the system is that, while plastic deformations occur in the dissipative device, the diagonals have to remain elastic both in tension and in compression.

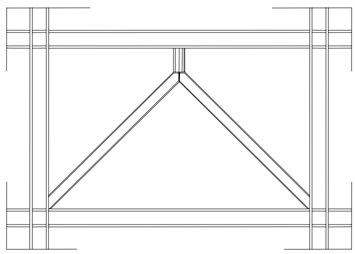

a. Y-braced eccentric braces

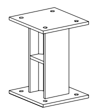

b. Conventional steel link

Figure 2.2. Typical dissipative chevron bracing systems.

Another way to improve the cyclic performance of traditional cross bracing system is based on the use of a special types of bracing members, which are notoriously called Buckling-Restrained Braces (*BRBs*) (Chen & LU, 1990) or also Unbonded Brace (*UB*) (Clark *et al.*, 2000) (see Figure 2.3).

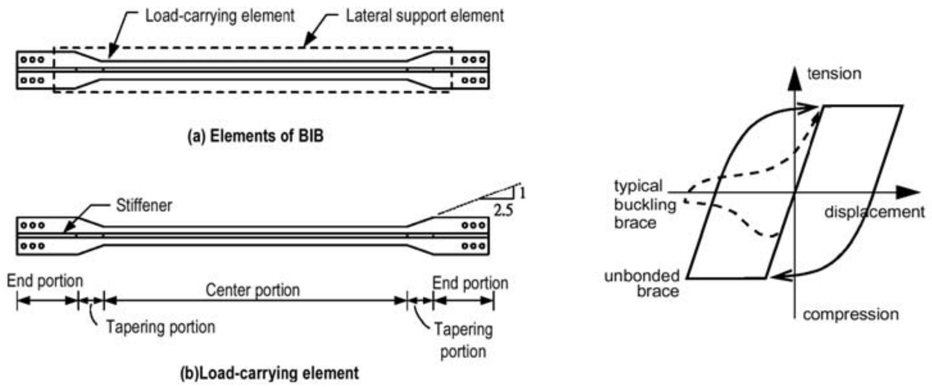

Figure 2.3. Typical Buckling-Restrained Brace (BRB) system and relevant cyclic behaviour.

The design technology of these dissipative systems consists in the use of special trusses composed by a steel core, as load-carrying element, placed inside a lateral support element, in order to obtain a buckling restrained bracing. While the load-carrying element takes the tensile and compressive axial forces, the lateral support prevents buckling of the central core when the member is compressed, owing to appropriate lateral restraining mechanisms. The flexural strength and stiffness of the lateral support prevent global and local buckling of the brace, obtaining axial yielding under both tension and compression force. Therefore a stable hysteretic behaviour is provided, without any pinching and/or degradation of strength and stiffness up to the failure, which is generally caused by the tensile rupture after significant necking of steel core. Due to the high energy dissipation capacity, a *CBF* made of *BRB* members is also called *DCBF* (Ductility Concentrically Braced Frame).

The present research focuses on both EBs and BRBs. Hence, in order to provide a complete knowledge of these bracing systems, the states of the art of both EBs and BRBs are respectively summarized in the following Sections.

2.2 ECCENTRIC BRACES

The eccentric braced frame (EBF) is a hybrid lateral force-resisting system. In fact, it can be considered as the superposition of two different framing systems: the moment-resisting frame and the concentrically braced frame. EBFs can combine the main advantages of each conventional framing system and minimize their respective disadvantages, as well. In general EBFs possess high elastic stiffness, stable inelastic response under cyclic lateral loading, and excellent ductility and energy dissipation capacity.

Research on the behaviour of EBFs started in the second mid-1970s (Roeder & Popov 1977, Roeder & Popov 1978) and continued up today. All these studies confirmed the reliability of EBFs to resist horizontal actions. Consequently the number of civil applications is increasing day by day. Eccentrically braced frames in buildings typically include the use of shear links, which are sections of beams that yield and plastically deform in shear, to provide a stiff and ductile lateral load resisting system.

Shear links in eccentrically braced frames have been studied for new buildings (Kasai & Popov 1983, Popov & Malley 1983, Hjelmstad & Popov 1986, Ricles & Popov 1987, Engelhardt & Popov 1989), but their use is now also becoming a viable method to retrofit RC structures and for protecting bridges. Two examples of bridge retrofitting are Richmond San Rafael Bridge (Itani 1997) and the use of shear links in the tower of the new San Francisco-Oakland Bay suspension cable bridge (Nader et al. 2002).

Figures 2.4 to 2.6 show some examples of structures with EBF systems designed to resist horizontal actions.

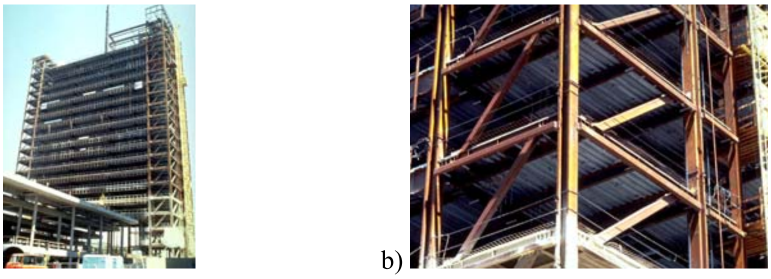

a) b)

Figure 2.4. Multi-story building with EBF system, San Diego (USA).

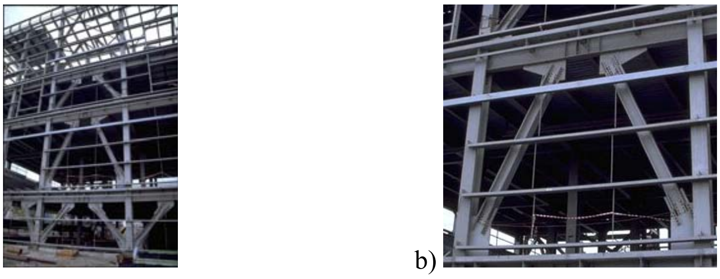

a) b)

Figure 2.5. Multi-story building with EBF system, Alikahya (Turkey).

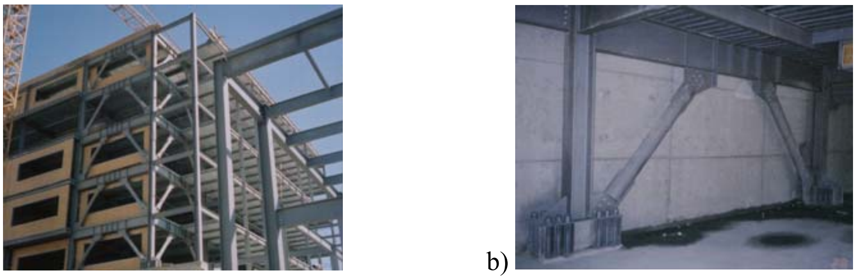

a) b)

Figure 2.6. Istanbul Bilgi University, Prep School Building (Turkey).

2.2.1 Static behaviour of EBs

The key distinguishing feature of an EBF is that at least one end of each brace is connected so as to isolate a segment of beam called “link”. EBF arrangements, usually adopted, are shown in Figure 2.7. In each framing scheme of Figure 2.7 the links are identified by a bold segment. The four EBF arrangements here presented are usually named as split-K-braced frame, D-braced frame, V-braced and finally inverted-Y-braced frame.

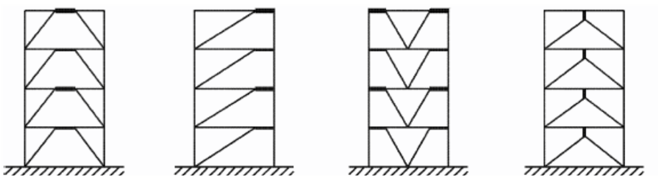

Figure 2.7. EBs configuration.

The static behaviour of EBs is deeply influenced by the link. The inelastic action is restricted in the links in order to keep the framing around in the elastic range by making them able to sustain the maximum forces that the links can develop. In this way the links act as ductile seismic fuses and preserve the integrity of the whole frame. For this reason the other components of the framing system (such as diagonal braces, columns and link connections) should be designed for the forces generated by the full yielding and strain-hardening of dissipative links. To do this it is important to explicate the distribution of internal actions in an EBF system and define a relationship between frame shear force and link shear force. This relationship depends only on the EBF configuration, in fact it is the same if the link response is elastic or plastic. The design actions in links can be calculated using equilibrium concepts. For example in a split-K-braced EBF (shown in Figure 2.8), assuming that the moment at the center of the link is equal to zero, the link shear force V can be expressed as:

$$V = \frac{F \cdot H}{L} \tag{1}$$

where F is the lateral force, H is the interstory height and L is the bay length.

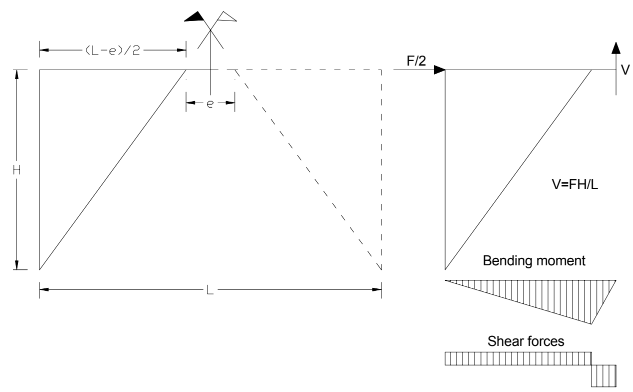

Figure 2.8. Design action in link for a split-K-EB configuration.

In case of an inverted-Y-braced EBF (Figure 2.9), assuming that the moment at the brace connections is equal to zero (i.e. in case of pinned braces), the link shear force V can be expressed as:

$$V = F \tag{2}$$

where F is again the lateral force.

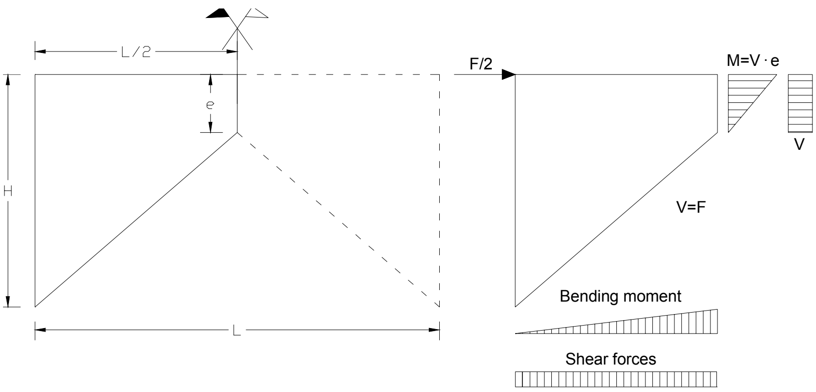

Figure 2.9. Design action in link for an inverted-Y-EB configuration.

2.2.2 Kinematic of plastic mechanism of ductile EB systems

An important aspect is the kinematic of plastic mechanism of the EB systems. In fact, in the design of a seismic resistant EB, it is necessary to estimate the plastic rotation demand on the links. In particular the relationship between story plastic drift angle and link plastic rotation is the main topic. This relationship can be simply derived by assuming the frame outside the link as rigid (because the elastic deformation in the frame outside the link is small if compared with the link plastic deformation), thus depending only on configuration of EBs and geometrical proportions, assuming the inextensibility and rigid plastic behaviour of members. Link rotation is denoted by the symbol γ to remind the importance of shear yielding in link rotation.

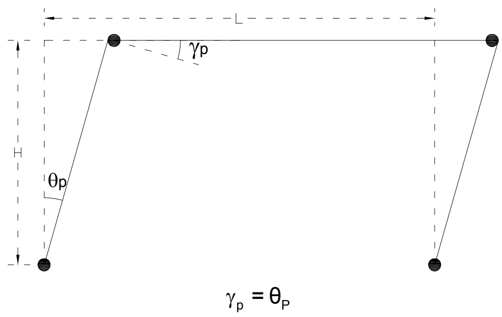

Figure 2.10. Kinematic of a moment resisting frame.

In case of a moment resisting frame (MRF), the kinematic of plastic mechanism is very simple and the relationship between the story drift angle and the plastic rotation of dissipative parts is given in Figure 2.10.

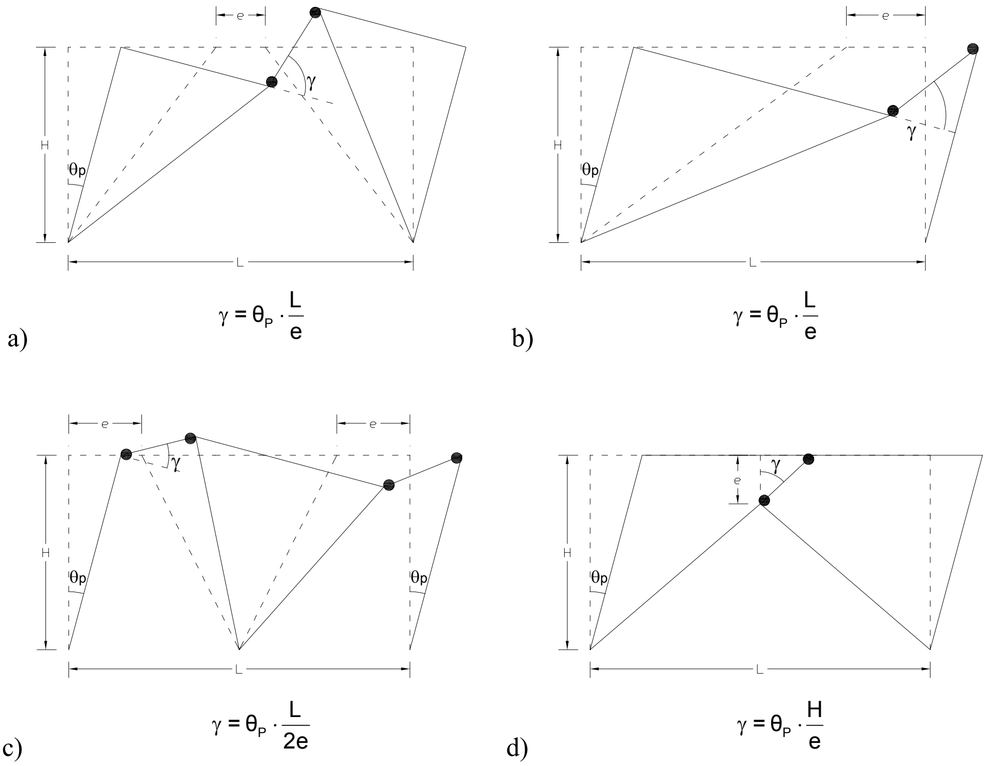

Figure 2.11. Kinematic of plastic mechanism of several EB configurations: split-K-braced frame (a); D-braced frame (b); V-braced frame (c); inverted-Y-braced frame (d).

Figure 2.12 shows a plot of link rotation demand versus the ratio *L/e* for a split-K-EB. This plot clearly shows that plastic rotation demand is larger in EB systems than in a MRF (where *L/e* = 1). The link rotation demand grows as the link length decreases. This plot demonstrates that links should not be too short, because the rotation demand may become excessive.

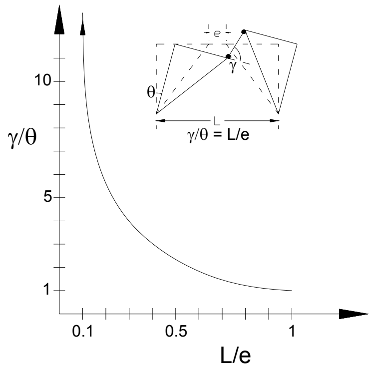

Figure 2.12. Variation of link rotation demand with e/L ratio.

2.2.3 Link mechanical behaviour

Besides the kinematic of plastic mechanism, another important aspect characterizing the EB inelastic behaviour is the cyclic hysteretic response of shear links. Figure 2.13 clearly shows that shear links can provide stable and well rounded hysteresis loops, which indicate a large energy dissipation capacity.

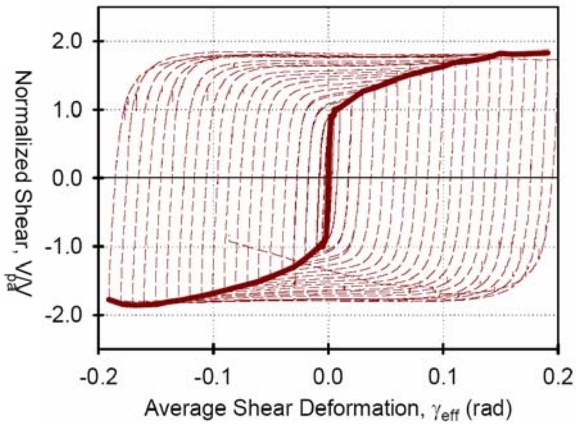

Figure 2.13. Shear link hysteretic response.

Three different domains characterize the link behaviour (Kasai & Popov, 1986): elastic, pre-buckling inelastic and post-buckling, bounded by three limit states: yield, buckling and failure. The inelastic pre-buckling behaviour is characterized by remarkable cyclic stability of the hysteresis loop and an active link functions most effectively as an energy damping system. After the web buckling, the link continues to dissipate energy. However, the predominant load carrying mechanism changes and therefore so does the way of dissipating energy. The post-buckling energy dissipation mechanism, based on the tension-field, is less efficient than the pre-buckling one. Failure of a link is defined as complete inability to sustain load, and is generally caused by low-cycle fatigue in highly localized regions which experience extreme strain reversals due to the cyclic changing of the buckled mode shape (Hjelmstad et al., 1983).

Link inelastic performance essentially depends on its length and cross-section properties. For a given cross-section, the link length controls the yielding mechanism and the ultimate failure mode. Short links are mainly dominated by a shear mechanism, instead flexure controls link response for long links. Moreover intermediate links are characterized by a *M-V* interaction.

Assuming perfect plasticity, no flexural-shear interaction and equal link end moments, the theoretical dividing point between a short link (governed by shear) and a long link (governed by flexure) is a length of $e = 2M_p / V_p$, where the plastic bending moment $M_p = Z \cdot f_y$ (in which Z is the plastic modulus and f_y is the value of steel yielding stress) and $V_p = 0.55 \cdot \left(d - 2t_f \right) \cdot t_w \cdot f_y$ (in which d is the depth of the cross section and t_w is the web thickness). A large number of experimental activities (such as Kasai & Popov 1986, Hjelmstad & Popov 1983, Foutch 1989) indicate that the assumption of no M-V interaction is reasonable, but an assumption of perfect plasticity is not correct. In fact, substantial strain hardening occurs in shear links. According to tests performed on American wide-flange steel profiles, the average ultimate link shear forces reach the value of $1.5V_p$. One implication of this strain hardening is that both shear and moment yielding occur over a wide range of link lengths. In case of shear links, end moments substantially greater than M_p can be developed. In fact, shorter is the link, greater the bending moment will be in order to necessarily have $V = 2M / e$. The large end moments, combined with the significant strain gradient that occurs in links, lead to very large flange strains, which in case of steel built up sections can prompt the flange welds failure. Kasai and Popov (1986) estimated that the maximum link end moments can be assumed $1.2M_p$. Thus, from link static of Figure 2.8, if the end moments are limited to $1.2M_p$ and the link shear is assumed to reach $1.5V_p$, the limiting link length is $e = \frac{2 \cdot (1.2M_p)}{1.5 \cdot V_p} = 1.6\frac{M_p}{V_p}$.

Then the following equations can be used to classify the link mechanical response:

Shear (short) links: $e \leq 1.6\frac{M_p}{V_p}$ (3)

Intermediate links: $1.6\frac{M_p}{V_p} < e < 2.5\frac{M_p}{V_p}$ (4)

Flexure (long) links: $e \geq 2.5\frac{M_p}{V_p}$ (5)

The ultimate failure modes of short and long links are quite different. In particular inelastic web shear buckling is the ultimate failure mode of short links. This buckling mode can be delayed by adding web stiffeners (Figure 2.14).

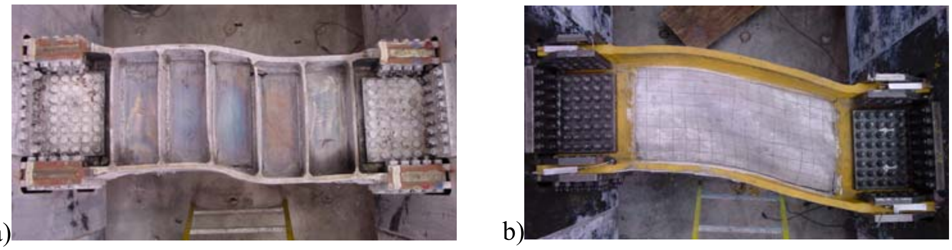

a) b)

Figure 2.14. Plastic deformation of short links: inelastic response of stiffened short link (a); inelastic response of unstiffened short link (b).

Hjelmstad & Popov (1983) developed several cyclic tests in order to relate the web stiffeners spacing to link energy dissipation, and Kasai & Popov (1986) subsequently developed simple rules to relate stiffeners spacing and maximum link inelastic rotation γ up to the web buckling. Starting from the consideration that the link web buckling modes are very similar to the ones of plates under shear loading they applied the plastic plate shear buckling theory to relate the stiffeners spacing to the maximum deformation angle of a shear link. In fact the theoretical plastic buckling shear stress τ_b was obtained starting from the elastic buckling solution τ_E and can be expressed as:

$$\tau_b = \eta \cdot \tau_E \qquad (6)$$

where η is a plastic reduction factor, that is a function of plate strain hardening history and it was experimentally derived, while the elastic buckling shear stress τ_E can be expressed as:

$$\tau_E = \frac{\pi^2 E}{12\left(1 - \nu^2\right)} K_S\left(\alpha\right) \cdot \left(\frac{1}{\beta}\right)^2 \qquad (7)$$

in which ν is the Poisson ratio, k_s is a plate buckling coefficient, which is a function of the aspect ratio α and the boundary conditions, that are assumed in this case as clamped end conditions. In particular the aspect ratio is equal to $\alpha = a/b$, where a is the stiffener spacing and b is the web panel height, while β is the web panel height-to-thickness ratio that is equal to $\beta = b/t_w$, where t_w is the web thickness.

The secant shear modulus G_s (Gerard 1948 and 1962) for the shear link was defined as:

$$G_S = \frac{\tau}{\overline{\gamma}} \qquad (8)$$

in which $\overline{\gamma}$ is the maximum shear deformation angle attained preceding the web buckling, which has to be experimentally measured, and τ is the corresponding shear stress approximately defined as $\tau = V/A_w$, where V is the shear force and A_w is the web area.

It was found that there is a linear relationship between η and the ratio G_S/G, in which G is the elastic shear modulus given by $G=E/2(1+\nu)$, where E is the Young's modulus and ν=0.3. Hence, this relationship is expressed by:

$$\eta = 3.7\frac{G_S}{G} \qquad (9)$$

Substituting Equations 8 and 9 into Equation 6 with $\tau = \tau_b$ at an incipient buckling stage it results:

$$\tau_b = 3.7\frac{\tau_b}{\overline{\gamma}G} \cdot \tau_E \qquad (10)$$

that can be rearranged leading to:

$$\overline{\gamma} = \gamma_b = 3.7\frac{\tau_E}{G} \tag{11}$$

Then using Equation 7, Equation 11 gives:

$$\gamma_b = 8.7K_S\left(\alpha\right)\cdot\left(\frac{1}{\beta}\right)^2 \tag{12}$$

Furthermore, instead of using the parameter β it is more convenient to approximate it by a beam depth to web thickness ratio d/t_w . Also, since it has been pointed out that the web stiffeners are effective in reducing the possibility of lateral torsional buckling (Hjelmstad & Popov 1983), a maximum spacing of a/d=1 is adopted. Considering these factors, for the range of γ from 0.03 to 0.09 radians, Equation 12 can be conservatively approximated as:

$$\frac{a}{t_w} + \frac{d}{5t_w} = C_B \tag{13}$$

where the constant C_B is equal to 56, 38, and 29, respectively for γ equal to 0.03, 0.06 and 0.09 rad. Thus rearranging Equation 13, it was possible to draw the following simple expressions for each required link deformation capacity (Kasai & Popov 1986):

$$a = 29t_w - \frac{d}{5} \qquad \text{for } \gamma\text{=0.09 radians} \tag{14}$$

$$a = 38t_w - \frac{d}{5} \qquad \text{for } \gamma\text{=0.06 radians} \tag{15}$$

$$a = 56t_w - \frac{d}{5} \qquad \text{for } \gamma\text{<0.03 radians} \tag{16}$$

where a is the distance between equally spaced stiffeners, d is the link depth and t_w is the web thickness.

In order to study the effect of inelastic web buckling in links, Popov & Engelhardt (1988) reported the results of two series of cyclic tests on both stiffened and unstiffened isolated links. In the first series fifteen full-size shear links were subjected to equal end moments to simulate the performance of a typical link in a split-K-braced frame. In this case the unstiffened links manifested severe web buckling shortly after yielding, hence their load-carrying capacity rapidly reduced. The specimens provided with stiffeners equally spaced on both link side according to Equation 14 showed a significant improvement in performance, achieving large inelastic rotations with full rounded hysteretic loops, confirming a plastic rotation capacity of about 0.10 radians under cyclic excitation and 0.20 radians under monotonic loading. Moreover link with stiffeners on only one side have been tested and their performance was adequate in shear links for beams of moderate depth, i.e. link depth up to 24in or 600mm. In the second series shear links were subjected to unequal end moments in order to simulate the performance of links located next to a column. In fact, in this configuration the typical ratio of elastic end moments can be on the order of 2 to 4 or more. If steel behaved as a perfectly plastic material, the equalization of link end moments could occur if the link is loaded to its ultimate state. However, because of steel strain hardening, this end moment equalization may not occur. The tests conducted on links with unequal end moments permitted to understand that:

1) for very short links, i.e. $e \leq M_p/V_p$, unequal end moments remain unequal throughout the loading history up to link failure. The ultimate link end moment at the column face is significantly larger than the predicted equalized moment. As link length increases, the ultimate link end moments tend to equalize. In particular, when link length is about $e \geq 1.3 M_p/V_p$, full equalization of end moments can occur.
2) The initial unequal end moments have little effect on the plastic rotation capacity and on the overall hysteretic behaviour.
3) Interaction between bending moment and shear force can be neglected when predicting the yield limit state of a link. In fact, even in the presence of high shear force, the full plastic moment can be assumed rather than a reduced value based on flanges only. This result is very important because contradicts the predictions from plastic theory, but it is confirmed by experimental tests. Moreover neglecting M-V interaction simplifies the analysis and design of shear links.

These results are very important because they permit to calculate the forces generated by the fully yield and strain hardened links. In fact, for links adjacent to columns, the ultimate link end moments can be taken as:

$$M_a = M_b = \frac{V_{ult}e}{2} \qquad \text{for } e \le 1.3\frac{M_p}{V_p} \qquad (17)$$

$$M_a = M_p \;\; ; \;\; M_b = V_{ult}e - M_p \qquad \text{for } 1.3\frac{M_p}{V_p} \le e \le 1.6\frac{M_p}{V_p} \qquad (18)$$

where M_a and M_b are the link end moments at the column face and at the opposite end of the link. For links not adjacent to columns, the ultimate moments given by Equation 17 are appropriate for links of any length.

Several authors (such as Dusicka et al. 2004, Okazaki et al. 2004), observed during the experiments the locations of initial cracking in the web of steel built up shear links at stiffener to web interface (Figure 2.15a). Shear links that did not have stiffeners (Figure 2.15b) had lower plastic strain demands in the web as compared to those with stiffeners and consequently did not develop cracks until larger deformations were imposed. Localized plastic strains were also present in the stiffeners and the flanges of the links. The stiffeners developed localized plastic hinging at the connection to the flange, resulting in the observed cracks during the experiments. The flange plastic strains developed near the ends of the effective length. Welding should be avoided in these locations in order to avoid potential for flange cracking, which may result in undesirable modes of failure (Figure 2.15c).

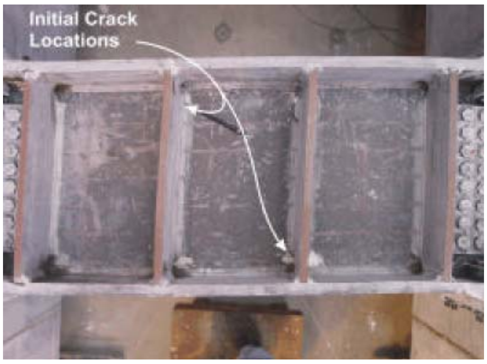

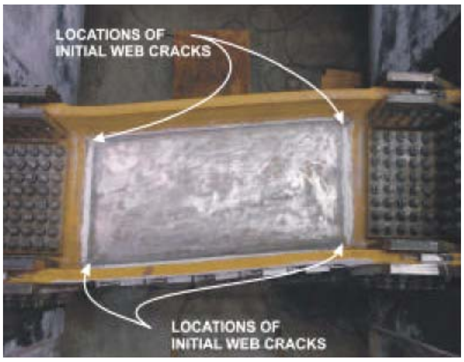

Figure 2.15. Short link web fracture: location of initial crack in a stiffened link (Dusicka et al., 2004) (a); location of initial crack in an unstiffened link (Dusicka et al., 2004) (b); web fractures after testing for stiffened shear link (Okazaki et al. 2004) (c). (continued)

c) 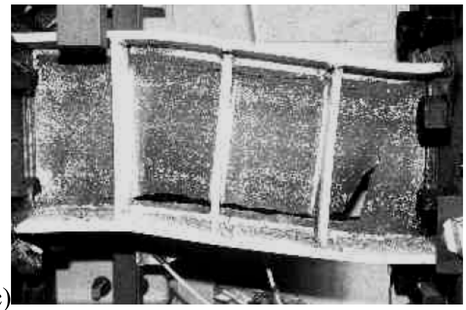 d) 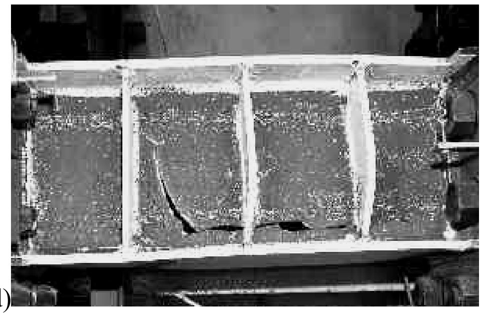

Figure 2.15. Short link web fracture: location of initial crack in a stiffened link (Dusicka et al., 2004) (a); location of initial crack in an unstiffened link (Dusicka et al., 2004) (b); web fractures after testing for stiffened shear link (Okazaki et al. 2004) (c,d).

Dusicka et al. (2004) developed detailed numerical models to investigate the plastic strain demands on the different components of the steel built up links (Figure 2.16). A consistent correlation was found between the location of the initial cracking during the experiments on shear links with stiffeners and the location of localized plastic shear strain in the numerical models. The increase in strain demand occurred consistently at the ends of the stiffener to web connection, next to the stiffener chamfer. The plastic strains in those locations were over 20% higher than in the middle of the panel and coincided with the welding start and stop locations of the stiffener fillet welds.

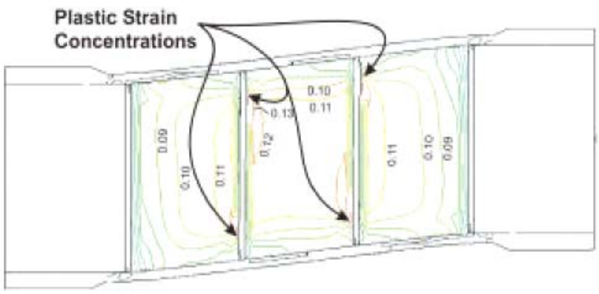

Figure 2.16. Plastic strain distribution in web of built-up shear links (Dusicka et al., 2004).

This indicates that the onset of cracking in the web observed during the experiments was likely caused by the combination of the influence of the heat affected zone from welding and the plastic strain concentrations caused by the link deformations. No localized plastic strain concentrations occurred in the web in the link length. The contours of the plastic shear strain showed lower demand at the ends of the link length as compared to mid-length and overall showed less plastic strain demand. Besides, Dusicka et al. (2004) carried out an experimental and numerical study on built up links with low yield point steel. In this way the web thickness could be increased and stiffeners excluded. From the strain demand perspective, removing the stiffeners from the link length eliminated the localized plastic shear deformations caused by the presence of web stiffeners. As a result, the initial cracking and ultimate failure mode occurred at significantly higher link deformations for links that did not utilized stiffeners.

2.2.4 Link energy dissipation

The ductile behaviour of EBs under severe seismic excitation relies on the capability of links to dissipate energy. For this reason, during the '70s and '80s, most of the experimental tests on steel links were carried out to quantify the energy dissipation capacity. Malley & Popov (1984) measured that the maximum ductility $\mu = \frac{\delta_{max}}{\delta_y}$ (where δ_{max} is the maximum relative link end displacement and δ_y is the relative link end displacement at yielding) varied from 31.9 to 66, while the cumulative ductility $\Sigma\mu$ (summation of μ for all cycles) from 237 to 751. The minimum values corresponded to unstiffened links, however all steel links manifested a significant energy dissipation capacity. Also, Kasai & Popov (1986a and 1986b) measured the link energy dissipation in their experimental activities. In particular, they measured:

1) E_e = elastic energy stored by the link at yield
2) E^* = the actual energy dissipated during each cycle

They verified that short links manifested larger values of E^* than longer links. Moreover they verified the existence of a constant relationship between E^*/E_e and a/t_w at the occurrence of web buckling.

As mentioned in the previous Sections, the main cause of energy absorption deterioration was the web buckling. In case of link with axial compressive force, the deterioration in energy was influenced by flanges buckling. In particular flange buckling more severely impaired the energy dissipation for the longer specimens than for the shorter ones.

Tests with an axial compressive force indicated the importance of preventing severe asymmetric local flange buckling in order to avoid premature failure. So an estimate of the flange yield zone length as it relates to the end moment is essential. Kasai & Popov (1986b) proposed a solution to define the shear link flange yield zone length. Their approach is summarized in Figure 2.17, in which e_i is the distance between the end of a link and the inflection point, while ρ is the ratio between the axial force and the shear force acting in the link.

In particular, they assumed that the critical distance l_y from the end is sufficient to make the idealization that flanges resist the moment and the web the shear force. This idealization was confirmed by the experimental tests, which indicated that the portion of shear taken by the web rapidly increased as the distance from the end increased. Hence, the yield zone length of flange in a shear link can be expressed as:

$$l_y = e_i\left(1 - \frac{M_p}{M_a}\right) + \rho\frac{M_p}{P_y} \tag{19}$$

where the first term is the contribution of bending and the second from the axial force.

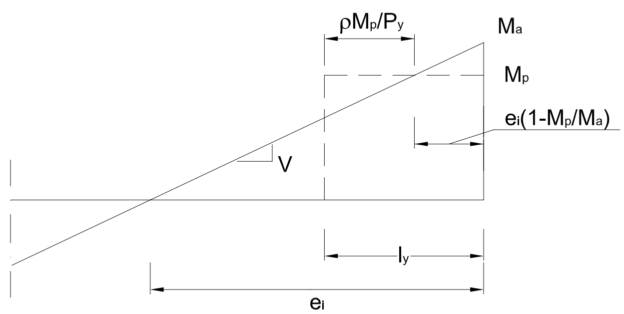

Figure 2.17. Yield zone length of flange in a shear link (Kasai & Popov, 1986b).

2.2.5 Link over-strength

One of the fundamental aspects characterizing the link behaviour is the over-strength factor defined as the ratio between the maximum shear force sustained by the element and the nominal shear yielding force (V_p).

Link over-strength is primarily due to strain hardening, but it can also be due to the development of shear resistance in the link flanges. The link over-strength factor is used to estimate the maximum forces that can be generated by a fully yielded link, which in turn, is then used to design the non-dissipative elements as the diagonal braces, the beam segment outside of the link and the columns of the EBs. Past researchers have generally recommended a link over-strength factor of 1.5 (Popov and Engelhardt 1988). Recently, the 2002 AISC Seismic Provisions specified a link over-strength factor of 1.25 for design of the diagonal brace, and an over-strength factor of 1.1 for the design of the beam segment outside of the link and for the columns. As described in the Commentary of the 2002 AISC Seismic Provisions, because of AISC consider the average yield strength of material, capacity design rules in the provisions are based on an assumed over-strength factor. The over-strength factor suggested by modern European design codes (Eurocode 8, 2003) is 1.5, a value basically coming from experimental results on American wide-flange shapes, carried out in the '80s (Kasai & Popov, 1986).

Test results demonstrate how the over-strength ratio varied significantly among the specimens and in most cases exceeded the expected values with a wide margin. In fact, recent tests on large built-up shear links for use in bridge applications and on European wide flange steel profiles showed over-strength factors greater than 1.5, reaching link over-strength of about 4 (Itani et al. 1998; McDaniel et al. 2003, Della Corte & Mazzolani 2005, Barecchia et al. 2006, D'Aniello et al. 2006).

Recently, in order to evaluate the consistency of this factor, numerous experimental tests have been carried out. Douglas (1989) suggests a value of about 2.0. Dusicka et al. (2004a) conducted some experimental tests and numerical studies on conventional and specialty steel for shear links and concluded that the over-strength factor ranges from 1.50 to 4.00. McDaniel et al. (2003) conducted cyclic tests on two full-scale built-up shear links for the main tower of the New San Francisco-Oakland Bay. The shear link over-strength factors were respectively 1.83 and 1.94.

The results of three experimental tests, carried out in the current research activity, showed values larger than 3.00 (Della Corte & Mazzolani 2006, D'Aniello et al. 2006).This has led to the concern that current over-strength factors may be unconservative, particularly for shapes with heavy flanges and in general for European wide flange hot rolled steel profiles (characterized by local slenderness ratio smaller than American ones), where shear resistance of the flanges can contribute significantly to over-strength. Moreover, these tests underlined the importance of the link boundary conditions. In fact, in case of end restraint conditions can be approximated as being fixed-fixed, It is contended that large deformations may produce an axial tension force whose effect is non-negligible. Tension axial forces are expected to increase ductility and peak inelastic shear strength.

Recently, Okazaki et al. (2004) conducted an experimental investigation to examine flange buckling and over-strength in links and this research program confirmed the importance of flange slenderness on rotational capacity and on the bearing capacity of short links, but the evidence of flange slenderness effects on link rotation capacity is still not clear. Moreover, the effect of link axial forces has been neglected.

2.2.6 Link end-connections

Link end-connections represent a crucial aspect. In fact, in order to provide the reliable and effective dissipative behaviour, the link end-connections should be able to transfer the maximum link forces to the remaining parts of the structure without any sort of damages.

Generally speaking, some of the typical EBs are arranged to have one end of the link connected to a column and, in the last years, the main research efforts have been addressed to study these local details. In such EBs, the integrity of the link-to-column connection is fundamental in order to provide the ductile performance of the link, and therefore, the ductile performance and safety of the EBF.

Malley and Popov (1984) observed that the large cyclic shear force developed in EBF links could cause repetitive bolt slippage in welded flange-bolted web connections. The bolt slippage ultimately induced sudden failure of the connection by fracture near the link flange groove weld. Engelhardt and Popov (1992) tested long links attached to columns, and observed frequent failures at the link-to-column connections due to fracture of the link flange. Since these failures typically occurred before significant inelastic deformation was developed in the link, the authors recommended that EB arrangements with long links attached to columns should be avoided.

Besides the exceptions discussed above, the most of EB link-to-column connections have been designed and detailed very similar to beam-to-column connections in moment resisting frames. Therefore, many of the features responsible for the poor performance of moment connections during the 1994 Northridge earthquake are also present in link-to-column connections in EBs.

Recently an experimental and analytical investigation has been conducted by Okazaki et al. (2004) to study the performance of link-to-column connections in seismic resistant EBs. They tested link-to-column specimens with four different connection types and three different link lengths for each connection type, ranging from a short shear-yielding link to a long flexure-yielding link. These link-to-column specimens failed by fracture of the link flanges near the groove weld (Figure 2.18). The Authors showed that the fracture typically developed rapidly, causing abrupt and severe degradation in the strength of the specimen. Moreover they report that link stiffeners provided an excellent buckling control by the left fracture at the link-to-column connection as the dominating failure mode of the specimens. Another important aspect underlined by the authors is that the performance of the link-to-column connection depended strongly on the link length, with the inelastic link rotation capacity decreasing significantly with the increase in the link length. In fact the effects of the link length are reflected in the substantial difference in link shear force and column face moment. Test results suggest that premature failure of the link flange is a concern not only for connections of a long link to a column, but also for connections with short shear links.

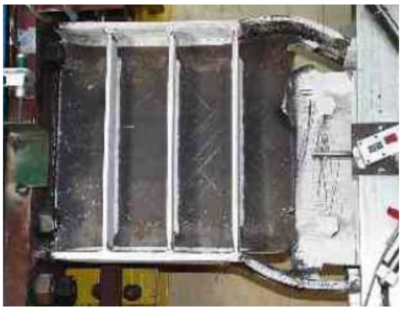

Figure 2.18. Failure of link-to-column connection (Okazaki et al. 2004).

2.2.7 Link modelling

Steel links are subjected to high levels of shear forces and bending moments in the active link regions. In the analysis of the performance of links, elastic and inelastic deformations of both the shear and flexural behaviours have to be taken into consideration. Few researchers attempted to develop link models for the dynamic inelastic analysis of EBs (Ricles & Popov 1994, Ramadan & Ghobarah 1995). Ramadan & Ghobarah modelled the link as a linear beam element with six nonlinear rotational and translational springs at each end. Three rotational bilinear springs were used to represent the flexural inelastic behaviour of the plastic hinge at the link end represented by the multilinear function shown in Figure 2.19a. Three translational bilinear springs were used to represent the inelastic shear behaviour of the link web represented by the multilinear function shown in Figure 2.19b.

Under the effect of cyclic loading, moment yielding obeys the kinematic hardening rule while shear yielding follows a combination of both isotropic and kinematic hardening. For the shear spring, a special function was derived to account for the upper bound of the shear capacity (Ramadan & Ghobarah 1995). The function determines the maximum attainable shear force capacity after a certain amount of plastic action. This function has the following form:

$$V = V_p \left[1 + 0.8 \left(1 - e^{-10S} \right) \right] \tag{20}$$

where V_p is the initial shear yield strength and S is the accumulated strain in the shear spring.

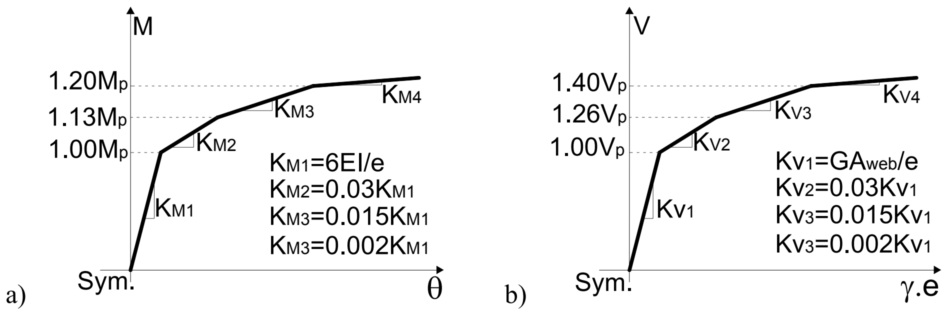

Figure 2.18. Flexural inelastic behaviour of link plastic hinge (a); Shear inelastic behaviour of link plastic hinge (b).

2.3 BUCKLING-RESTRAINED BRACES

Among seismic performance upgrading systems, there are several options normally available, one of which is to employ energy dissipation devices, such as friction, viscoelastic and metallic dampers, buckling-restrained braces (BRBs), etc.. Energy input by a strong earthquake is expected to be greatly dissipated by these devices, and if they are damaged they make the rehabilitation easy after the earthquake, since these devices are designed to be replaceable.

BRBs can be a good system for protecting reinforced concrete (RC) structures from severe earthquake damage. BRBs can provide stable energy dissipation capacity under seismic excitations with the same behaviour both in tension and compression. With these added energy-dissipating members, damage due to large plasticization is anticipated to occur in BRBs, while other members will be protected under strong earthquake actions.

In addition, BRBs represent the effective solution to the problem of the limited ductility of classic concentric bracing, thanks to the avoidance of global compression buckling. BRBs are characterized by the ability of bracing elements to yield inelastically in compression as well as in tension.

As shown in Figure 2.19, BRBs are characterized by a stable hysteretic behaviour and, differently from traditional braces; they permit an independent design of stiffness, strength and ductility properties.

Traditional brace, buckled in compression

BRB, unbuckled in compression

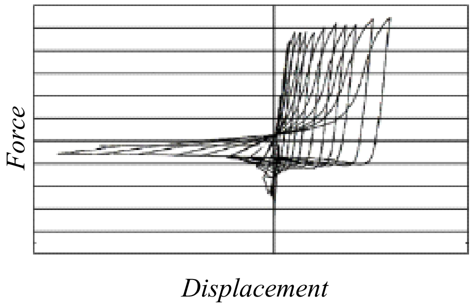

Hysteresis loop:
poor nonlinear behaviour

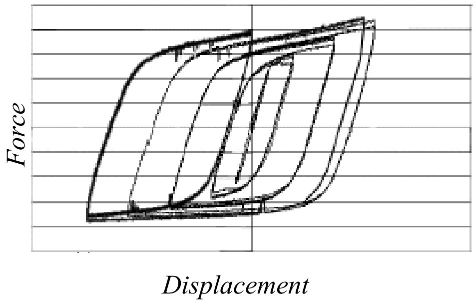

Hysteresis loop:
excellent nonlinear behaviour

Figure 2.19. Traditional brace vs buckling restrained brace.

This behaviour is achieved through limiting buckling of the steel core within the bracing elements. The axial strength is decoupled from the flexural buckling resistance; in fact, the axial load is confined to the steel core, while the buckling restraining mechanism resists overall brace buckling and restrains high-mode steel core buckling (rippling).

The first studies about inhibiting global buckling of braces in compression were developed by Wakabayashi et al. (1973). They developed a pioneering buckling restrained system in which braces (made of steel flat plates) were sandwiched between a pair of precast reinforced concrete panels (Figure 2.20).

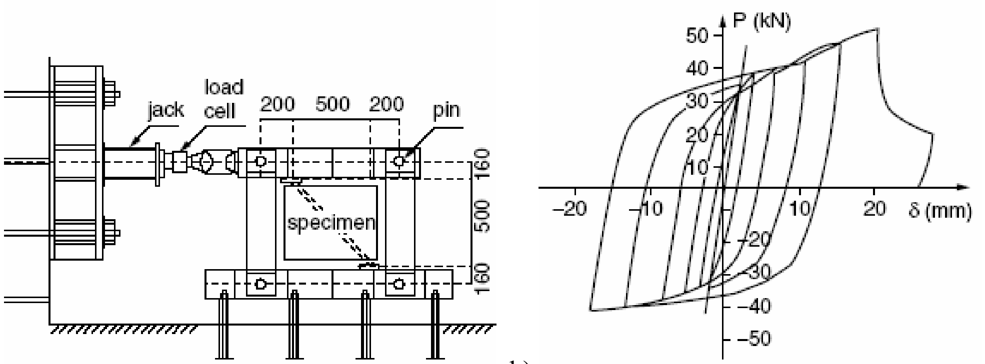

a) b)

Figure 2.20. Sub-assemblage test of buckling-restrained braces sandwiched between precast concrete panels: Test setup (a); hysteresis behaviour (b) (Wakabayashi et al 1973).

The research included the following: (1) pull-out tests to explore the methods of debonding, (2) compression tests of plates sandwiched between pre-cast panels to examine the required stiffness and strength for the panels, (3) sub-assemblage tests to examine the effectiveness of end connection details and (4) two-story frame tests for system verification. In the pull-out tests, epoxy resin, silicon resin, vinyl tapes, etc. were experimented as the debonding material and it was concluded that a layer of epoxy resin covered by silicon resin was most effective as the debonding material in terms of debonding effect, constructability and durability. In the compression tests various reinforcing details were adopted for the pre-cast concrete panels, and a special emphasis was placed on the reinforcement along the edges of the panels. Inadequate reinforcement at these locations was found to cause damage earlier in the loading cycles because of the transverse forces that were produced by the out-of-plane deflection of the braces. In the sub-assemblage test, a pair of flat plates, arranged in either a diagonal or chevron pattern, was connected to a pin-connected steel frame and encased by pre-cast concrete panels; the specimens were about 1/5 in scale. It was confirmed that the embedded flat plates were uniformly strained. At higher deformation levels the strength of the brace in compression (i.e., positive d value) is higher than that in tension. In the system verification tests, 2 two-story and 2 two-bay frames of about a half scale, one with braces arranged diagonally and the other with braces arranged in a chevron pattern, were cyclically tested (Figure 2.21). Although the compressive strength of an individual brace is higher than the tensile strength at higher deformation levels.

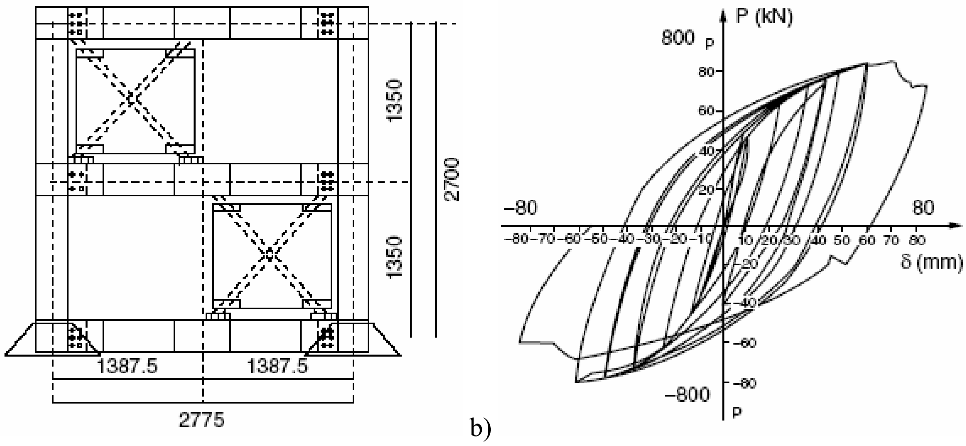

Figure 2.21. System test of buckling-restrained braces sandwiched between precast concrete panels: Test setup (a); hysteresis behaviour (b) (Wakabayashi et al 1973).

Extending the concept of Wakabayashi et al. (1973), various developments on BRBs with a steel core confined by a steel casing were made in Japan from the second part of the 1970s up to 1990s. Among the first researchers, Kimura et al (1976) studied and tested the first example of a steel brace able to dissipate energy without buckling. This early type of BRB consisted of a conventional brace encased in a square steel pipe filled with mortar. These braces were characterized by few stable hysteretic characteristics, because of the transverse deformation of the mortar resulted in permanent void space that were large enough to allow local buckling. Mochizuki et al. (1980) conducted tests on similar braces, which were wrapped in reinforced concrete, with the concrete kept from adhering to the internal brace by use of a shock-absorbing material. It was found however, that under repetitive loading, the concrete cracks and its buckling restraining effect diminishes (Wada et. al 1989). This concept was further refined by Fujimoto et al. (1988), Watanabe et al. (1988) and Wada et al.(1998) and lead to the so called unbonded brace (Figure 2.22).

It consists in a ductile steel core (rectangular or cruciform plates, circular rods, etc.) either in a continuous concrete filled tube.

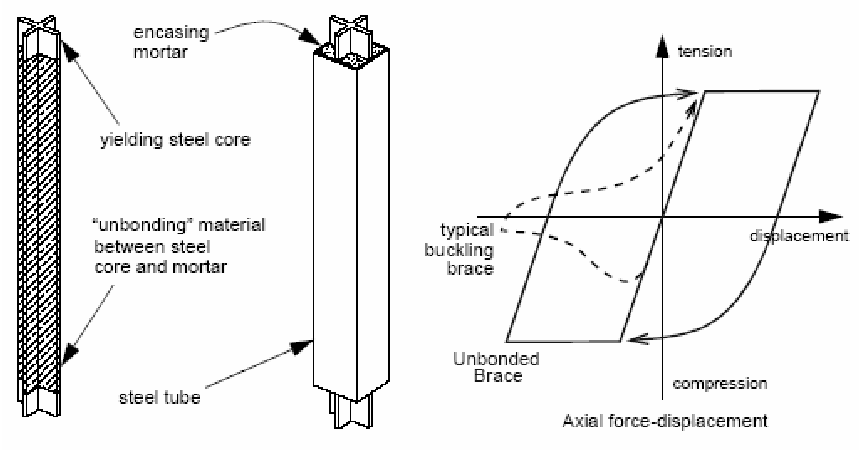

Figure 2.22. Geometrical scheme of a typical Unbonded Brace.

Watanabe et al. (1988) studied the influence of the ratio between the Euler buckling load (N_e) of the sleeve and the actual yield force (N_y) of the internal steel core (N_e/N_y). A total of five specimens were tested, three of them were designed to have the ratio of N_e/N_y larger than 1, while the last two specimens below 1. Each specimen was loaded cyclically up to 2% story drift. Test results showed that specimen designed with N_e/N_y <1 buckled globally in compression, while the remaining three specimens exhibited stable and symmetric hysteresis under both tension and compression. Afterwards Watanabe et al. suggested that for practical applications the N_e/N_y ratio be at least equal to 1.5.

In the next year, a part from the above-mentioned "unbonded", a number of different typologies of BRBs have been suggested such as enclosing a steel core within a continuous steel tube, or within a tube with intermittent stiffening fins, and so on. The assembly is detailed so that the central yielding core can axially deform in independent manner from the mechanism that restrains lateral and local buckling. Through appropriate selection of the strength of the material, and the areas and lengths of the portions of the core that are expected to remain elastic and to yield, a wide range of brace stiffness and strength can be attained. Since lateral and local buckling behavior modes are restrained, large inelastic capacities are attainable.

Nagao and Takahashi (1990) developed a BRB composed of a wide flange section encased in a reinforced concrete member and in their experimental study they evaluated the reinforcing, stiffness and strength requirements of the concrete casing. Moreover, among the first, Kuwahara and Tada (1993), Manabe et al. (1996), Suzuki et al. (1994), Shimizu et al. (1997) studied the use of an only steel BRB, adopting hollow steel tube as restraining unit. However, the simplicity of its design and the outstanding performance of the unbonded brace have attracted the interest of industry and have been made commercially available by Nippon Steel Corporation. Up today, more than 300 buildings have been equipped with ‘unbonded’ braces manufactured by Nippon Steel Corporation. In particular, after several tests carried out in 1999 at the University of California, Berkeley, the technology has also been implemented in the US, by utilizing BRBs for the seismic retrofitting of the UC Davis Plant and Environmental Sciences. An other significant example in this sense was the Wallace F. Bennett Federal Building (Salt Lake City, Utah, USA), an 8-story RC building constructed in the early 1960s and then seismically retrofitted by BRBs placed externally. As shown in Figure 2.23, this intervention also successfully satisfy architectural needs. In fact, in this case, BRBs have been used as architectural elements (Brown et al. 2001).


Before the seismic retrofitting with BRB


After the seismic retrofitting

Figure 2.23. Wallace F.Bennet Federal building (USA).

In Italy, BRBs have been successfully adopted for seismic protection of one building of the University of Ancona (Figure 2.24).

Figure 2.24. University of Ancona (Italy).

Different types of BRBs (Figure 2.25) have been studied, all based on the basic concept to use tubes for restraining lateral displacements while allowing axial deformations of the core.

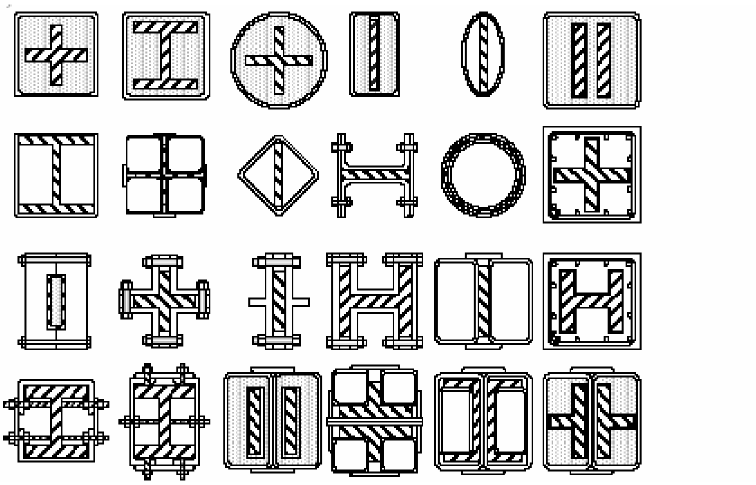

Figure 2.25. Typical types of BRBs (Tsai et al. 2004a).

In the most classical form, the restraining tube is filled with concrete and an unbonding layer is placed at the contact surface between the core plates and the filling concrete, thus this version is called ‘unbonded brace’. The unbonding material both ensures the brace to freely slide inside the buckling restraining unit and lets transverse expansion of the brace to take place when the brace yields in compression. ‘Only-steel’ solutions have been also proposed, with two or more steel tubes in direct contact with the yielding steel plates. In the latter case, the restraining tubes can also be connected by bolted steel connections, thus allowing an easy inspection and maintenance during the life-time or after a damaging earthquake (Tsai et al. 2004a). An adequate gap size between the brace and the restraining tubes is also required in case of "only-steel" BRBs, in order to provide the necessary space for relative deformation between both members.

The BRB technology is currently ongoing a strong development, with a growing number of buildings using buckling restrained braces as primary lateral force-resisting system. This strong development is also testified by several research studies which are ongoing in the US, Taiwan, Japan (Tsai et al. 2004, Sabelli & Aiken 2004, Wada & Nakashima 2004) and in Italy too (Della Corte et al. 2005, D'Aniello et al. 2006). In particular, in USA now three industrial proprietary BRBs have been developed. These BRBs feature a steel core encased in a concrete-filled steel hollow tube. Chronologically, the first patented BRB uses flat or cruciform steel core with bolted end splice connections (Figure 2.26). To facilitate erection, holes on the gusset plate and brace are oversized; faying surfaces of the gusset and connection plates were also sandblasted to reduce the number of high-strength bolts, and hence the length of gusset connection. Satisfactory performance has been demonstrated from both uniaxial testing and sub-assemblage testing (Merritt et al., 2003a). The second industrialized patent uses a pin-and-collar assembly at each end of the brace (Figure 2.27). The use of a pin connection at the gusset plate isolates the brace from any moment or shear that could be transmitted because of frame drift. Also by directly connecting the brace to the gusset by using a pin, the overall connection length is reduced, resulting in a long yielding core that reduces the axial strain. The pin also reduces the number of pieces being connected. The collar assembly adds to the overall stability of the brace by preventing out-of-plane buckling of the core section extending beyond the confining unit. The third industrialized development uses a prismatic steel core along the entire length of the brace; each end is reinforced with welded stiffeners for the bolted splice connection with oversized holes for ease of erection. Uniaxial testing (Merritt et al., 2003c) has also been conducted to verify the cyclic performance.

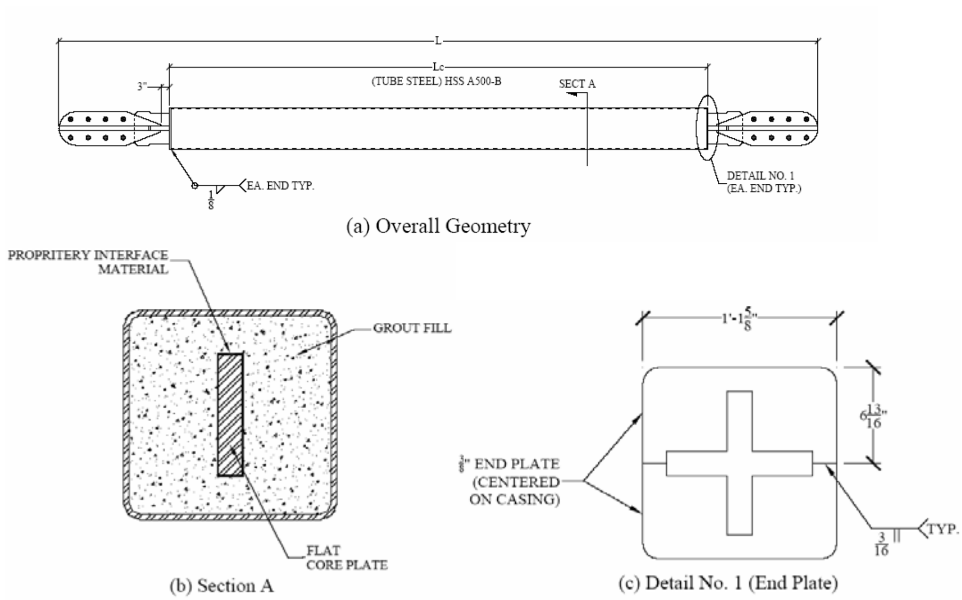

Figure 2.26. First patented BRB developed in USA (COREBRACE patent).

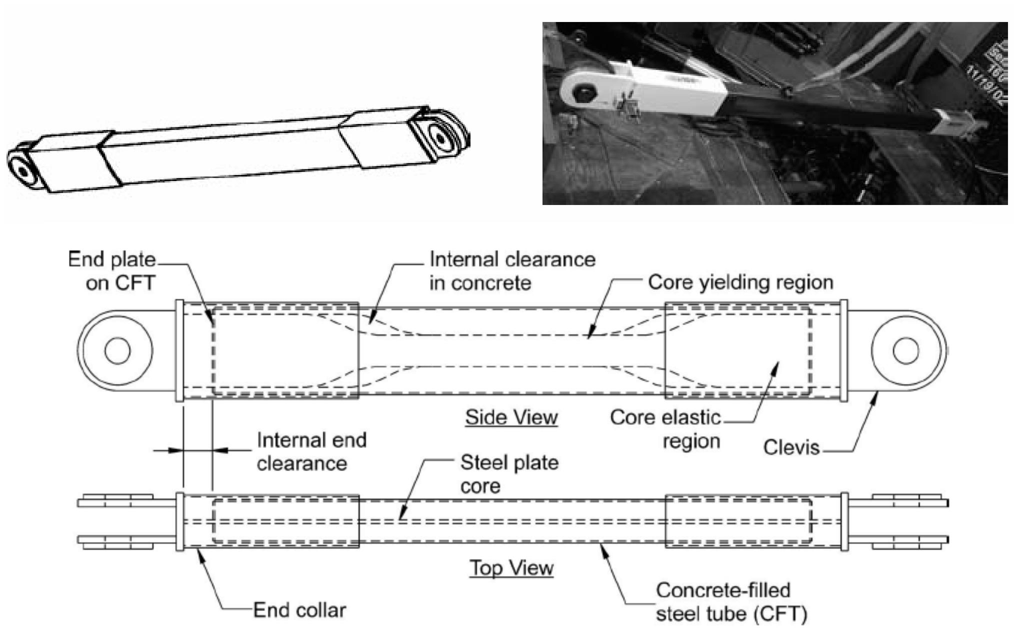

Figure 2.27. Second patented BRB developed in USA (STAR-SEISMIC patent).

Parallel to US applications, in Taiwan Chen et al. (2002) studied the cyclic behaviour of a type of BRB with low-yield strength steel. The brace, called buckling-inhibiting brace (BIB), used a concrete-filled tube to confine the steel plate (Figure 2.28). A layer of silicon grease was used a debonding material. The adopted low-yield steel did not have a well-defined yield plateau, but the ultimate strain was very high (>50%). For the first time a stopper at the center of the load-carrying element that was inserted into the core in order to center the buckling-restrained system and to prevent it from slipping down.

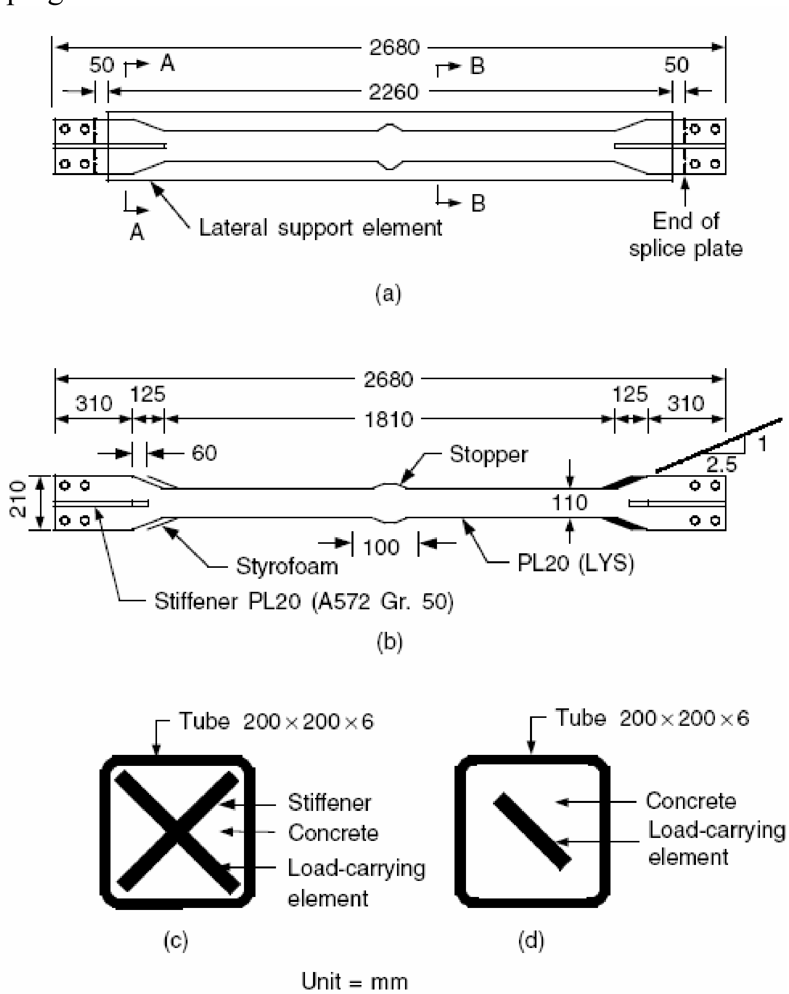

Figure 2.28. Details of buckling-inhibiting brace. (a) Overall view; (b) load-carrying element; (c) A–A section; (d) B–B section (Chen et al. 2002).

The experimental studies on this typology showed that the maximum compressive strength was much higher than the maximum tensile strength. As a result, Chen et al. suggested that this type of bracing be used in a diagonal configuration, not V or inverted-V configuration. Chen et al. (2002) also investigated the steel-only BRBs with built-up steel sections as the buckling-restraining mechanism.

More recently, Tsai and Lai (2002) studied the effect of unbonding material on the cyclic response of BRBs. A total of 10 identical braces were tested, the only difference being the unbonding materials used. They demonstrated that the axial load difference $\Gamma=(C_{max}-T_{max})/T_{max}$ is equal to 2ε, where C_{max} and T_{max} are the maximum compressive and tensile brace strengths at a given axial deformation level, while ε is the axial brace strain. The above equation shows that Γ is about 4% for $\varepsilon = 2\%$. But the test results show much higher Γ values, precisely 30% for $\varepsilon = 2\%$. Other than the Poisson's effect, factors such as the friction between the steel core yielding element and mortar also contribute to the higher brace strength in compression cycles.

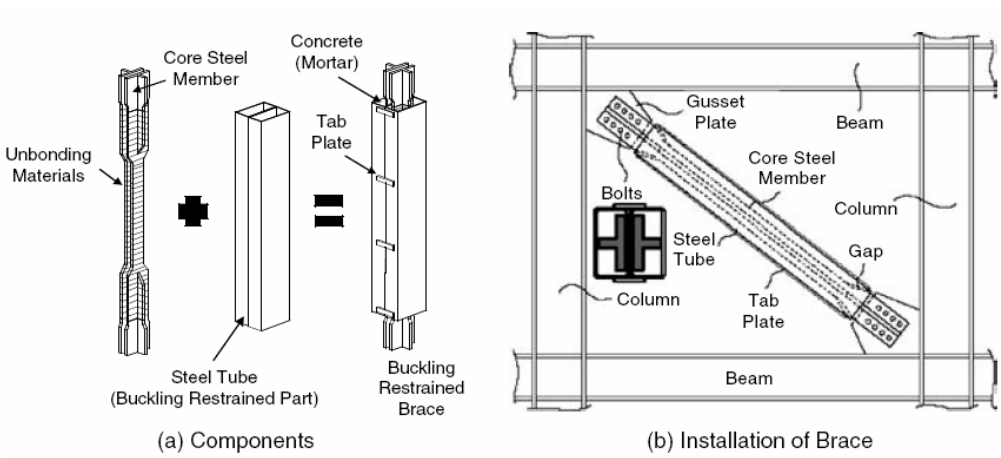

Figure 2.29. Double-tube buckling-restrained brace. (Tsai, K.C. and Lai, J.W. 2002).

Moreover, to reduce the size of the connections and to improve the constructability in the field, double-tube BRBs have been developed and extensively tested by Tsai and Lai (2002) (Figure 2.29). Each brace is composed of two identical parts. Each part comprises a steel core, which is either a plate or a structural tee, encased in a rectangular steel tube. Both ends of the steel core are tee-shaped, thus each part of the brace can be conveniently connected in the field to the gusset in the same manner as the conventional double-T brace is connected to gusset plate connections. Tsai et al. (2004) proposed a detachable BRB type, to provide the possibility of disassembling the BRBs for inspection after an earthquake or during the life-time. They studied several configurations of bolted connection for joining together the restraining tubes. Their test results suggest that the all metallic and detachable BRBs can stably sustain severe cyclic increasing and constant fatigue inelastic axial strain reversals.

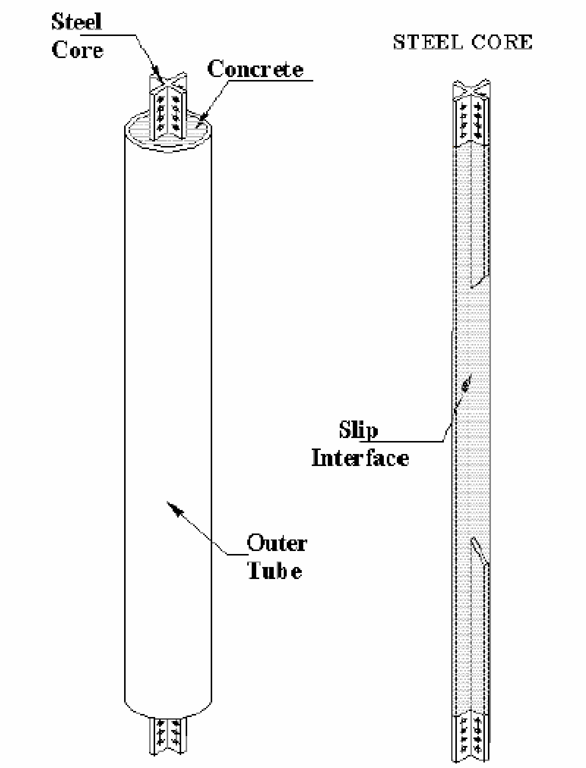

Figure 2.30. Scheme of the Italian patented buckling restrained axial damper on the left and its steel core member on the right (FIP patent).

In Italy, the first studies about BRBs are relatively recent. Both unbonded and only steel BRBs have been studied. One Italian unbonded proprietary

BRB type has been developed (Figure 2.30). It is very similar to the Japanese typologies, in fact it is made of a steel rectangular core restrained by a steel sleeve infilled by high strength mortar. These BRBs (called Buckling Restrained Axial Damper or BRAD) have been successfully adopted for seismic protection of one building of the Faculty of Engineering of Ancona (Antonucci et al. 2006). It represents the first professional application of buckling restrained braces in Italy and Europe (Figure 2.31).

Figure 2.31. Two BRADs installed in the new building of the University of Ancona (Antonucci et al. 2006).

In Italy, parallel to these applications only-steel BRBs have been studied too (Della Corte et al. 2005, D'Aniello et al.2006). These devices have been studied and develop in the contest of the current research activity. Contrary to the "unbonded", this type of BRBs can be designed to be detachable. This aspect implies that is possible to design these systems to be inspected, so that it is possible to control their condition after each seismic event and to allow an ordinary maintenance during the life-time. To do this the restraining tubes should be connected by bolted steel connections. Moreover an 'only-steel' BRB is lighter than an 'unbonded' one; this implies a technical and economical advantage during the assembling. These considerations led to study a special only-steel detachable BRB to be used for improving the seismic response of RC buildings. Therefore, this research has been one of the main the topic of the current work.

2.3.1 BRB design concept

Yielding of this special type of bracing occurs when the plastic strength of the core steel plates is achieved. The axial stiffness is determined by the combination of two or more springs in series, having the axial stiffness of the internal core and terminal tapered plates. Length and size of the latter can be independently fixed to some extent. In any case, the possibility to avoid compression buckling allows very slender steel plates to be used as core of the BRB, with a relatively low plastic strength and without impairing the system ductility. In this way, yielding of the BRB can be regulated to very low inter-story drifts, thus permitting the dissipative action to be activated soon.

The basic principle, that characterizes the BRB response, is based on the possibility of decoupling of the axial-resisting and flexural-resisting aspects in the compression field. In fact, the steel core plate has to resist axial stresses, while buckling resistance is provided by a sleeve, which may be of steel, concrete or composite.

Figure 2.32 shows the parts which constitute a common BRB. It is possible to divide the core into three zones: the yielding zone, that has a reduced cross section area within the zone of lateral restrain provided by the sleeve (zone C); the transition zones, which have a larger area than the one of the yielding zone, and similarly restrained (zone B); the connection zones, which extend past the sleeve and connect to the frame by means of gusset plates (zone A).

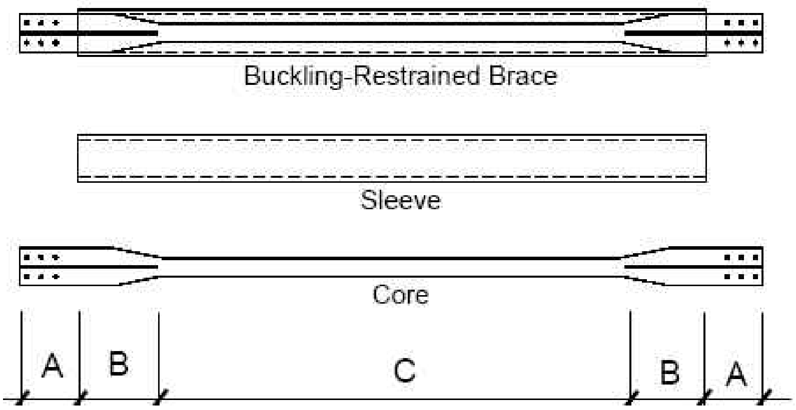

Figure 2.32. Schematic view of a typical BRB element (Sabelli & Lopez 2005).

2.3.2 Global stability of BRBs

Assuming that local buckling does not occur along the steel core, the global stability of BRBs can be estimated directly from the Euler theory of buckling. Figure 2.33a shows the schematic of a BRB in compression, while Figure 2.33b and c show the distributed forces on the steel core and the retaining tube in their deformed configuration (Black et al. 2002).

a)

b)

c)

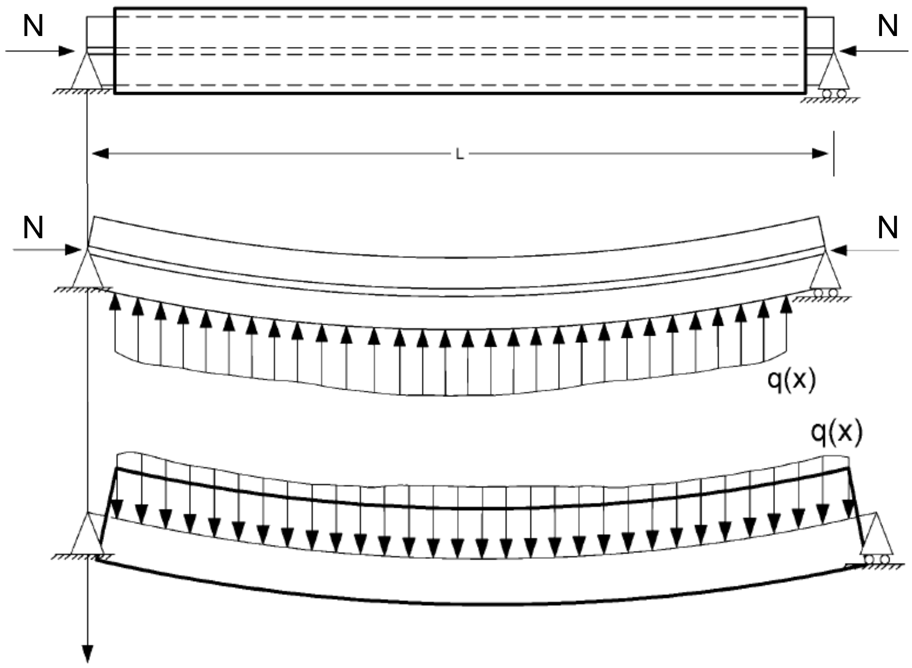

Figure 2.33. (a) BRB under axial loading, (b) distributed load along the inner core at its deformed configuration, (c) distributed load along the outer tube (Black et al. 2002).

The unknown distributed load shown in Figure 2.33b is the transverse reaction of the outer tube along the inner steel core. Following the system of axis shown in Figure 2.33, the equilibrium of the inner steel core in its deformed configuration is given by:

$$E_i I_i \frac{d^4 y(x)}{dx^4} + N \frac{d^2 y(x)}{dx^2} = -q(x) \tag{21}$$

where I_i is the second moment of area of inner core and $q(x)$ is the distributed reaction of the outer tube. So, because the deflection of the inner core is the same as that of the retaining unit, the equilibrium of the outer tube in its deformed configuration is given by (Black et al. 2002):

$$E_o I_o \frac{d^4 y(x)}{dx^4} = q(x) \tag{22}$$

Using Equations 21 and 22 a homogenous Euler equation is obtained:

$$\frac{d^4 y(x)}{dx^4} + \frac{N}{E_i I_i + E_o I_o} \frac{d^2 y(x)}{dx^2} = 0 \tag{23}$$

For a brace with length L, Equation 23 yields the critical buckling load of the brace:

$$N_{cr} = N_e = \frac{\pi^2}{(KL)^2}\left(E_i I_i + E_o I_o\right) \tag{24}$$

where KL is the effective (or equivalent) length (K = 1 for pinned ends and K = 0.5 for fixed ends). Since the bending rigidity of the inner steel core, $E_i I_i$, is two to three orders of magnitude smaller than the bending rigidity of the encasing mortar/outer tube, $E_o I_o$, Equation 24 simplifies to (Black et al. 2002):

$$N_{cr} = N_e \simeq \frac{\pi^2 EI_{tube}}{(KL)^2} \tag{25}$$

where E and I_{tube} are the Young's modulus and moment of inertia of the outer tube, respectively. The flexural resistance of the encasing mortar has been neglected. Therefore, Equation 25 indicates that the critical load of the unbonded brace is merely the Euler buckling load of the outer tube. Accordingly, the global stability of the brace is ensured when the Euler buckling load of the tube, N_{cr}, exceeds the yielding load of the core, $N_y = f_y A_{core}$.

2.3.3 Key Mechanical Properties of BRBs

In order to properly confine the BRB inelastic deformations inside the restraining tube, the cross sectional area (A_c) of the energy dissipation core segment (L_c) is smaller than that of the end joint regions (L_j).

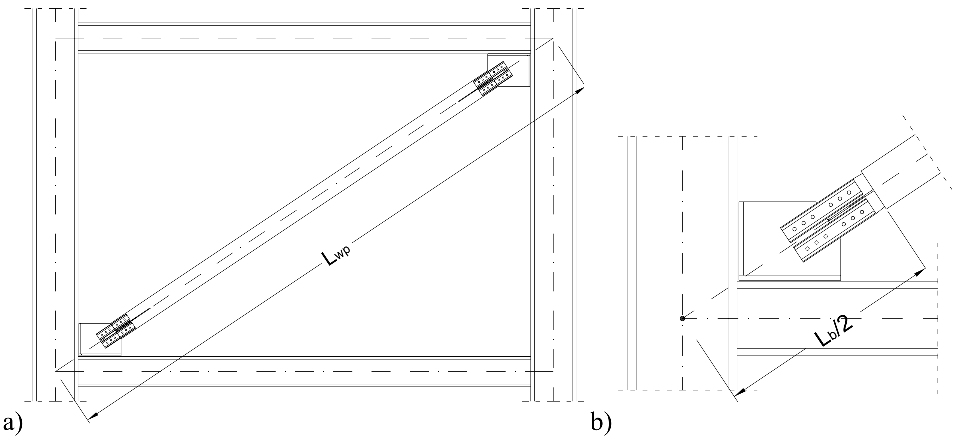

Figure 2.34. Dimensions of theoretical total BRB length (node-to-node length) (a); Dimensions of theoretical effective length of end connections (b) (Tsai et al. 2004a,b).

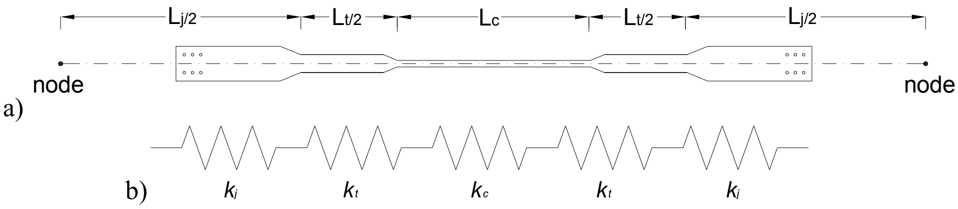

Figure 2.35. Profile of steel core member in BRB.

A schematic configuration of a BRB in the frame is illustrated in Fig. 2.34a, in which L_c and L_{wp} represent the core length and the node-to-node length, respectively. Between the end and the core segment, a transition region can be deviced as illustrated in Figure 2.35a. Moreover, referring to Figure 2.35b, it is confirmed by tests (Lin et al. 2004, Tsai & Huang 2002) that the effective stiffness, K_e of the BRB, considering the variation of cross sectional area along the length of the brace, can be accurately predicted by:

$$K_e = \frac{1}{\sum \frac{1}{k_i}} = \frac{EA_j A_c A_t}{A_j A_t L_c + 2A_c A_t L_j + 2A_c A_j L_t} \tag{26}$$

which simply combines axial stiffness of three axial springs connected in series.

According to Tsai et al. 2004, the relationship between the brace overall strain (ε_{wp}) and the inter-story drift θ can be approximated as:

$$\varepsilon_{wp} = \frac{\theta \cdot sin2\varphi}{2} \tag{27}$$

where φ is the angle between the brace and the horizontal beam as illustrated in Figure 2.36. The strain-to-drift ratio versus the beam angle φ relationship given by Equation 27 is plotted in Figure 2.37.

Introducing the ratio between the core length and the node-to-node length:

$$\alpha = \frac{L_c}{L_{wp}} \tag{28}$$

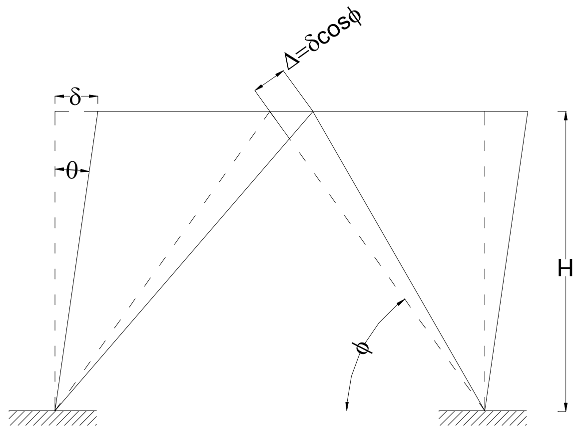

Figure 2.36. Brace deformation vs inter-story drift angle (Tsai et al.2004a,b).

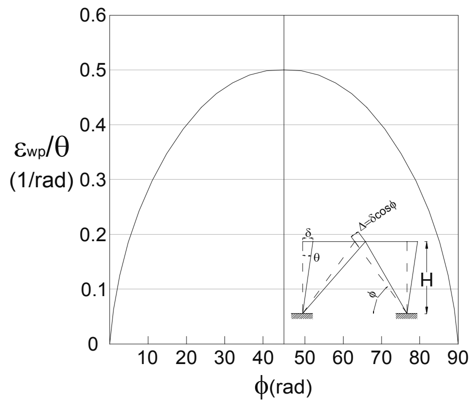

Figure 2.37. Brace strain to story drift ratio vs brace angle relationship (Tsai et al.2004a,b).

The following upper bound to the BRB core strain (ε_c) can be defined:

$$\varepsilon_c \leq \frac{\varepsilon_{wp}}{\alpha} \tag{29}$$

Since the elastic strain outside the core segment is relatively small compared to the inelastic core strain, from Equations 27 through 29, it can be found that if the inter-story drift demand is 0.02 radians, then the peak core strain would be close to 0.02 for a BRB having a length aspect ratio α = 0.5 and oriented in a 45 degree angle.

A significant aspect of BRBs is their hardening behaviour (Figure 2.38), which includes both isotropic and kinematic components. Tests typically result in hysteretic loops having nearly ideal bilinear hysteretic shapes, with moderate kinematic and isotropic hardening evident.

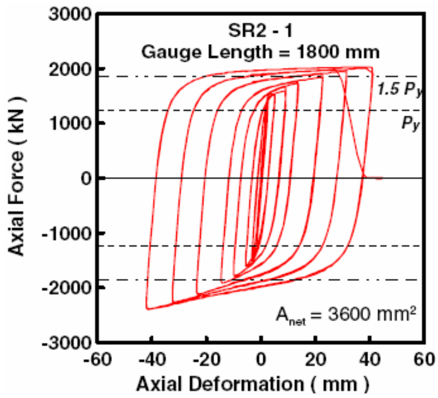

Figure 2.38. Hysteresis loop of BRBs (Tsai et al. 2004a,b).

The following equation may be applied when estimating the maximum compressive strength possibly developed in a BRB (Tsai et al. 2004b):

$$N_{max} = \Omega \cdot \Omega_h \cdot \beta \cdot N_y \tag{30}$$

where $N_y = A_c f_y$ is the nominal yield strength of the core section, Ω and Ω_h take into account the possible material over-strength and strain hardening factors of the core steel, respectively, and the bonding factor β represents the imperfect unbonding, i.e. the fact that the peak compressive strength is somewhat greater than the peak tensile strength observed during large deformation cycles.

The lateral strength of the BRB device is closely related to the lateral stiffness of the support element. Chen (2002) suggested that the nominal limit strength in compression N_{max}, sustained by the outer retaining tube, can be calculated according to the following relationship:

$$N_{max} = \frac{N_E}{1 + N_E \delta_o / M} \tag{31}$$

where N_E is the Euler buckling load of the restraining unit, δ_o is an initial crookedness, usually assumed equal to $L/1000$ and M is the bending moment at midlength of the lateral restraining unit. Then re-arranging Equation 31 the maximum moment M_{max} can be written as:

$$M_{max} = \frac{N_{max}\delta_o}{1 - N_{max}/N_E} \tag{32}$$

Introducing the yielding moment of the encasing member M_y, the stiffening criterion (Xie 2005) can be written as follows:

$$M_{max} < M_y \tag{33}$$

Based on Equations 32 and 33, according to Xie (2005), the overall buckling criterion can be expressed as:

$$\left(1 - \frac{1}{n_E}\right) m_y > \frac{\delta_o}{L} \tag{34}$$

in which:

$$n_E = \frac{N_E}{N_y} \text{ and } m_y = \frac{M_y}{N_y L} \tag{35}$$

where n_E and m_y are non-dimensional parameters corresponding to the flexural stiffness EI_{tube} and moment strength M_y of the restraining member, respectively.

When some gaps between steel cores and encasing members are designed, the stiffening criterion expressed in Equation 34 can be modified into the following expression:

$$\left(1 - \frac{1}{n_E}\right) m_y > \frac{\delta_o + s}{L} \tag{36}$$

in which s is the size of the gap (which usually varies from 0.7 to 3.5 mm).

Therefore, referring to Equation 25, the required stiffness of the steel sleeve in order to prevent the BRB from a global flexural buckling is given by (Watanabe et al. 1988):

$$I_{tube} = FS \cdot \frac{N_{max}\left(KL\right)^2}{\pi^2 E} \qquad (37)$$

FS being a safety factor which considers imperfections.

Global buckling failure modes of BRBs may be also triggered by incorrect design of end connections. In fact, in order to prevent the instability of the lateral restraint and to permit the full axial yielding of the steel core, the end-connections of these devices have to be able to transfer forces to the core without the development of a significant stress in the sleeve.

Because the core length changes when the BRB yields, in order to permit inelastic deformations of the steel core, the ends of the sleeve are detailed so that for the core there are no possibilities of bearing on it (Figure 2.39). This is obtained by interposing an interior reserve space.

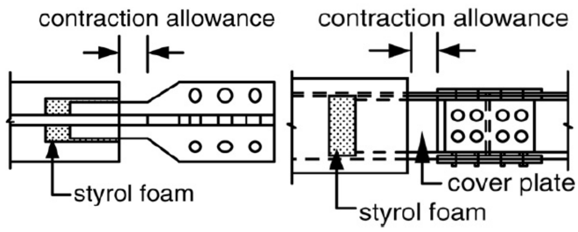

Figure 2.39. End detail of a BRB element (Xie 2005).

Furthermore, the end-connections have to be designed to avoid modes of overall instability of the bracing member such as shown in Figure 2.40 (Watanabe et al. 1988, Tsai et al.2004a).

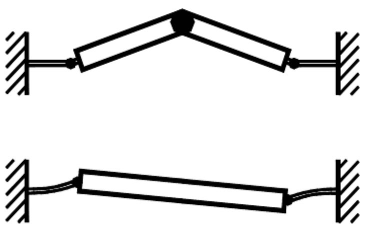

Figure 2.40. Typical undesirable modes of overall instability for BRBs (Sabelli & Lopez 2005).

Hence, it is recommended that the following stability criterion be met for connection details:

$$N_{e,trans} = \frac{\pi^2 EI_{trans}}{(KL_b)^2} \geq N_{max} \tag{38}$$

where N_{max} is given in Equation 30, EI_{trans} is the flexural stiffness of the core member at a section near the end of the steel tube and KL_b is the effective (or equivalent) length, where K is usually assumed equal to 1 and L_b is two times the length measured from the theoretical brace node to the end of the sleeve (Figure 2.34b).

Finally, in order to allow the extension and contraction of the two ends of a BRB, a "stopper" such as shown in Figure 2.41, to lock the core into the restraining concrete or other buckling restraining part, has been adopted to prevent the buckling restrainer from slipping off.

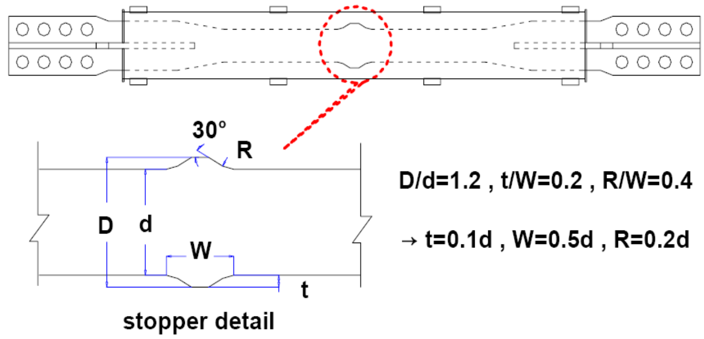

Figure 2.41. Detail of the stopper (Tsai et al. 2004a).

2.3.4 Brace Rotational Deformation

The current practice in U.S.A. is that BRBs are usually manufactured rather than built. That is, they are typically made by a specialty manufacturer, rather than by a contractor or steel fabricator (although such a method of producing them is possible). Specifications should address the furnishing of the braces, including the associated brace-design calculations and quality-control procedures, and the documentation of successful tests that qualify the furnished braces for use in the project.

AISC/SEAOC Recommended Provisions for Buckling-Restrained Braced Frames (2001) requires that experimental tests have to be carried out to provide assurance that certain failure modes do not limit the performance of BRBs. In particular two types of brace tests are required by the Recommended Provisions. The first is a uniaxial test in which braces are loaded axially and cycled through displacements based on the design story drift until they have dissipated a sufficient amount of energy.

The second type of brace test is called a subassemblage test. In this test braces are loaded axially while the end connections are rotated to simulate the conditions to be expected when braces are employed in a frame. Rotations can be imposed in a number of ways:

1) braces can be loaded on an eccentric path, so that a rotational deformation proportional to the axial deformation is imposed (Figure 2.42a);
2) a constant rotational deformation can be maintained while the brace is cycled axially (Figure 2.42b);
3) a column-brace assembly can be tested (Figure 2.42c);
4) finally, a full frame can be tested (Figure 2.42d).

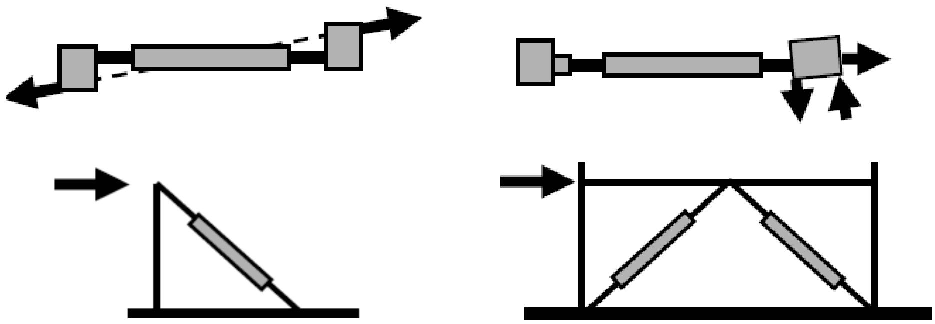

Figure 2.42. Subassemblage tests according to AISC/SEAOC Recommended Provisions for BRB Frames: eccentric loading of brace (a); loading of brace with constant imposed rotation (b); loading of Brace and Column (c); loading of braced frame (d).

The subassemblage test is of great importance because it is intended to verify that the brace-end rotational demands imposed by frame action will not compromise the performance of the brace.

In this sense Nishimoto et al. (2004) studied the bending deformations that occurred in the brace test specimens shown in Figure 2.43.

These tests were directed at providing assurance that certain failure modes do not limit the performance of the BRBs and thereby of the whole system. In the subassemblage tests, braces were loaded axially while the end connections are rotated to simulate the conditions to be expected when braces are employed in a frame.

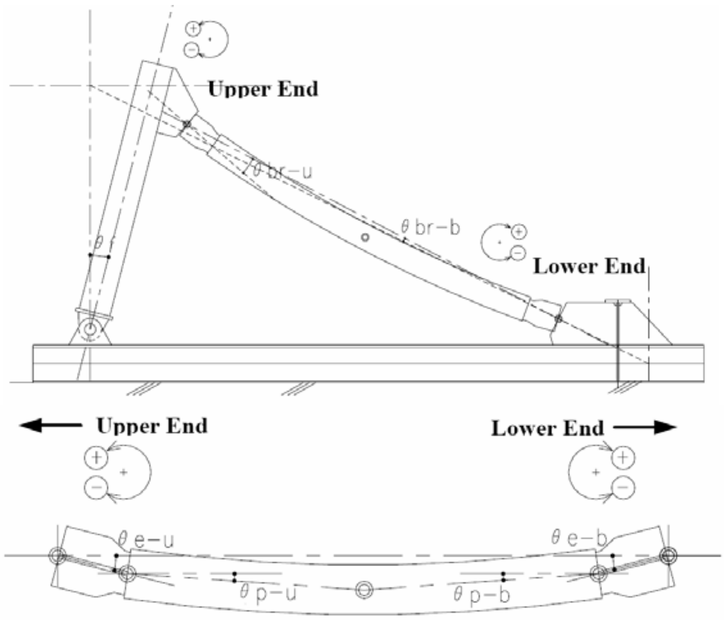

Figure 2.43. Definition of rotational deformation (Nishimoto et al. 2004).

The specimens were subjected to a loading program consisting of elastic and post-yield cycles of displacement with increasing amplitude based on the recommendations for Qualifying Cyclic Tests of Buckling-Restrained Braces contained in the AISC/SEAOC Recommended Provisions for Buckling-Restrained Braced Frames (2001). The loading program (Figure 2.44) was designed to impose pre- and post-yield, fully reversed, displacement corresponding to: the brace yield displacement, 0.5, 1.0 and 1.5 times the maximum expected brace deformation at the design story drift, as well as the brace deformation corresponding to 2.5% story drift. For the purposes of the testing program, the design story drift was assumed to be 1.5%. Additional loading cycles corresponding to 3.0% story drift were imposed on the braces in order to study the fatigue characteristics of the braces. Hence they measured for each specimen:

1) the column rotation, θ_f,
2) the brace axis rotations, θ_{br-u} and θ_{br-b},
3) the brace end rotations, θ_{e-u} and θ_{e-b} and
4) the flexural rotations of the steel tube, θ_{p-u} and θ_{pb}.

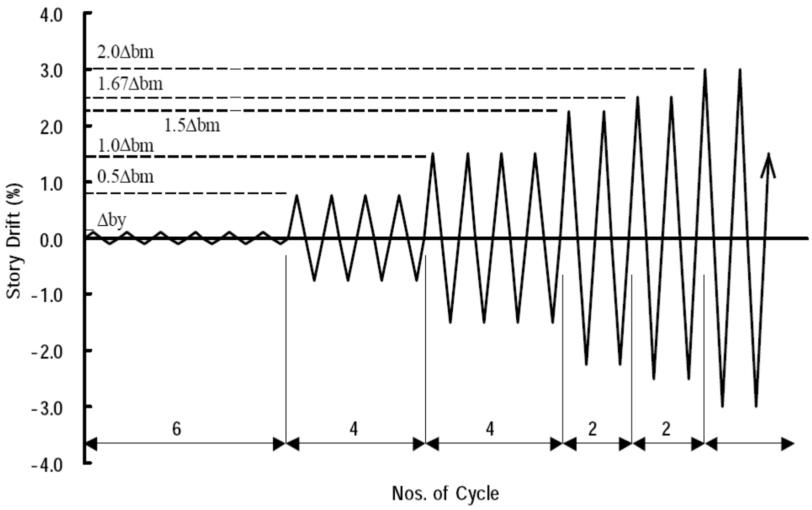

Figure 2.44. Brace loading history (AISC/SEAOC Recommended Provisions for Buckling-Restrained Braced Frames 2001).

It was seen that for the longer braces, the upper end of the brace (connected to the propped column) experienced rotations three to five times greater than at the lower end (connected to the floor), while for the shorter braces the difference in rotational deformation between the upper and lower brace ends was less significant. Besides, the experimentation showed that the flexural rotations at the ends of the steel tube, θ_{p-u} and θ_{p-b}, are similar. Moreover it was observed experimentally that the rotational deformation of the end of a brace depends on its inclination, and that the rotational deformation was greater at the brace end connected to the propped column than at the lower end. This result was particularly true for the longer braces (with smaller inclination angle). Finally test results demonstrated that the flexural engagement of BRBs can impair the brace ductility capacity and the overall fatigue resistance (as more in detail explained in the following Section) respect to braces subjected to uniaxial loading only.

2.3.5 Fatigue Properties

Up to now, experimental test results indicate that BRBs may be characterised by very large cumulative ductility capacity, with average values larger than 1000 (Black et al. 2002, Merrit et al. 2003). This large cumulative ductility capacity has been established using a maximum ductility demand not larger than 15. However, some analytical studies (Sabelli et al. 2003, Fahnestock et al. 2003) indicate that larger maximum ductility demands could be expected under real earthquakes. In particular, Fahnestock et al. (2003) computed maximum ductility demands up to 15.8 under 12 ground motions scaled to the design level spectral acceleration. But maximum ductility demands up to 25.6 were computed by the same Authors under six ground motions scaled to the maximum expected design intensity, which is 1.5 times larger than the design level intensity. According to the same Authors, the cumulative brace ductility demand reached a maximum value of 99 and 171, under the design and the maximum expected earthquake intensity, respectively. According to more recent research results (Nishimoto et al. 2004), which take into account the flexural engagement of BRBs coming from partially restrained rotational connections at the brace ends, the cumulative brace ductility capacity is somewhat smaller than the values coming from first test results. However, also using a conservative value of cumulative ductility capacity equal to 400, the value of demand/capacity ratio is so small (171/400 = 0.43) to suggest that seismic design of BRBs is not governed by low-cycle fatigue phenomena. Contrary, the need to further investigate about the maximum ductility demand/capacity ratio exists. In particular, it must be remembered that the maximum ductility demand is very important for defining the ending free-length portion of the core, which is required to allow free relative movement of the BRB core and the restraining elements.

However, low cycle fatigue (failure) characteristics have been shown to depend on a variety of factors, including the restraining mechanism used, material properties, local detailing, workmanship, loading conditions and history, etc.

2.3.6 Effects of different unbonding materials

As mentioned before, a separation unit between core braces and buckling-restraining units is of great importance, because it ensures both the brace to slide freely inside the buckling-restraining unit and the transverse expansion of the brace (when the brace yields in compression) to take place. This typically requires some debonding material to be employed as the separation unit (Figure 2.45). Otherwise, a gap should be kept between the two units.

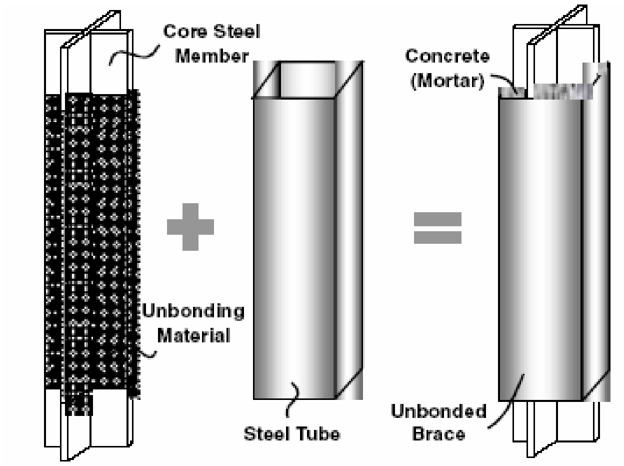

Figure 2.45. Schematic of BRBs (Tsai et al. 2004a).

When the concrete is employed as encasing member in BRBs, many types of debonding materials can be employed. Wakabayashi et al. (1973) firstly tested a lot of possible debonding materials, such as epoxy resin, silicon resin, vinyl tapes, etc. and they finally selected a silicon resin layer. The term “unbonded brace” was first used by Mochizuki et al. (1979, 1980 and 1982). They also checked some types of debonding material with different thickness in unbonded braces consisting of steel plates encased by reinforced concrete.

Researchers also employed other methods of debonding, such as coating a silicon painting on top of the brace, VMtape or styrol foam, coiling two layers of polyethylene film sheet with thickness 0.15–0.2 mm, 1.5 mm thick butyl rubber sheets, 2 mm thick silicon rubber sheets and so on. The thickness of the debonding layer varied from 0.15 to 2 mm, depending on the material employed.

As an alternative to the use of a debonding material, a small gap between the brace member and the encasing mortar may be provided in order to accommodate the relative deformation between them, resulting from the transverse expansion of the brace core due to the Poisson's effect. Typical dimensions of the gap for real application in BRBs are 1 mm at each side.

For some types of BRBs, such as those called "all-steel" or "only-steel" BRB, it is common that no infilling material is utilized. Therefore, no debonding material has to be provided. However, adequate gap size between the brace and the restraining member is required to provide the necessary space for relative deformation between both members, but preventing the core from buckling. The gap size may vary from 0.7 to 3.5 mm depending on the type of BRB.

Tsai et al. (2004) tested a total of ten BRBs identical in core cross sectional area and Table 2.1 summarizes the unbonding material used for each specimen and the corresponding cyclic loading protocol (the standard one refers to the protocols similar to the one provided by SAC 1997). Test results of the ten specimens are summarized in Figure 2.46, in terms of parameter Γ defined as follows:

$$\Gamma = \frac{\left(C_{max} - T_{max}\right)}{T_{max}} \tag{39}$$

where C_{max} and T_{max} are the maximum compressive and tensile brace forces at the same absolute axial deformation level.

Theoretically speaking, after the core member is yielded, the Poisson ratio $\nu = 0.5$ may be applied in the calculations. Besides, the volume of the yielding steel segment should remain constant, that is:

$$A_o \cdot L_o = A \cdot L \tag{40}$$

where A_o and L_o correspond to the original core cross sectional area and length, respectively, while A and L correspond to those after the brace is deformed in either tension or compression. Therefore, it can be shown that the axial strain is:

$$\varepsilon = 1 - \frac{L_o}{L} = 1 - \frac{A}{A_o} \quad \text{and} \quad A = A_o\left(1 - \varepsilon\right) \tag{41}$$

Thus, the ratio between the compressive and tensile brace forces for a given (absolute) strain level may be estimated as follows:

$$\Gamma = \frac{(C_{max} - T_{max})}{T_{max}} = \frac{A_o(1+\varepsilon) - A_o(1-\varepsilon)}{A_o(1-\varepsilon)} = \frac{2\varepsilon}{1-\varepsilon} \simeq 2\varepsilon \qquad (42)$$

Equation 42 suggests that Γ is about 4 % for ε = 2 %. But the test results shown in Figure 2.46 indicate much higher Γ values (the maximum is about 30% for ε = 2 %). This should be due to the imperfect unbonding mechanism and a substantial friction developed between the steel core member and the buckling restraining part.

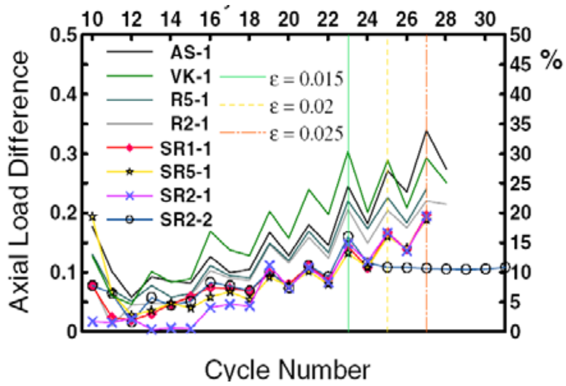

Figure 2.46. Axial load difference Γ measured by Tsai et al. (2004a).

Table 2.1. Different unbonding materials tested by Tsai et al. (2004a).

Specimen (1)	Unbonding Material (2)	Unbonding Material Thickness (3)	Loading History (4)
AS-1	Asphalt Paint	N. A.	Standard
VF-1	Vinyl Sheet + Foaming Tape	2 mm	Standard
VK-1	Vinyl Sheet + Kraft Tape	2 mm	Standard
R2-1	Rubber Sheet	2 mm	Standard
R5-1	Rubber Sheet	5 mm	Standard
SR1-1	Silicone Rubber Sheet	1 mm	Standard
SR2-1	Silicone Rubber Sheet	2 mm	Standard
SR2-2	Silicone Rubber Sheet	2 mm	Low-Cycle Fatigue
SR2-3	Silicone Rubber Sheet	2 mm	Near-Fault
SR5-1	Silicone Rubber Sheet	5 mm	Standard

2.3.7 Detachable BRBs

Detachable BRBs provide the possibility of disassembling the BRBs for inspection after an earthquake or during the life-time. This is typically achieved in all-steel BRBs by using bolted connections for joining together the restraining tubes (Figure 2.47).

Test results suggest that the all metallic and detachable BRBs can stably sustain severe cyclic increasing and constant fatigue inelastic axial strain reversals (Tsai et al. 2004a).

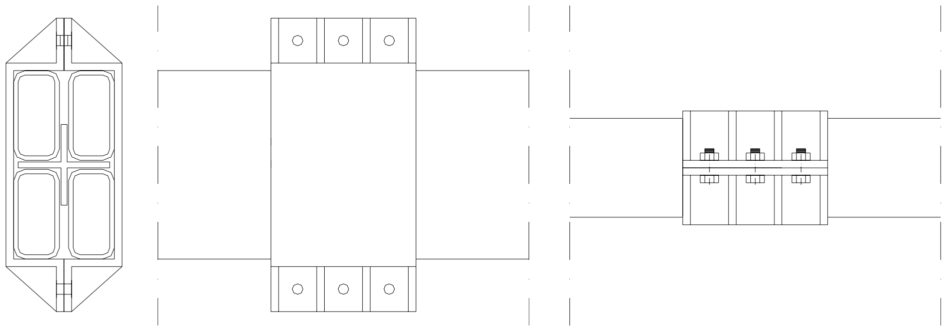

Figure 2.47. Tie connection details for detachable BRBs.

As shown in Figure 2.47, tube-to-tube tie connections are adopted to join the retaining sleeves. Tie connections between two units can be continuous or properly spaced. It is found, by using the elastic stability theory (Timoshenko and Gere 1961), that the required strength N_{req} and stiffness β_{id} of the tie connection can be expressed in the following form (Tsai et al. 2004a):

$$N_{req} = \frac{3}{L_{tube}}\left(\frac{N_{max}}{2} - N_{cr}\right)\cdot\left(\frac{B\cdot f_y}{E} + e\right) \tag{43}$$

$$\beta_{id} = \frac{9}{2L_{tube}}\left(\frac{N_{max}}{2} - N_{cr}\right)\cdot\left(1 + \frac{E\cdot e}{B\cdot f_y}\right) \tag{44}$$

where L_{tube} is the length of the buckling restraining tube, N_{max} is the maximum axial force (Equation 30), N_{cr} is the critical eccentric load of the single tube (Timoshenko & Gere 1961), B is the width of the short side of the rectangular tube, E is Young's modulus of steel, f_y is yield stress of steel tube, e is the load eccentricity measured from neutral axis of the single tube.

2.3.8 BRB modelling

The BRB response can be simulated with bi-linear axial force-deformation relationship (Tsai et al, 2004), or adopting the more accurate Bouc-Wen model (1976) (suggested by Black 2002). In particular, in case of Bouc-Wen model, the nonlinear hysteretic behaviour of a BRB can be approximated by Equation 45:

$$N(t) = \alpha K u(t) + (1-\alpha) K u_y z(t) \tag{45}$$

where *u(t)* is the axial deformation of the brace, K is the brace elastic stiffness, α is the ratio of the post-yielding to elastic stiffness, u_y is the yield displacement, and *z(t)* is a hysteretic dimensionless quantity governed by the following differential equation:

$$u_y \dot{z}(t) + \gamma |\dot{u}(t)| z(t) |z(t)|^{n-1} + \beta \dot{u}(t) |z(t)|^n - \dot{u}(t) = 0 \tag{46}$$

In the Equation 46 β, γ and n are dimensionless quantities that control the shape of the hysteretic loop. This hysteretic model was originally proposed by Bouc (1971) for n=1, and subsequently extended by Wen (1975, 1976) and used in random vibration studies of inelastic systems. When parameter n assumes large values (say n>10) the transition from the elastic to the post-yielding regime is sharp and the Bouc-Wen model reasonably models bilinear behaviour.

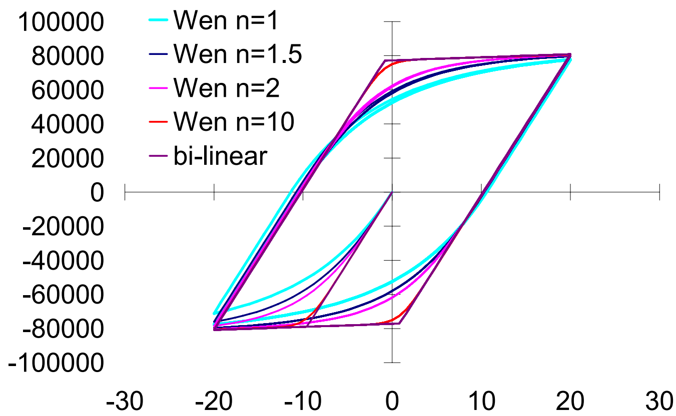

Figure 2.48. Comparison of different hysteretic models to simulate the inelastic behaviour of BRBs.

In Figure 2.48 this aspect is clearly shown comparing the hysteretic Bouc-Wen model with different values of "*n*" compared with the bilinear axial force-axial deformation model. In particular, according to Black et al. (2002) the value of *"n"* that better match the experimental cyclic behaviour of BRBs is for n=1 with a post-yield to elastic stiffness ratio of about 0.025 the initial elastic one.

2.3.9 BRB geometric design parameters

BRBs are generally introduced in the existing structures in the form of special dissipative steel braces, with some special detailing allowing the maximization of their energy dissipation capacity. Changing the type of implementation technique gives rise to different behaviours and, consequently, different design rules. Moreover, thanks to their own typological scheme, BRBs can be design decoupling into an effective range their strength, stiffness and ductility. In order to clarify this aspect it is interesting to show in which terms the equivalent yield strain ε_y varies changing the geometrical proportions of the inner core. In fact, the equivalent yield strain ε_y is a fundamental parameter to design BRBs because it is strictly related to the interstory drift ratio θ_y by means of the following relations:

$$\theta_y = \frac{2\varepsilon_y}{sin2\varphi} \tag{47}$$

where φ is the tilt angle of brace respect to the horizontal plane.

Hence, referring to the core geometry shown in Figure 2.35 and assuming that $A_j=2A_t$ (where A_j is the gross area of the end part of the BRB to be connected, A_t is the gross area of the tapered portion of BRB), Figures 2.49 to 2.55 show the variation of the equivalent yield strain ε_y changing the geometrical proportions of the inner core in technical and feasible way.

The direct analysis of these plots underlines that in the considered geometrical range the equivalent yield strain can vary from 0.50‰ to 1.51‰ (more than 3 times the lower limit). Thus it is evident the great design flexibility of the BRB system.

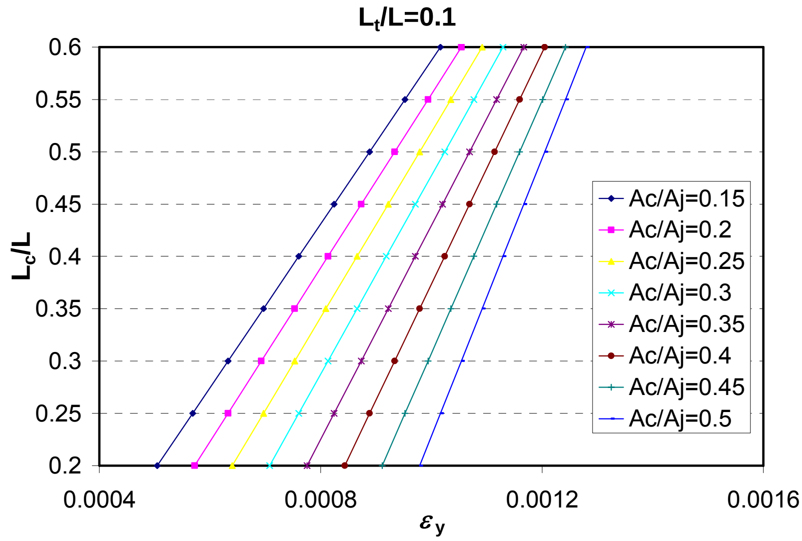

Figure 2.49. BRB equivalent yield strain for $L_t/L=0.1$.

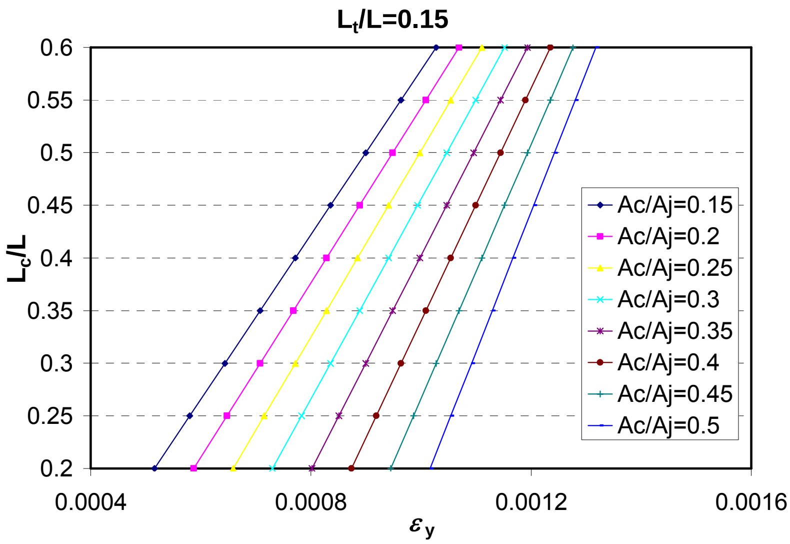

Figure 2.50. BRB equivalent yield strain for $L_t/L=0.15$.

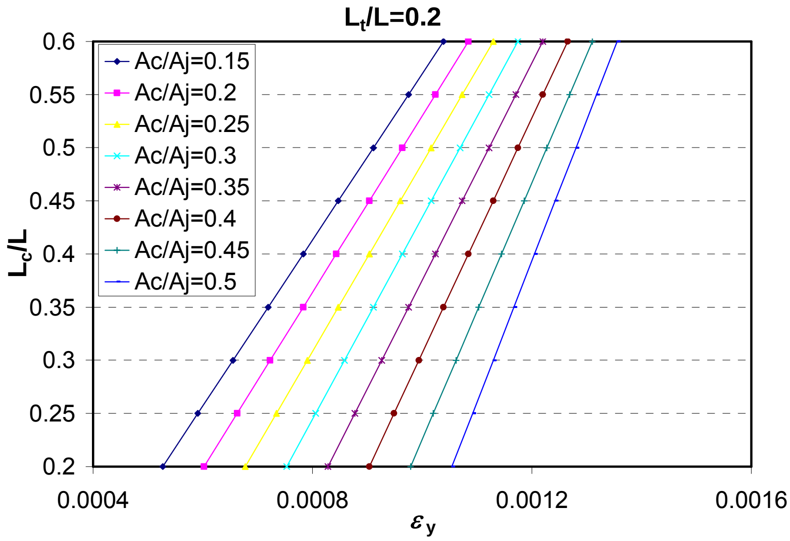

Figure 2.51. BRB equivalent yield strain for $L_t/L=0.2$.

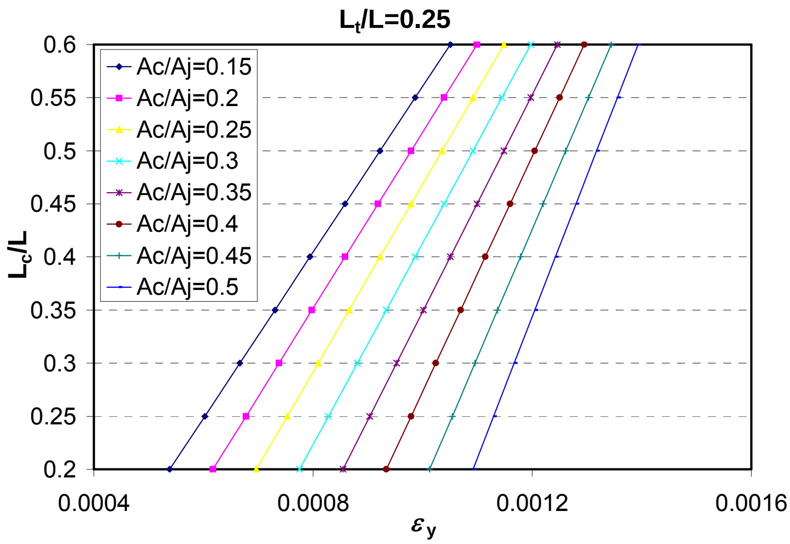

Figure 2.52. BRB equivalent yield strain for $L_t/L=0.25$.

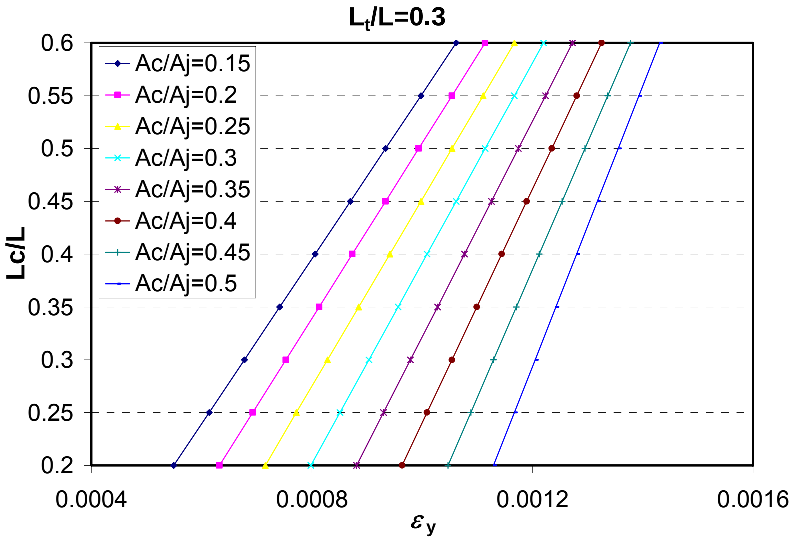

Figure 2.53. BRB equivalent yield strain for $L_t/L=0.3$.

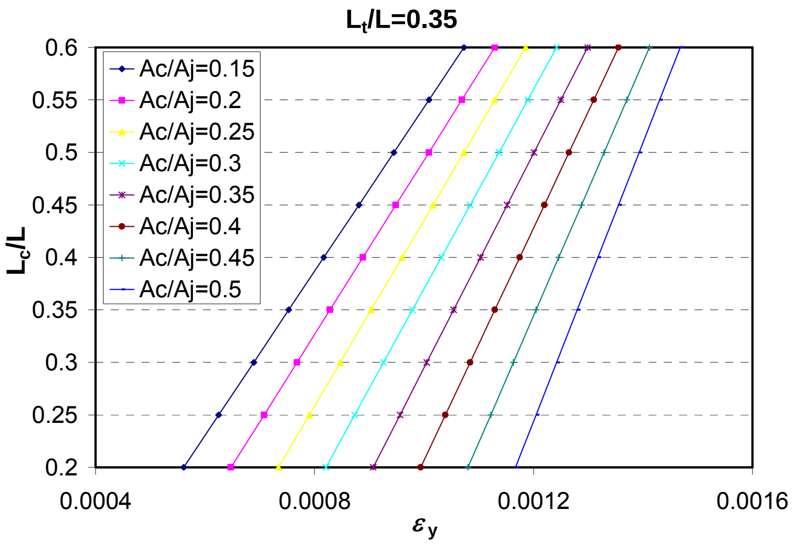

Figure 2.54. BRB equivalent yield strain for $L_t/L=0.35$.

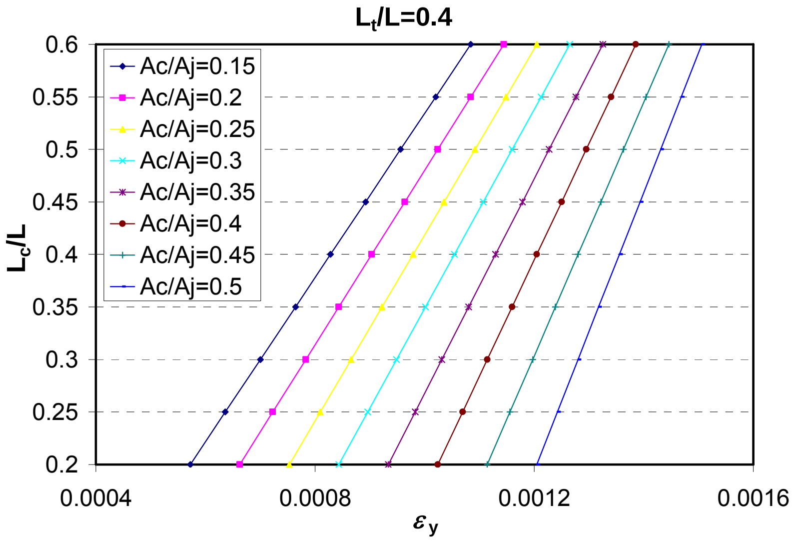

Figure 2.55. BRB equivalent yield strain for $L_t/L=0.55$.

Chapter III

Seismic behaviour of Gravity Load Designed RC structures

3.1 INTRODUCTION

RC buildings represent a consistent part of the world construction heritage (in Italy over 50%) and a remarkable part of them has been built either without the application of any seismic code or adopting poor criteria of anti-seismic design. In Italy, more than a half of such a patrimony has been built before 1971, when the observance of specific technical provisions for the seismic zones foreseen by the Law 64/74 became obligatory. In that period the design of RC buildings was based on the use of the Law 1684/1962, which did not give any specific indication on constructional details (minimum percentage of steel bars, stirrups, etc.) and regularity prerequisites able to guarantee an acceptable behaviour of constructions under earthquakes.

Therefore, the evaluation of the RC building resistant capacity is a important topic in the engineering practice and also in the research field for both the assessment of the seismic vulnerability and the choice of opportune retrofitting solutions to be applied. To achieve this goal, the effects on constructions caused by past earthquakes represent a useful tool to understand the seismic behaviour of RC structures with non-ductile details and to clarify the possible retrofitting strategies. In detail, during violent seismic events (Irpinia 1980, Turkey 1999, Greece 1999) a not satisfactory behaviour of such structures has been observed, especially when the design was performed taking into account only the presence of gravitational loads, since the seismic classification was not still introduced. Framed RC structures designed without adequate seismic rules and therefore able to exclusively withstand vertical loads (Gravity Load Design, GLD) show in many cases a deficient behaviour characterized by a low ductility of beam-to-column joints and the absence of an appropriate resistance hierarchy able to provide collapse mechanisms of global type. Other observed problems were generally represented by the lack of in plane and/or in elevation regularity, the elevated torsional deformability and the presence of short columns which determine a not satisfactory seismic behaviour of the building. Based on these circumstances, the key concepts of the modern seismic codes are based on the achievement of the following objectives:

- prevent a non structural damage under seismic events of moderate intensity, which can frequently occur during the life of the structure.
- prevent a structural damage, reducing the not structural one, when seismic events of moderate intensity, which can happen less frequently, occur.
- avoid the structural collapse danger under high intensity earthquakes.

These prerequisites are able to fix different performance levels for the structures, according to the methodology of the "Performance Based Design", in the certainty that the principal purpose of the different design criteria is to allow the evaluation of the desired performances of the structure under the applied load conditions. All these considerations underline a sequence of problems in the evaluation of the seismic behaviour of the existing RC structures. Generally all resistant mechanisms resulting either of brittle type or sensitive to the cyclic degradation have to be correctly evaluated by means of adequate calculation models in order to obtain reliable results in the evaluation of the actual seismic resistance. In this context, by evaluating the constructional details of RC structures designed for carrying vertical loads, the deficiencies reported in Figure 3.1 can be mainly recognised.

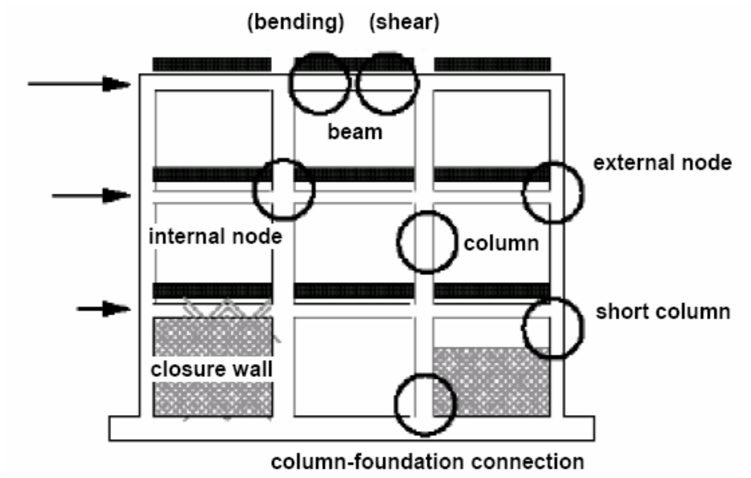

Figure 3.1. Traditional and dissipative bracing.

3.2 THE STRUCTURAL CONCEPTION OF THE ‘70ES AND ‘80ES BUILDINGS

The structural typology of RC frames of non-seismic buildings reached his “maturity” just in the period between ‘70es and ‘80es. Many studies carried out on a number of RC buildings realized before 1970 have underlined as the calculation formalities of the structural elements conceived for withstanding gravitational loads do not differ significantly from the ones designed after the introduction of the law 1086/71. The main constructional differences between the structural typologies characterising these two constructive epochs are represented by the adopted materials.

The design of this kind of building was developed by initially defining the position of the beams (generally deep beams) at each storey only with reference to the needs to support vertical loads. So making, plane frames were realized along only one of the main orthogonal directions of the plan (usually the longitudinal one). The further needs “to close” the building with walls gave rise to perimeter frames and some internal frames (e.g. in the staircase area) along the other direction.

For standardization and simplicity reasons, the deep beams in a storey were made adopting the same transversal section. But, due to the fact that the beams were designed only for carrying vertical loads, they were the same also along the whole height of the buildings, giving rise to a unique typical structural plan for all the storeys. This plan differed at each storey only for the cross-section of the columns, which obviously grew going from the upper to the lower levels.

The staircase was usually made with a knee sloping beam supporting cantilever steps (and then subjected to torsional actions too). Therefore the staircase structure on the whole behaved as a very stiff frame, due to the knee beam, which represents a sort of bracing for the frame, usually oriented along the transversal direction of the building plan, in parallel with the floor structure. Nevertheless this structural scheme, even if provides lateral stiffness in one direction, gives rise to stocky columns (in both directions) which could be prone to dangerous brittle shear failure when the building is subjected to significant horizontal actions.

The floor structure was designed with reference to vertical loads only. Nevertheless the current technology provided the thin upper slab with some weak reinforcements (transversal distribution reinforcement), in order to distribute concentrated load. Some times, when the constructional process was particularly accurate, also one or two transversal girders were made, with the scope to both better distribute any concentrated load and face transversal boundary effects.

Even if no conceptual reference to floor diaphragm effect was made at that time, this effect is naturally performed by the slab, but limited by its resistance related to the small thickness of concrete and to the amount and continuity of the reinforcements.

Generally, the columns had rectangular cross-section. The small dimension of the cross-section was ever not greater than 30-40 cm, in order to hidden the columns in the perimeter walls. Consequently the stiff direction (the depth) of the columns resulted in the plane of the perimeter walls, providing the building with a quite good distribution of the column stiffness along both the main direction of the plan for withstand horizontal loads, even if the designer usually did not consider these loads.

In short, the design criteria used for proportioning the structural elements can be summarized as following:

- the beam cross-sections and reinforcements were sized with reference to only vertical loads. A simple continuous beam model was usually adopted, neglecting the rotation constraint given by the columns. The standardization of the cross- sections provided the beams of the transversal plan direction (which carried very low vertical loads) with significant over-strength;
- the columns were dimensioned on the base of axial forces only, neglecting any bending moment, considering a reduced value of the concrete compressive nominal strength (70%). The longitudinal (vertical) steel reinforcement area was defined as the 0.5 - 1.0% of the cross-section gross area.

The allowable stresses method was used for safety verifications. Besides, this method is used in Italy also nowadays, even if it can not be adopted for seismic design of structures and for seismic upgrading design anymore.

It is well known that the allowable stress method (ASM) and the ultimate limit states method (ULSM) give quite the same results only for members in bending without reinforcement in compression (Calderoni et al 2000). In fact the ULSM differs practically from ASM (in axial stress verifications) just for considering the reinforcement in compression more effective. For this reason, if we analyse and verify by means of ULSM an existing building, which has been designed without considering seismic actions but adopting the ASM, we should find an amount of over-strength in the columns (which have been dimensioned only for compressive forces) greater than in the beams (which have been verified only in bending). It can be said that the adoption of ASM provide the structure with a sort of capacity design, which is nowadays one of the most important criteria to be followed in seismic design.

The foundation system was usually made by plinths based directly on the ground or on piles. Usually the plinths were not connected one another, without any concerns on possible relative horizontal displacements among the column bases. Only on the perimeter of the building and around the staircase there were beams, connecting the plinths, in order to sustain the heavy perimeter walls of the basement. Anyway the connections among internal columns should have been difficult to realise, because the columns usually were not aligned, particularly along transversal direction.

When continuous foundation beams were used instead of plinths, they were placed along the same alignment of the supporting beams of the floors, i.e. in longitudinal direction. In this case the foundation system was completed by transversal beams (not supported by the ground) for sustaining the perimeter walls. It is worth to notice that the foundation system was originally designed without considering any seismic horizontal load, but with reference to the effects of the maximum vertical loads. On the contrary, in case of seismic upgrading of the building, the foundation shall be verified for the effects of high horizontal (seismic) loads and reduced vertical loads (as prescribed by EC8 or by new Italian Code). For this reason the amount of reinforcing interventions on the foundation system could be more limited than on the rest of the structure.

The most sensitive aspect in seismic analysis and upgrading of existing building is the quality of detailing and materials, which directly influences both strength and ductility of beams and columns. Particularly the beam-to-column joints (panel zones) and the end zones of beams and columns were usually realized without any specific attention: they are generally affected by lack of stirrups and of re-bars anchorage, which lower in significant way the ductility capacity of the structural members.

As far as the quality of materials is concerned, fortunately it is not very difficult to determine the compressive resistance of concrete and the typology and yield strength of re-bars, even if by means of destructive in-situ tests. Anyway the quality level of the material used in that period results usually acceptable, even if the use of smooth re-bar can be detected in few cases.

3.3 THE STRUCTURAL INADEQUACY OF GLD RC STRUCTURES AND RELEVANT TYPICAL DAMAGES DURING SEISMIC EVENTS

Usually, the structural system of existing RC buildings is composed by resisting frames placed in one direction only, perpendicular to the floor slab orientation. Such frames are usually made of emergent beams, but in some cases beams having the same depth of the slab are of concern. Therefore, in the other direction they are connected by the slab only, without any specific beam. The structural elements of these constructions are designed without any reference to the effect of horizontal forces, including explicitly also the wind action too. As a consequence, flexible resisting systems having a very poor ductility have been adopted.

The typical lacks of GLD buildings, according to the evidences reported in previous experimental and theoretical studies (Bracci et al.1995), are:

1. *Inadequate structural scheme.* In fact, GLD buildings are characterized by the absence of a coherent structural configuration, without the proper presence of continuous frames in the two main plan directions (Figure 3.2);

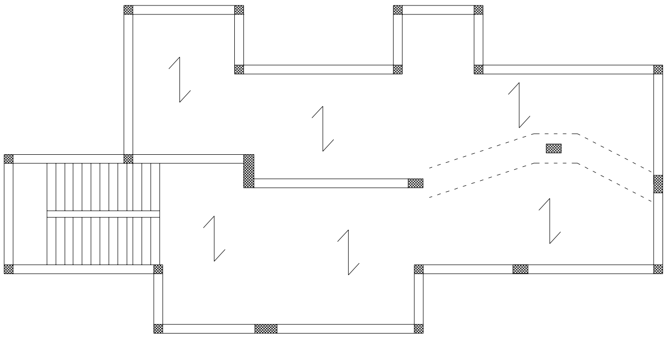

Figure 3.2. Example of irregular and chaotic plan, typical of GLD structures.

2. *The lack of in plane regularity and an elevated torsional deformability.* This deficiency is mainly due to a large eccentricity between the centroid of stiffness and the centroid of floor masses (as shown in Figure 3.3). As a result of this inadequate plan configuration, torsional coupling effects may concentrate the lateral forces in some perimetric frames, thus resulting in an excess of local ductility demand.

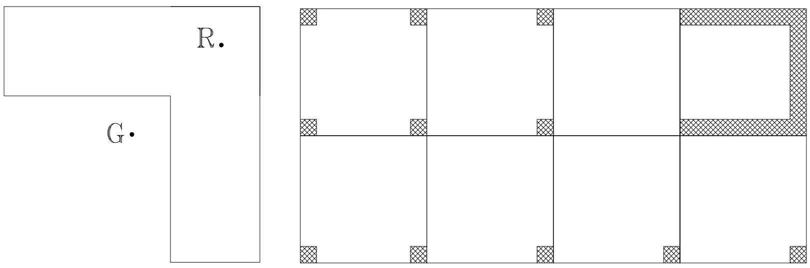

Figure 3.3. Example of in plan irregularity.

3. The lack of in elevation regularity. This issue derives from typical architectural needs. It generally consists in an irregular distribution in elevation of lateral resisting systems. This improper structural configuration implies the concentration of ductility demand (and, as a consequence, of structural damages) in one or in a few stories. It is possible to identify two different types of elevation irregularity: an in-plane discontinuity irregularity and an out-plane discontinuity irregularity. In detail, an in-plane discontinuity irregularity shall be considered to exist in any primary element of the lateral-force-resisting system whenever a lateral-force resisting element is present in one story, but does not continue (as shown in Figure 3.4a), or is offset within the plane of the element, in the story immediately below (as shown in Figure 3.4b). An out-of-plane discontinuity irregularity shall be considered to exist in any primary element of the lateral-force-resisting system when an element in one story is offset out-of-plane relative to that element in an adjacent story, as depicted in Figure 3.5.

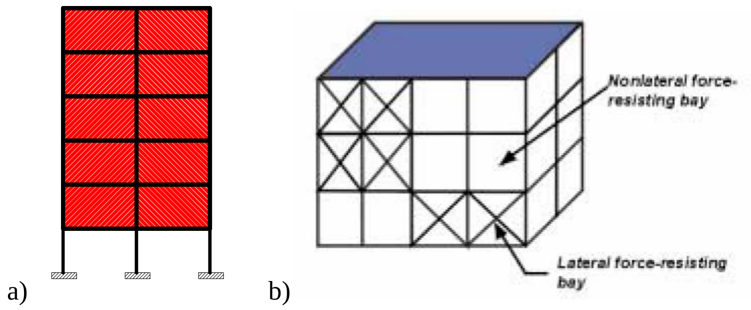

Figure 3.4. Example of in-plane discontinuity irregularity in elevation (FEMA356).

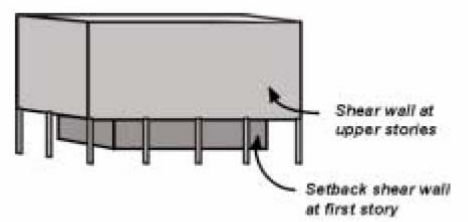

Figure 3.5. Example of out-plane discontinuity irregularity in elevation (FEMA356).

As above mentioned, the result of irregularity in elevation consists in a concentration of the structural damages in a few stories, thus resulting in a so-called soft story or in a weak story. Generally speaking, a soft story is one that shows a significant decrease in lateral stiffness from that immediately above. A weak story is one in which there is a significant reduction in strength compared to that above. The condition may occur at any floor, but is most critical when it occurs at the first story, because the forces are generally greatest at this level. Therefore, if all the stories are approximately equal in strength and stiffness, the entire building deflection under earthquake forces is distributed approximately equally to each story. If the first story is significantly less strong or more flexible, a large portion of the total building deflection tends to concentrate there, with consequent concentration of forces at the second-story connections (Figure 3.6).

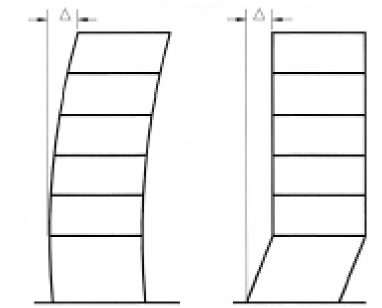

Figure 3.6. The typical effect of soft-story formation.

In more detail, the soft-story problem may result from four basic conditions. These are summarized as follows:

- Discontinuous load paths, created by a change of vertical and horizontal structure at the second story (Figures 3.5 and 3.6).
- A first-story structure significantly taller than upper floors, resulting in less stiffness and more deflection in the first story (Figure 3.7a).
- An abrupt change of stiffness at the second story, though the story heights remain approximately equal. This is caused primarily by material choice: the use, for instance, of heavy precast concrete elements above an open first story (Figure 3.7b), or, more commonly in residential buildings, the presence of stiff masonry infill walls in the RC frame (Figure 3.7c).

• The use of a discontinuous shear wall, in which shear forces are resisted by walls that do not continue to the foundations, but stop at second floor level, thus creating a similar condition to that of the second item above (Figure 3.7d).

The above characteristics, individually or in combination are readily identifiable in existing buildings provided that the building structure can be studied in its entirety, either in the field or by reference to accurate as-built construction documents.

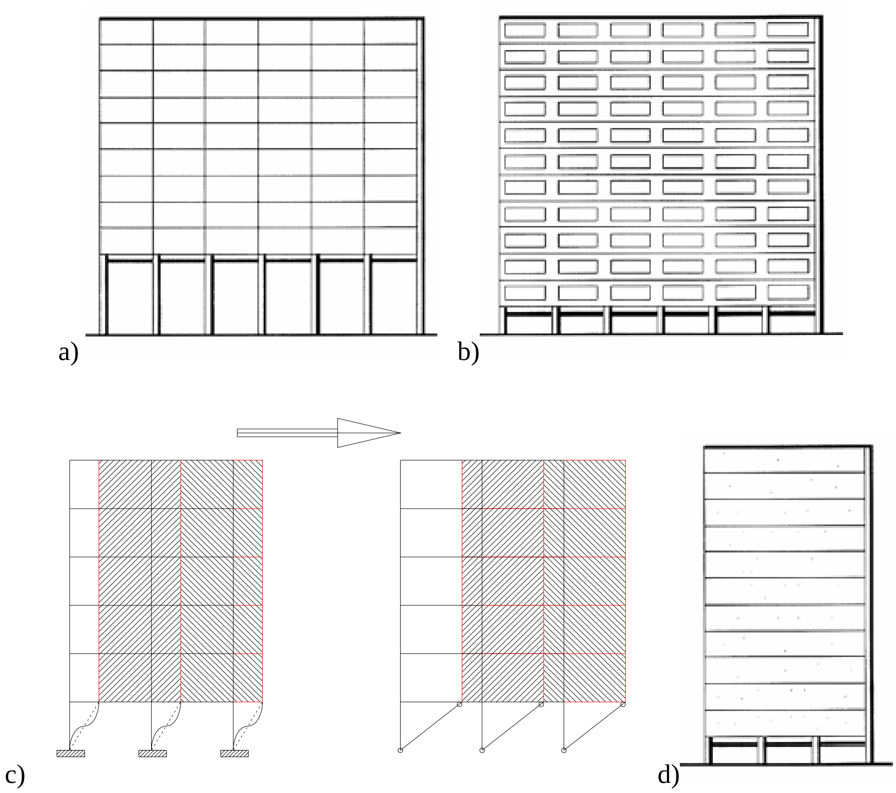

Figure 3.7. Typical motivating causes for soft story.

Typical damages and collapse mechanisms induced by soft story formation are summarized in Figures 3.8 through Figures 3.10.

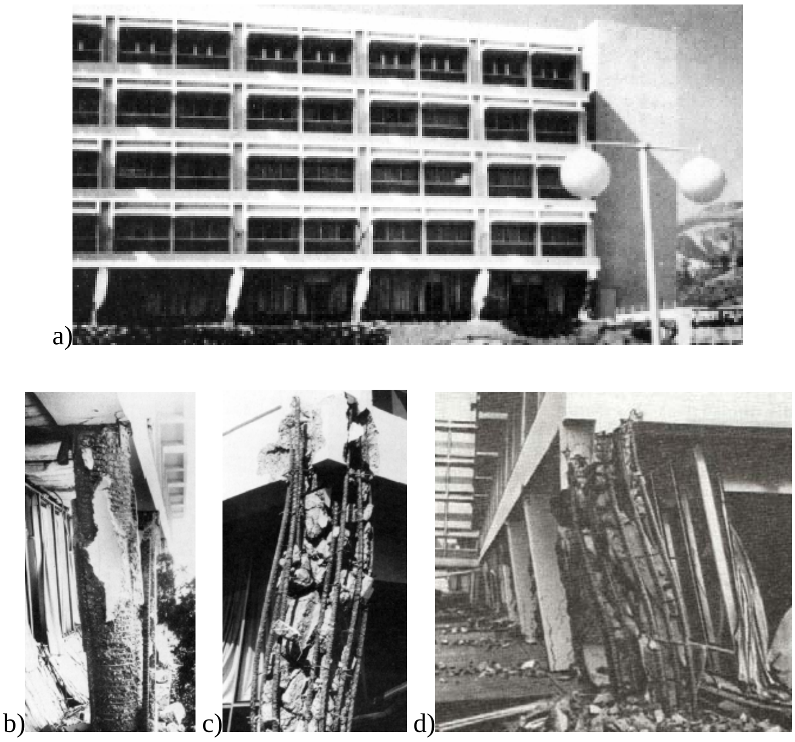

Figure 3.8. Damage to columns due to the formation of a soft story in the 4-story Olive View Hospital building during the February 9, 1971 San Fernando, California, earthquake: a wing of the building showing approximately 60cm drift in its first story (a); spirally reinforced concrete column in first story (b); tied rectangular corner column in first story (c, d).

Figure 3.9. Irpinia earthquake (1980), the global collapse of an hospital building due to formation of a soft story and poor local details.

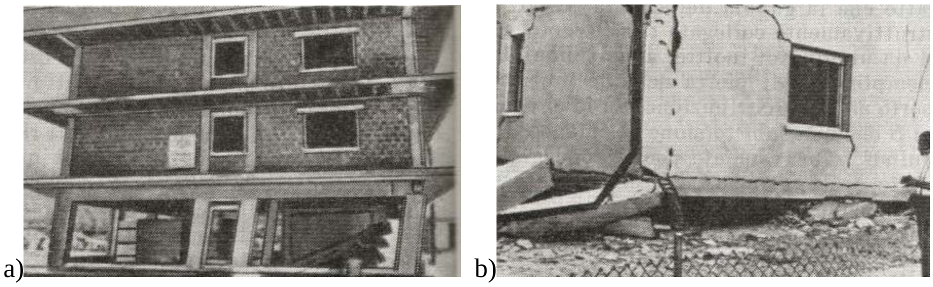

Figure 3.10. Friuli earthquake (1976): soft story mechanism in a residential building (a); global collapse due to the formation of a soft story (b).

Figure 3.11. Kobe earthquake (1995), failure in a setback building at the plane of weakness created by a combination of the setbacks and adjoining openings in the wall.

3. Insufficient in-plane strength and stiffness of floor diaphragms. The inadequate in-plane strength and stiffness of the floor slabs can be considered as one of the most serious structural deficiency. In fact, the slab is of a great importance in distribution of seismic forces between each resisting elements. This problem is evident in the following cases:

- in case of floor without slabs or with a small thickness slab;
- in case of stretched out plan (that unavoidably induce a stress concentration);

-in case of pre-cast floor, without correct connection with the surrounding structure;

- in case of significant openings respect to the plan dimensions.

In all these cases the resulting effects are insufficient in-plane bending and in-plane shear strength and excessive in-plane flexibility.

Some examples of structural damages under seismic event due to this structural inadequacy are shown in Figures 3.12 and 3.13.

Figure 3.12. Irpinia earthquake (1980), detachment of pre-cast slab because of incorrect connection details.

Figure 3.13. Irpinia earthquake (1980), detachment of reinforce concrete floor due to stress concentration near a shear RC wall.

3. Short and stocky columns. The excessive presence of stocky columns, usually located near the staircase structure, can be considered as a serious source of structural deficiency in case of seismic actions. In fact, seismic forces are distributed in proportion to the stiffness of the resisting members. Hence, if the stiffness of the supporting columns (or walls) varies, the stiffer (usually shorter) ones will "attract" the most forces. The important point is that stiffness (and hence forces) varies approximately as the cube of the column length. Similarly, a uniform arrangement of short columns supporting a floor will attract greater forces to that floor, with a corresponding possibility of failure. Typically such an arrangement may also involve deep and stiff spandrel beams, making the columns significantly weaker than the beams. Typical cases characterized by the presence of short columns are summarized in Figure 3.14.

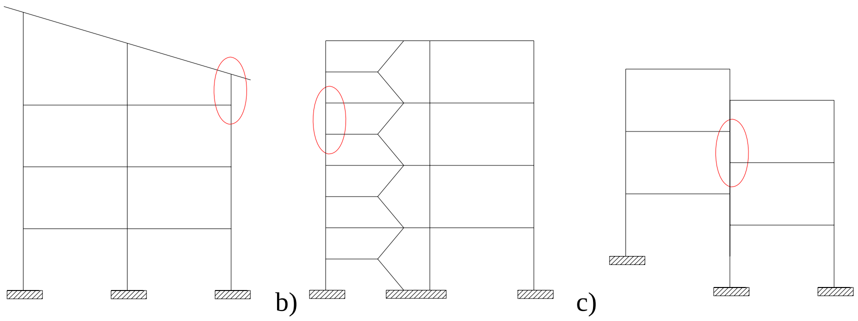

a) b) c)

Figure 3.14. Typical arrangement of short columns in RC buildings: under over-pitched roof (a); in staircase structure (b); in case of staggered roofs (c).

Such a design is in conflict with a basic principle of seismic design, which is to design a structure characterized by the plastic engagement of beams before columns under severe seismic forces. This is based on the reasoning that as beams progress from elastic to inelastic behaviour they start to deform permanently. This action will dissipate and absorb some of the seismic energy. Conversely, if the column fails first and begins to deform and buckle, major vertical compressive loads may quickly lead to overall collapse. Mixing of columns of varying stiffness on different facades may also lead to torsional effects, since the building assumes the attributes of varying perimeter resistance discussed above.

Typical shear failure mechanisms (clearly characterized by crossed cracks tilted of about 45°) occurred in stocky columns under past earthquakes are shown from Figure 3.15 to Figures 3.16a, b, c.

Figure 3.15. Miyagi-ken-oki, Japan(1978), short column failure in a school building.

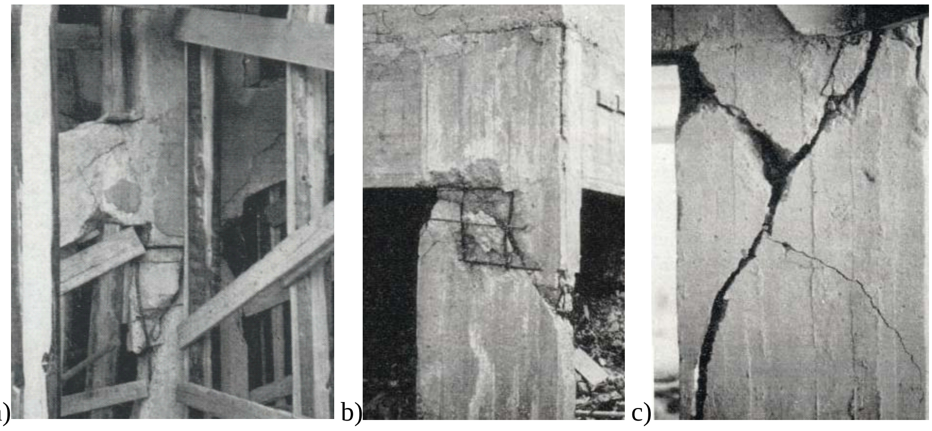

a) b) c)

Figure 3.16. Irpinia earthquake (1980): brittle failure of stocky columns of the staircase structure in a residential building (a); short column failure in a residential building (b,c).

3. Inadequate local details and lack of ductility. A good design concept is the proper detailing of members and their connections to achieve the requisite strength and ductility. Such detailing should aim at preventing non-ductile failures, such as those associated with shear and with bond anchorage. In fact, dynamic response to strong earthquakes, characterized by repeated and reversed cycles of large-amplitude deformations in critical elements, tends to concentrate deformation demands in highly stressed portions of yielding members. Hence, it is clear the great importance of proper detailing of potential hinging regions. Indeed, the experience and observation have shown that properly designed, detailed, and constructed reinforced-concrete buildings can provide the necessary strength, stiffness, and inelastic deformation capacity to perform satisfactorily under severe earthquake loading.

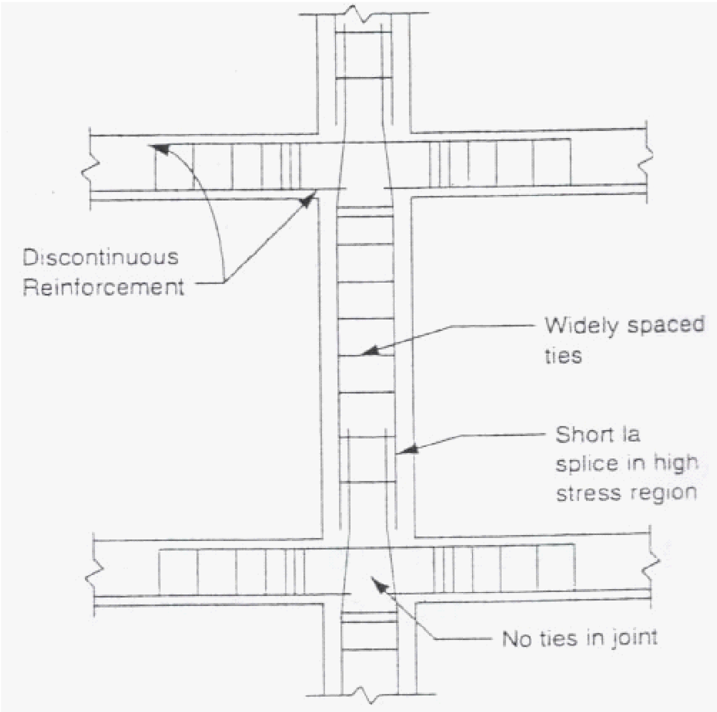

Figure 3.17. Typical deficiencies in local details (ATC40).

In case of GLD RC structures, significant lacks in local details can be usually recognized (Figure 3.17). Therefore, an accurate list of typical local deficiencies is summarized as follows:

- Discontinuous transverse stirrups in beams and columns, largely spaced and not well bended inside the cross section. An insufficient reinforcement of the concrete in terms of bars and stirrups may induce undesirable brittle failures in the zones prone to develop plastic hinges.

As an example in this sense, Figure 3.18 shows typical shear cracks due to the absence of adequate transverse reinforcement in a beam;

- Incorrect positioning of steel rebars and/or improper bars bending details. An example in this sense is shown in Figures 3.19 and 3.20, where it is clearly highlighted the concrete cover spalling due to an incorrect positioning of bended steel rebars in a staircase flight and the detachment between the staircase flight and half pace;

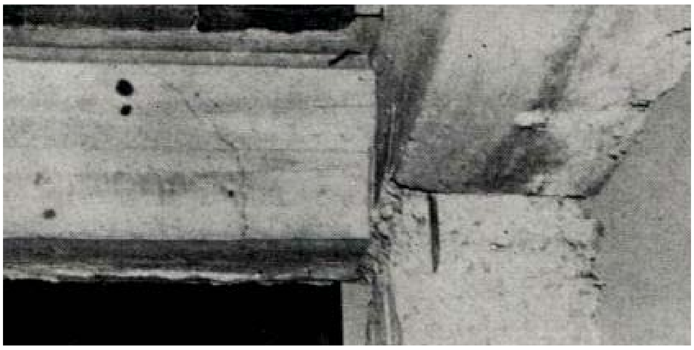

Figure 3.18. Irpinia earthquake (1981), shear failure due to the absence of adequate transverse reinforcement in a beam.

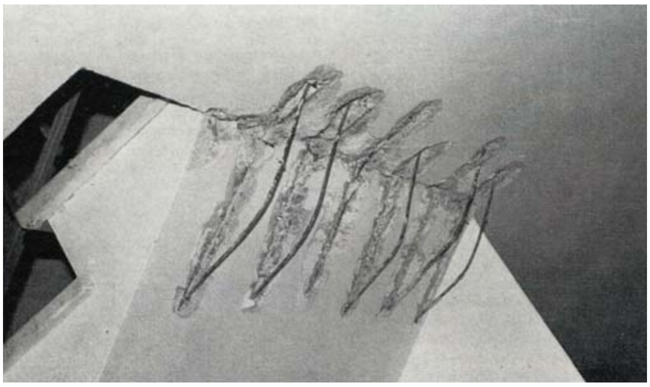

Figure 3.19. Irpinia earthquake (1981), concrete cover spalling due to an incorrect positioning of bended steel rebars in a staircase flight.

Figure 3.20. Irpinia earthquake (1981), detachment between the staircase flight and half pace.

- Insufficient anchorage and incorrect overlaps of the longitudinal steel rebars. The scarce care of these details may induce strong damage concentration with one single large crack forming for each plastic hinge, thus indicating strong fixed-end rotation effects at large plastic story drift angles. This can be particularly evident for plastic hinges at the base of columns, where the presence of the lap-splice joint of the longitudinal steel reinforcement was present (Figure 3.21);

Figure 3.21. Fixed-end rotation at the base of column.

- Eccentricities in beam to column joints;
- Scarce care of the resumptions of concrete casting of columns;

- The weakness of the columns in comparison to the beam, which can determine a soft-storey mechanism. This local deficiency is very common in GLD RC structure. In fact, in these structures the columns are usually design to resist vertical loads. Consequently the design bending actions can be considered negligible respect to column axial loads. As a consequence, the results of this design process are slender columns with scanty amount of longitudinal and transverse steel reinforcement. This improper details induce a significant damage concentration in both column ends, usually characterized by concrete crushing and rebar buckling, thus assuming the so-called sharpened pencil shape (as shown from Figure 3.22a to 3.22g);

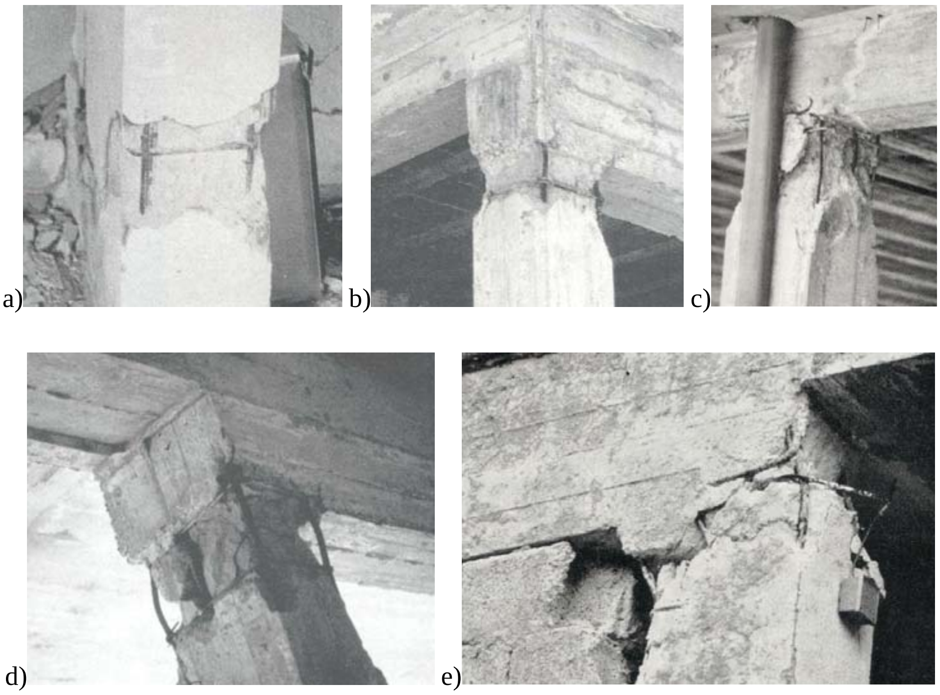

Figure 3.22. Irpinia earthquake (1981), typical column failures due to inadequate local details and to weakness of the columns in comparison to the beam (continued).

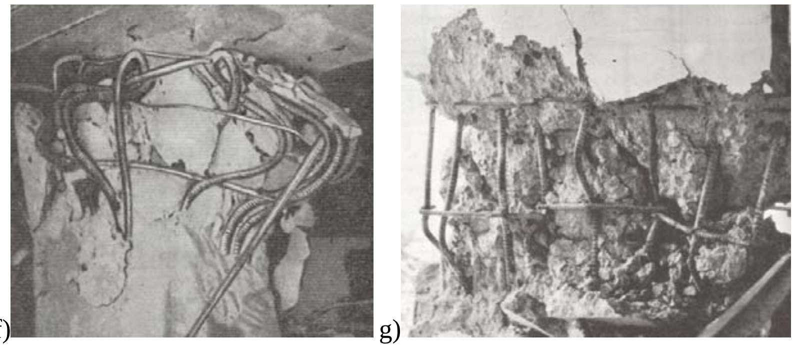

f) g)

Figure 3.22. Irpinia earthquake (1981), typical column failures due to inadequate local details and to weakness of the columns in comparison to the beam.

- Absence of suitable confinement (that is transversal reinforcement) of beam-to-column joints and discontinuous bending reinforcement in correspondence of connections. Beam-column joints are critical elements in frame structures. These elements can be subjected to high shear and bond-slip deformations under earthquake loading. Beam-column joints have to be designed so that the connected elements can perform properly. This requires that the joints be proportioned and detailed to allow the columns and beams framing into them to develop and maintain their strength as well as stiffness while undergoing large inelastic deformations. A loss in strength or stiffness in a frame resulting from deterioration in the joints can lead to a substantial increase in lateral displacements of the frame, including possible instability due to P-delta effects. The design of beam-column joints is primarily aimed at (i) preserving the integrity of the joint so that the strength and deformation capacity of the connected beams and columns can be developed and substantially maintained, and (ii) preventing significant degradation of the joint stiffness due to cracking of the joint and loss of bond between concrete and the longitudinal column and beam reinforcement or anchorage failure of beam reinforcement. Of major concern here is the disruption of the joint core as a result of high shear reversals. As in the hinging regions of beams and columns, measures aimed at insuring proper performance of beam-column joints have focused on providing adequate confinement as well as shear resistance to the joint. The forces acting on a typical interior beam-column joint in a frame undergoing lateral displacement are shown in Figure 3.23a. It is worth noting in Figure 3.23a that each of the longitudinal beam and column bars is subjected to a pull on one side and a push on the other side of the joint. This combination of forces tends to push the bars through the joint, a condition that leads to slippage of the bars and even a complete pull through in some test specimens. Slippage resulting from bond degradation under repeated yielding of the beam reinforcement is reflected in a reduction in the beam-end fixity and thus increased beam rotations at the column faces.

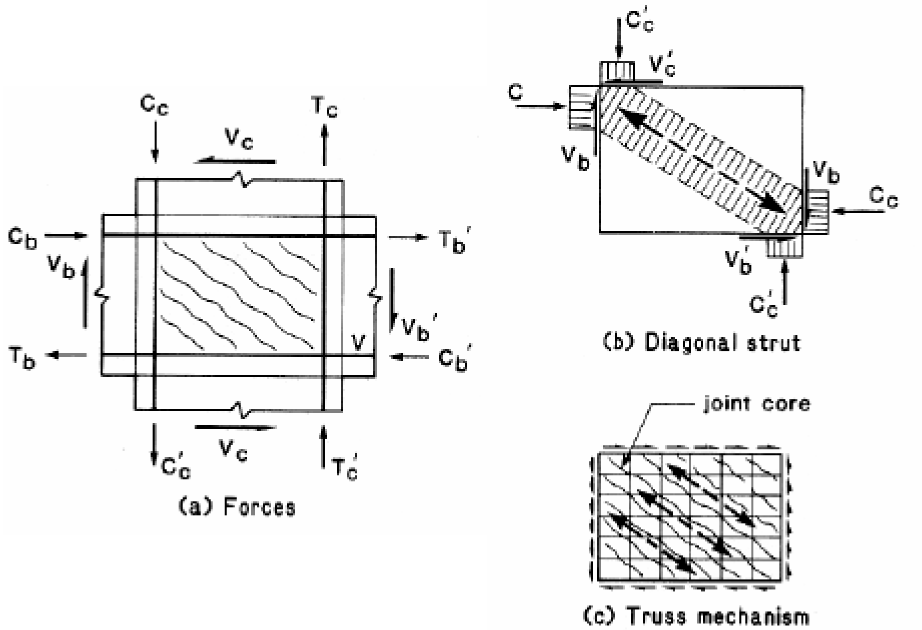

Figure 3.23. Forces and postulated shear-resisting mechanisms in a typical interior beam-column joint: forces acting on beam-column joint (a); diagonal strut mechanism (b); truss mechanism (c).

This loss in beam stiffness can lead to increased lateral displacements of the frame and potential instability. Two basic mechanisms have been postulated as contributing to the shear resistance of beam—column joints. These are the diagonal strut and the joint truss (or diagonal compression field) mechanisms, shown in Figure 3.23b and c, respectively. After several cycles of inelastic deformation in the beams framing into a joint, the effectiveness of the diagonal strut mechanism tends to diminish as through-depth cracks start to open between the faces of the column and the framing beams and as yielding in the beam bars penetrates into the joint core. The joint truss mechanism develops as a result of the interaction between confining horizontal and vertical reinforcement and a diagonal compression field acting on the elements of the confined concrete core between diagonal cracks. Ideally, truss action to resist horizontal and vertical shears would require both horizontal confining steel and intermediate vertical column bars (between column corner bars).

Experimental tests cited in Park et al. 1986 indicate that where no intermediate vertical bars are provided, the performance of the joint is worse than where such bars are provided. Tests of beam-column joints (Ehsani et al. 1985, Hanson et al. 1967, Meinheit et al. 1982) in which the framing beams were subjected to large inelastic displacement cycles have indicated that the presence of transverse beams (perpendicular to the plane of the loaded beams) considerably improves joint behaviour. Results reported in Ehsani et al. 1985 show that the effect of an increase in joint lateral reinforcement becomes more pronounced in the absence of transverse beams. However, the same tests indicated that slippage of column reinforcement through the joint occurred with or without transverse beams. The use of smaller diameter longitudinal bars has been suggested (Paulay et al 1978) as a means of minimizing bar slippage. Another suggestion has been to force the plastic hinge in the beam to form away from the column face, thus preventing high longitudinal steel strains from developing in the immediate vicinity of the joint. This can be accomplished by suitably strengthening the segment of beam close to the column (usually a distance equal to the total depth of the beam) using appropriate details, as a combination of heavy vertical reinforcement with cross-ties, intermediate longitudinal shear reinforcement, and supplementary flexural reinforcement and haunches.

However, as shown in Figures 3.24 and 3.25, during past earthquakes the absence of these contrivances resulted in severe damage in beam-to-column joints, characterized by slipping phenomena of the bars, especially in case of employment of smooth bars without enough extremity hooks, that especially occurred in the external joints, which appear to be the most critical parts of the structure, but also in the intermediate ones, in case of not continuous longitudinal reinforcements. Besides, the absence of adequate quantity of stirrups at the beam-to-column intersection, due to the high shear stresses determined the collapse of the joints.

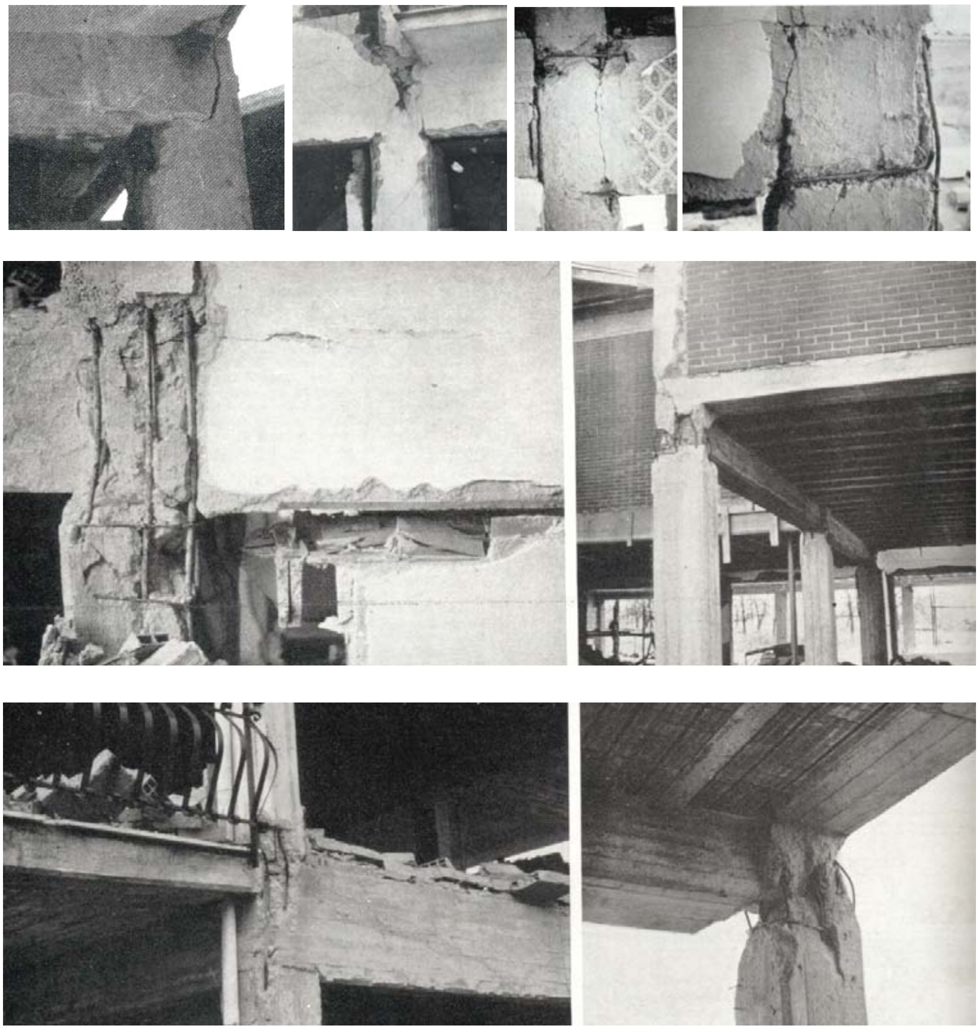

Figure 3.24. Irpinia earthquake (1981), beam-to-column joint failures.

Figure 3.24. Kobe earthquake (1995), beam-to-column joint failure.

Chapter IV

Experimental activity on real bare RC structures equipped with steel ductile braces

4.1 INTRODUCTION

The current research activity consisted of a series of full-scale tests on a reinforced concrete (RC) building, located in Bagnoli (Naples, Italy), in the area where the plants of the previous steel mill named ILVA (former Italsider) have been destined to be demolished. Such an experimental activity was developed within a semi-voluntary project called ILVA-IDEM, whose acronym “Intelligent DEMolition” was inspired by the ongoing occurrence in the area, being coincident with the final destiny of this building itself.

The building was designed and constructed at the end of ‘70s, for mainly resisting gravity loads, as the area was not yet declared seismic prone at that time. Figure 4.1a shows the building in its original configuration. External and partition walls, as well as all other non-structural elements, were removed in order to get a bare RC structure. Besides, the potential number of tests has been increased by cutting the slabs at the first and second floor, in such a way to divide the whole building into six separate structures to be upgraded with different techniques. Figure 4.1b shows the six sub-structures and highlights the different seismic upgrading systems which were selected for testing.

Figure 4.1. The original building (a); the six separate sub-structures (b).

Multiple tests for each of the investigated systems have been carried out on Building No.1, thus summing up to 15 full-scale tests, including three tests on the bare RC structures. The following is the complete list of the tested techniques and the corresponding number of tests:

1. Base isolation with rubber bearings (2 tests).
2. Buckling restrained braces (2 tests).
3. Composite fibre-reinforced materials (2 tests).
4. Eccentric braces (3 tests).
5. Shape memory alloy braces (3 tests).
6. Shear panels (both in steel and pure aluminium) (3 tests).

The base isolation system has been submitted to free vibration and ambient vibration tests. Static inelastic tests have been carried out for all the other systems. Exceptionally the shape memory alloy bracing system was tested both statically and dynamically (free vibration).

The whole building has been divided into six separate sub-structures in order to increase the potential number of specimens for testing different upgrading solutions. To this purpose slabs were cut at both the first and the second floor. Figure 4.2 roughly shows the sub-structuring operations.

The sub-structuring consists of several successive demolition activities: a) demolition of external walls (Figure 4.3a), the demolition of the internal partition walls (Figure 4.3b); b) the demolition of all the completion elements such as electrical and finishing system, waterworks, pavement and its sand substrate; c) cutting of the slabs at both first and second floor which have been evidenced the RC bare frame of the building. Finally, Figure 4.4 illustrates the six obtained sub-structures.

Figure4.2. Cutting of the slabs.

Figure 4.3. The building sub-structuring: the removal of external partition walls (a); the demolition of internal walls (b).

Sub-structure n.1 *Sub-structure n.2* *Sub-structure n.3*

Sub-structure n.4 *Sub-structure n.5* *Sub-structure n.6*

Figure 4.4. The six different sub-structures.

In the following Sections, a summary of test results is given, also showing a comparison between them.

The RC sub-structures, which were submitted to test after upgrading, are n°. 2, 4. They are composed by four columns on two stories and a couple of perimetral beams per each floor. Namely, results on eccentric braces (EBs), buckling restrained braces (BRBs) are illustrated.

4.2 DESCRIPTION OF THE TESTED STRUCTURES

4.2.1 Geometry

The structure here studied is essentially constituted by four columns sustaining two floors. Columns have a square 300 mm x 300 mm cross-section. The structure of the two floors can be essentially described as made of T-section beams going parallel in one direction and supported by two longitudinal L-section beams.

The T-section floor-beams are spaced 500 mm on centre, the space in between the beam webs being filled by hollow clay tiles, which do not have any structural function. These beams are connected by a 40mm-thick slab on the top, which constitutes the flange of the T-section, and by a mid-span small rectangular beam with the axis in the perpendicular direction.

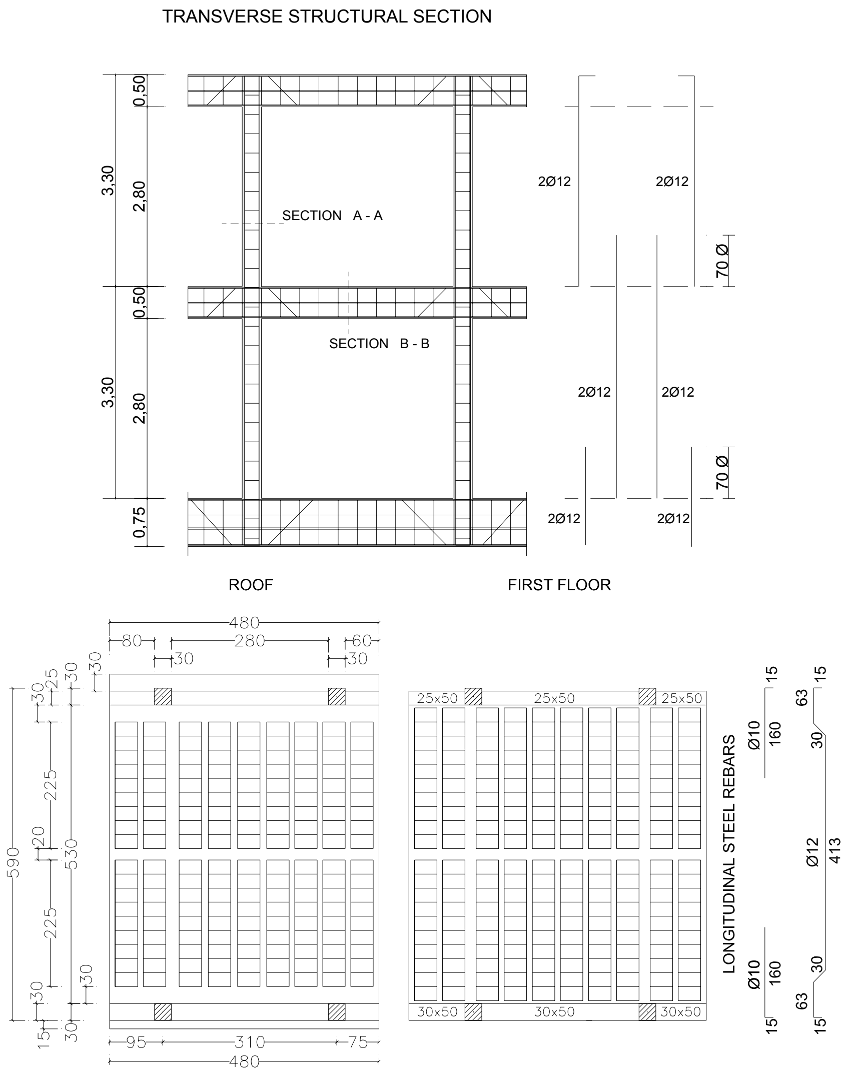

Sub-structure n.2 (equipped with BRBs)

Figure 4.5. Geometry and reinforcement of the existing structure. (continued)

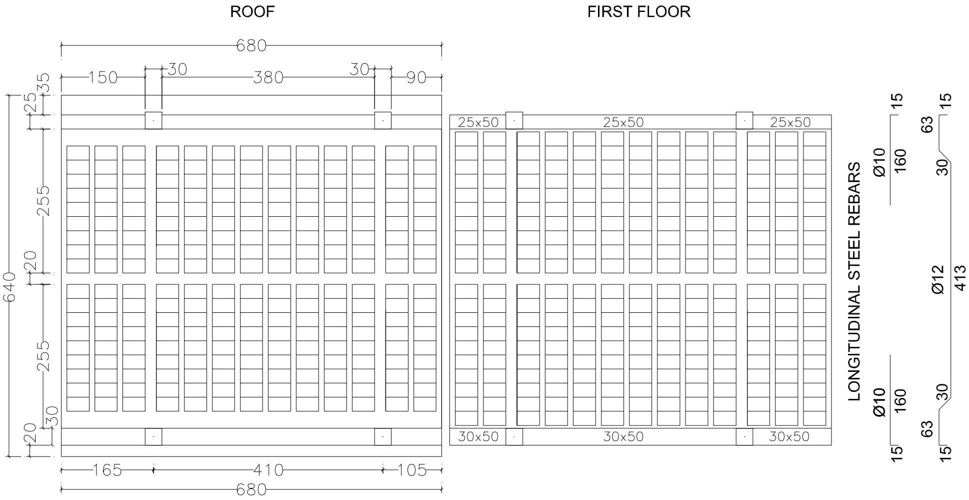

Sub-structure n.4 (equipped with EBs)

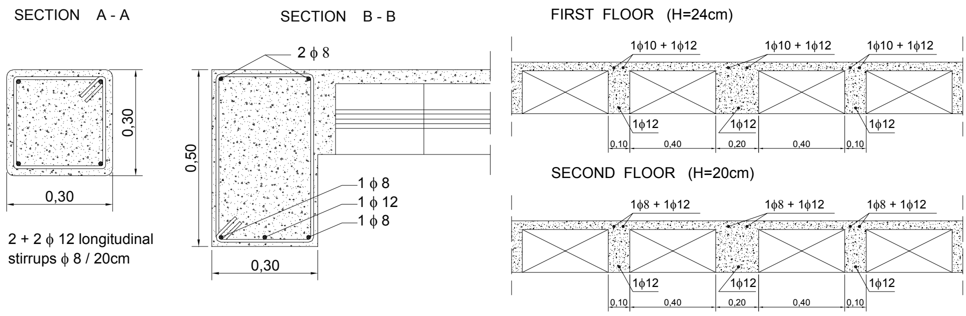

Figure 4.5. Geometry and reinforcement of the existing structure.

Both the essential geometry and the main existing steel-reinforcement detailing of the tested structure are shown in Figure 4.5. In these figures is also showed the highlight of the T-section floor-beams, with the web width equal to 100 mm, the flange thickness equal to 40 mm, the flange width equal to 500 mm and the depth equal to the total thickness of the floor-slab. The latter thickness is 240 mm at the first story and 200 mm at the second one. Column longitudinal steel re-bars are in number of four, placed at the section corners and have a diameter of 12 mm. Transverse stirrups have a diameter of 8 mm and are spaced of about 200 mm.

The longitudinal column reinforcement is characterized by the typical lap-splice at the base, immediately upon each horizontal slab. The lap-splice length has been measured equal to about 70 bar-diameters (600 mm) on structure n.6 (see Figure 4.1b). Details of the steel reinforcement in both the floor-beams and the supporting longitudinal beams are also plotted in Figure 4.5, where it is clearly shown that the floor-beams have a doubled width (200 mm) and reinforcement in correspondence of columns. The structure was loaded in the transverse direction with respect to the perimeter longitudinal beams sustaining the floor-slabs.

Then, the lateral-load resisting structural system is essentially constituted by the bending response of the columns and of the floor T-section beams, the latter contribution depending also on the torsional stiffness of the longitudinal supporting beams.

4.2.2 Material properties

The main mechanical properties of both concrete and steel have been measured in the laboratory, using sample specimens draw from the existing structures. Moreover, a number of NDT tests have been carried out on site. These tests aim evaluating the quality and the distribution of the concrete properties across the structure. Such an information is of viable importance when addressing the seismic behaviour of a structure and allows to get a very accurate calibration of the numerical models in the low vibration range, as it will be seen later in the paper. Figure 4.6 illustrates some phases during the compression tests on concrete cylinders. Table 4.1 summarizes the Young modulus and the axial compression strength measured for each of three specimens. Average values are also given in the same table.

Tension test results on steel are analogously summarized in Table 4.2, where Φ refers to the nominal bar diameter and the stresses are evaluated accordingly. All different bar diameters used in the construction of the existing structure has been tested, namely: Φ12 for columns, Φ10÷Φ12 for beams, Φ8 for stirrups. It could be useful to remark that, according to available design drawings, nominal values of strength of concrete and steel are 20MPa (cylindrical strength) and 380MPa, respectively.

The NDT tests consisted in measuring ultrasonic pulse velocity V and the rebound index of the sclerometer Ir. A summary of the results is given in Table 4.3 and Table 4.4. In particular, Table 4.3 reports, for the same vertical alignment (column no 1), the measures taken at three different locations: top (T), middle (M), and base column (B); whereas Table 4.4 reports the measures taken at the middle height location of all the columns. It can be observed that the measured values generally increase from top to bottom within the same column, therefore the elastic deformation capacity is not uniform; further, there exist some scatter in the average values (location M) from column to column. Both these two aspects should be taken in proper account when establishing numerical models. Finally, even if V and Ir do not present high correlation, they have been combined together to derive the Young modulus and the concrete strength that were found respectively equal to 17214MPa and to 21.4MPa slightly than the lab values but well compared with them and hence meaningful.

As far as the steel reinforcement is concerned, the listen values show that a present variation of about ± 20% and ± 10%, for the yield stress and ultimate stress respectively, is to be expected and that the ultimate to yield stress ratio varies in the range 1.14 ÷ 1.67. Such large variation intervals suggest a quite different behaviour of the rebars. This aspect is apparent in Figure 4.8 where the force-displacement diagrams of the tested rebars are plotted. At this stage, some further observations deserve to be draw: in only three of the six tests plotted a well defined yield plateau is detectable; the ductile branch in the hardening range presents variation as large as 100%: in one case a brittle rupture is observed; the results do not depend on the rebars diameter.

In order to explain these deficiencies, the specimens were subjected to a deeper inquiry, involving chemical composition, possible inclusion, micro-structural shape and fracture surfaces. The study was carried out by CSM SpA (Center for Material Development) and the following conclusion was draw. The steel contains high impurity, particular in lead (P=0.035%) and sulphur (S=0.036%) that is responsible of the high content of sulphide of manganese (MnS) inclusions; the steel presents non homogeneity at the micro-structural level due to the lamination external defects due presumably to defects in the category products.

Figure 4.6. Specimens tested in compression before and after the tests.

Table 4.1. Main measured mechanical properties of concrete.

Specimen n.	Unit weight (kg/m3)	Elastic modulus (MPa)	Strength (MPa)
1	2244	17692.0	20.5
2	-	16666.7	21.0
3	2235	16129.2	19.9
Average	2239	16829.3	20.5

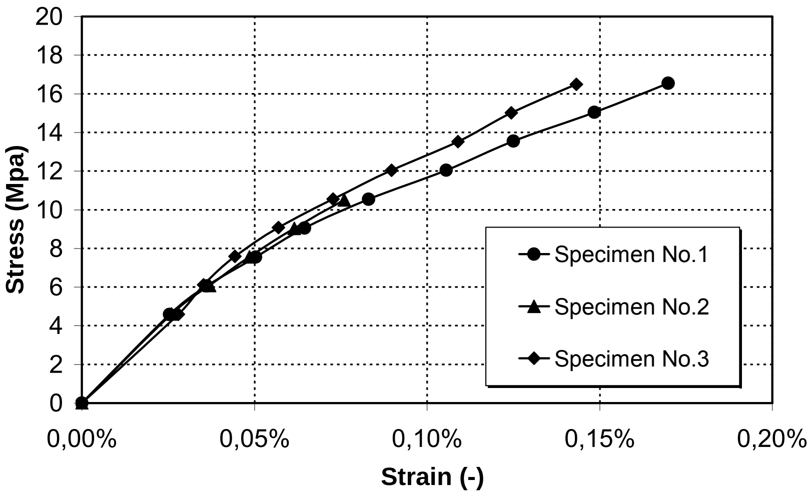

Figure4.7. Stress-strain diagram of concrete specimens.

Table 4.2. Summary of the main mechanical properties of steel.

Specimens n.	Φ (mm)	Length (mm)	Yielding load (kN)	Ultimate load (kN)	Ultimate Stress (MPa)	Yielding Stress (MPa)
1	8	1040	29.0	33.0	656.5	576.9
2	8	975	-	41.0	815.7	-
3	8	500	23.1	33.4	664.5	459.6
Average					712.2	518.25
4	10	558	39.5	59.2	753.8	502.9
5	10	520	38.9	58.8	748.7	495.3
6	10	485	-	62.7	798.3	-
Average					766.9	499.1
7	12	850	44.1	73.8	652.5	389.9
8	12	570	53.1	82.2	726.8	469.5
9	12	860	53.0	79.0	698.5	468.6
Average					692.6	442.7

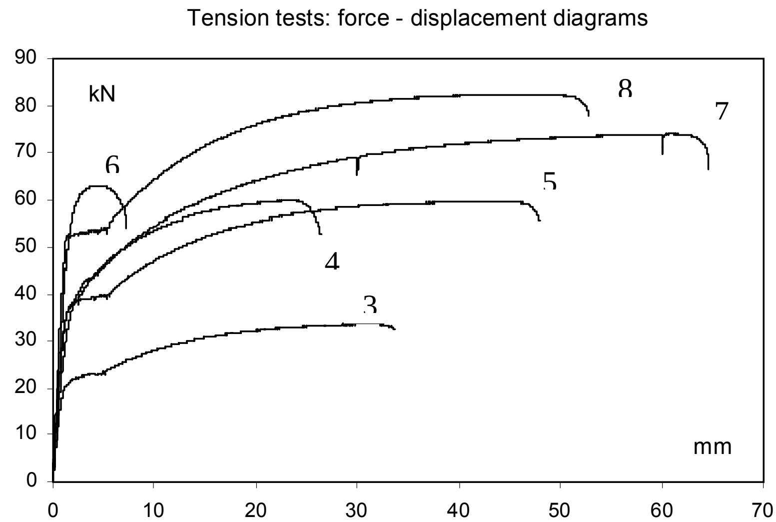

Figure 4.8. Stress-strain diagram of steel specimens.

Table 4.3. ND tests. Column 1, different locations.

Column n.	Floor n.	Position -	V (m/s)	Ir -
1	2	T	2930	35.1
1	2	M	3920	38.6
1	2	B	4168	38.9
1	1	T	3790	32.5
1	1	M	3800	33.1
1	1	B	3910	32.3

Table 4.4. ND tests (all columns, middle height location).

Column n.	Floor n.	Position -	V (m/s)	Ir -
1	2	M	3920	38.6
1	1	M	3800	33.1
2	2	M	4039	28.4
2	1	M	4050	38.1
3	2	M	4039	28.4
3	1	M	4090	38.0
4	2	M	3810	32.4
4	1	M	4145	35.0

4.2.3 Description of tested inverted-Y EB system

In the current study a vertical shear link was used, as shown in Figures 4.9a-b-c. Link-to-slab connections have been realized by end-plate bolted connections. An important aspect to be remarked is that the link connection to the existing RC structure was quite easy, allowing substitution of the damaged link after each test.

Link sections have been selected in such a way to match, as close as possible, the minimum web area required to resist the design force. More details on links are given in the following Sections, since they are somewhat different each other for the three tests carried out.

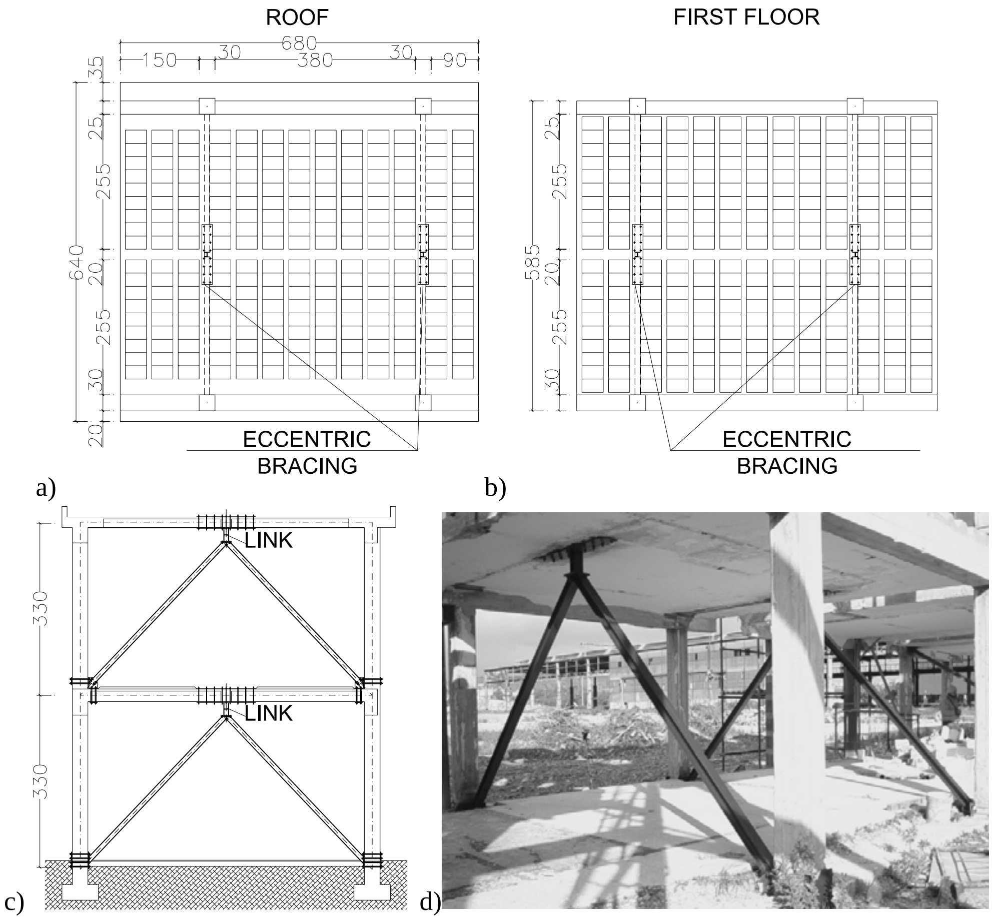

Figure 4.9. Inverted-Y EB specimen configuration.

An important aspect in the design of steel bracing for RC structures is the correct design of brace-to-RC structure connections. Maheri and Sahebi (1997) have studied and tested different types of such connections. In case of existing RC structures the best solution seems to adopt gusset plates bolted to RC beam-to-column joints by means of bolts passing through holes drilled in the RC members, as shown in Figure 4.10. Analogously, link-to-RC beam connections can be made by bolting end plates to the RC structure by means of bolts passing through holes drilled in the RC beams, as shown in Figure 4.10. A similar solution is adopted for connecting diagonal brace to foundation RC beam (Figure 4.11).

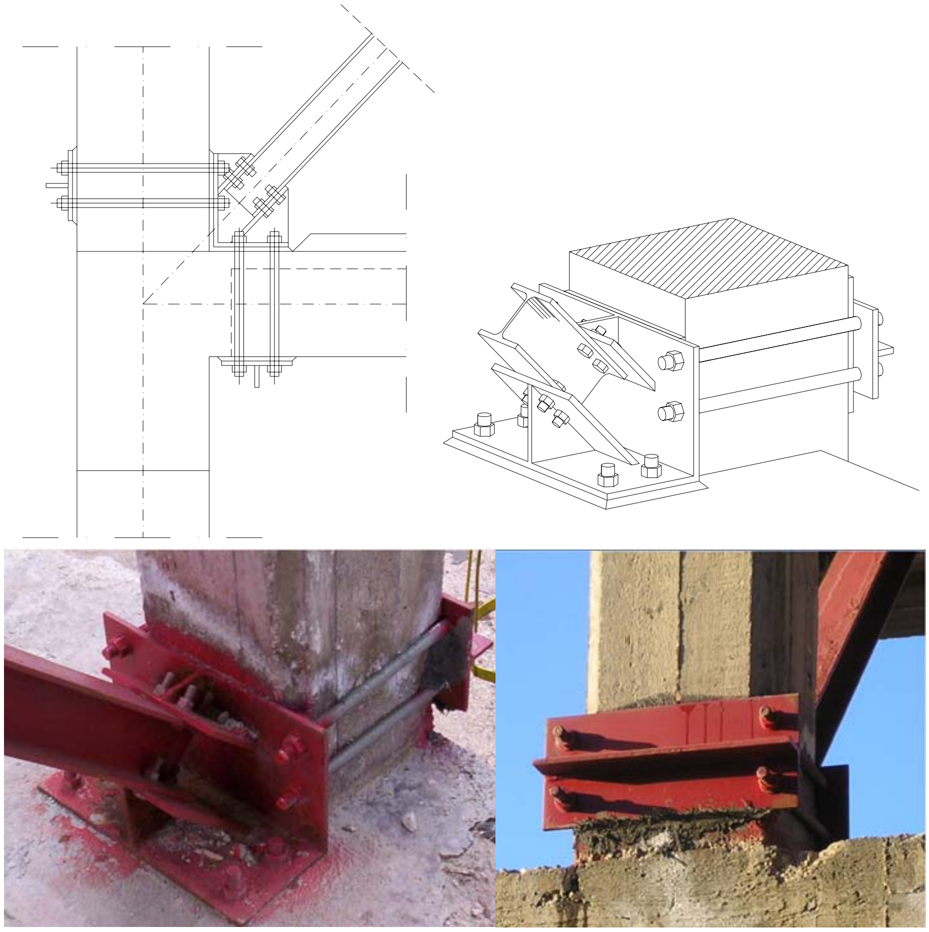

Figure 4.10. Diagonal brace-to-RC connections.

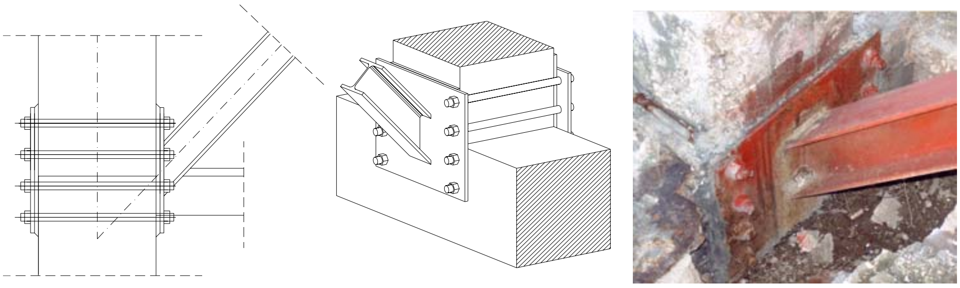

Figure 4.11. Diagonal brace-to-RC foundation connections.

4.2.4 *Description of tested "only-steel" BRB system*

In the present study, the diagonal Buckling-Restrained Braces were directed in alternate way, in order to evaluate any possible asymmetry in the response of the studied braces in tension and in compression. In particular, the location of these braces is shown in Figures 4.12 and 4.13.

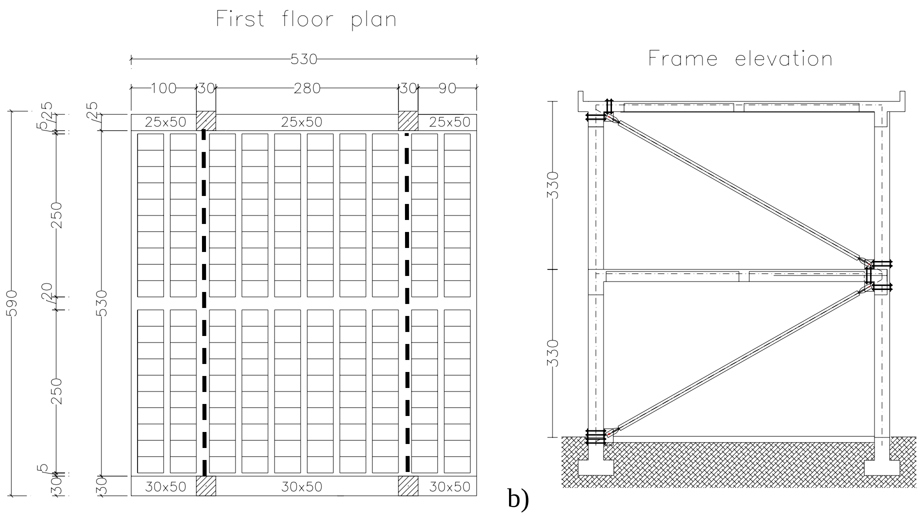

a) b)

Figure 4.12. Geometry of the RC structure equipped with BRBs.

a) b)

Figure 4.13. The RC structure with BRBs.

As in the case of EBs, also for BRB system the correct conception and design of brace-to-RC structure connections is fundamental in order to provide an effective and reliable upgrading of existing RC structures. Similarly to the previous system, gusset plates bolted to the RC beam-to-column joints by means of bolts passing through holes drilled in the RC members have been adopted, as shown in Figures 4.14. The experimental response of this type of connection revealed to be linear up to the final load of the brace (Maheri and Sahebi, 1997).

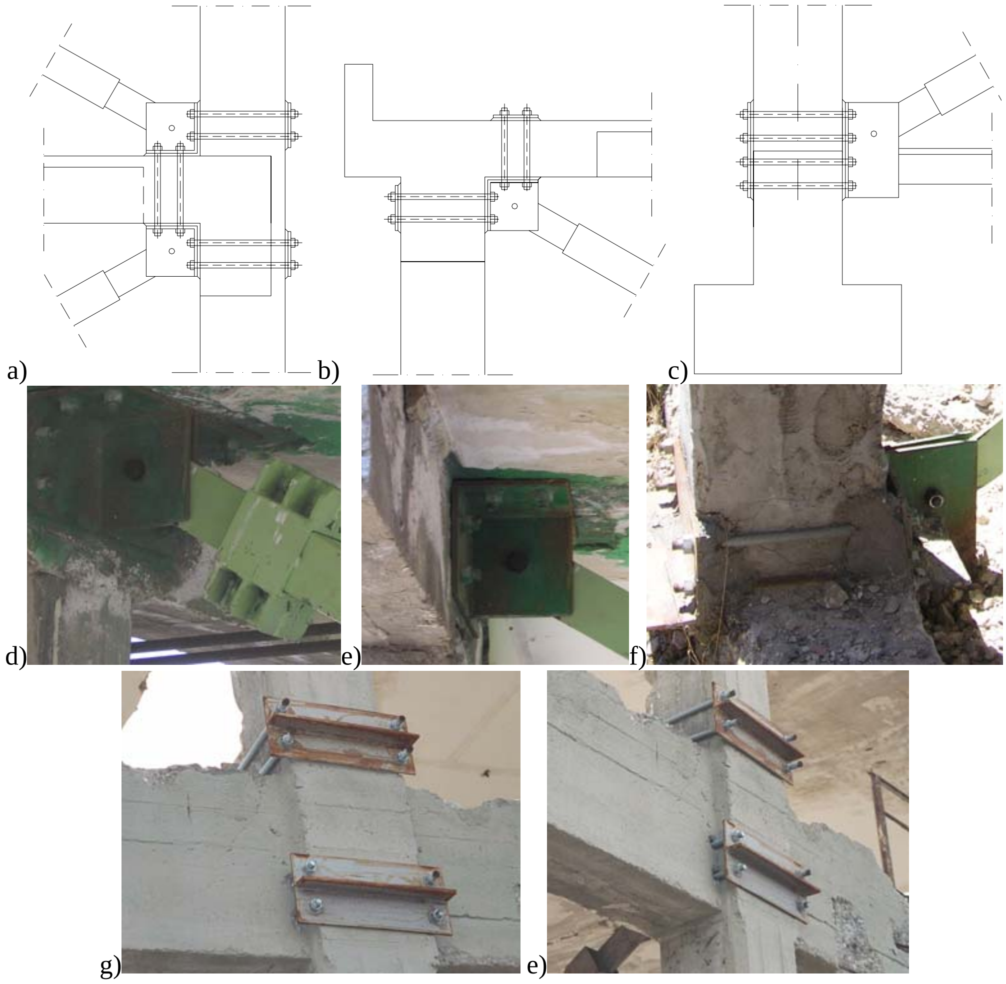

Figure 4.14. Diagonal brace-to-RC end connections.

4.3 DESCRIPTION OF THE TEST SETUP

Figure 4.15 illustrates the test set-up, showing a global view of the reacting steel frame (a-b), close-up views of the two loading jacks (c-d-e) and the supporting steel beam used (f). In particular, this vertical steel beam (Figure 4.15f) was used for distributing the applied lateral force between the two stories of the structure to be tested. This arrangement reproduces an inverted triangular lateral load pattern which is often assumed in theoretical pushover studies. The strengthened structure was subjected to a cyclic loading history up to the development of a clear collapse mechanism. During the test, floor displacements have been measured, by using a video-camera installed above each floor for measuring the floor lateral displacements (Figure 4.16). This displacement-measuring device proved to give lateral displacements with the same precision of a topographic total station, which was used in a former test on a similar structure.

Figure 4.15. Test setup (continued).

e)  f) 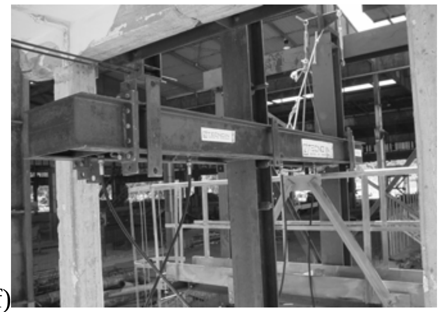

Figure 4.15. Test setup.

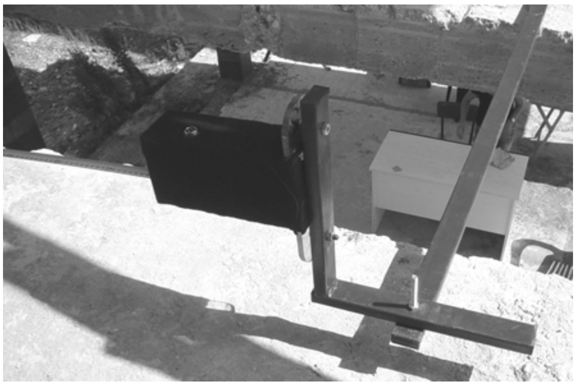

Figure 4.16. Displacement-measuring device.

4.4 EXPERIMENTAL RESPONSE OF THE STRUCTURE EQUIPPED WITH ECCENTRIC BRACES

4.4.1 Inverted-Y EBs: Test No.1

The first eccentric bracing system was designed according to EC8 code prescriptions, but neglecting capacity design criteria. The base shear strength demand under earthquakes having a 475 years return period has been fixed equal to 117.76kN. Accordingly, the link cross section (HEA100) and the steel grade (S275) have been selected. The shear strength capacity was evaluated according to the first-yielding definition given in Popov & Engelhardt (1988). As far as the link length is concerned, it was chosen using the intersection of three conditions:

1) to have short links;

2) to achieve the maximum inelastic link shear rotation when the first plastic hinge forms in the RC structure;

3) to satisfy inter-story drift limitations suggested by EC8 (2003) for non-structural damage control under frequent earthquakes.

In particular both the first and the second point implicitly require satisfying the ultimate limit state by appropriately selecting the link length.

In case of equal values of bending moments at both link ends, to have a shear link, the link length has to satisfy the condition introduced by Kasai & Popov, (1986), as follows:

$$1.5V_p \cdot \frac{e}{2} \leq 1.2M_p \Rightarrow e \leq 1.6\frac{M_p}{V_p} \tag{47}$$

According to the definitions given by Eurocode 8, the yield values of link bending moment and shear force, to be used in both resistance checks and link classification, are as follows:

$$M_p = f_y b_f t_f (d - t_f) \tag{48}$$

$$V_p = \frac{f_y}{\sqrt{3}} t_w (d - t_f) \tag{49}$$

where b_f is the flange width, t_f is the flange thickness, d is the section depth, t_w is the web thickness, f_y is the material yield stress.

Classification of links is based on Equations 48 and 49, with the addition of the following definition of the limit value of link length corresponding to the short link range:

$$e_S = 0.8(1+\alpha)\frac{M_p}{V_p} \tag{50}$$

where α is the ratio of the absolute values of minimum to maximum bending moments acting at the link ends under the design seismic load combination. If $e < e_s$ then shear yielding will precede flexural yielding and the link is termed a short link. In the case under analysis this ratio resulted equal to about α = 0.23.

In order to explain the second condition it may be useful to analyze the plastic mechanism of inverted-Y EB system, as shown in Figure 4.17. In fact, because of displacement congruence, the second condition can be explained as follows:

$$\theta_p \cdot h = \gamma_u \cdot e \Rightarrow e = \frac{\theta_p \cdot h}{\gamma_u} \tag{51}$$

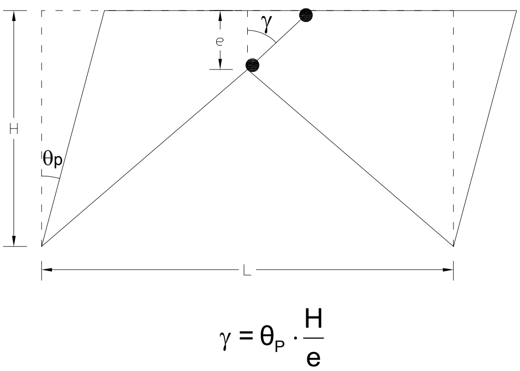

Figure 4.17. Plastic mechanism of inverted-Y EB system.

To satisfy the third condition, it was necessary to force the retrofitted structure to guarantee the EC8 interstory drift limitation, that is:

$$\frac{d_r}{v} \leq 0.004 \cdot h \tag{52}$$

where d_r is the interstory drift and v is a reduction factor which take into account the different extent of the serviceability earthquake respect the seismic event used in ultimate limit state. Thus the Equation 51 can be expressed as:

$$\theta_{SLS} = \frac{\theta_u}{v} = \frac{\gamma_u \cdot e}{v \cdot h} \leq 0.004rad \Rightarrow e \leq 0.004 \cdot \frac{v \cdot h}{\gamma_u} \tag{53}$$

Summarizing all the aforesaid conditions, the solution is obtained by solving the following system:

$$min \begin{cases} e \leq \dfrac{0.8 \cdot M_p}{V_p} \leftarrow ULS \\ e = \dfrac{\theta_p \cdot h}{\gamma_u} \leftarrow ULS \\ e \leq 0.004 \cdot \dfrac{v \cdot h}{\gamma_u} \leftarrow SLS \end{cases} \tag{54}$$

Thus the link length was chosen equal to e = 0.25m and the most limiting condition was relative to the serviceability limit state. Moreover for each link a web stiffener on one side only was adopted.

The nominal yield strength of steel selected at the design stage is 275 MPa, corresponding to the European *S275* structural steel grade. Four coupon tests on plates taken from the flanges showed an average yield strength equal to $f_{y,av}$ = 342 MPa, as shown in Figure 4.18. Unfortunately, no experimental value is available for the web yield stress, and then one single value of 342 MPa will be used in the following for both the web and the flanges of the tested links.

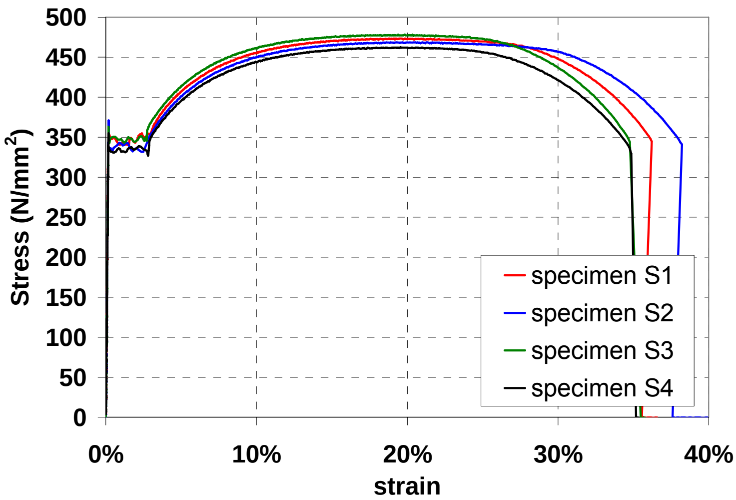

Figure 4.18. Stress-strain curves of four specimens sampled from the flanges of the first tested link.

Therefore, applying Equations 48 and 49, the link flexural resistance is computed equal to M_p = 24.08 kNm, while the link shear strength is V_p = 86.88 kN, and the limit value of the short link length is consequently equal to e_s = 0.273 m. The normalised link length, which is defined as the ratio of the actual link length (0.25 m) to the limit value e_s, is thus equal to e/e_s = 0.92.

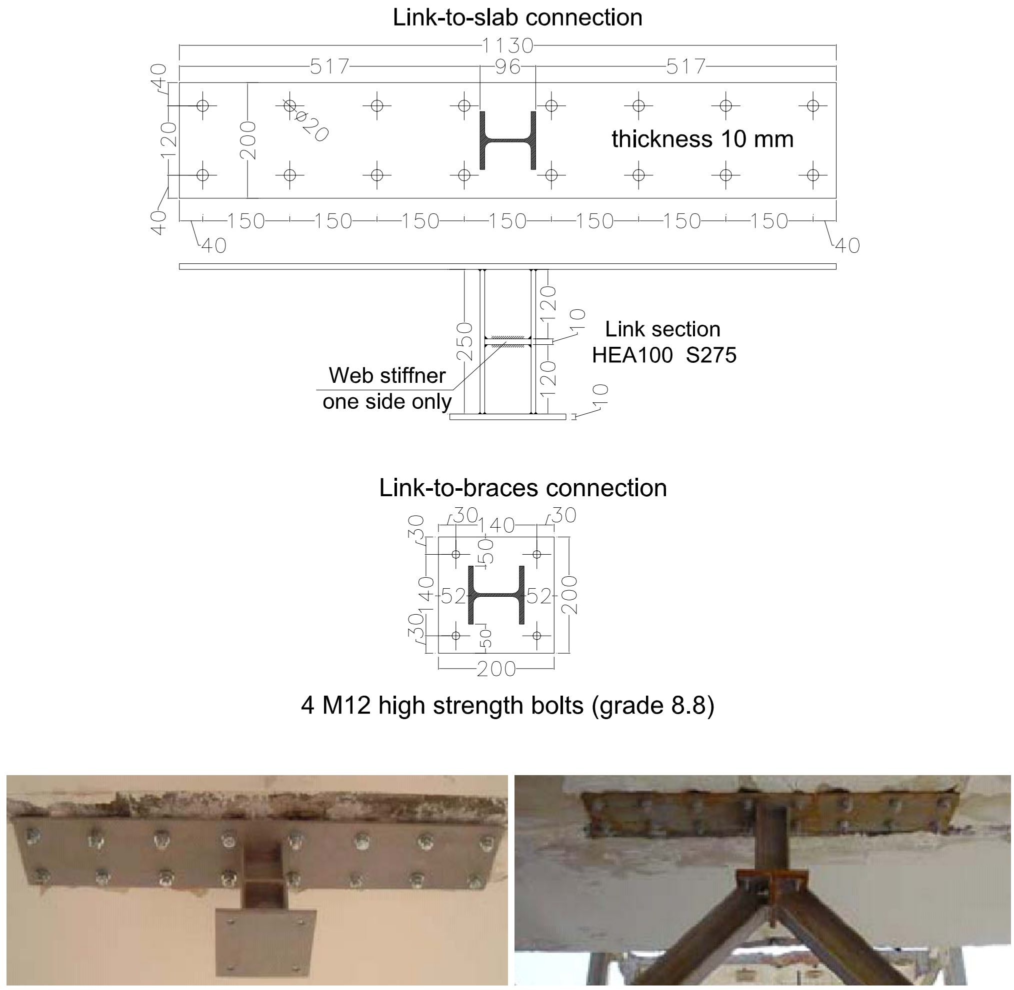

Figure 4.18. Inverted-Y EB, First test: link and its connections.

The diagonal braces, the link and its connections to the RC slab and to the diagonal braces are shown in Figure 4.19.

The experimental test has shown that the collapse was due to the failure of connections. In fact, as illustrated in Figure 4.20, the global response curves soften from the peak value, corresponding to the failure of the connection between the link and the 10mm thick plate connecting it to the RC slab (Figures 4.24a-b). With the passing of the test, both the failure of fasteners and welds at the bottom connection and plastic bending of the corresponding end-plate, connecting the link to diagonal braces, occurred (Figures 4.24c-d).

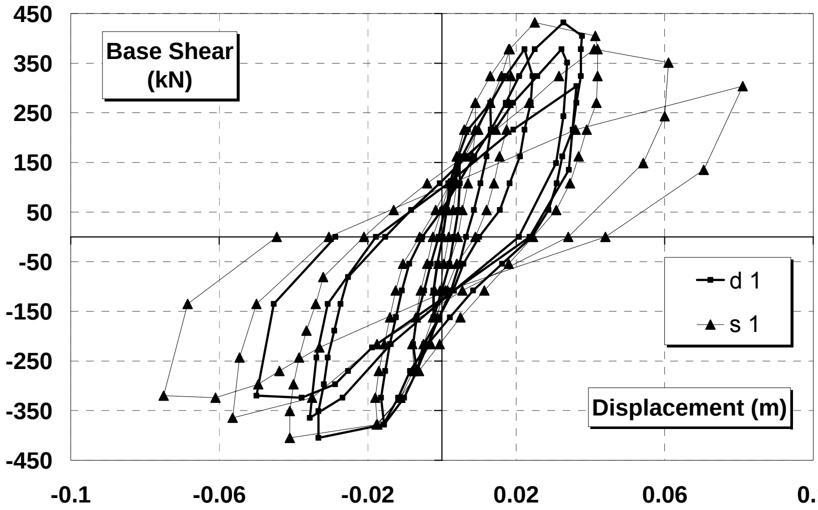

a)

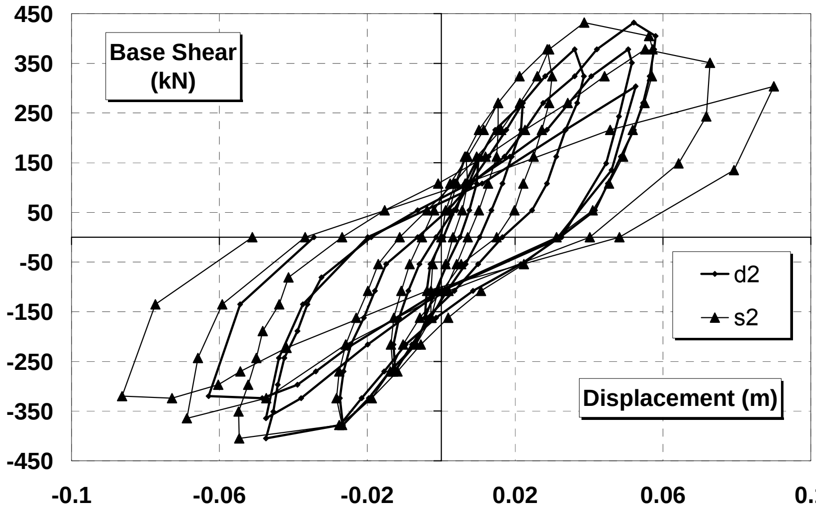

b)

Figure 4.20. Inverted-Y EB, First test: cyclic response curve at first floor (a); Cyclic response curve at second floor (b).

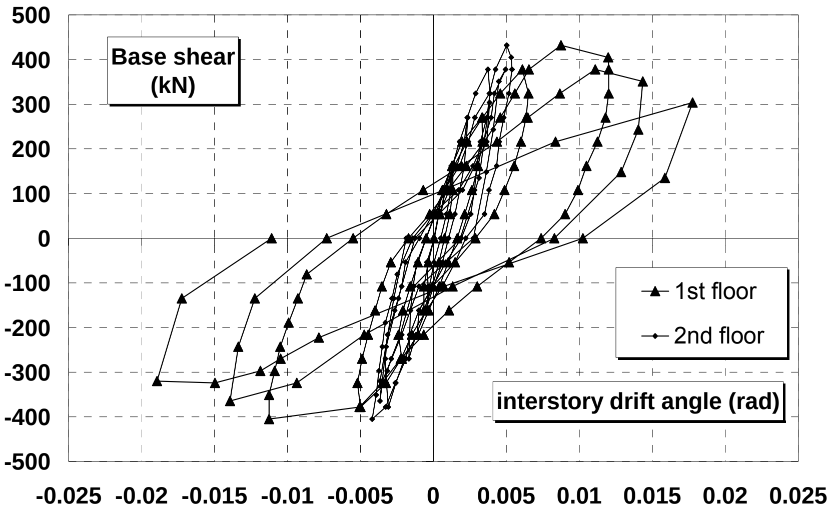

a)

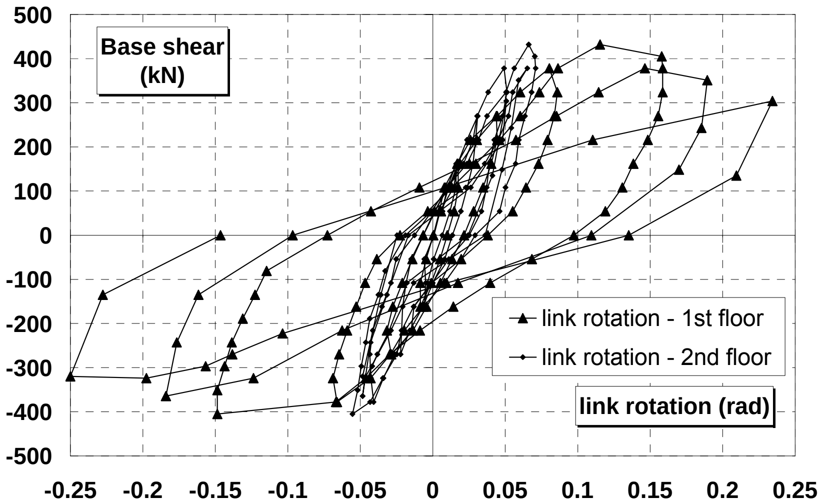

b)

Figure 4.21. Inverted-Y EB, First test: Base shear vs. average interstory drift angle (a); Base shear vs. average link shear rotation (b).

Figures 4.21a,b give indication of the average inter-story drift angles reached during the test. The maximum first-story drift was 1.90% of the first-story height, while the maximum top-story drift was 0.54% of the structure height. Notwithstanding the undesired localization of damage at the link end connections, considering the values of inter-story drift angles reached during the test and the large increase of the story stiffness and strength, it can be concluded that the upgrading technique is very promising.

As well known the link response is characterised by the shear distortion angle γ - shear force V relationship. For classical links, the distortion γ is determined as the difference of end displacements divided to the link length, (Engelhardt and Popov, 1992):

$$\gamma = \frac{\Delta}{e} \tag{52}$$

where Δ is the relative displacement between link ends and e is the link length.

In the case of removable bolted links, the behaviour of the link is more complex, and angle γ determined from Equation 52 will be different.

Referring to Figure 4.22 for clarity sake, the total link deformation is given by the sum of:

(1) shear distortion of the link panel - γ,

(2) rotation in the two end connections $\theta_M=\theta_{Sup}+\theta_{inf}$ (where θ_{Sup} and θ_{inf} are the joint rotation in link-to-beam connection and in link-to-brace connection, respectively),

(3) slip in the connections, characterised by the equivalent rotation $\gamma_{slip}=(\Delta_{slip,sup}+\Delta_{slip,inf})/e$, (where $\Delta_{slip,sup}$ and $\Delta_{slip,inf}$ are the slipping in link-to-beam and in link-to-brace connections, respectively and e is the link length),

and can be expressed as:

$$\gamma_T = \gamma + \theta_M + \gamma_{slip} \tag{53}$$

It can be directly obtained from the total relative displacement Δ_T:

$$\gamma_T = \frac{\Delta_T}{e} \tag{54}$$

Since during the test instrumentation did not permit to measure each deformation contribution, the total shear deformation of link and its connections is shown in Figure 4.23, in order to give indication about average link rotation reached during the test. Hence the maximum total shear deformation of link and its connections (computed as the ratio of the maximum displacement reached at the first floor and the link length) was approximately 30%.

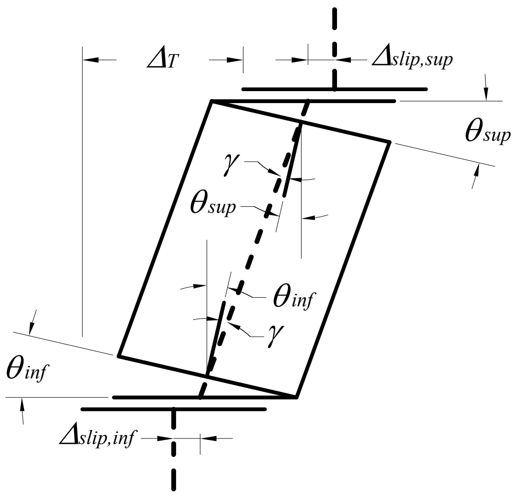

Figure 4.22. Total deformation components in a removable bolted link.

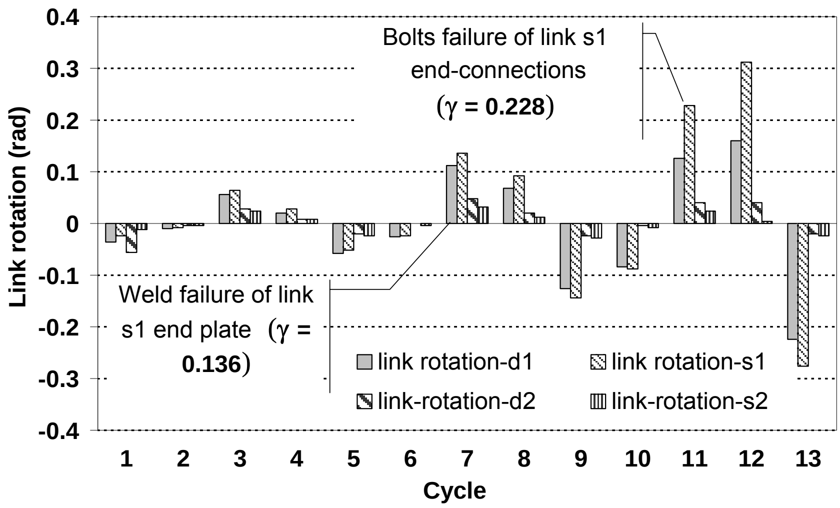

Figure 4.23. Inverted-Y EB, First test: Link shear angle at each cycle.

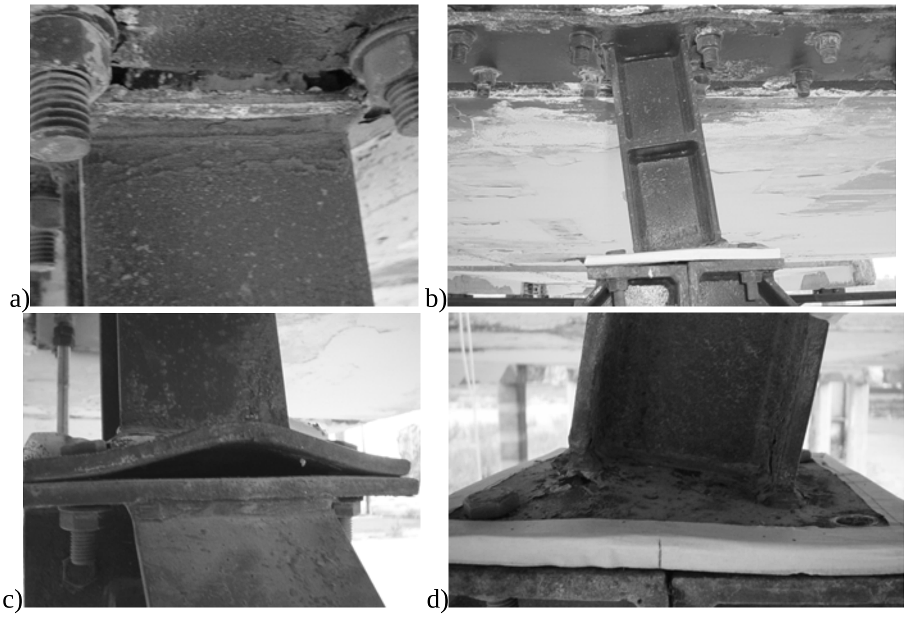

Figure 4.24. Inverted-Y EB, First test: failure of link end connections.

4.4.2 Inverted-Y EBs: Test No.2

For the second test, connections were designed considering an ultimate shear strength of links equal to 1.5 times their yielding strength and applying capacity design criteria. According to Engelhardt & Popov (1989), Kasai & Popov (1986) and Popov & Engelhardt (1988) the ultimate forces transferred by links can be conservatively evaluated through static balance. In particular, it is important to evaluate the flexural action on the link-to-brace connection. In fact, as shown by the previous test, important flexural actions have to be transferred by links to diagonals through the bolted connection. The link cross section and the steel grade were again selected as HEA100 and S275, respectively (Figure 4.26). Once again web stiffeners on one side only were adopted. In this case, as shown in Figure 4.25, three nominally identical material specimens taken from the flanges showed an average yield stress of steel equal to $f_{y,av}$ = 360 N/mm^2. Again, this value is used also for the web.

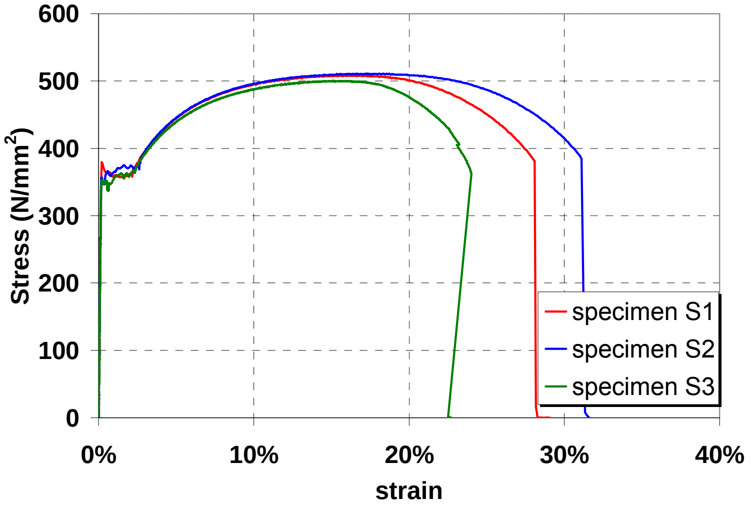

Figure 4.25. Stress-strain curves of three specimens sampled from the flanges of the second tested link.

According to Equations 48, 49 and 50, the bending resistance, shear strength and normalised link length are equal to M_p = 25.34 kNm, V_p = 91.45 kN, e/e_s = 0.81 (= 0.220/0.273).

According to the design procedure suggested in Popov & Engelhardt (1988), the bending moment acting on the link-to-brace connection corresponds to 4.33% of the link plastic strength (M_p). Under this bending moment, the nominal shear strength of the link-to-diagonal connection ($V_{j,Rk}$) resulted to be 1.89 times larger than the link yielding strength (V_p). Using a partial safety factor for connections equal to 1.25, the ratio between the design shear strength of the joint and the link yielding force was equal to $V_{j,Rd}/ V_p$ = 1.52. To achieve this requirement plate thickness increased from 10 to 25mm.

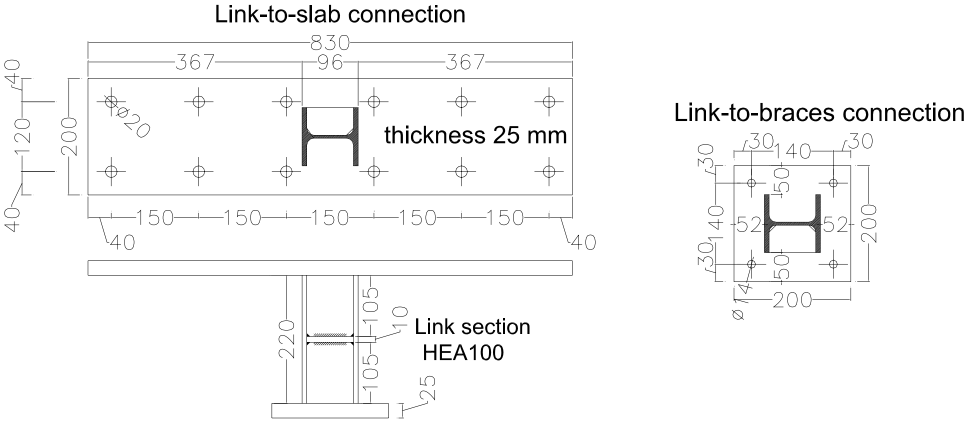

Figure 4.26. Inverted-Y EB, Second test: link and its connections.

Test results have shown that collapse was due to the brittle shear failure of bolts. In fact, as shown in Figure 4.27, the global response curves stop suddenly at a base shear value corresponding to the brittle failure of link-to-brace connections, as shown in Figure 4.29.

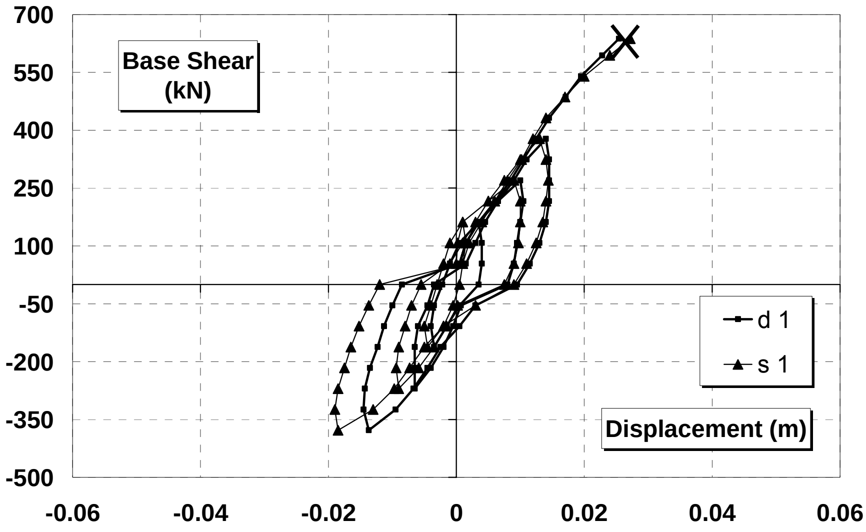

a)

Figure 4.27. Inverted-Y EB, Second test: cyclic response curve at first floor (a); Cyclic response curve at second floor (b). (continued)

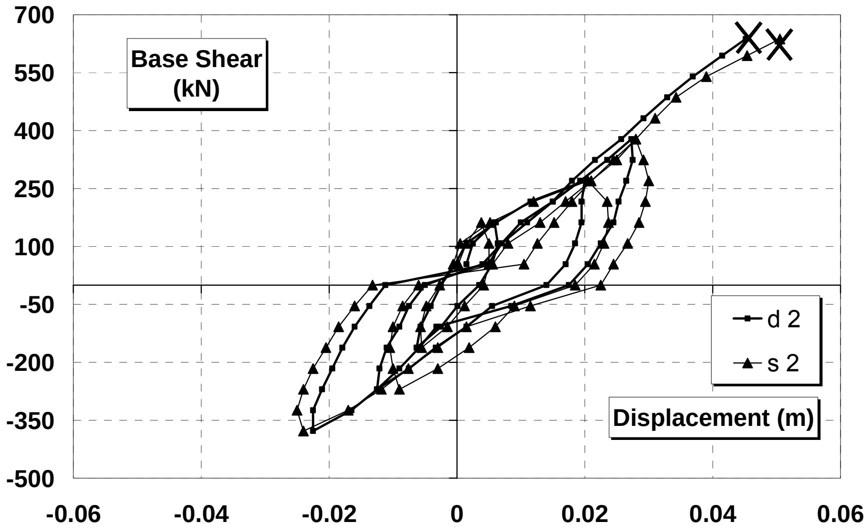

b)

Figure 4.27. Inverted-Y EB, Second test: cyclic response curve at first floor (a); Cyclic response curve at second floor (b).

Figure 4.28 gives indication of the average inter-story drift angles reached during the test. The maximum first-story drift was 0.80% the first-story height, while the maximum top-story drift was 0.65% of the structure height.

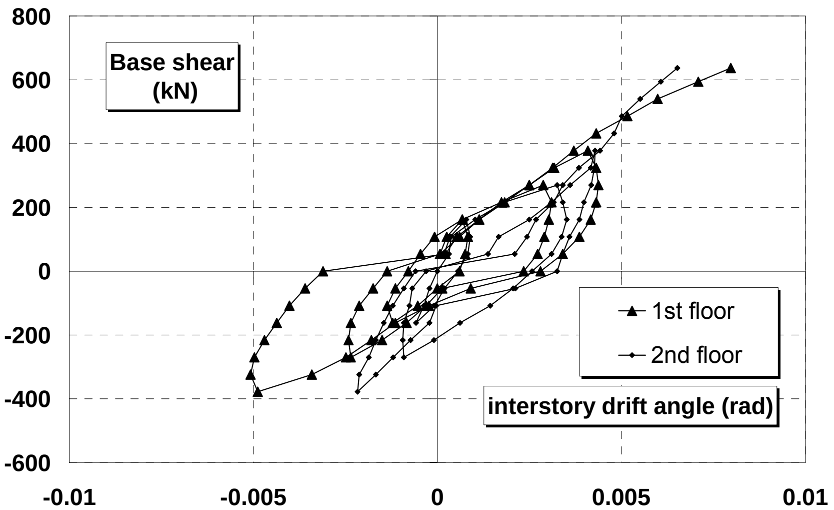

a)

Figure 4.28. Inverted-Y EB, Second test: Base shear vs. average interstory drift angle (a); Base shear vs. average link shear rotation (b). (continued)

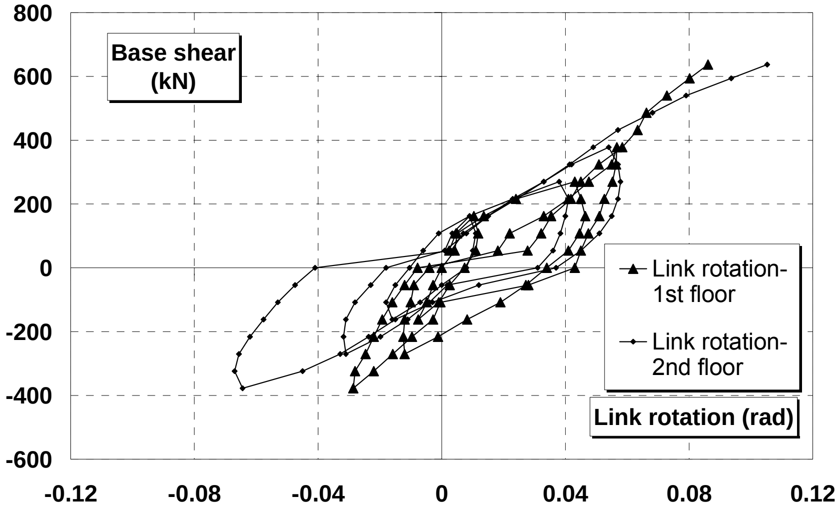

b)

Figure 4.28. Inverted-Y EB, Second test: Base shear vs. average interstory drift angle (a); Base shear vs. average link shear rotation (b).

Figure 4.28 gives indication of the average inter-story drift angles reached during the test. The maximum first-story drift was 0.80% the first-story height, while the maximum top-story drift was 0.65% of the structure height.

a)  b)  c) 

Figure 4.29. Inverted-Y EB, Second test: failure of link end connections.

As shown in Figure 4.29a, plastic bending of connection end-plates was now completely avoided, while a moderate plastic engagement of links along with a strong plastic deformation concentrated as shear hinging of bolts at the link-to-brace joints was observed (Figure 4.29b,c).

As in the previous test, instrumentation did not permit to measure each deformation contribution. The total shear deformation of link and its connections is shown in Figure 4.28b, in order to give indication about average link rotation reached during the test. However, in this case the maximum total shear deformation of link and its connections (γ) was computed as the ratio of relative displacement between both link ends and the link length $\gamma=\Delta/e$ and in this case it was approximately 10.5%. Moreover, it was possible to define the link shear force vs. its average shear deformation. In fact, the link shear force can be computed per each experimental phase as the half of experimental base shear, the latter reduced by the aliquot of base shear force carried only by the bare RC structure. In particular, a range criterion has been adopted to schematize the response of RC structure as alone. In fact, an upper bound of the response of the bare RC structure has been easily obtained by a refined finite element model (further details can be found in Chapter VI) developed considering the RC structure without an initial damage state. Moreover, a lower bound of the RC response has been obtained scaling the numerical RC response up to its lateral resistance (about 30kN) finally measured after all experimental investigations. Hence, Figure 4.30 clearly shows the experimental envelope curves compared with the numerical responses of both undamaged and damaged bare RC structure. While Figure 4.31 shows the link shear force vs. average shear deformation calculated at the end of the above explained process.

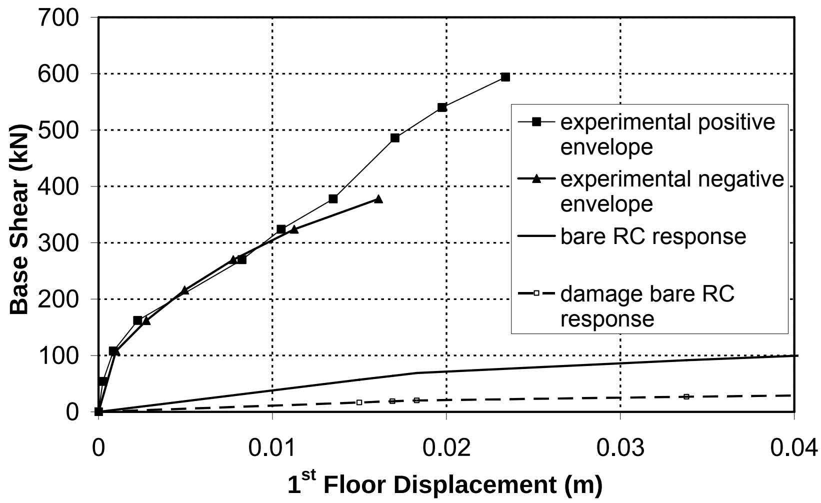

Figure 4.30. Inverted-Y EB, Second test: experimental envelope curves vs. numerical responses of the bare RC structure.

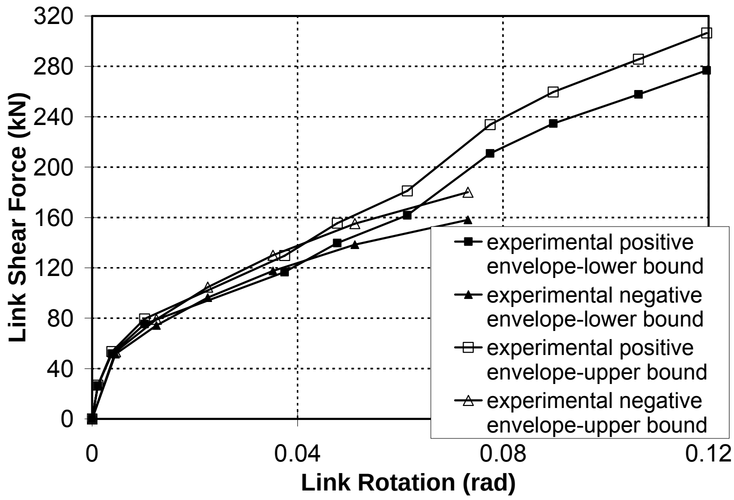

Figure 4.31. Inverted-Y EB, Second test: experimental link shear force vs. average shear deformation.

4.4.3 Inverted-Y EBs: Test No.3

Since the second test revealed link over-strength larger than that expected, another link has been designed in order to increase the system ductility by forcing plastic deformation to be confined within links.

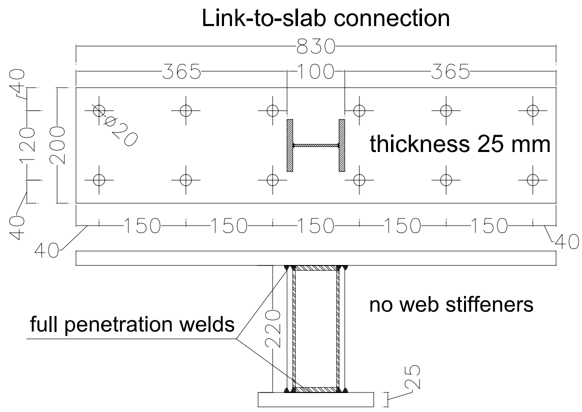

Figure 4.32. Inverted-Y EB, Third test: link and its connections (continued).

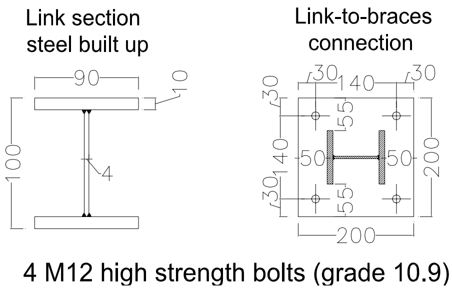

Figure 4.32. Inverted-Y EB, Third test: link and its connections.

Because it was impossible to modify the geometry of link-to-brace joints, a steel built-up section was now designed for the links of the first story, in order to have design shear strength of connections at least 2 times larger than the actual shear strength of links. Four high-strength bolts (grade 10.9) with a diameter of 12mm resulted to be sufficient for this purpose, having a link built-up section constituted by 90mm x 10mm rectangular plates for flanges and 80mm x 4mm rectangular plate for the web (Figure 4.32). The local slenderness ratios were chosen to be similar to the ones of HEA100. This link was short, being its length smaller than the limit value. Contrary to the previous cases, link web stiffeners were not adopted.

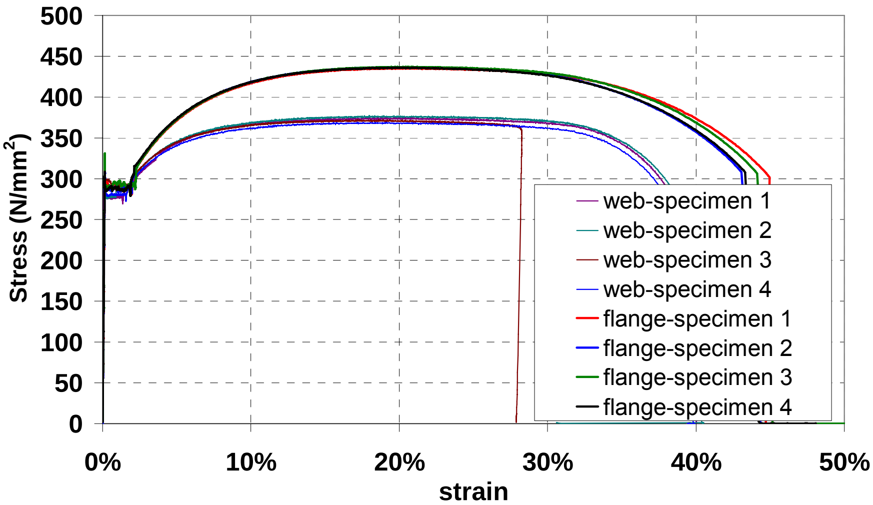

Figure 4.33. Stress-strain curves of specimens sampled from the flanges and from the web plates of the third tested link.

Steel of the web plate exhibited an average yielding stress of 284 N/mm^2, while steel of flange plates had a 319 N/mm^2 yield stress (Figure 4.33). In this case, the ratio α (Equation 50) is equal to 0.20, while the link flexural and shear strength are equal to M_p = 25.84 kNm (Equation 48) and V_p = 59.03 kN (Equation 48), respectively. Consequently, the normalized link length is now equal to e/e_s = 0.52 (= 0.220/0.420).

In this case the bending moment acting on the link-to-brace joint was equal to 28.86% of the link plastic bending moment. The ratio between the joint characteristic shear resistance ($V_{j,Rk}$) and the link yielding shear strength (V_p) was equal to $V_{j,Rk}/V_p$ = 2.84. Based on a partial safety factor of connections equal to 1.25, the ratio between the design strength of the connection and the yielding strength of link was $V_{j,Rd}/ V_p$ = 2.27.

Collapse was due again to the brittle shear failure of bolts of link-to-brace joints. As in previous test, plastic bending of connection end-plates was now completely avoided (Figures 4.34a,b,c), while a significant shear plastic engagement of links was observed. However, the response curves (Figure 4.35) show that the retrofitted structure had now a good behaviour characterized by full stable hysteresis loops. It is interesting to underline that the peak shear force (V_{max}) acting on the links, computed according to the approximate procedure described for the second test, was now 2.23 times larger than the design shear strength of joints and 1.78 times larger than the characteristic value of the joint strength.

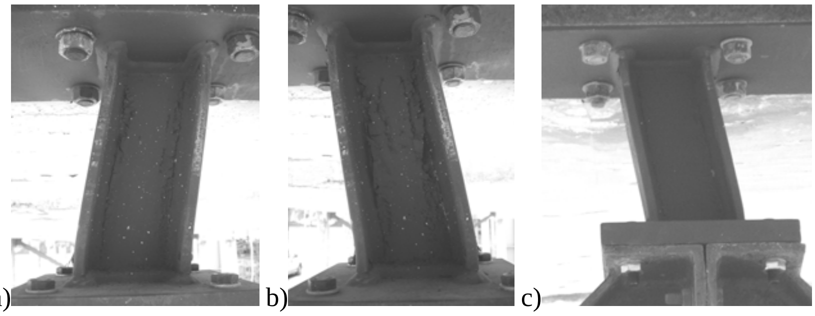

a) b) c)

Figure 4.34. Inverted-Y EB, Third test: failure of link end connections.

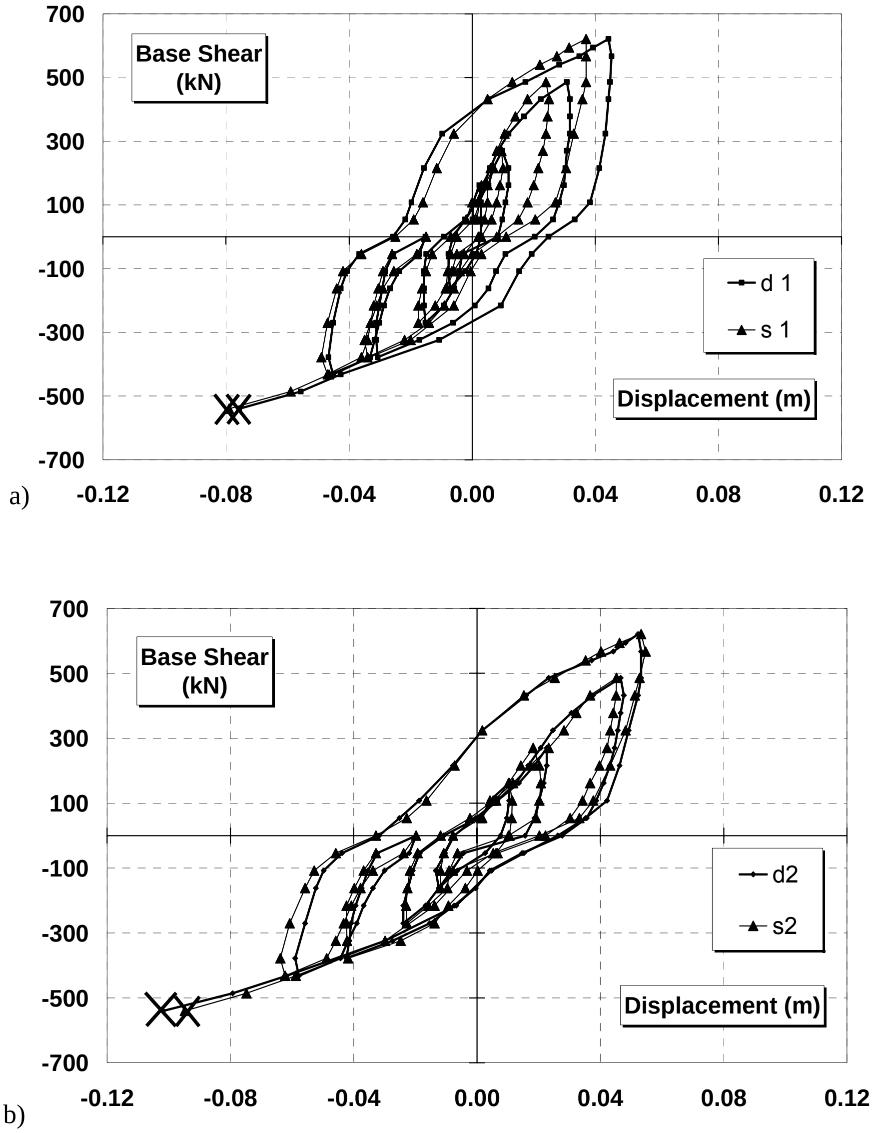

Figure 4.35. Inverted-Y EB, Third test: cyclic response curve at first floor (a); Cyclic response curve at second floor (b).

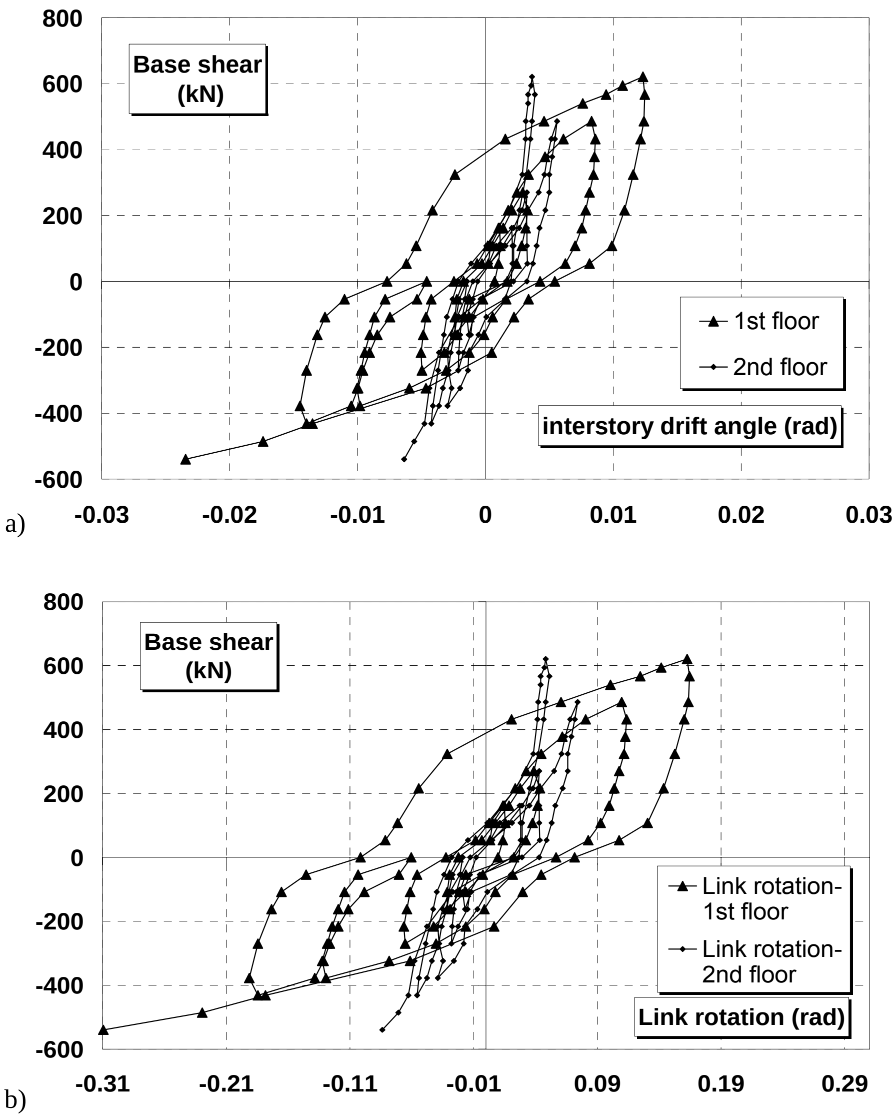

Figure 4.36. Inverted-Y EB, Third test: Base shear vs. average interstory drift angle (a); Base shear vs. average link shear rotation (b).

Moreover Figure 4.36a gives indication of the average inter-story drift angles reached during the test. The maximum first-story drift was 2.34% the first-story height, while the maximum top-story drift was 0.64% of the structure height.

As in the previous test, instrumentation did not permit to measure each deformation contribution. The total shear deformation of link and its connections during the test is shown in Figure 4.36b, in order to give indication about average link rotation reached during the test. In this last test the link local ductility was surely larger than that measured in the previous tests. As in the previous test, instrumentation did not permit to measure each deformation contribution. However, the maximum total shear deformation of link and its connections (γ) was computed in the same manner of the previous case, namely as the ratio of the measured relative displacement between both link ends and the link length $\gamma = \Delta / e$. Similarly to the Test No.2 it was possible to define the link shear force vs. its average shear deformation. Hence, Figure 4.37 clearly shows the experimental envelope curves compared with the numerical response of both undamaged and damaged bare RC structure. While Figure 4.38 shows the link shear force vs. average shear deformation calculated at the end of the above explained process.

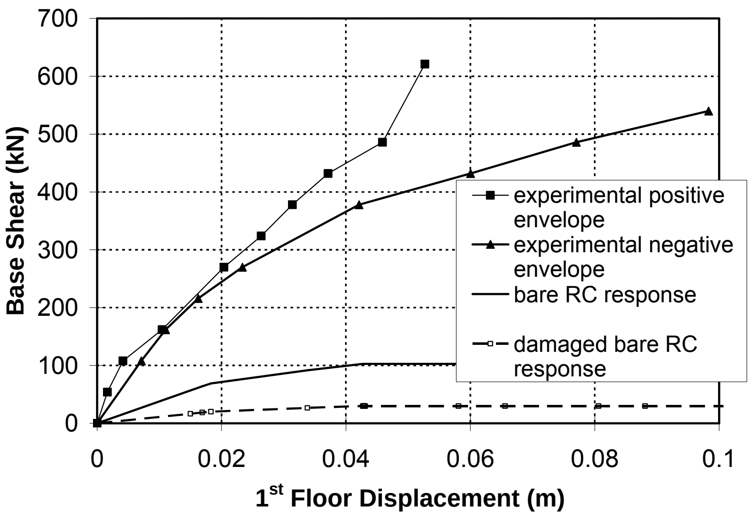

Figure 4.37. Inverted-Y EB, Third test: experimental envelope curves vs. numerical responses of the bare RC structure.

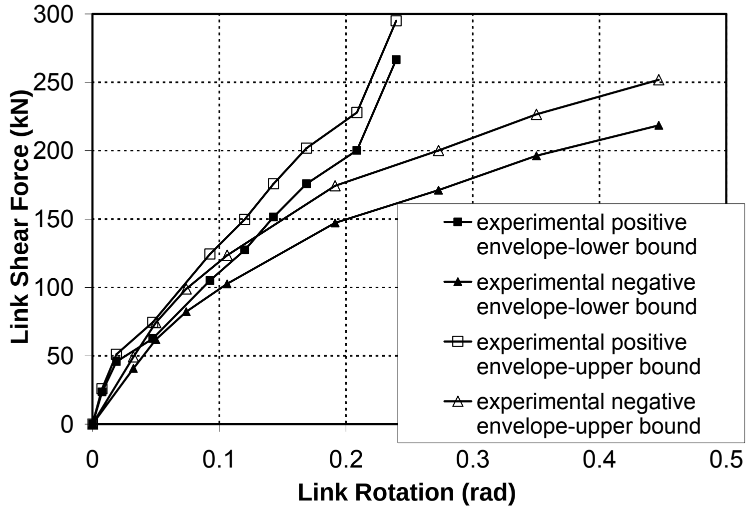

Figure 4.38. Inverted-Y EB, Third test: experimental link shear force vs. average shear deformation.

4.5 EXPERIMENTAL RESPONSE OF THE STRUCTURE EQUIPPED WITH BUCKLING-RESTRAINED BRACES

4.5.1 BRBs: Test No.1

In the current study, two different BRB systems for seismic upgrading of an existing two-story RC structure, which has been subjected to lateral pushover test. These experimental experiences have shown excellent performance of this type of device, but also the need to carefully design end-brace connections against local buckling failure modes. The latter problem has also been emphasized by previous experimental research carried out by Tsai et al. (2004b) and Chen et al. (2004).

The first type (henceforth called type 1) was made using two restraining rectangular tubes that are fully welded together with steel plates. Figure 4.39 gives the essential geometric properties of the first type of BRB tested.

The yielding steel core is a rectangular plate (25mm x 10mm), made of European S 275 steel. The actual yield stress (Figure 4.40) of the core was measured to be 319MPa (i.e. 1.16 times the nominal value).

The buckling-restraining action is attributed to two rectangular steel tubes (100 x 50 x 5), with a ratio between the Euler buckling load (N_E) of the two tubes and the actual yield force (N_y) of the internal steel core $N_E/N_y = 2.1$. As it can be seen in Fig. 28, the restraining effect is given by the flexural stiffness of the tube walls in one direction (vertical direction in Figure 4.39), while in the perpendicular direction two small steel bars were designed to be welded to the tubes with a total clearance with the core of about 1mm (0.5mm for each side).

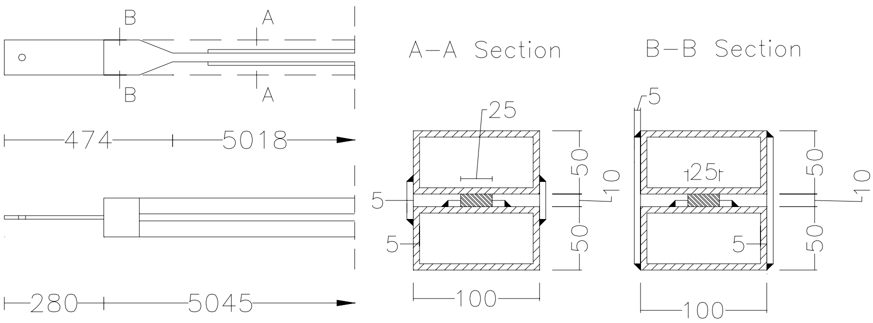

Figure 4.39. Geometry and cross section details of BRB type 1.

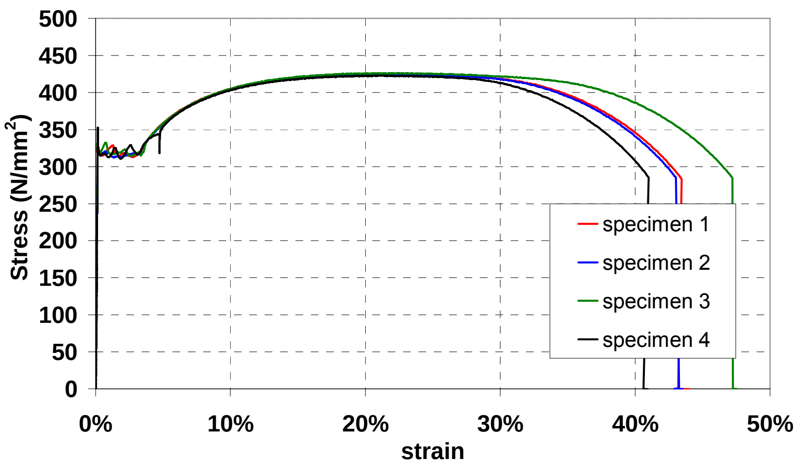

Figure 4.40. Stress-strain curves of specimens sampled from the flanges and from the core plates of the tested BRB type 1.

Test results showed a good response of the brace when it is in tension, with the expected relative displacements developing between the internal yielding core and the restraining tubes (Figure 4.41a). However, the brace ductility was limited by the local buckling of the core, near the brace ends. This buckling produced strong flexural deformation of the closing plates, which were welded for joining the tubes at their ends (Figures 4.41b, c and d). Moreover, increasing the external load, the local deflection of the end tapering plates punched the welded closing plates, as highlighted by the white circle in Figure 4.41e. Because of their flexural failure, the end closing plates were unable to restrain the end portion of brace core. This localization of damage ultimately led to a significant plastic engagement at the transition section between the reduced core and the end tapering (Figures 4.41f, g and h). Hence, this strong flexural plastic engagement of the core at its ending portion led to its premature fracture. Damage in the RC structure is shown in Figures 4.41i and l, where strong flexural cracking is visible.

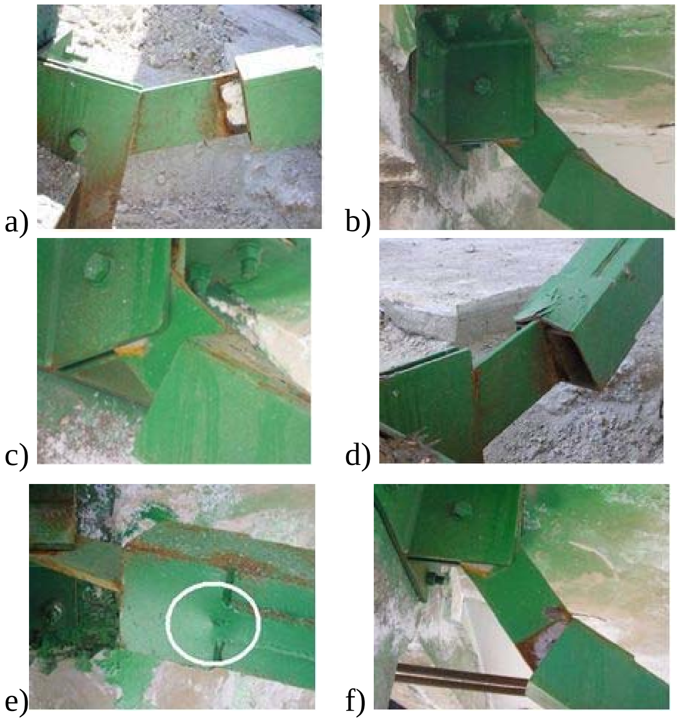

Figure 4.41. BRB Test No.1: damage pattern (continued).

g)  h) 

i)  l) 

Figure 4.41. BRB Test No.1: damage pattern.

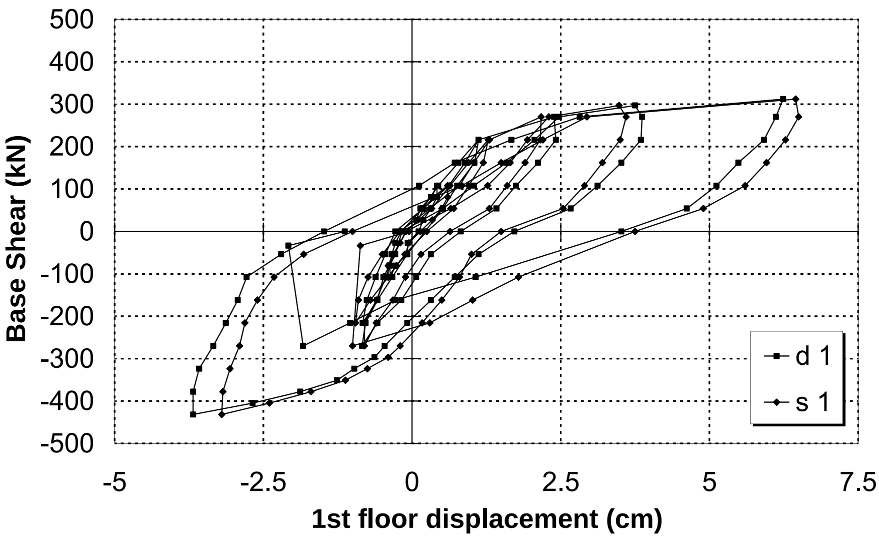

a)

Figure 4.42. BRB-Test No.1: cyclic response curve at first floor (a); cyclic response curve at second floor (b). (continued)

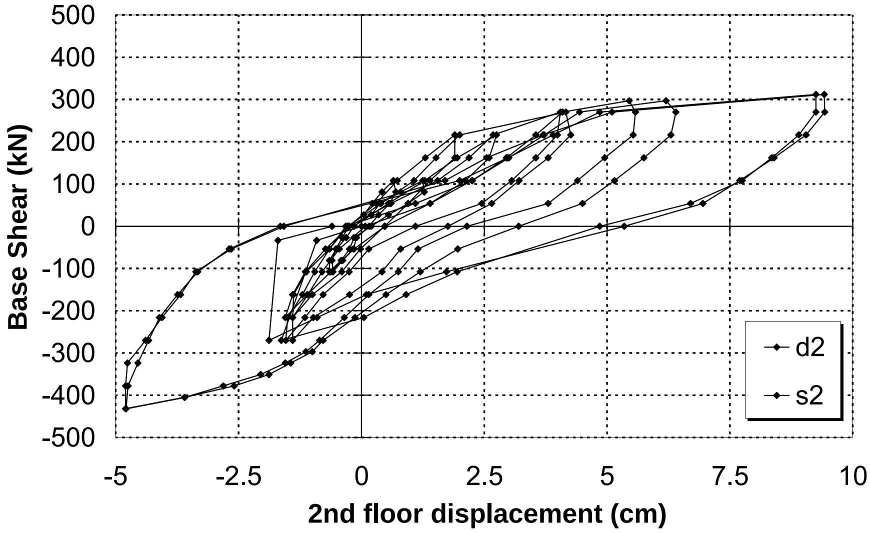

b)

Figure 4.42. BRB-Test No.1: cyclic response curve at first floor (a); cyclic response curve at second floor (b).

The measured base shear vs. first and second story lateral displacement relationships are plotted in Figures 4.42a, b. At each floor, two measures of lateral displacement were taken, approximately symmetric with respect to the loading axis. As it can be seen, the difference between the two displacements at each floor (hence the floor rotation) is small, with a maximum of about 15% of the average displacement in the inelastic range. Hence, the difference in the axial response of the two braces is similar to what recorded by other researchers (Tsai et al. 2004a).

The loading protocol in terms of interstory drift ratio applied to the structure is summarized in Figure 4.43. Figures 4.44a,b give indication of the average inter-story drift angles reached during the test. The maximum first-story drift was 1.9% of the first-story height, while the maximum top-story drift was 1.4% of the structure height. The average plastic strain developed by the inner yielding core was calculated with the following expression:

$$\frac{\delta \cos \alpha}{L_c} \bullet \frac{K_{eq}}{K_{core}} \simeq 1.07\% \qquad (55)$$

where δ is the maximum relative floor displacement, α is the slope of brace respect to the horizontal plan, L_c is the core length, K_{eq} is the BRB equivalent axial stiffness calculated according to Equation 26 and K_{core} is the core axial stiffness.

The global story ductility μ reached a maximum of about 4.75. In fact, the yielding value of the first story drift angle (which corresponded to yielding of BRBs at first story) was equal to about 0.004rad, hence μ = 0.019/0.004 = 4.75.

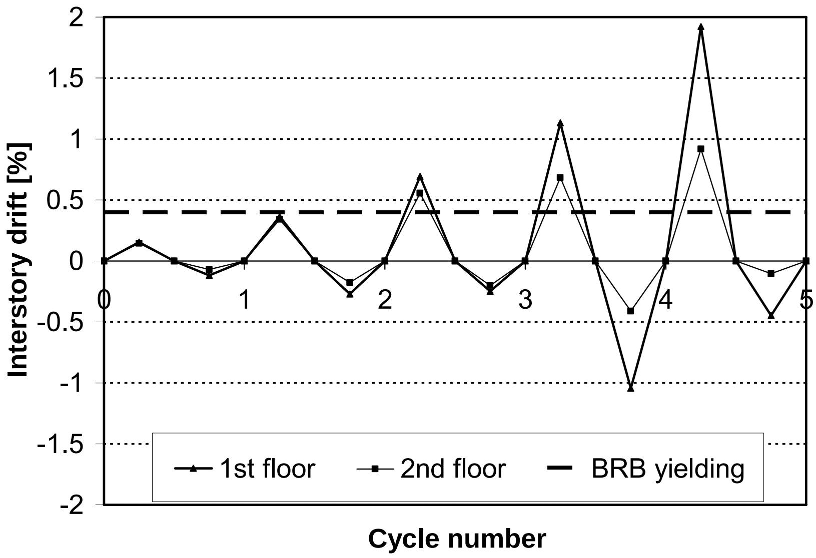

Figure 4.43. BRB-Test No.1: loading protocol in terms of interstory drift ratios.

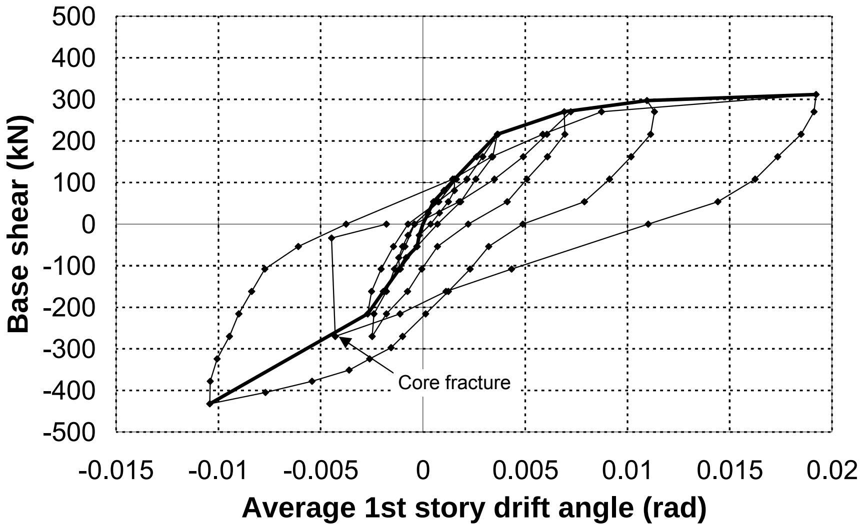

a)

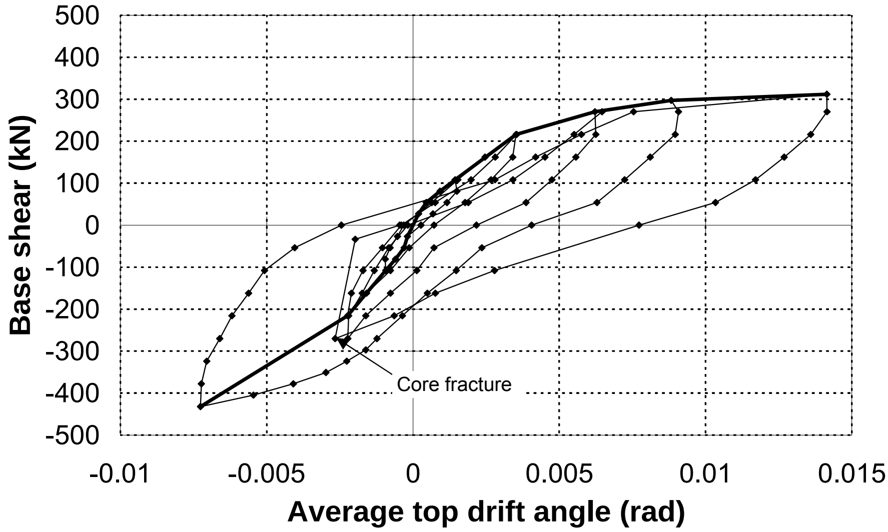

b)

Figure 4.44. BRB-Test No.1: Base shear vs. average interstory drift at first floor (a); Base shear vs. average interstory drift at second floor (b).

4.5.2 BRBs: Test No.2

Figure 4.45 illustrates the geometry of the second prototype of BRB tested (henceforth called type 2). Three main changes were made with respect to the test No.1.

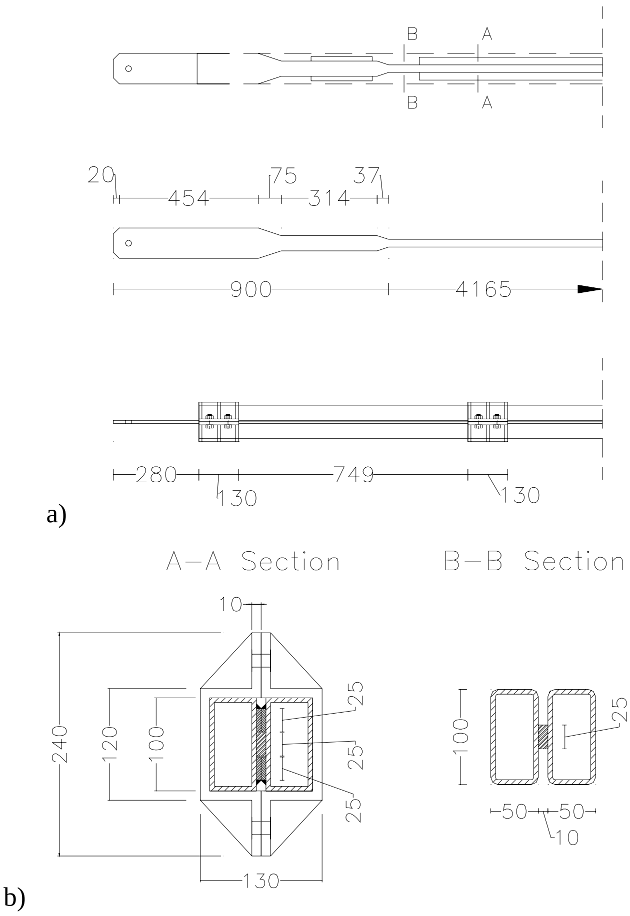

Figure 4.45. Geometry and cross section details of BRB type 2.

First, the inner core was now tapered in a more gradual manner in order to provide extra flexural stiffness for higher buckling strength and to elastically transfer the axial yield force of the core. Moreover, the tapered end-part was restrained by two parallel bars welded to tubes, so that the flexural deformation of the terminal parts was avoided. The slope of tapering portions has been assumed of 1 to 2.5 according to Chen (2002).

Second, the two restraining tubes were now joined together by means of bolted stiffened elements (Figures 4.45b and 4.46), allowing the BRB to be opened for inspection and monitoring at the end of the test. However, analogously to the previous case, in BRB type 2 the buckling-restraining action was also obtained by the same two rectangular steel tubes (100x50x5), with a similar ratio between the Euler overall buckling load (N_E) of the two tubes and the yield force (N_y) of about 2. The yielding steel core was a rectangular plate (25mmx10mm), made of the European S275 steel. In particular, as shown in Figure 4.47, the actual average yield stress of the core was measured to be 295MPa).

Figure 4.46. Bolted connection of restraining unit of BRB type 2.

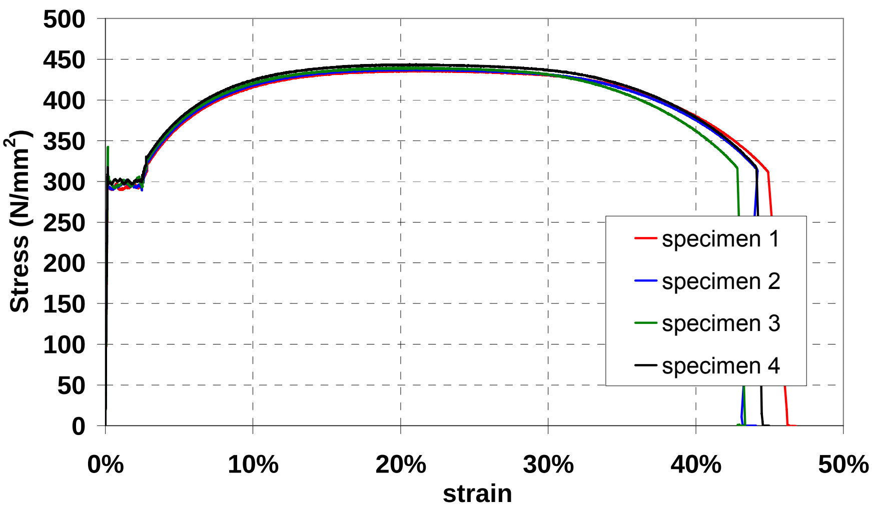

Figure 4.47. Stress-strain curves of specimens sampled from the flanges and from the core plates of the tested BRB type 1.

Third, the inner clearance between the core and the restraining unit was 1mm per each side.

In addition, the local details such as the stopper and slide guides are shown in Figures 4.48a and b, respectively.

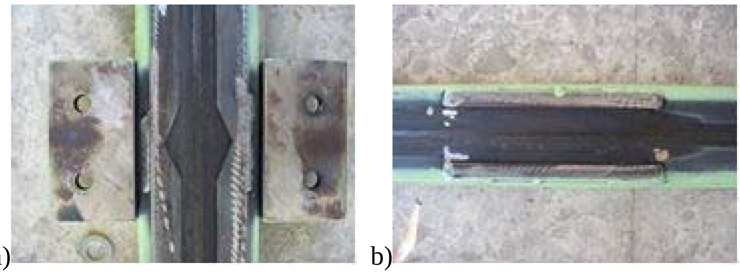

a) b)

Figure 4.48. Local details of BRB type 2.

The BRB type 2 experimental response showed a significant improvement of performance with respect to the previous type. Figure 4.49 summarizes the damage pattern evidenced during the test. The dark part of BRB core visible in Figures 4.49a,b highlights the relative displacement between the internal core and the restraining tubes, developed when the BRB was either in tension (Figure 4.49a) or in compression (Figure 4.49b).

Figure 4.49c shows the initial inelastic higher buckling mode of the inner core, which was expected as a normal response of this system because of the presence of an inner clearance of 1mm per each side of yielding core. In particular, the local buckling in the weak axis direction occurred at the end of the core plastic region. This phenomenon became very apparent at the maximum first-story drift reached during the test, corresponding to the end of core free length working stroke. In Figures 4.49d, e and f the local buckling of the internal core of one BRB placed at the first story at the maximum inter-story drift reached during the test (about 5.6% of the story height) is shown. Figures 4.49g and h illustrate the local buckling failure of one end plate connection during compression of one BRB at the first story. This unexpected phenomenon occurred at just one location and it may be attributed to some damage produced in the gusset plates during the mounting of BRBs. In fact, in that occasion the gusset plates were forced and deformed, thus introducing geometric imperfections and losing some parts of the restraining effect against out-of-plane rotation of the BRB. This implied that the buckling length of the

BRB end portion significantly increased and consequently its local buckling capacity rapidly decreased. Another confirmation of this consideration is the fact that the local buckling phenomenon occurred during the third cycle in compression. This underlines again that the undesired end-connection failure mechanism was induced by the local imperfections produced by the damages during the erecting phase of the braces. However, the maximum lateral deflection of the end portion was measured during the test and it was about 85mm. It is important to highlight that the other braces stably behaved in compression up to the maximum interstory drift of 5.6% at the first floor.

Figures 4.49i, l show the localization of plastic flexural strain at the transition section between the reduced core and the end tapering. This phenomenon was essentially due to the combined effect of sliding friction between the core and the restraining tubes and the small thickness (hence flexural stiffness) of the tube walls. Figure 4.49m shows the tube wall of one tube after the test that revealed to be punched by the buckled inner core. Finally, Figure 4.49n shows large flexural cracking occurred in columns at the first story in correspondence of the peak values of story drift.

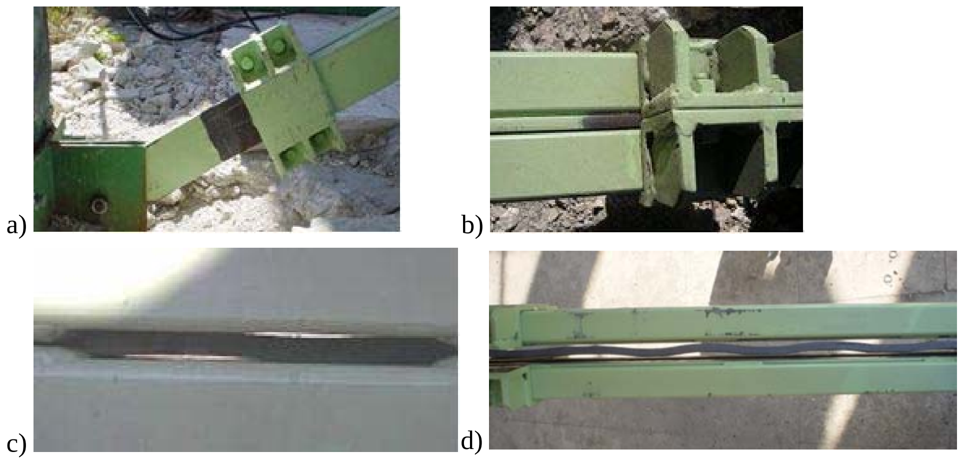

Figure 4.49. BRB Test No.2: damage pattern. (continued)

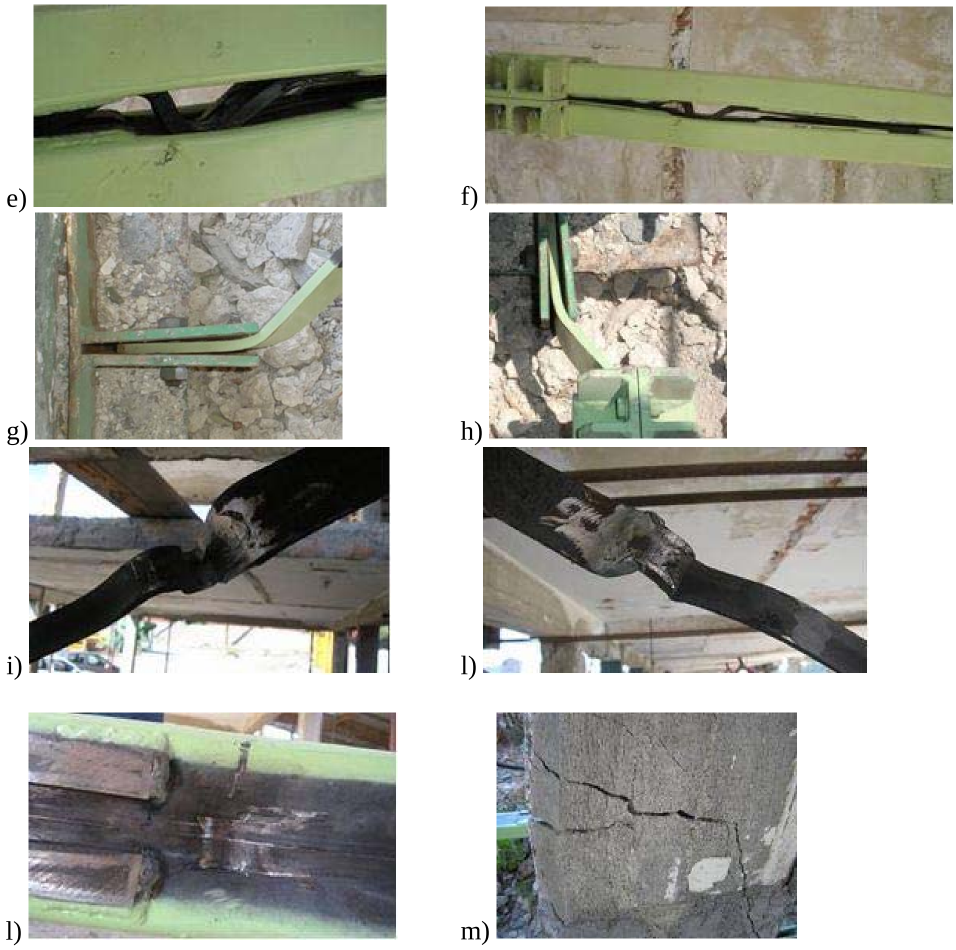

Figure 4.49. BRB Test No.2: damage pattern.

Figures 4.50a,b show the base shear vs. first-story and top-story lateral displacements. Also in this second test, difference between the tension and compression behaviour of the BRBs was within the expected range of behaviour, originating relatively small torsion of floors. Obviously, this difference became larger when local buckling of one gusset plate affected the compression response of one BRB at the first story.

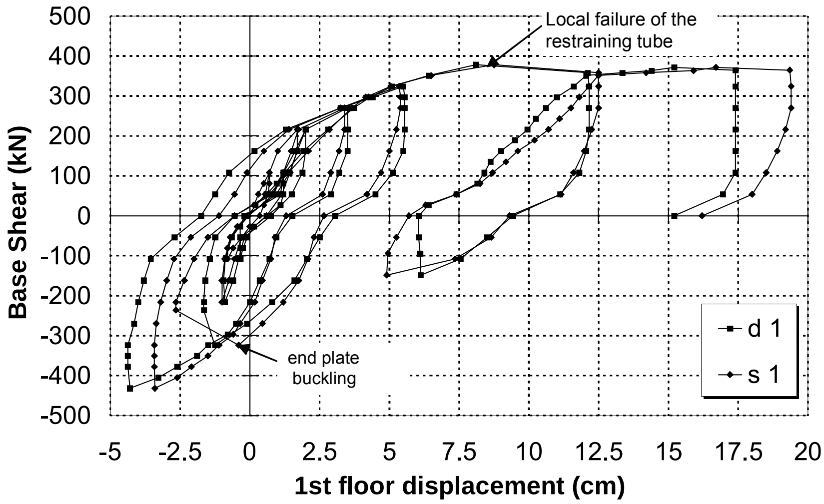

a)

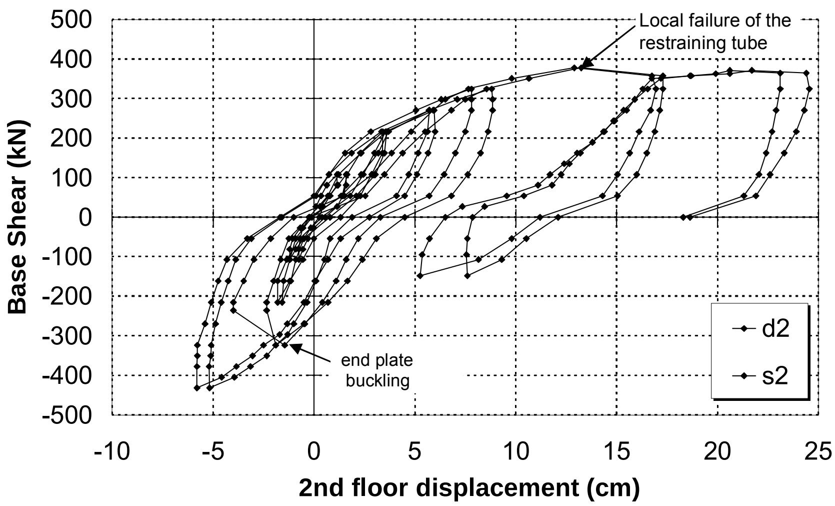

b)

Figure 4.50. BRB-Test No.2: cyclic response curve at first floor (a); Cyclic response curve at second floor (b).

Notwithstanding some localization of local buckling at one end of the internal steel core of the compressed BRB, the global story ductility (μ) was quite large, reaching a maximum of about 19. This value can be computed assuming the yielding value of the first story drift angle, calculated according

Equation 27 and equal to 0.00296rad, which corresponds approximately to a base shear equal to about 40% of its maximum value. Hence the ductility can be calculated as follows: $\mu = 0.056/0.00296 = 18.9$.

The loading protocol applied to the structure in terms of interstory drift is summarized in Figure 4.51. Figures 4.52a, b give information about the range of inter-story drift angles applied during the test.

The local strain concentration at the end of the yielding zone (figure 4.49e) occurred at a high level of axial core deformation (2.54%), corresponding to an inter-story drift of 3.84%. The maximum average core deformation was 3.80%, corresponding to an inter-story drift of 5.60%. This maximum value was reached in the loading direction producing tension in the BRB that exhibited local buckling of the not restrained end plate in the previous loading cycle in the opposite direction.

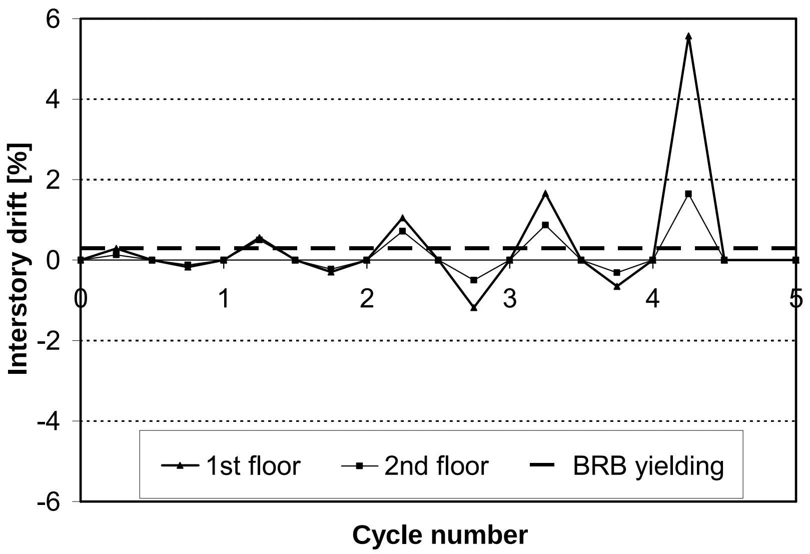

Figure 4.51. BRB-Test No.2: loading protocol in terms of interstory drift ratios.

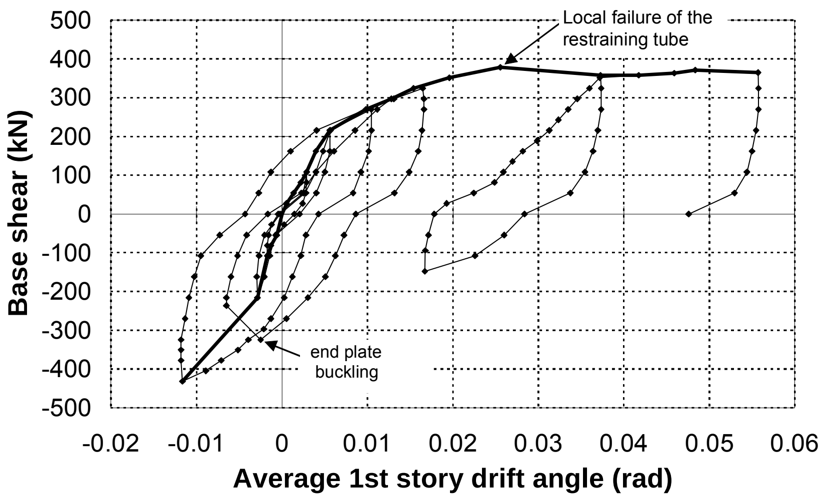

a)

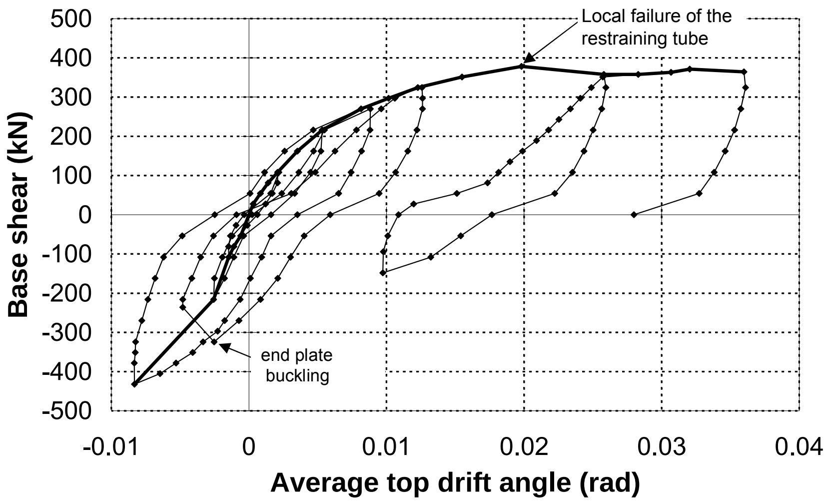

b)

Figure 4.52. BRB-Test No.2: Base shear vs. interstory drift at first floor (a); Base shear vs. interstory drift at first floor (b).

4.6 COMPARISON OF TEST RESULTS

Both the bracing system presented in the previous Sections demonstrated to be a reliable solution to improve the seismic performance of existing RC structure. In Figure 4.53 the lateral-load response of the all tests on the two tested bracing systems (EBs and BRBs) is compared in terms of envelope curve corresponding to the positive loading direction. Besides, the behaviour is also compared with the results of a previous pushover test, which was carried out on a bare RC structure very similar to the one tested with the bracing systems (Mazzolani 2006).

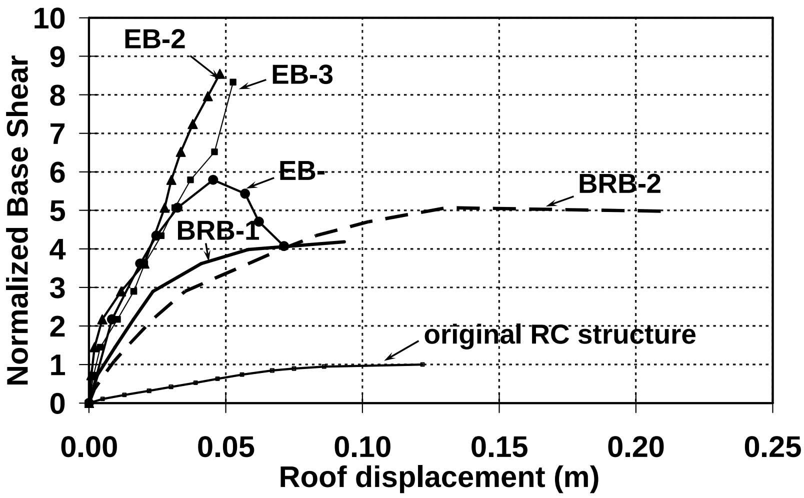

Figure 4.53. Comparison of response curves of tested bracing systems.

All tests showed a significant increase of lateral stiffness and strength respect of the one of the original unbraced RC structure. In particular, in case of EBs it was observed an increase of the lateral capacity from 5.65 to 8.34 times respect to the capacity of the original unbraced RC structure, while in case of BRBs from 4.08 to 4.95 times. The main cause of the larger values of the lateral strength achieved by EBs can be found in the shear over-strength exhibited by the tested steel links. In fact, the maximum shear developed in links during test can be approximately estimated by taking one half of the value of the measured peak base shear, the latter reduced by the aliquot of base shear force carried only by the bare RC structure. In particular, since it was impossible to properly characterize at each experimental stage the contribution of the RC members to the lateral capacity. In addition another difficulty comes from the fact that the three cyclic tests have been carried out using always the same RC structure, hence producing strength deterioration in the RC columns. In particular, at the end of the test No. 3 the RC structure appeared to be strongly damaged, with measured peak strength of about 30 kN. Therefore, a range criterion has been adopted to schematize the response of RC structure as alone. In this way it was possible to define the range of the possible link shear over-strength. In fact, an upper bound of the response of the bare RC structure has been easily obtained by a refined finite element model (further details can be found in Chapter VI) developed considering the RC structure without an initial damage state. Moreover, a lower bound of the RC response has been obtained scaling the numerical RC response up to its lateral resistance (about 30kN) finally measured after all experimental investigations

Hence, the maximum shear force developed in the link during the test may be computed using the following expression:

$$V_{link,max} = \frac{V_{max} - V_{RC}}{2} \tag{56}$$

where $V_{link,max}$ is the maximum shear force per link, $V_{,max}$ is the maximum base shear force recorded during the test, V_{RC} is the contribution of reinforced concrete columns to the base shear force. In this way, the maximum link shear force developed during test No. 2 and No. 3 may range in the following intervals: $V_{link,max}$ = $(2.77 \div 3.07)V_p$ for the test No. 2, and $V_{link,max}$ = $(4.06 \div 4.5)V_p$ for the test No. 3. In particular, instead of the one calculated according to Equation 49, it was adopted $V_p = f_y d t_w \big/ \sqrt{3}$ because it is deemed to be the most appropriate. In fact, the aim of this study is the interpretation of the shear link response for seismic modelling, where the response into the inelastic range of deformation is of interest. However, such values of the over-strength ratio appear rather larger values than the design assumptions and clearly explain failure of link end connections.

The main reason of these large link shear over-strength can be found in the particular configuration of the tested EB system. In fact, in classic eccentric bracing of steel buildings, shear links belong to the floor beams and are placed either in a symmetric configuration at the middle of the beam or adjacent to the column. In the first case, the axial force in the link is theoretically zero; in the second case, it is usually deemed to be minimal, and therefore negligible, with respect to shear and moment actions. Consequently, the effect of link axial forces has been neglected in past studies. In the case of vertical links in an inverted Y-shaped assemblage the end restraint conditions may be approximated as being fixed-fixed. It is contended that large deformations may produce an axial tension force whose effect is non-negligible. Tension axial forces are expected to increase ductility and peak inelastic shear strength. Finite element numerical simulations of the shear response of links in a fixed-fixed configuration show that axial forces develop because of the axial restraint given to the link (Della Corte et al. 2007). Such axial forces appreciably contribute to the link post-yield stiffness at large shear deformation angles, thus leading to increased peak strength.

Instead of EBs, BRBs are characterized by lower over-strength capacity (at the most equal to the material axial over-strength), but they can provide for the structure a larger displacement capacity than EBs. In fact, referring to the studied cases, short shear links should develop shear deformation angles larger than 0.60 radians in order to provide the same displacement capacity of the tested BRB type-2. This large shear deformation is not reasonable, since no shear link is able to provide it. This implies that BRBs let to control stiffness, strength and ductility better than EBs. Moreover, Respect to EBs, BRBs revealed to provide a more complete structural performance, since they can improve not only the lateral stiffness and strength capacity but also the displacement capacity of the structure. In fact, test results on two different types of "only steel" BRBs showed good ductility of this system.

The efficiency of the first type of BRB (test No. 1) was impaired by the flexural failure of the end closing plates, which were unable to restrain the end portion of the brace core. This produced a strong flexural plastic engagement of the core at its ending portion. Hence, ductility of the system was quite limited, even if the strength and stiffness of the upgraded RC structure met the expected improvement.

The second type of BRB (test No. 2) showed instead large ductility, being able to adequately restrain the core from buckling, though some additional improvements are required in the design. In fact, the combined effect of sliding friction between the core and the restraining tubes and the small thickness (hence flexural rigidity) of the tube walls produced some localization of damage in the yielding core, hence some limitation in the expected system ductility. In addition, local buckling of one end plate was observed during this second test, even if the end plate satisfied a capacity design criterion. In fact, the local buckling Euler load (conservatively estimated by the assumption of beam-type behaviour and assuming a buckling length equal to the distance between the bolt centre-line and the starting section of the restraining tubes) can be computed to be 3.8 times larger than the maximum expected compression load. Hence, buckling of the end plate (occurred at just one location) may be attributed to: (i) strong local geometric imperfections, which grew up during cyclic loading; (ii) a flexible end-restraint, which produced an increase of the buckling length and also some coupling of lateral and torsion effects. Anyway, the maximum story-drift angle reached during test No. 2 (5.6% of the story height) is appreciably larger than the maximum values commonly applied in the past testing of BRBs. Therefore, results can be considered satisfactory and encouraging for the future.

Chapter V
Experimental tests on a masonry infilled RC structure

5.1 INTRODUCTION

The experimental research presented herein is being developed within the PROHITECH project and RELUIS project – Task 5 "Development of innovative approaches to design steel and composite steel-concrete structures" (Chapter I). In this contest, the study has been framed around two main directions consisting in the study and development of an innovative BRB typology and the planning of a wide experimental activity, respectively.

The BRB device under studying consists in an upgrading of an only-steel version that was previously studied and implemented within the ILVA-IDEM project (Mazzolani 2006), as shown in Chapter 4. In detail, this last version has been designed to improve the seismic performance of an existing RC building. In particular, it was designed to be detachable and to be hidden between two facings of masonry infill walls (D'Aniello et al 2007). The RC structure equipped with BRB was built at the beginning of '80s within the steel mill ILVA in Bagnoli (Naples, Italy) and, as the one shown in Chapter IV, it was destined to demolition by competent Authority. The building under study can be considered as representative of a large number of existing RC buildings in the South of Italy, built during the 60s and 70s when Naples was considered a non seismic area. Figures 5.1a,b,c shows the building at the beginning of the investigation. This RC structure has been initially tested in its original conditions (Della Corte et al. 2006) in order to take into account the presence of the stair, the partition walls and all the other constructive elements (internal walls, coverings, windows and door frames). It was pushed by lateral loading up to severe damage of both structural frame members and infill walls. Lateral loads have been applied according to an inverted triangular distribution. The test showed the formation of a weak story at the first floor.

a)
b)
c)

Figure 5.1. The building under investigation.

Then, after the first experimental test the structure was re-centred, repaired and upgraded by means of C-FRP in the form of Near Mounted Surface Bars

(NMS-B). Finally, after these tests, the structure has been re-centred and repaired and the above mentioned new BRB system (henceforth called type 3) has been designed. The BRBs will be placed at the perimeter. In particular, in one bay the external facing wall will be reconstructed, in such a way to directly evaluate the interaction between the brace and the wall.

After a short introduction of the previous tests carried out on the building (as it was and repaired with FRPs), the experimental results of the lateral-load response of a real RC structure seismically upgraded by means of the above mentioned innovative “only-steel” Buckling-Restrained Brace are widely presented and discussed. In particular, the braced RC structure showed an important improvement of lateral strength capacity.

After the physical testing activity, a numerical study has been conducted, investigating the ability of current structural modelling options to correctly capture the observed lateral load response of both the original and strengthened structures by means of BRBs. The model calibrating process considered the experimental evidence and the actual material properties. Good agreement between numerical and experimental results was achieved.

5.2 DESCRIPTION OF THE BUILDING

The geometrical survey and the constructional details in the original design drawings clearly show that the structure has been designed to resist vertical loads only. Figures 5.2a,b show two drawings representing the architectural plans, while in Figures 5.3a,b the structural plans show the essential characteristics of the RC frame structure at first and second floor, respectively. At first floor, all beams have rectangular 20cmx60cm cross–section except the transverse beam in X direction that is 25cmx60cm. At second floor, all beams are rectangular 15cmx60cm cross–section, except for the transverse beam in X direction which is 25cmx60cm. All columns have square 30cmx30cm cross–section, with twelve longitudinal ribbed bars (12 mm in diameter) as reinforcement uniformly distributed along the perimeter of the cross–section.

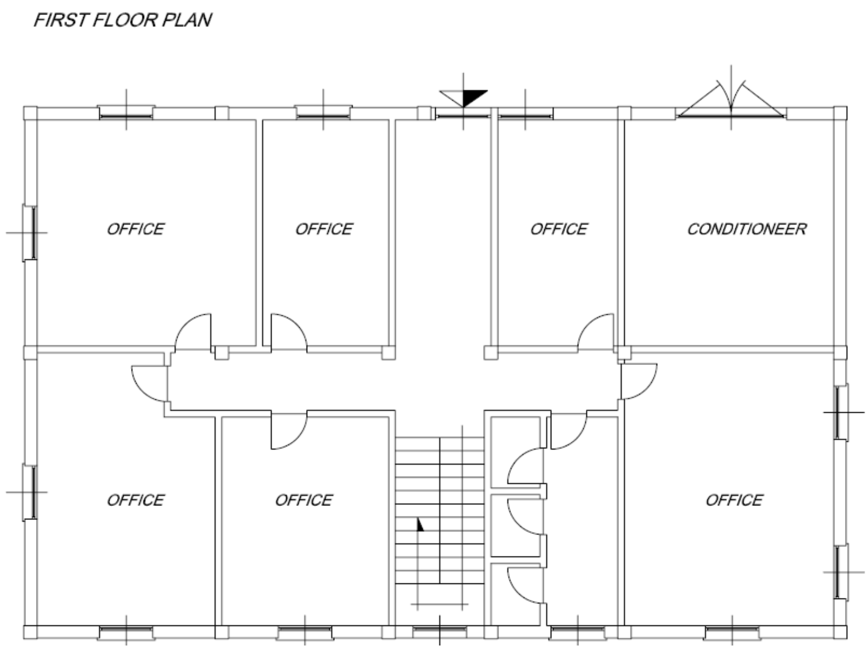

a)

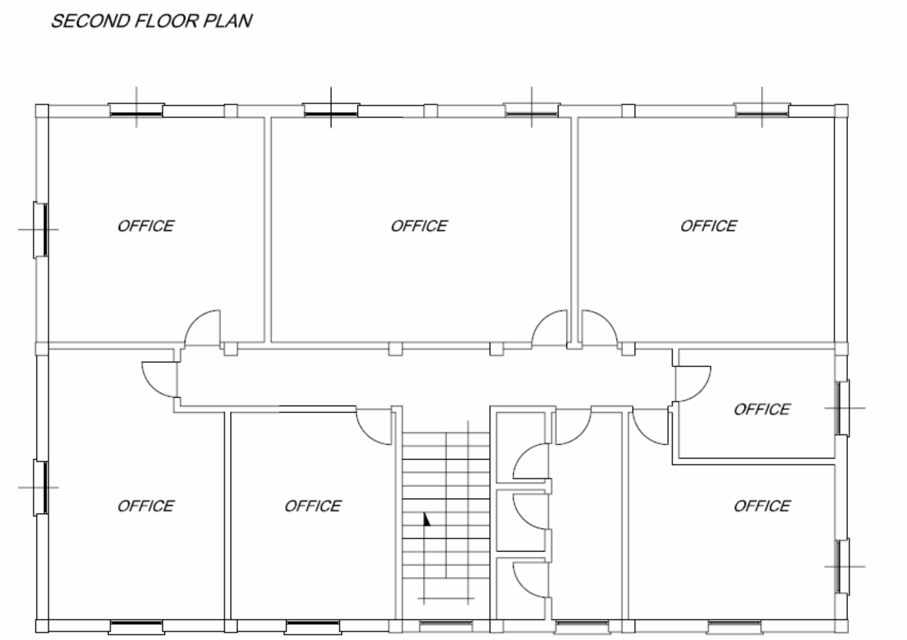

b)

Figure 5.2. The building under investigation- architectural plans: first floor plan (a); second floor plan (b).

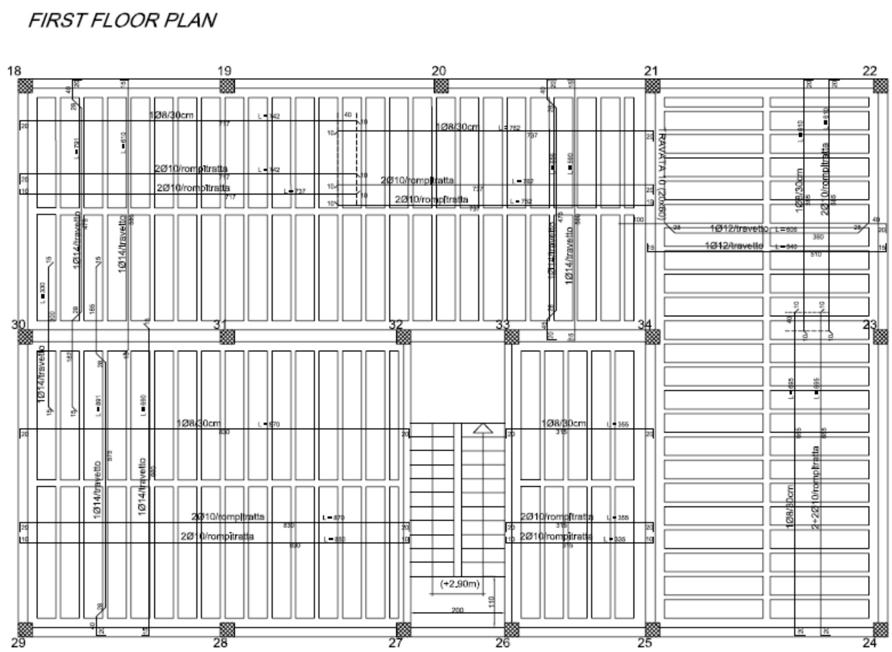

a)

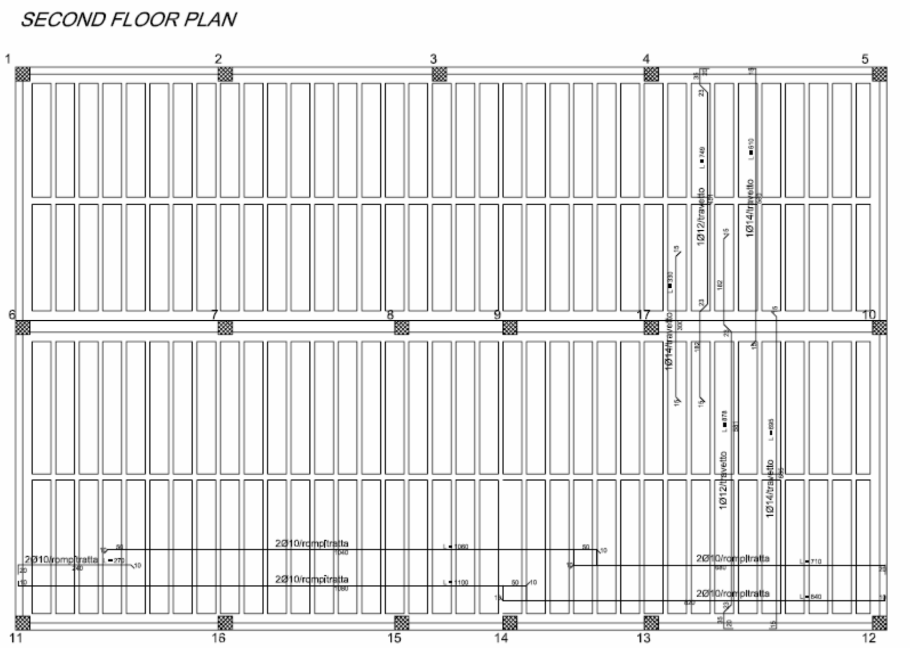

b)

Figure 5.3. The building under investigation- structural plans: first floor plan a); second floor plan (b).

The extrados floor heights, measured from foundations, are respectively 4.60 m at first floor and 8.95 m at second floor. Structural details are in accordance with the past Italian non–seismic code. For example, transverse stirrups in beams and columns are discontinuous, largely spaced and not well bended inside the cross section. Also insufficient anchorage and incorrect overlaps of the longitudinal steel rebars can be observed, together with the absence of suitable confinement of joints, eccentricities in beam to column joints, scarce care of the resumptions of concrete casting of columns. The partition masonry infill walls are made of 10 cm thick semi-hollow light concrete blocks (Figure 5.4a).The perimeter infill masonry walls are made of external facing walls made of 10 cm semi-hollow tile blocks and internal walls 10 cm thick semi-hollow light concrete blocks (Figure 5.4b). All masonry walls are composed by site-made mixed cement lime and sand mortar.

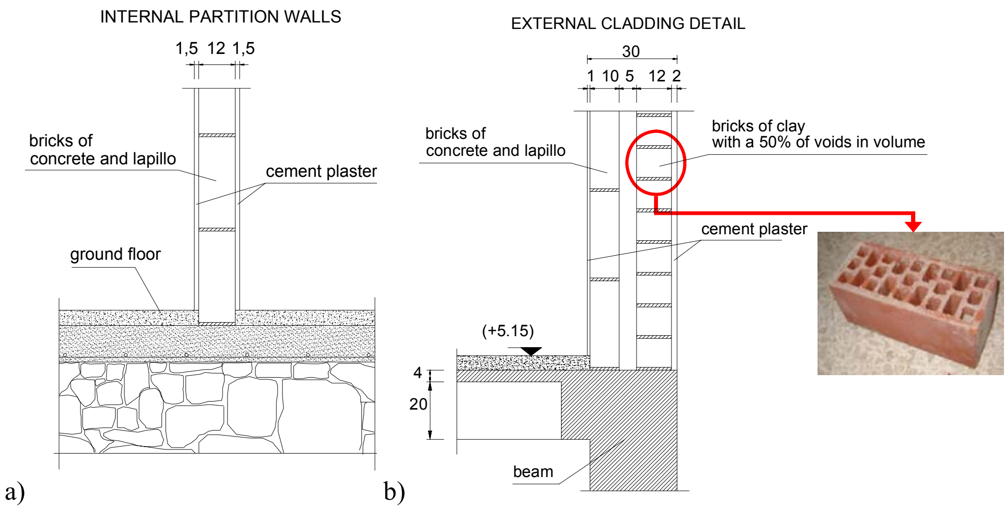

Figure 5.4. The building under investigation: partition infill wall details (a); perimeter infill masonry wall details (b).

The structural response was strongly affected by the presence of the staircase structure at the first level. As shown in Figures 5.5a and b, this staircase is made of two inclined RC slabs connecting the ground floor to the first floor, with an intermediate horizontal slab. Another main difference between first and second floor is the presence of an internal beam in the transverse direction only at the first floor.

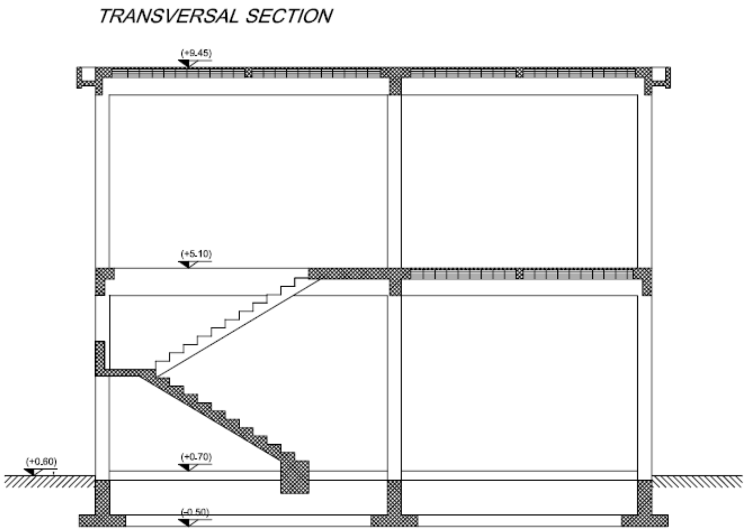

a)

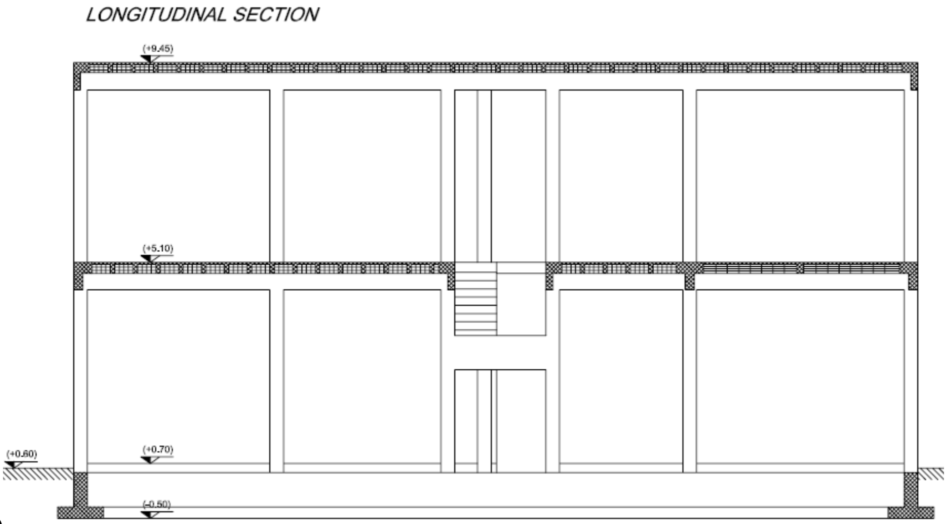

b)

Figure 5.5. The building under investigation- structural sections: transverse section (a); longitudinal section (b).

5.3 THE PUSHOVER TEST OF THE UNBRACED RC STRUCTURE

5.3.1 Test setup

The building has been subjected to a horizontal inverted triangular force distribution which simulates an action of seismic nature.

The only vertical loads have been only those produced by the building weight, including all the weights of elements of finishing (internal walls, inside and outside frames and some furnishings).

The lateral load has been applier by means of six hydraulic jacks (Figure 5.6b,c,d,e) each one having a maximum stroke of 60 cm and a higher flow rate equal o 496 kN in compression and 264 kN in tension (corresponding to a total force maximum of 2976 kN and 1584 kN respectively in push and in pull action).

They have been connected to a hydraulic pump by means of a circuit in order to guarantee always the same pressure in all the jacks. The jacks have been put at a height of 7.31 m and distant each other 3.64 m. The lateral load has been transferred to the two slabs of the building through a steel structure.

Figure 5.6. Reactive structure and hydraulic jacks.

Figure 5.6a illustrates a view of both the reacting frame and the loading jacks used for applying the lateral force. As it can be observed, this reacting structure is a trussed structure, whose foundations have been made of two steel tanks filled with the ground dug around it. Thanks to its weight, this arrangement provide a large safety factor against the global turnover of the reacting frame under the maximum horizontal force potentially transmitted by hydraulic jacks.

The loading protocol has foreseen three load cycles. In particular, the first cycle has been achieved first pushing the structure till the total force of +1872 kN, then inverting the loading direction till to reach the value of -1588 kN (maximum capability of the pulling jacks) at last the structure has been unloaded.

With the second cycle, like the first one, a maximum pushing force as +2106 kN has been applied and a maximum pulling load as -1572 kN has been applied.

The third cycle, having the aim of bringing the structure at a very high level of damage, has foreseen the thrust of the building till the complete overcoming of the maximum carrying capability.

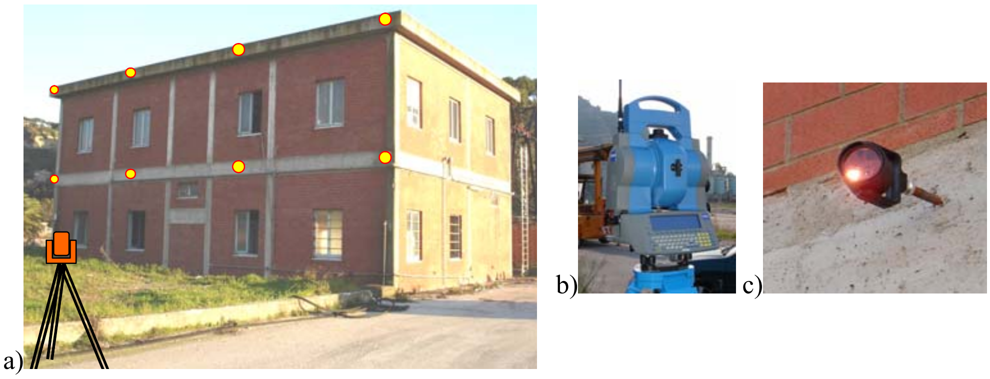

Figure 5.7. Position of station and reflecting targets.

The lateral displacements of the building have been monitored by a Zeiss-Trimble S10 total station (Theodolite laser with a precision of 10 mm, shown in Figure 5.7) by means of the application of reflecting targets. In particular, 8 important points have been monitored, 4 at first floor and 4 at second floor (Figure 5.7a). The measures have been done at the end of each loading step.

5.3.2 *Experimental Results*

The structure was forced to an increasing lateral displacement, up to the development of a clear plastic collapse mechanism. Figure 5.8 shows the structural performance in terms of base shear – lateral displacement diagram.

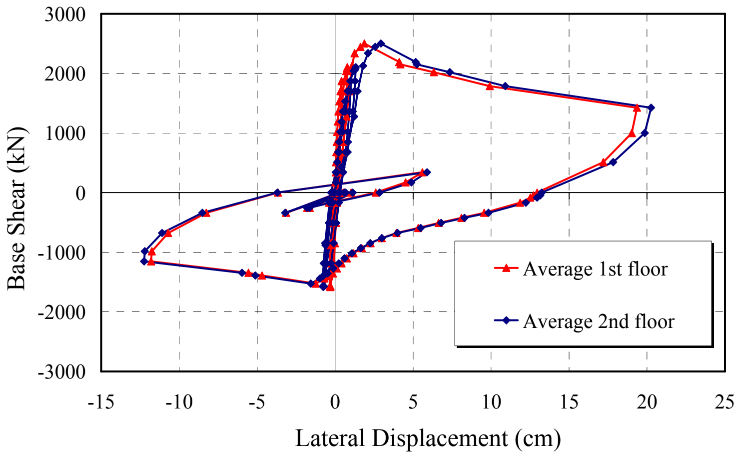

Figure 5.8. Performance of Original RC structure, Base-shear vs. average floor displacements.

The structure showed a clear weak story mechanism characterized by the shear diagonal fracture of the perimetric masonry infill walls of the first floor. Moreover, on the west side, beside the increase of the width of cracks at 45° in the wall panel between the two windows, in correspondence of the top right side of the next wall, the break for local crushing of the corners of the separation walls was early visible, due to the concentration of the horizontal forces transmitted by the reinforced concrete frame. The damage of the separation walls in this place is accompanied by the evident crack of the head of the column which herald the cut break of such on element.

Figures 5.9 show the damage pattern of the original RC structure at the end of the test. In particular, it is clearly shown the full collapse of external walls (Figure 5.9a,b), the damage of the staircase with the significant plastic engagement at both ends of the staircase flights (Figure 5.9c,d,e,f) and the plastic hinges developed at the ends of the columns (Figure 5.9e,f).

a) b) c) d) e) f) e) f)

Figure 5.9. Performance of Original RC structure, structural damage at the end of the test.

After the first test, the building was partially repaired and tested again. In particular, only the perimeter damaged columns and the external masonry infills was rebuilt and strengthened by mans of FRP according to the Near Mounted Surface Bars techniques. The other elements, as internal columns, internal partition walls and staircase structure, were not repaired. Hence, their contributions in the structural response are negligible.

The masonry panels were rebuilt using materials having geometrical and mechanical properties as close as possible to those of the original elements. After the erection of the external masonry infill panels, the facing walls were strengthened by means of the fiber reinforced polymers (FRP) structural repointing technique. This technique consists in placing composite FRP bars in the masonry bed joints, using a common mortar for bonding. The repairing and strengthening of the damaged end portions of the external columns was carried out by removing degraded concrete and reconstructing concrete covering with the “Emaco® Formula Tixo” pre-mixed cement mortar.

Figure 5.10 shows the structural performance of the building repaired and strengthened with FRPs, while Figures 5.11 highlight its damage pattern after the pushover test. It may be noted that repaired infill walls exhibited different failure modes, characterized by a reduced influence of diagonal tension cracking. In addition it may be noted that the damage level in the repaired structure was smaller than that exhibited by the original building at the same level of lateral displacement.

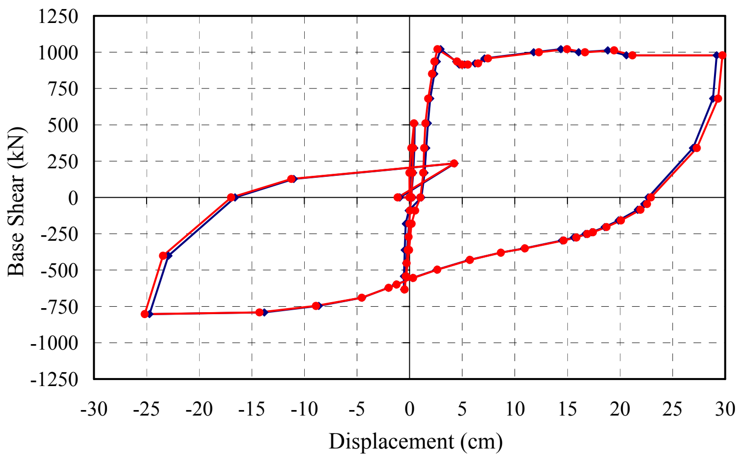

Figure 5.10. Performance of RC structure repaired and strengthened with FRPs, Base-shear vs. average floor displacements.

Figure 5.11. Performance of RC structure repaired and strengthened with FRPs, structural damage at the end of the test. (continued)

i) 

l) 

Figure 5.11. Performance of RC structure repaired and strengthened with FRPs, structural damage at the end of the test.

It is interesting to note the formation of plastic hinge at middle height of the column (Figure 5.11g) due to the presence of the partially fallen down masonry infill wall. Moreover, after the second test the damage at both ends of inner columns clearly appeared (Figures 5.11h,i). As shown in Figures 5.12 and 5.13, the comparison of the structural response of the structure, as it was in its original conditions and strengthened with FRPs, shows a significant reduction of lateral strength of about 60%. This result can be attributed to the limited repairing carried out after the first test, which did not involve the staircase structure, the internal column and the internal partition walls.

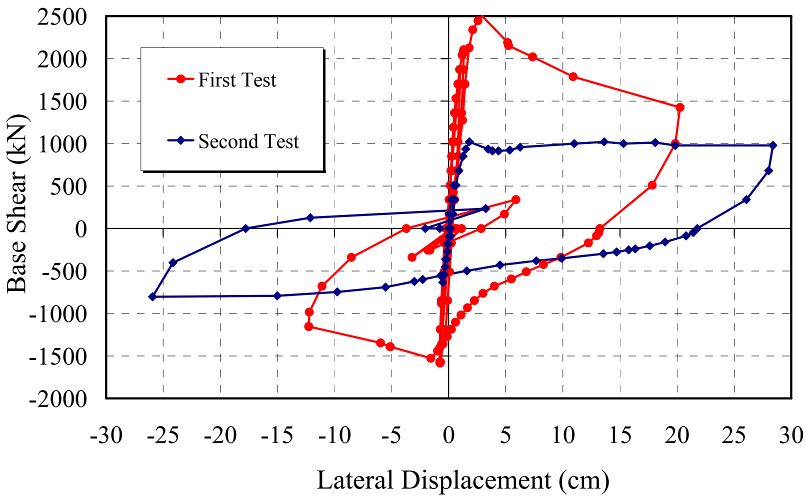

Figure 5.12. Comparison of structural performance of RC building as it was and strengthened with FRPs: Base-shear vs. average floor displacements.

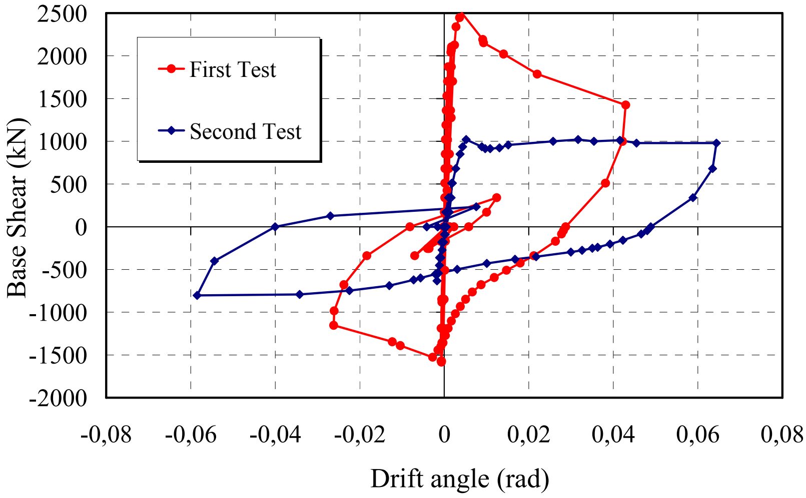

Figure 5.13. Comparison of structural performance of RC building as it was and strengthened with FRPs: Base-shear vs. average interstory drifts.

5.4 THE PUSHOVER TEST OF THE RC STRUCTURE EQUIPPED WITH INNOVATIVE "ONLY-STEEL" BRBS

5.4.1 Description of the tested "only-steel" BRB

As deeply discussed in Chapter II and in Chapter IV, "Only-steel" BRBs have some advantages over "unbonded" braces. In fact, this type of BRBs can be designed to be detachable. Hence, they could be inspected after each seismic event and, if necessary, the yielded steel core could be replaced by a new one. Moreover, a detachable BRB allows maintenance during the life-time. To do this, the restraining tubes are connected by bolted steel connections (Tsai et al. 2004a,b). Moreover, an "only-steel" BRB is lighter than an 'unbonded' one; this implies a technical and economical advantage during the assembling. These considerations led to study a special "only-steel" detachable BRB, to be used for improving the seismic response of existing buildings. To reach this objective, full-scale tests on real RC structures equipped with BRBs have been carried out.

The concept of the novel device descends from the experience matured within the ILVA-IDEM project, deeply explained in Chapter IV. The BRB type under examination was derived from the concept of type 2, with some modifications. Hence, in order to clarify this process, the main properties of type 2 are summarized here.

In type 2, the buckling-restraining action was obtained by two rectangular steel tubes (100x50x5) (Figure 4.41, Chapter IV), with a ratio between the Euler overall buckling load (N_E) of the two tubes and the yield force (N_y) of the internal steel core N_E/N_y = 2.1. The yielding steel core was a rectangular plate (25mmx10mm), made of the European S275 steel (the actual average yield stress of the core was measured to be 295MPa). As it can be observed in Figure 4.41a, the inner core was gradually tapered in order to elastically transfer the axial yield force of the core. Moreover, the tapered end-part was restrained by two parallel bars welded to tubes, so that the flexural deformation of the terminal parts was avoided. The inner clearance between the core and the restraining unit was 1mm per each side. The two restraining tubes were joined together by means of bolted stiffened elements (Figure 4.41b), allowing the BRB to be opened for inspection and monitoring at the end of the test. Moreover, as shown in Chapter IV, this type of brace showed a satisfactory performance.

The new tested BRB prototypes have also been designed to be detachable, but they differ in several aspects from the previous one. First, the restraining unit differs from the previous typology. In fact, it is constituted by two omega-shaped built-up sections bolted in some spaced out zones. As it is shown in Figures 5.14 and 5.15, the two omega-shaped sleeve couplings are stiffened by two longitudinal bars, providing the required restraining action to the core. Thanks to this arrangement, the transverse dimension of the sleeve was strongly reduced (from 130mm to 94mm, comparing Figure 4.41 to Figure 5.15), thus allowing the brace to be hidden in the inner hole of facing walls. In this case, the sleeve has ultimately been designed with a restraining force similar to the previous cases; in particular, the minimum ratio N_E/N_y=2.06. A second aspect of distinction is the ratio between the core length (L_c) and the total BRB length (L). In the new BRB, the ratio is L_c/L = 0.4, while it was 0.7 in the case of previous tests (BRB type 2).

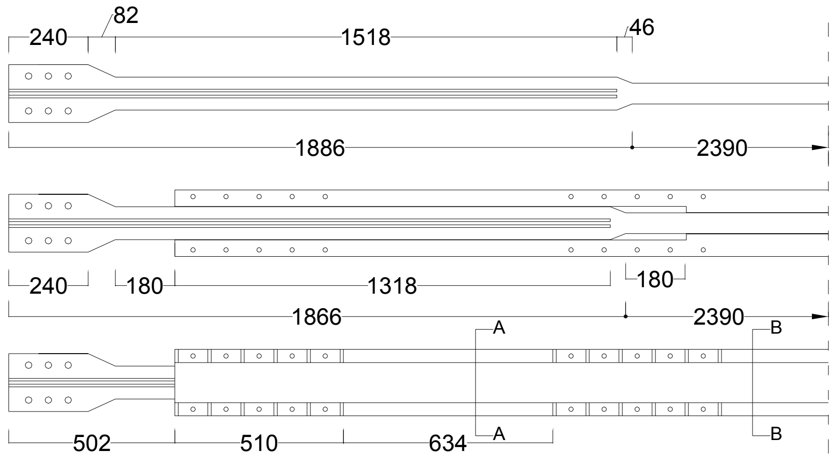

Figure 5.14. Geometrical properties of the tested BRB type 3.

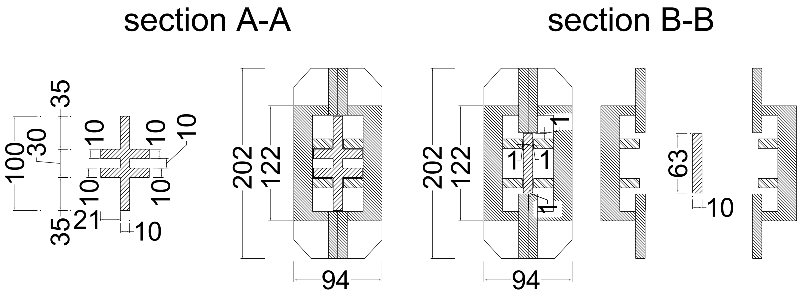

Figure 5.15. Cross section details of the tested BRB type 3.

Finally, the last aspect differencing the new prototype from the previous one is the detail of the unrestrained non-yielding end-plate. In this case, in order to avoid the occurrence of local-buckling phenomena, it was stiffened (Figure 5.15) with two welded longitudinal bars per each core side. This arrangement theoretically provides a safety factor against out of plane buckling larger than the one of the previous typology. Moreover, in order to investigate the device performance in case of severe earthquake that could involve the brace to get out the displacement design range it was decided to enlarge three times the length of the free end portion. This arrangement was chosen to understand in which terms the system is able to provide an increase of displacement demand. In Figure 5.16 some details of the prototype during assembling are shown. In particular, Figure 5.16a shows one of the two omega-shaped restraining units that constitute the sleeve, while Figures 5.16b,c show the inner plate inside the sleeve. Figure 5.16d shows a detail at the middle of the sleeve where the stopper (Tsai et al 2004) is inserted to avoid slipping of the core under its own weight. The stopper is also important in order to allow a symmetric yielding of the two ends of the BRB.

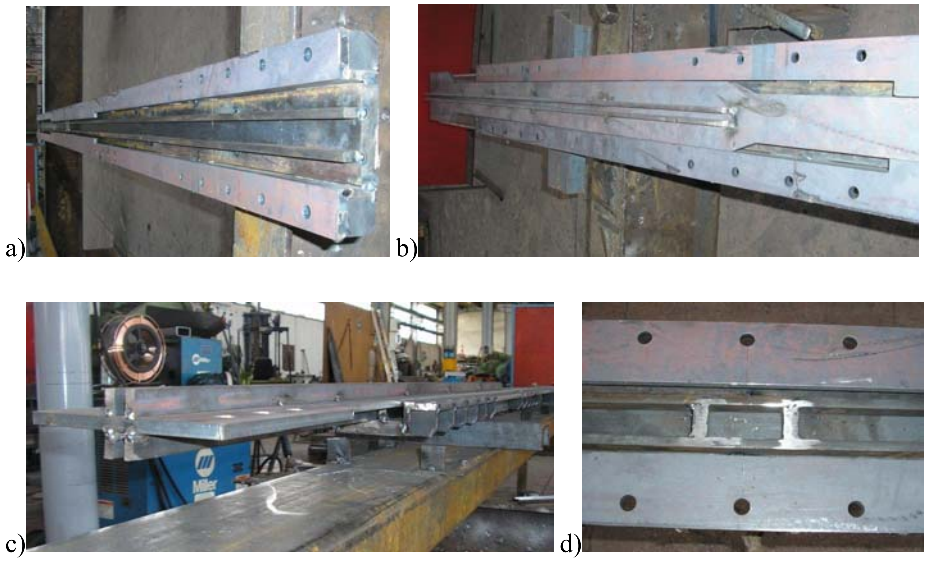

Figure 5.16. Assembling and local details of the tested BRB type 3.

5.4.2 *The repaired structure equipped with BRB type 3: design and erection phases of retrofitting BRB system*

As shown in the previous Sections, the tested RC structure equipped with the BRB type 3 has already been tested two times, in the original condition and after some repairing carried out by means of FRPs.

After the two tests, the structure has been repaired and the new BRB system has been applied. In particular, Figure 5.17 shows the position of the braces (indicated with the dotted lines), while Figure 5.18 shows the brace configuration, with the BRBs mounted only at the first floor. In one bay the external facing wall has been reconstructed, in such a way to directly evaluate the interaction between the brace and the wall.

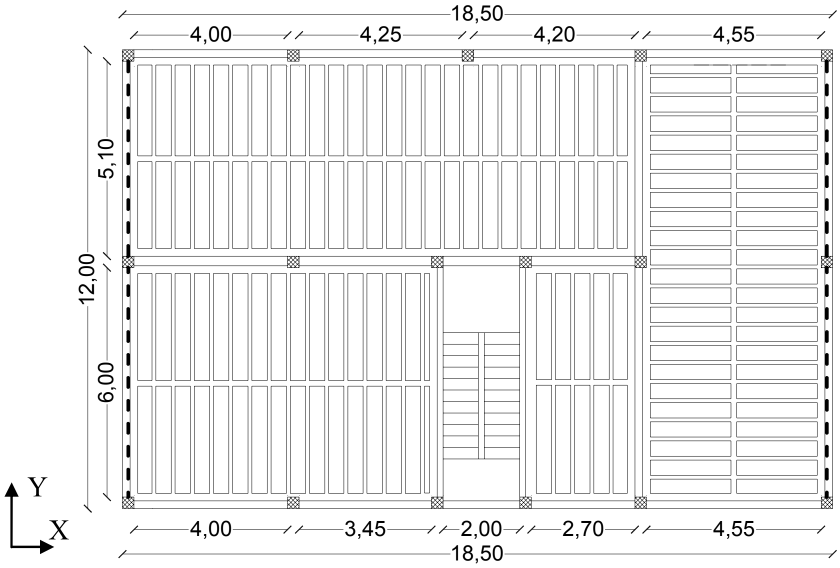

Figure 5.17. Plan location of the tested BRB type 3.

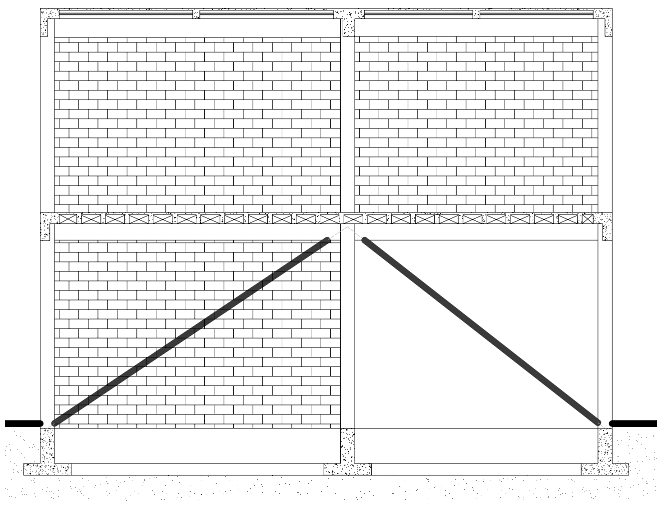

Figure 5.18. Configuration of the tested BRB type 3.

The BRB system shown in the previous Section has been design to seismic retrofit the above mentioned RC building. Therefore, according to Seismic Performance Design philosophy, multi-level design criteria have been applied to achieve the following design objectives (SEAOC Vision 2000, 1995):

Operational, in which moderate damage to non-structural elements and contents, and light damage to structural elements has occurred; the damage does not compromise the safety of the building for occupancy;

Life safe (damage state), in which moderate damage to structural and non-structural elements has occurred; the structure's lateral stiffness and ability to resist additional lateral loads has been reduced, but some margins against collapse remains.

In particular, the former should be achieved for the earthquake of characterized by a return period of 475, the latter by a return period of 970years. In particular, the achievement of the first non linear event in the RC structure has been assumed as the target performance for the life safe damage state.

Hence, to size the BRB system a displacement design procedure has been adopted based on the use of capacity spectra (Chopra 2004). As it is generally known, the displacement design procedure is based on the definition of the substitute structure that models a multi-degree of freedom system as a single-degree equivalent system. In such a way the inelastic structural system can be designed and analysed using elastic response spectra. In this case, the first step is the definition of capacity response of the bare RC building. So, starting from the experimental capacity response curve of the building repaired with FRPs, it was define the lateral response of the bare RC frame without the presence of facing infill walls. In fact, the initial stiffness has been assumed equal to the one of the experimental negative unloading branch of last cycle, while the remaining curve is defined as shown in Figure 5.19. This assumption is due to the fact that for that loading step, the perimetric infill walls completely failed, so the experimental response was only representative of remaining RC structure.

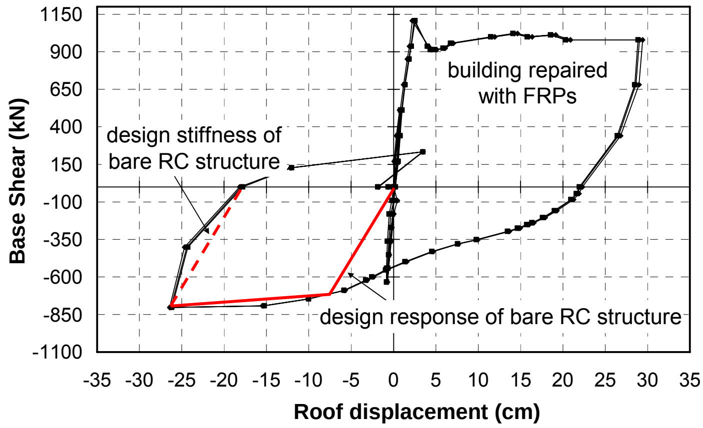

Figure 5.19. Definition of lateral capacity response of bare RC building.

Moreover, in addition to the capacity curve, it is necessary to define the displacement shape distribution of the multi-degree of freedom structure. In this case, because of the significant stiffness of the infill walls of the second story, it was assumed that the displacement of the first and the second floor were equal. This assumption is recognized by the fact that in both experimental tests on unbraced building, the differences between the monitored displacement of both first and second story were very small in the final phases, thus showing a clear weak-story mechanism at the first floor. These considerations led to consider the building to be retrofitted as a single-degree of freedom structure. Figure 5.20 show the shape of first ortho-normalized mode obtained under this hypothesis.

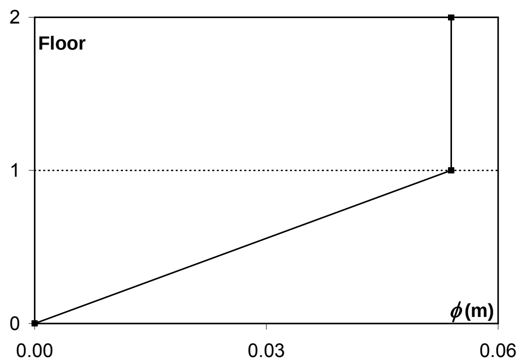

Figure 5.20. Fundamental ortho-normalized mode of the bare RC structure to be retrofitted.

Finally, the substitute structure is defined by a target displacement. The target displacement corresponds to the performance level to be assured. According to the equal-displacement rule (in case of system characterized by period belonging to the interval of constant spectral velocity, the displacement of the inelastic system is equal to the one of the elastic system), the displacement demand of the unbraced RC building was significantly large (more than 5.8%, as it can be deduced by Figure 5.21), corresponding to a severe damage state. Hence, the BRB has been designed to reduce the displacement demand. In fact, the target displacement of the retrofitted structure has been assumed in order to provide a maximum interstory drift of 1.5% for the earthquake of return period of 970 years, thus theoretically corresponding to the first non-linear event that occurs in the idealized RC structure. Hence, by means of Acceleration-Displacement Response Spectra it is possible to obtain the design capacity curve of the retrofitted structure as the sum of the only-RC curve and the only-braces curve. The latter has been ideally schematized as a bilinear elastic-perfectly plastic curve, characterized by a displacement ductility μ_{global}=8. Consequently, because of the truss scheme, the global ductility is equal to the brace ductility. Hence, the BRB has been designed to ideally provide a μ_{BRB}=8 for the earthquake of return period of 970 years. Finally, because of the larger stiffness of the retrofitted structure (thus resulting a significant reduction of the theoretical fundamental period of vibration), the yielding point of the design response has been obtained applying the equal-area rule (in case of system characterized by period belonging to the interval of constant spectral acceleration, the area subtended by the response curve of the inelastic system is equal to the one of the elastic system). In case of seismic event of return period equal to 475 years, the overall ductility demand is equal to 5.5 and the RC building is theoretically in elastic field. In particular, Figures 5.21a,b show the definition of the design response curve of the retrofitted structure for the design seismic events at 970 years and 475 years, respectively.

The difference between the theoretical design curves with the experimental one of the bare RC structure gave the design base shear to size the bracing system. The final result was that the rectangular core section areas of the BRBs to be tested were 63mmx10mm (for the longer braces) and 67mmx10mm (for the shorter braces).

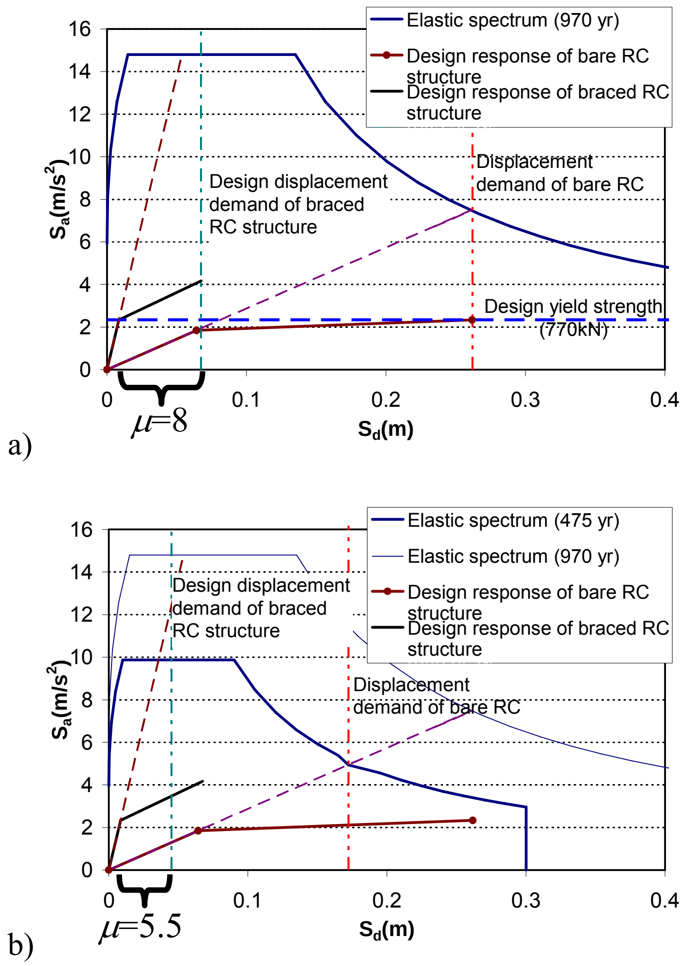

Figure 5.21. Definition of the design response curve of retrofitted structure by means of capacity spectra: seismic event of return period equal to 970 years (a) and 475 years (b).

The repairing and strengthening of the damaged end portions of the external columns was carried out by removing degraded concrete and reconstructing concrete covering with the “Emaco® Formula Tixo” pre-mixed cement mortar. In particular, Figures 5.22 show some details of the end parts of RC columns: before reconstruction with the straightened longitudinal steel rebars and the bended transverse steel stirrups (Figure 5.22a,b); the final reconstructed columns.

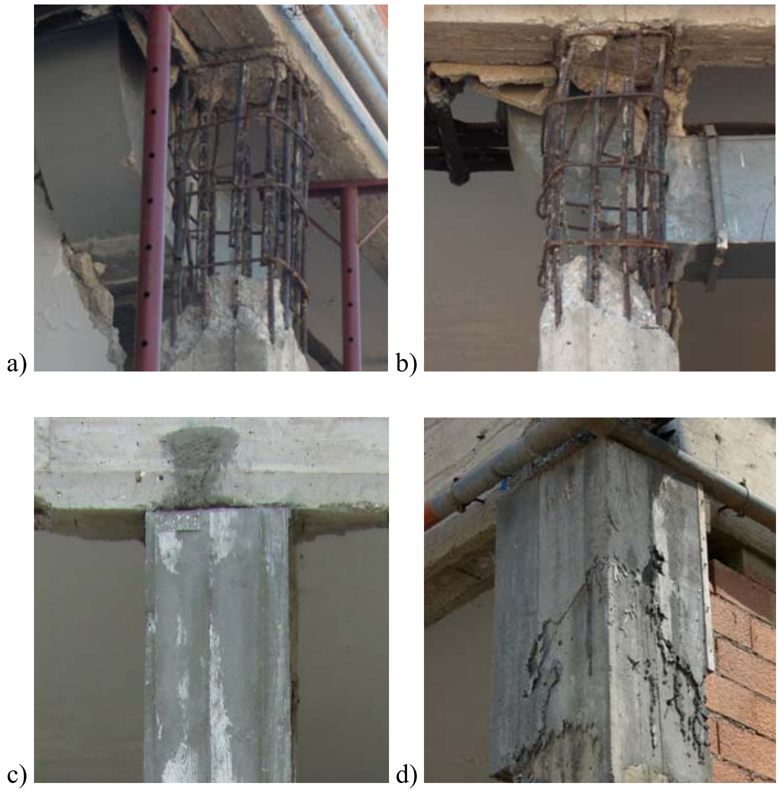

Figure 5.22. Columns' reconstruction.

The erecting phases of brace system are summarized in the following sequence of figures. In particular, Figure 5.23 shows the positioning of hole gauges in order to precisely position the bracing members by means of brace templates (Figure 5.23c). Moreover, the use of these metal molds made easy and accurate to drilling the RC members for fastening the brace connections. In this sense, Figures 5.24 show the RC drilling through the holes of the mold plates, while Figures 5.25 show the final positioning of brace-to-RC member splices. Moreover, Figures 5.26 show some phases of the erection in site of BRBs.

a)  b) 

c)  d)  e) 

Figure 5.23. Positioning of hole gauges.

Figure 5.24. Drilling of RC members to fasten brace connections .

Figure 5.25. Final position of brace-to-RC connections.

Figure 5.26. Phases of erection in site of BRBs.

The final step of erection of BRBs consisted in sealing the splice between steel plates of brace connections and the RC structure, as shown in Figure 5.27. To do this, the commercial pre-mixed shrinkage compensated cement mortar “Mapefill” has been used. This product is very fluid and it was poured into the interstice between the steel splices and the RC members. In order to get easy this operation, the steel plates constituting the brace connections to RC structure have been designed with some holes, where it was easily poured the mortar mixture (Figure 5.27a).

Figure 5.27. Phases of sealing the splice between steel plates of brace connections and the RC structure.

The last constructional step was the reconstruction of the facing walls. In particular, the external facing walls have been reconstructed only in one bay. This arrangement was chosen because it gave the possibility to directly evaluate the interaction between the brace and the wall. Hence, Figures 5.28 show the phases of reconstruction of facing walls, made of concrete and lapillo bricks. In particular, Figures 5.28c, d, e and f clearly show that the brace is easily inserted between the two facings. Figure 5.28h shows the final configuration of the facing wall, characterized by a central window allowing the direct observation of the BRB system during the test.

a) b)

c) d) e) f)

Figure 5.28. Phases of reconstruction of facing walls (continued).

g)  h) 

Figure 5.28. Phases of reconstruction of facing walls.

Figures 5.29 illustrate the test set-up, showing both global views of the structure equipped with BRBs and the reacting steel frame (a, b) and the digital theodolite for measuring the floor lateral displacements (e).

a)

b)

Figure 5.29. Test setup: west side view (a); east side (b); digital theodolite to measure floor displacements (c) (continued).

c) 

Figure 5.29. Test setup: west side view (a); east side (b); digital theodolite to measure floor displacements (c).

5.4.3 Test Results

Test results showed a good response of the brace up to a calculated (with Eq. 55, Chapter IV) core brace strain of about 1.2% (Figure 5.24a shows the brace elongation in tension respect to the black line), corresponding to an interstory drift of about 1.1%. For larger strains, local buckling of the unrestrained non-yielding end-plate occurred. The reason for this undesired effect may be found in the negative synergy of three combined events:

1) the actual yield stress for the steel of the core plate was appreciably larger than the expected value;

2) improper, unintentional, fabrication of the welds connecting the unrestrained portion of non-yielding plate and the stiffening steel bars, with consequent failure of the welds.

3) the inner clearance between yielding core and restraining sleeve has not been complied with. In fact, the design clearance has been fixed to be 1mm per core side (Figure 5.15). While, having detached the devices after the test, the actual measured clearance between the thin core side and the sleeve was lower than 0.5mm per side, thus resulting less than half of the design value.

In fact, getting to the heart of matter, all devices have been designed with a steel grade S275, while the measured yielding stress (Figure 5.25) of steel constituting the core corresponds to grade S355 (with an average yield stress of 378MPa). Secondly, the fillet welds were designed to be continuous for the overall length of the stiffeners. Regrettably, these welds were interrupted; they have been spot welded with alternate stretches with a large pitch between each spot weld. Thirdly, the absence of an adequate side clearance between the thin side and the built up sleeve probably contributed to impair the device performance limiting its shortening deformation capacity avoiding the beneficial formation of the plastic buckling waves, thus constricting the potential dissipative behaviour of the tested system.

However, because of the relatively large safety factor used in the design, the main responsible for the buckling of the unrestrained end portion is deemed to be the incorrect welding of stiffeners. However, for clarity sake, the structural response is summarized per each load cycle as follows:

Loading cycle 1: During the first load cycle the maximum first story displacement was +4.563 mm (corresponding to an average drift of +0.101%), while the maximum applied Base shear was +425.4 kN. The minimum first story displacement was -4.843 mm (corresponding to an average drift of -0.1076%) while the maximum applied Base shear was -407.16 kN. It is interesting to note that for the maximum interstory drift of the first cycle the detachment between the facing walls and the RC structure occurred for the maximum interstory drift of the first cycle (Figure 5.30) and some cracks near the windows of the walls (Figure 5.31).

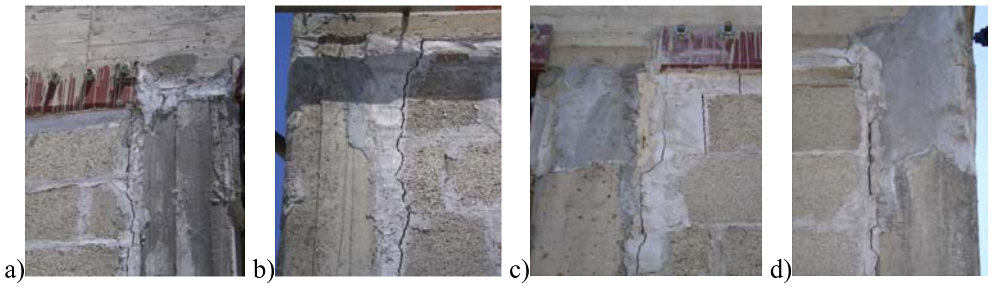

Figure 5.30. Loading cycle 1: detachment between facing walls and RC structure.

Figure 5.31. Loading cycle 1: first cracks near the windows of the facing walls.

Loading cycle 2: During the second load cycle the maximum first story displacement was +10.30 mm (corresponding to an average drift of +0.229%), while the maximum applied Base shear was +680.64 kN. The minimum first story displacement was -10.53 mm (corresponding to an average drift of -0.234%) while the maximum applied Base shear was -701.22 kN. During this cycle the main damages noticed were the increase of cracks' width.

Loading cycle 3: During the third load cycle the maximum first story displacement was +11.22 mm (corresponding to an average drift of +0.249%), while the maximum applied Base shear was +680.64 kN. The minimum first story displacement was -12.02 mm (corresponding to an average drift of -0.267%) while the maximum applied Base shear was -678.6 kN. Once again, as in the previous load cycle, the noticed damages were the increase of cracks' width (Figure 5.32).

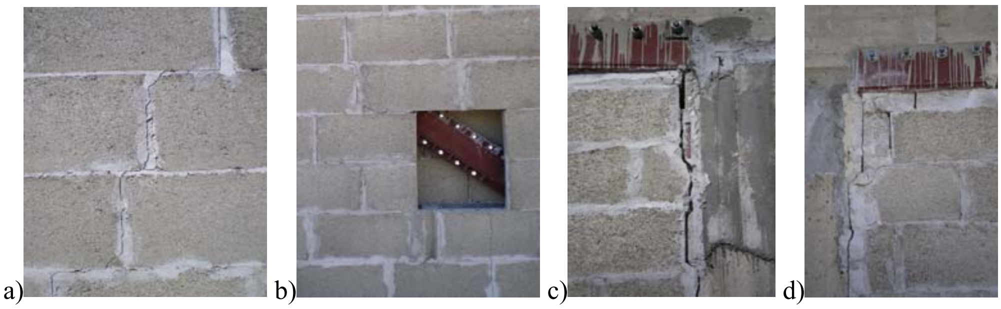

Figure 5.32. Loading cycle 3: increase of cracks in facing walls.

Loading cycle 4: During the forth load cycle the local buckling of BRB end maximum first story displacement was +56.25 mm (corresponding to an average drift of +1.11%). The maximum first floor displacement was +72.44mm (corresponding to an interstory drift of 1.61%) while the maximum applied Base shear was +1573.98 kN. The minimum first story displacement was -74.44 mm (corresponding to an average drift of -1.654%) while the maximum applied Base shear was -1131kN.
Figure 5.33 summarizes the damage pattern. In particular, Figure 5.33b shows the collapse of the external facing wall caused by buckling of the unrestrained end-portion of the BRB. Figures 5.33c, d, e clearly show failure of welds and the excess pitch between the spot welds.

a) 

b) 

c) 

d) 

Figure. 5.33. Damage pattern: plastic tensile elongation (a); collapse of the external facing wall (b); failure of welds between stiffeners and inner plate (c, d, e); final configuration of buckled end portions (f); Lüder lines testifying the core yielding with the absence of plastic buckling waves (g,e); the sleeve detached after the test remained totally undamaged (i,l). (continued)

e)  f) 

g)  h) 

i)  l) 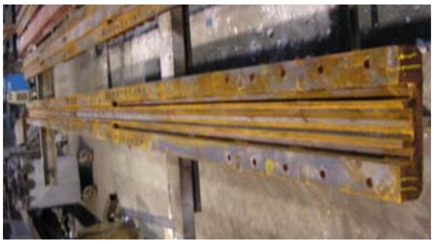

Figure. 5.33. Damage pattern: plastic tensile elongation (a); collapse of the external facing wall (b); failure of welds between stiffeners and inner plate (c, d, e); final configuration of buckled end portions (f); Lüder lines testifying the core yielding with the absence of plastic buckling waves (g,e); the sleeve detached after the test remained totally undamaged (i,l).

Figure 5.33f shows the final buckled configuration of the braces. Moreover, it is interesting to examine the final state of the detached BRB after the test. In this sense, Figures 5.33g,e clearly show the presence of the Lüder lines tilted of about 45° testifying the yielding of inner core. However, as previously mentioned, no plastic buckling wave developed all along the core. However, no damages occurred in the steel built up sleeve, as shown in Figures 5.33i,l.

Finally, the measured base shear vs. first story and second story lateral displacement relationships are plotted in Figures 5.34 and 5.35. In detail, Figure 5.35 shows the global response for the first three cycles, characterized by a perfectly symmetric response of the braces in both directions. Figures 5.36a,b show the base shear vs. floor displacements. As it can be observed by comparing them, the difference between the two curves is very small. This indicates that all the plastic deformation was concentrated at the first floor. Figure 5.37 shows the response curve of the first floor in terms of interstory drift ratios and Figure 5.38 shows the applied load pattern in terms of interstory drift ratios vs. cycle number. As it can be seen the maximum interstory drift reached during the test was 1.65%, while the estimated drift corresponding to the local buckling was 1.11%.

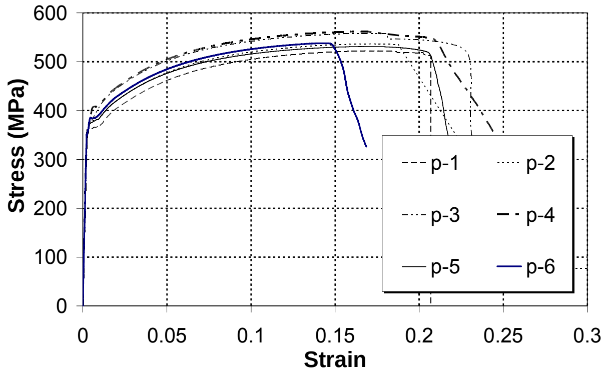

Figure 5.34. The actual stress-strain relationship of steel constituting the core plate.

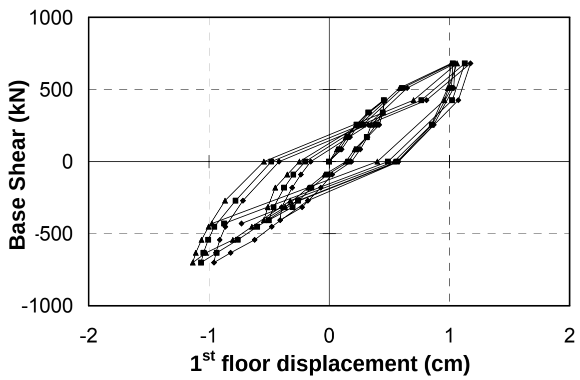

Figure 5.35. Base shear vs. first story lateral displacement relationships for the first three cycles.

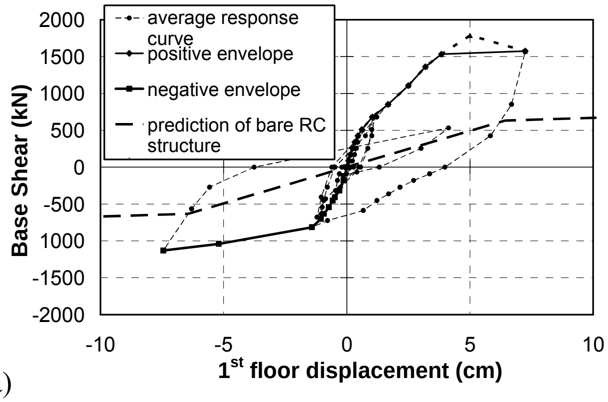

a)

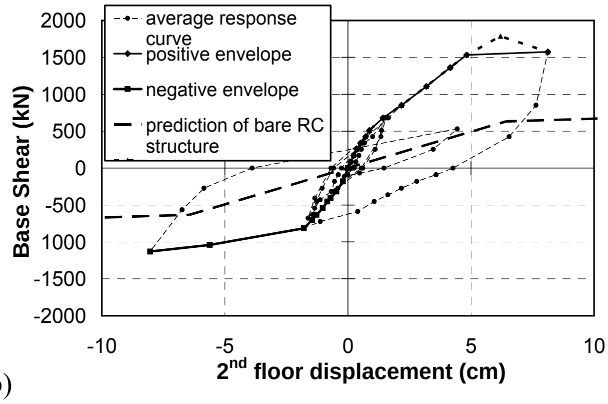

b)

Figure 5.36. Base shear vs. first (a) and second (b) floor displacement curves.

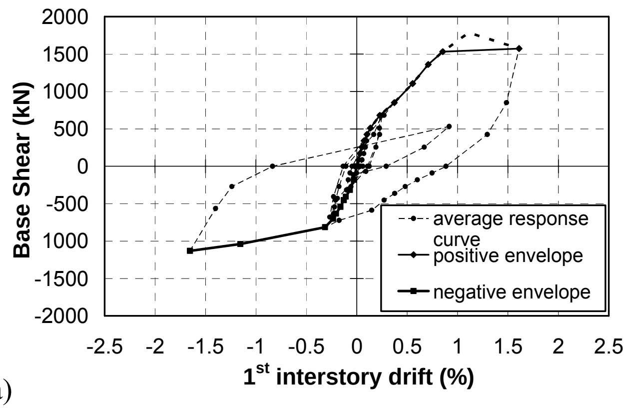

a)

Figure 5.37. Base shear vs. interstory drift of first floor.

b) 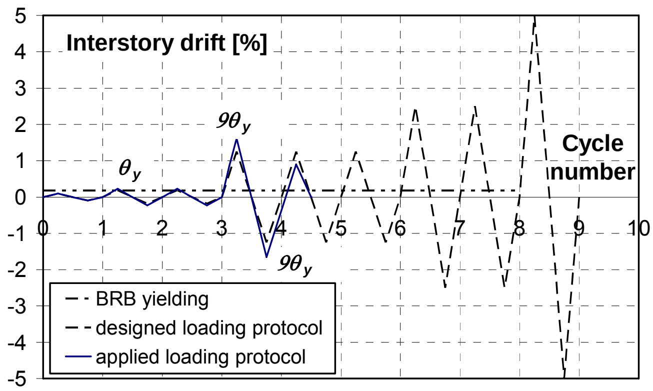

Figure 5.38. Loading protocol.

The loading program was designed to impose pre- and post-yield, fully reversed, displacement corresponding to: the brace yield displacement (θ_y=0.18%), 7, 14 and 28 times the expected brace yield deformation at the design story drift.

5.5 UNBRACE VS. BRACED RC STRUCTURE: COMPARISON OF EXPERIMENTAL RESPONSES

Notwithstanding the lateral response of the braced structure was impaired by buckling of the unrestrained non-yielding segment, the global response was satisfactory. In fact, the bracing system increased more than twice (2.22) the lateral strength and more than eleven (11.22) times the lateral stiffness of the RC structure. Moreover, it is important to underline that the system ductility was finally quite large. In fact, even if the overall maximum displacement was limited by the local failure of BRB unrestrained end-portions (corresponding to a maximum interstory drift of 1.11%) the measured global ductility was significantly large corresponding to the local brace buckling was $\mu=\theta_b/\theta_y$=1.11%/0.18%≈6 (Figure 5.39). Both these results reveal that notwithstanding the lack of accuracy in the manufacturing process of local details and the use of a higher steel grade than designed one, this system is robust enough to be able to provide high global ductility, improving strength and stiffness. However, the design goal was not entirely achieved because the designed ductility to be attained was μ=8. In spite of this aspect, the achieved experimental results give rise to the need to investigate in which terms a hysteretic steel device like a BRB performs after its range of design functioning.

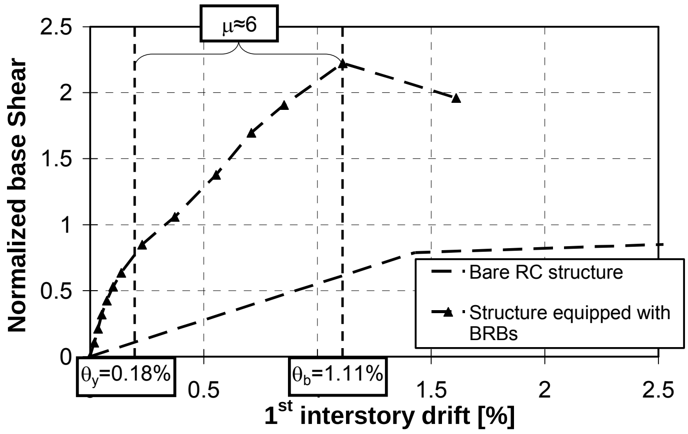

Figure 5.39. Overall ductility measurement.

Figure 5.40 shows the comparison of the experimental response curves of braced and unbraced structure normalized to the maximum strength of the latter.

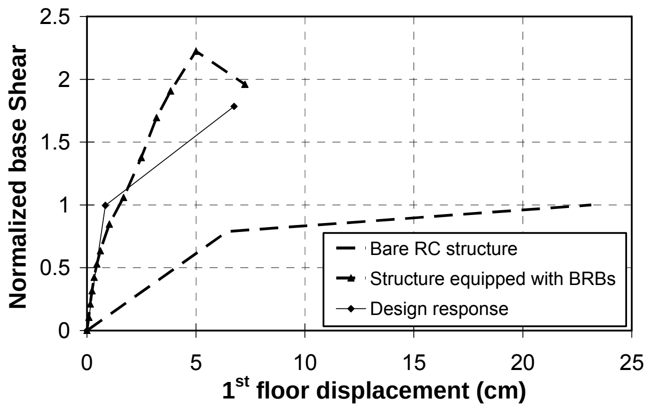

Figure 5.40. Unbrace vs. braced RC structure.

As it was expected, because of the great amount of the lateral stiffness was influenced by the braces, the initial stiffness of predictive curve accurately matches the one of the experimental curve. However, respect to the design response curve, the experimental curve shows a larger strength. This effect is mainly due to the core steel, which resulted with a yield stress larger than the one assumed in design. This effect along with improper, unintentional, fabrication of the welds connecting the unrestrained portion of non-yielding plate and the stiffening steel bars underline the weak points that could affect the response of BRB devices: 1) if not properly controlled, steels commonly used to fabricate the restrained yielding segment may have a wide range of yield strength; 2) the difficulty to provide a reliable quality control in the manufacturing process, that is characterized by erection tolerances generally lower than those of conventional braced frames, combined with more complex local details.

Chapter VI

Numerical modelling and analyses of retrofitted bare RC structures

6.1 GENERAL

This Chapter summarized the numerical studies carried out in order to deeply investigate the performance of tested devices and the behaviour of the retrofitted RC structures. In particular, several 3D numerical models have been developed and calibrated in order to schematize the experimental global response of the bare RC tested structures.

Moreover, in case of EBs, several finite element models have been developed in order to deeply investigate about the causes that induced the high shear over-strength measured during the tests. The numerical analyses emphasized the role of axial restraints on the links as one of the main responsible for the anomalous values of over-strength factors measured in the performed tests.

In addition, some time history analyses have been performed in order to quantify in which terms the retrofitted structure can overcome seismic events as it is and how the presence of the studied bracing systems (EBs and BRBs) can improve the structural performance.

6.2 NUMERICAL MODELLING OF THE RC STRUCTURE EQUIPPED WITH INVERTED-Y ECCENTRIC BRACES

6.2.1 Numerical models of the bare RC structure

A 3D model of the structure has been initially defined. In particular, the floor slab has been fully modelled in such a way that all floor joists have been schematized with beam-column members. In fact, the experimental evidence on similar RC structure clearly showed the participation of the full floor slab to resist with the columns horizontal action. Moreover, all the structural elements of the RC frame were modelled with “beam-column” elements. In detail, at one or both ends of the members rigid end-blocks were modelled to simulate the localized increase of stiffness due to the presence of the edge beams at the two floor levels and at the foundation.

However, the first step to model the bare RC structure was the schematization of its elastic behaviour, which is the calibration of its lateral stiffness. This purpose was obtained thanks to the knowledge of dynamic properties of the bare RC Unit. In fact, experimental dynamic identification of the bare (unbraced) RC structure has been initially performed by the Italian Department of Civil Protection. It was carried out with two different methods:

1) a direct method adopting impact hammer (Figure 6.1);

2) an indirect method measuring the vibration caused by the fall of heavy body (Figure 6.2).

a) b)

Figure 6.1. Impact hammer test: a) instrumented hammer; b) a test phase.

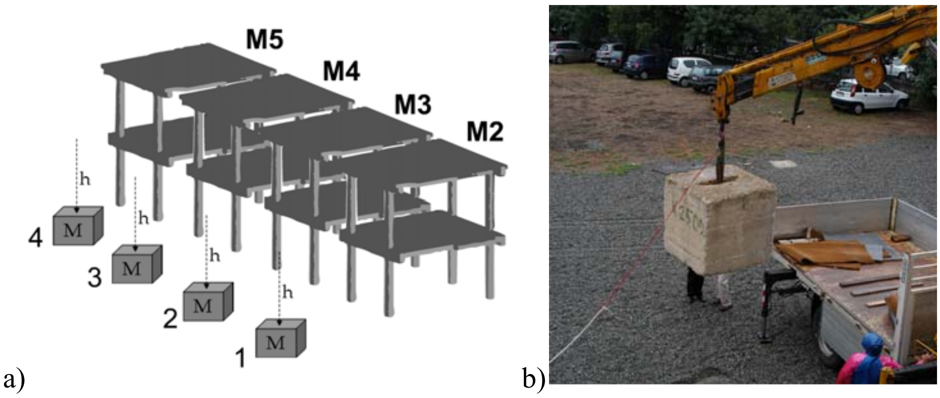

Figure 6.2. Falling mass test: a) the testing scheme; b) a detail of the falling mass (each mass weighted about 2.5kN) .

Figure 6.3 shows the acquisition system (a) and location of accelerometers on building.

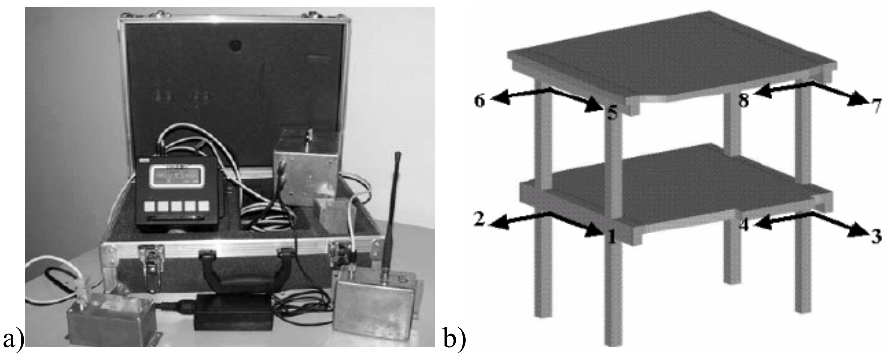

Figure 6.3. Setup of vibration tests.

The numerical model of the bare RC structure was implemented in SAP2000 in order to compare with experimental results. Inertial properties of the studied RC structure are given in Table 6.1. As shown in Figure 6.4, vibration properties of the uncracked model differs significantly from the actual ones, with a difference of 18% for the first period of vibration. Average mechanical properties of structural materials (concrete and steel) have been used.

Table 6.1. Inertial properties of retrofitted RC structure.

	Translational Mass (kNs^2/m)	Rotational Mass (kNm^2)
1st floor	16.72	137.12
2nd floor	16.64	159.25

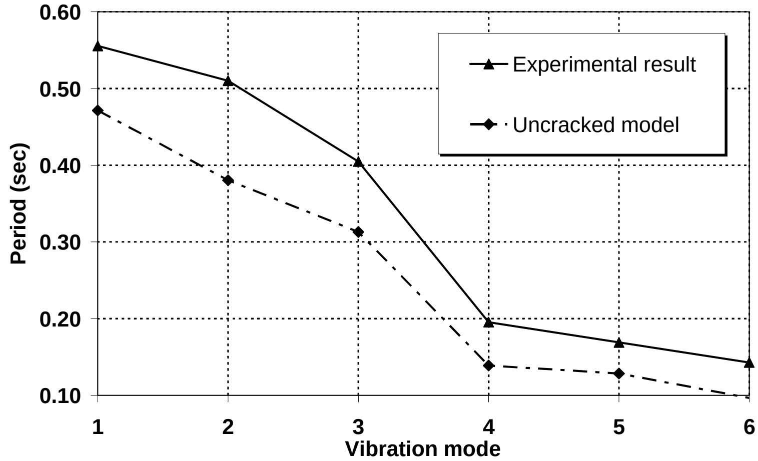

Figure 6.4. Fundamental periods of uncracked model vs experimental one.

As shown in Table 6.2, reduction factors of cross sectional properties of RC members have been used to reduce such differences. Suggestions of OPCM 3274, Park & Paulay and FEMA 356 have been initially adopted. As shown in Figure 6.5, these values have been modified in order to adjust the elastic model on the base of the experimental results. Calibrated values of reduction coefficients are also given in Table 6.2. Figure 6.6 shows the modal shapes of the bare RC structure based on the calibrated numerical model.

Table 6.2. Reduced stiffness for RC members (continued).

		Flexural stiffness	Shear stiffness
beam	OPCM3274	0.50 Ig	0.50 Av
	Park&Paulay (rectangular beam)	0.40 Ig	0.40 Av
	Park&Paulay(T-beam)	0.35 Ig	0.40 Av
	FEMA 356	0.50 Ig	0.40 Av
	Calibrated model	0.40 Ig	0.50 Av

Table 6.2. Reduced stiffness for RC members.

		Flexural stiffness	Shear stiffness
column	OPCM3274	0.50 Ig	0.50 Av
	Park&Paulay	0.60 Ig	0.40 Av
	FEMA 356	0.70 Ig	0.40 Av
	Calibrated model	0.60 Ig	0.50 Av

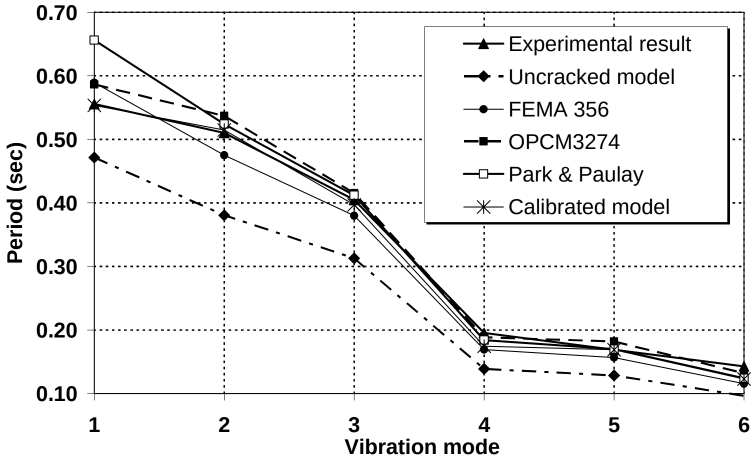

Figure 6.5. Fundamental periods of numerical models vs. experimental one.

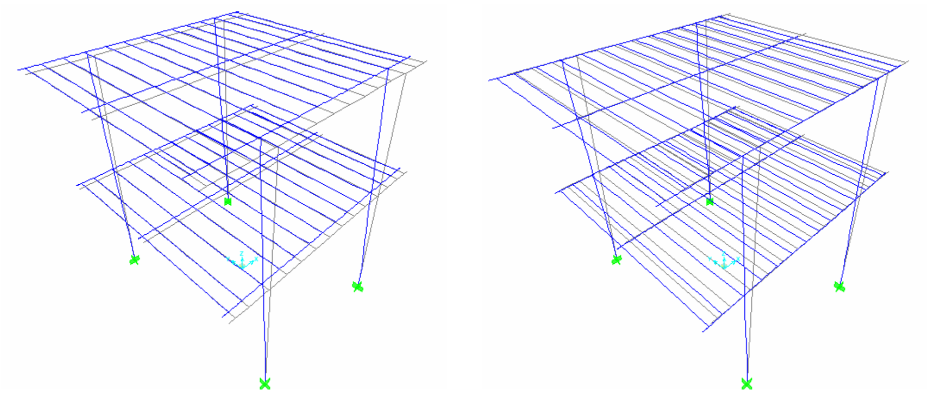

1st mode of vibration (T = 0.5628s) 2nd mode of vibration (T = 0.5234s)

Figure 6.6. Modal shapes of the bare RC structure (continued).

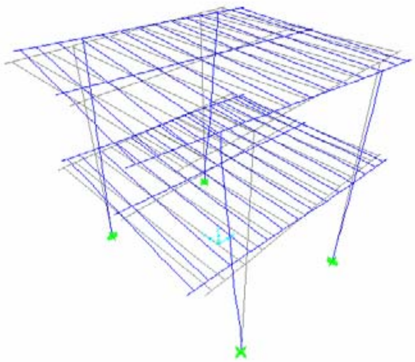

3rd mode of vibration (T = 0.36875s)

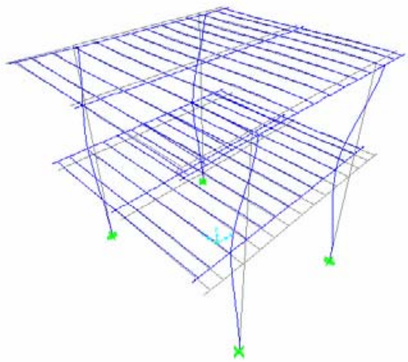

4th mode of vibration (T = 0.17825s)

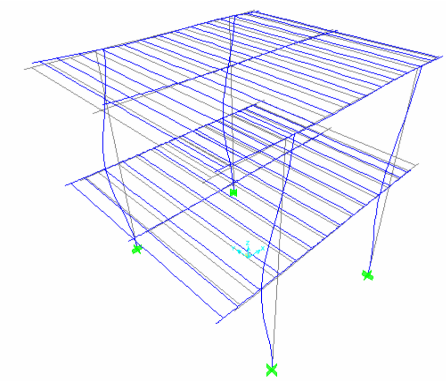

5th mode of vibration (T = 0.17255s)

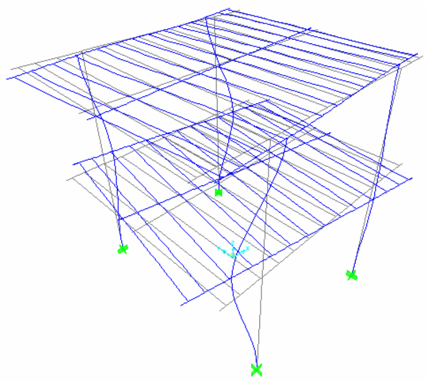

6th mode of vibration (T = 0.1199s)

Figure 6.6. Modal shapes of the bare RC structure.

The inelastic behaviour of RC unit has been schematized by means of a lumped-plasticity modelling approach. In particular, inelastic response parameters (i.e. plastic hinges properties) for the bare RC structure numerical model have been deducted from average material properties coming from laboratory tests (see Chapter IV). Finally, Figure 6.7 summarizes the pushover response curves of the bare RC unit.

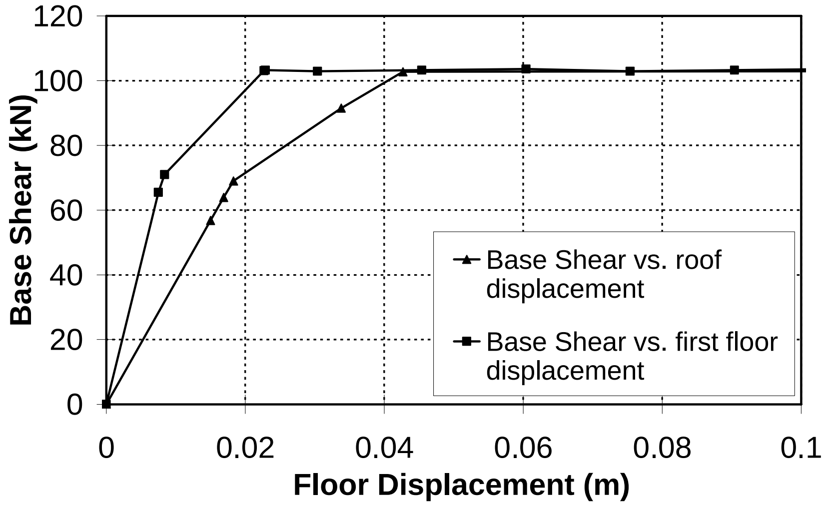

Figure 6.7. Pushover response curves of the bare RC structure.

6.2.2 Numerical models of the braced structure

Numerical models of the EB systems have been setup introducing the bracing system in the model previously for calibrated on the bare RC structure (Figure 6.8).

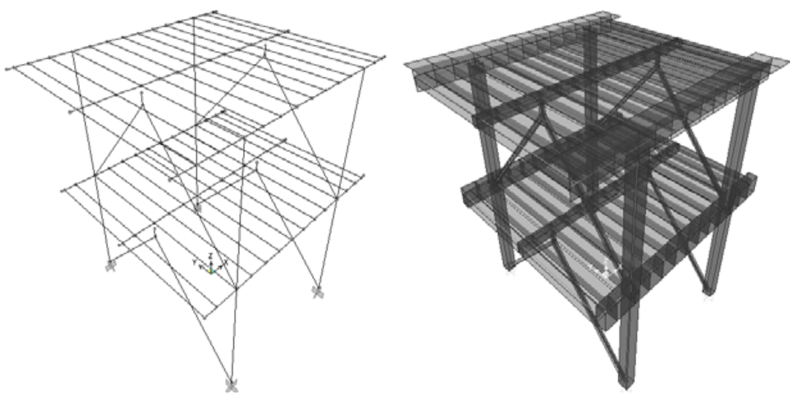

Figure 6.8. Numerical model (SAP2000).

As a consequence, the presence of EBs in the structure modifies the dynamic response. In fact, this aspect is clearly shown in Figure 6.9, where the modal shapes of the RC unit equipped with Y-inverted EBs are summarized.

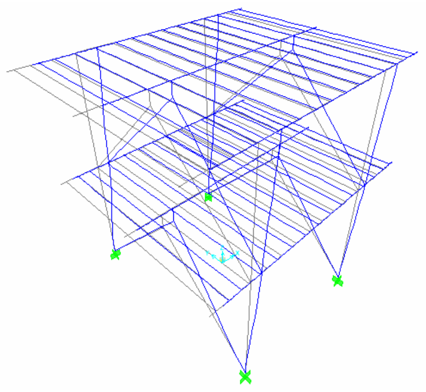

1st mode of vibration (T = 0.48812s)

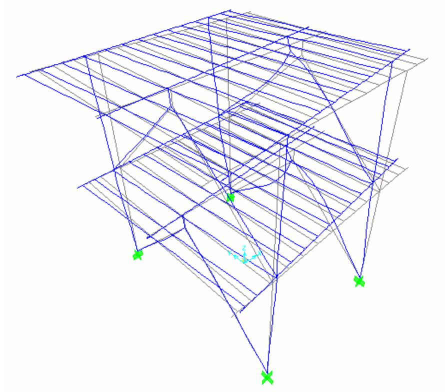

2nd mode of vibration (T = 0.20439s)

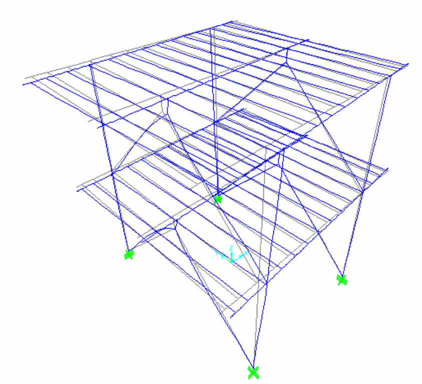

3rd mode of vibration (T = 0.19896s)

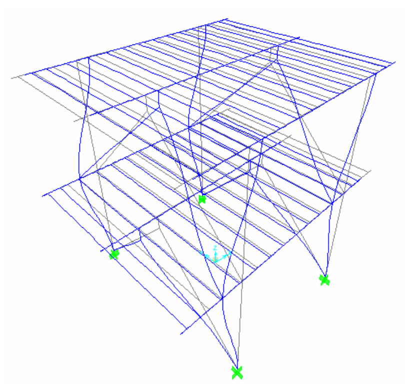

4th mode of vibration (T = 0.18017s)

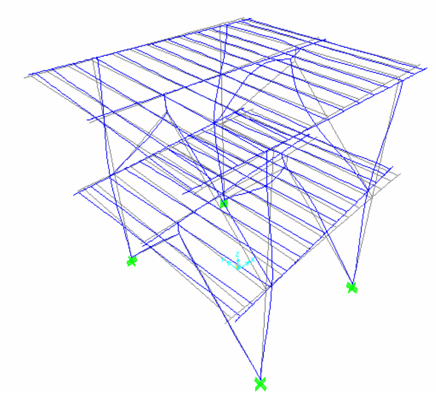

5th mode of vibration (T = 0.07853s)

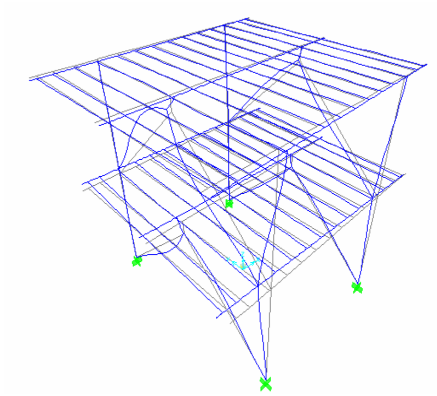

6th mode of vibration (T = 0.7286s)

Figure 6.9. Modal shapes of the RC structure equipped with EBs.

Once defined the elastic properties, the following step has been the characterization of the inelastic response of the RC unit equipped with EBs. To do this it needs to adequately model the non linear behaviour of dissipative members and the failure modes of non-dissipative members as well.

Since during each pushover test the main structural subcomponents (i.e. the link member and its end-connections) have not been monitored, a simplified approach was pursued, in order to minimize the number of parameters to be calibrated. However, the modelling assumptions and the relevant results are described for each test and the numerical curves are compared with the experimental ones.

Hence, in case of first test the main modelling assumptions concern the link end connections. In fact, the first test showed the failure of link end connections (Figure 4.24, Chapter IV), so the main modelling issue was to schematize the inelastic behaviour of connections. Flexural plastic hinges have been used for this purpose.

According to Eurocode 3 (2003) classification, tested link end connections were semi-continuous (semi-rigid and partial strength). Consequently, both the design resistance and initial stiffness of link-to-brace and link-to-slab joints have been derived adopting the components' method proposed by Eurocode 3 (2003). A tri-linear relationship has been assumed for joint hinging, based on the moment-rotation curve suggested by Eurocode 3 (2003). Figure 6.10 illustrates the moment-rotation relationship adopted in the numerical model. The third linear branch of this idealized curve has been given a negative slope equal to -1/9 the initial stiffness. This value was obtained by calibration with experimental results.

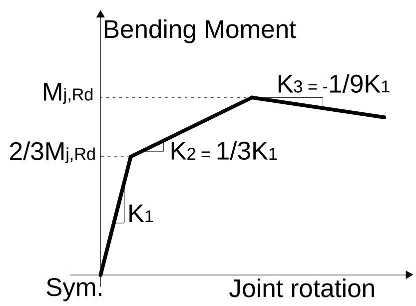

Figure 6.10. Moment-rotation curve of link-end-connections (EBs-Test No.1).

Shear plastic hinges were considered for modelling the inelastic link behaviour. Shear hinging was schematized by means of the force-deformation relationship suggested by Ricles & Popov (1994) and Ramadan & Ghobarah (1995). In particular, the link shear plastic hinge was located where the elastic bending moment was zero.

Finally, as shown in Figure 6.11, the model adequately predicts the initial stiffness. Hence, the effective joint stiffness seems to be very important in order to correctly define the global response of the structure. Moreover, in perfect agreement with the experimental results, the numerical model confirmed that the lateral capacity of the retrofitted structure is mainly due to the achievement of maximum bending capacity of link end connections.

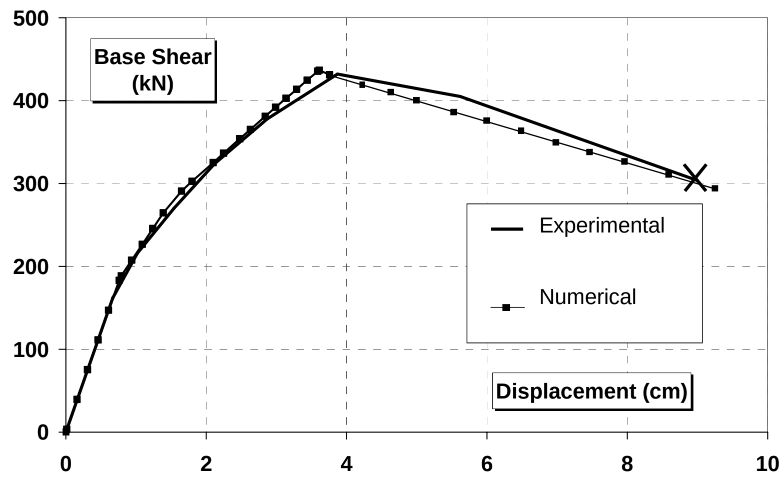

Figure 6.11. Numerical response curve vs experimental backbone curve (EBs-Test No.1).

As in the previous case, in the test No.2 the collapse was due to weakness of link connections. But, differently from the previous case, the second test showed the brittle shear failure of bolts (Figure 4.29, Chapter IV). As a consequence, link end connections can be considered as rigid according to EC3. According to this, links have been assumed to be fixed respectively to the RC slab and to the braces. In this case, significant link over-strength has been revealed by the test. Then, as mentioned above, a simplified modelling approach has been adopted to characterize link shear hinging. Instead of the model proposed by Ricles & Popov (1994), shown in Figure 2.19b, Chapter II, the adopted shear hinge relationship is bi-linear, as shown in Figure 6.12, with the post-elastic stiffness calibrated in order to match the experimental response curve.

The link flexural hinging has been schematized with the moment-rotation relationship suggested by Ricles & Popov (1994), as shown in Figure 2.19a of Chapter II.

As in the previous case, the link shear plastic hinge was located where the elastic bending moment in link element is zero. Link flexural hinges were located at both link ends.

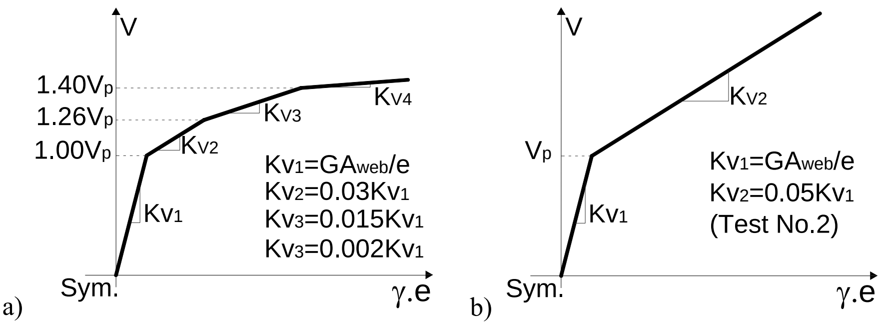

Figure 6.12. Shear plastic hinge: Ricles & Popov (a), simplified approach (b)

As shown in Figure 6.13 the model adequately predicts the initial elastic stiffness and the final strength and stiffness. Moreover this numerical model confirmed the significant link shear over-strength, in fact the computed peak shear force is equal to 3.44 times the link plastic shear strength.

Differences of the numerical response curve in post-elastic zone are mainly due to the difficulties in predicting the response of the RC structure, which was significantly damaged in the previous test. Moreover the slipping and flexural deformation of bolts in both link end-connections contributed to drift away the experimental curve from the numerical one, as well.

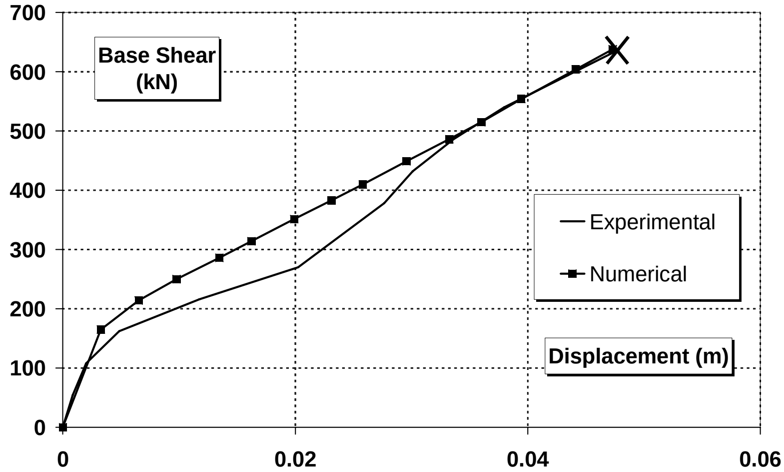

Figure 6.13. Numerical response curve vs experimental backbone curve (EBs-Test No.2).

Finally, the last modelling effort was to interpret the third test. So, since the third test showed a global response similar to that one of the previous test, this last model is very similar to the previous one. Once more the value of the link shear post-elastic stiffness has been deduced from the back analysis of the experimental response curve. In fact, the adopted shear hinge relationship is still bi-linear and the post-elastic stiffness has been calibrated to the experimental response curve. In this case for the post-elastic stiffness it was assumed $K_{V2} = 0.03K_{V1}$.

Flexural hinges have been characterized by the moment-rotation relationship of Ricles & Popov (1994), shown in Figure 2.19a of Chapter II. Moreover, the location of both shear and flexural plastic hinges has been fixed as in the previous model.

Once again, this simplified modelling confirmed the significant link shear over-strength, in fact the computed peak shear force is equal to 5.36 times $V_{y,link}$.

As in the previous case, the deviations of numerical results from the experimental response curve (Figure 6.14) are mainly due to the difficulties to properly model the damages induced by previous tests on RC structure.

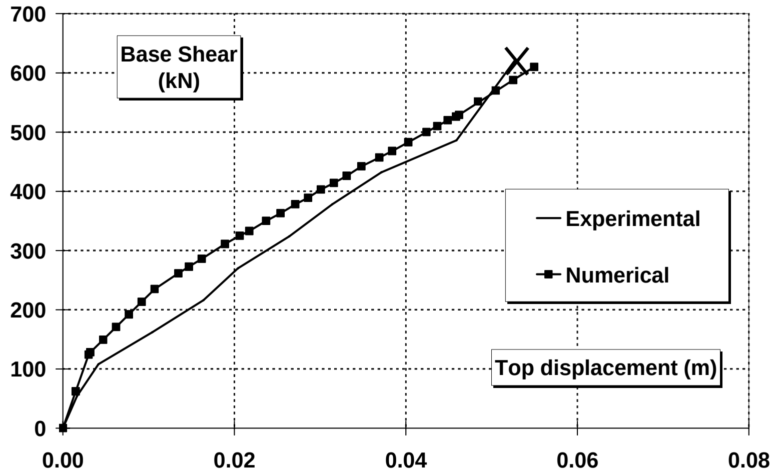

Figure 6.14. Numerical response curve vs experimental backbone curve (EBs-Test No.3).

6.2.3 Finite element analyses of the testes shear links

Modern design building codes prescribe that non-dissipative elements should be designed with a sufficient over-strength in order to allow the development of cyclic plasticity in the dissipative zones (capacity design). Hence, in a reliable capacity design it is fundamental to know the proper over-strength of the dissipative zones. The tested shear links (see results presented in Chapter IV) clearly showed over-strength factors (ratio of the ultimate plastic shear strength and the yielding shear strength) appreciably larger than the value 1.50 suggested by the current seismic codes. The codified shear over-strength (1.50) derives from the experimental tests performed on American wide-flange profiles in case of uniform shear forces, restraining all link end rotations but without axial restrains (consequently it was permitted the free link axial shortening). It is worth to notice that comparing depth for depth European hot-rolled steel profiles with American ones it is evident that the former are more compact with local slenderness lower than the latter. So, this aspect combined with the presence of significant axial tensile forces due to the axially fixed boundary conditions in case of large deformations had originated a shear link capacity larger than the expected value.

To underline in which terms the local geometric proportion of link section and boundary conditions can influence the link inelastic response, several finite element analyses have been carried out. In particular, both monotonic and cyclic loading numerical simulations have been performed. The analyses indicate that, in all the examined cases, the plastic bending moment is reached at the link ends without any loss of shear strength, even if no stiffener is adopted.

Finally, as previously maintained in Section 4.6, for the purpose of this work, the fully plastic shear strength has been estimated by the following equation:

$$V_y = \tau_y d t_w \tag{57}$$

Equation 57 is deemed to be the most appropriate. In fact, the aim of this study is the interpretation of the shear link response for seismic modelling, where the response into the inelastic range of deformation is of interest. Besides, the unit shear strength τ_y is assumed according to the Von Mises yield criterion that is:

$$\tau_y = f_y \big/ \sqrt{3} \tag{58}$$

Moreover, in the following, the link shear deformation angle (or link rotation) γ is defined as the ratio between the relative transverse displacement of the two cross-sections at link ends and the link length.

Basic modelling assumptions

The finite element computer program ABAQUS 6.5 was used to model shear links. Three dimensional solid continum elements were utilized and the ABAQUS-8 node brick continum element C3D8R with 8 nodes per element, 3 degrees of freedom per node and a linear interpolation function. In particular, nodes belonging to cross-sections at the ends of the link were slaved to have the same displacements of two different reference points: RP-A is the master node at the left end and RP-B is the master node at the right end. In such a way it was possible to modify the type of link end constraint by properly restraining the reference point degrees of freedom. In particular, three different boundary conditions have been analyzed:

a. Both link ends (i.e. the reference points) were restrained against displacements and rotations in all directions (Figure 6.15a);

b. Only the axial is freely permitted (Figure 6.15b);

c. Both link ends were restrained by equivalent springs simulating the presence of the RC floor slab and the presence of the steel diagonal braces, respectively (Figure 6.15c).

In all cases, the link shear deformation was imposed by applying a displacement at RP-A in the 2-direction (vertical), while providing a restraint for the remaining degrees of freedom. The combination of the boundary conditions imposed a constant shear force in the element and equal moments at link ends for the scheme of Figures 6.15a,b (hypothesis a and b), while a bi-linear unsymmetrical bending moment distribution for the scheme of Figure 6.15c.

Moreover, in case of hypothesis c, the stiffness of the equivalent springs simulating the restraining effects of RC slab and of the steel diagonal braces have been calculated by static schemes shown in Figure 6.16. In particular, in case of slab a linear response has been assumed and the equivalent flexural stiffness has been defined characterizing the global response of the RC structure, as deeply shown in Section 6.4.2.

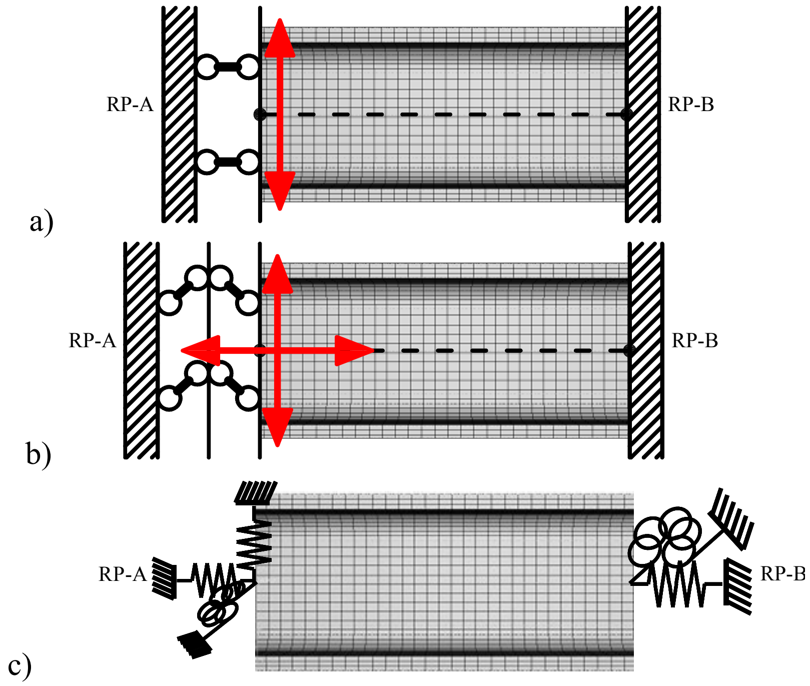

Figure 6.15. Different hypotheses on link boundary conditions.

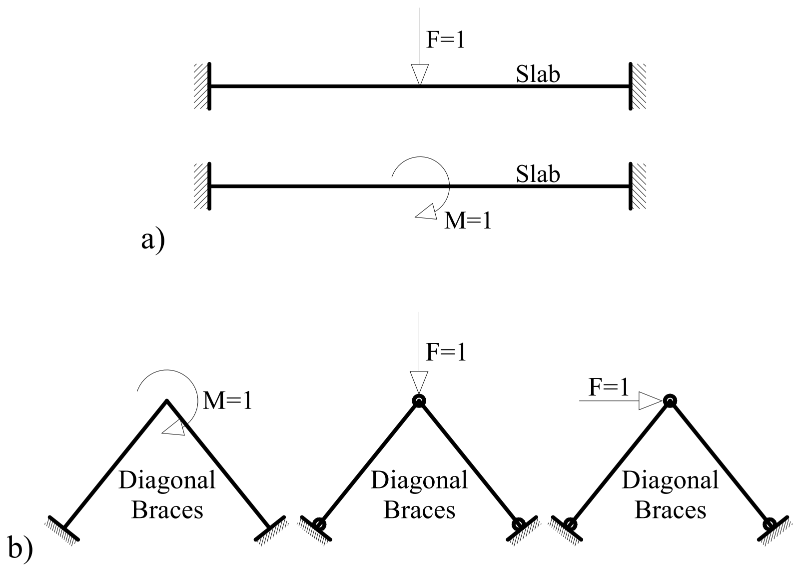

Figure 6.16. Theoretical schemes to calculate the stiffness of equivalent springs simulating the restraining effects of RC slab (a) and steel braces (b).

In addition, large deformation effects have been considered. So that in case of fixed- and partially fixed-end restraint conditions (hypothesis a and c) a tension axial force is developed in the link.

Moreover, the possible pre-stressing of the tested links has been taken into account. In fact, during the erection phases, the tested links were forced to be positioned and bolted to the steel braces. The average imposed axial deformation was about 10mm. Hence, apart the above mentioned modelling assumptions, other refined models have been analyzed considering the effect of link pre-stressing.

Finally, the non-linear material properties have been defined by a yield stress along with plastic strain associated stress data. In particular, the average stress-strain curves derived from the lab tests on coupon specimens sampled by the tested link profiles (see Chapter IV) have been adopted. In particular, the real material constitutive law has been considered. So, the engineering stress-strain curves can be converted into the true stress-true strain curves by means of the following expressions:

$$\sigma_{true} = \sigma_{eng} \cdot \left(1 + \varepsilon_{eng}\right) \tag{59}$$

$$\varepsilon_{true} = Ln\left(1+\varepsilon_{eng}\right)-\sigma_{eng}/E \qquad (60)$$

The plasticity behaviour was based on Von Mises yield surface criterion. Isotropic strain hardening was used for the material, with one single type of post yield material relationship: cyclic stress-strain behaviour.

Modelling and analysis of HEA100 link (2nd tested EB)

Figures 6.17a,b,c illustrate the geometry of the F.E. model of the link that has been the object of the second test on EBs. The shear link was made of a HE A 100 profile with a length of 220 mm.

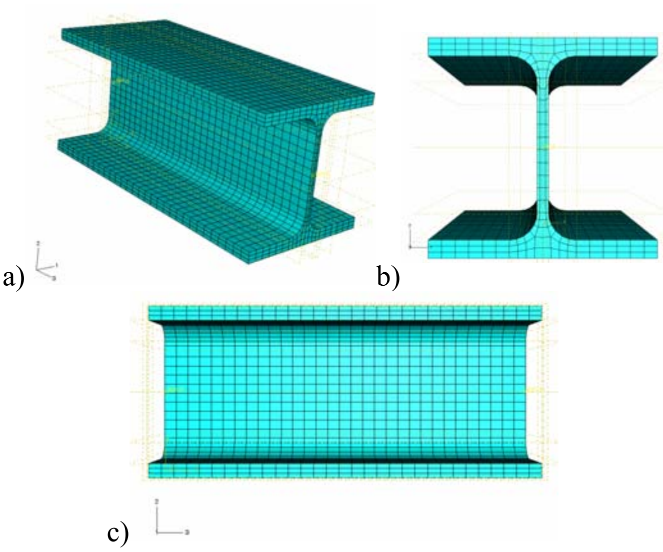

a) b) c)

Figure 6.17. Geometric model of HEA100 link (EBs-Test No.2).

As mentioned in the previous Section, the presence of link axial restraints generates large axial forces under large transverse deformation because of the lace effect that counters the free link shortening. In fact, under these assumptions Figure 6.18 clearly shows that in case of axial restraints the axial force (here normalized to link axial plastic capacity) is not negligible and it can achieve the nominal full plastic capacity. Moreover, the axial force in the link starts to develop appreciable values only after web yielding. Tension axial forces are expected to increase ductility and peak inelastic shear strength.

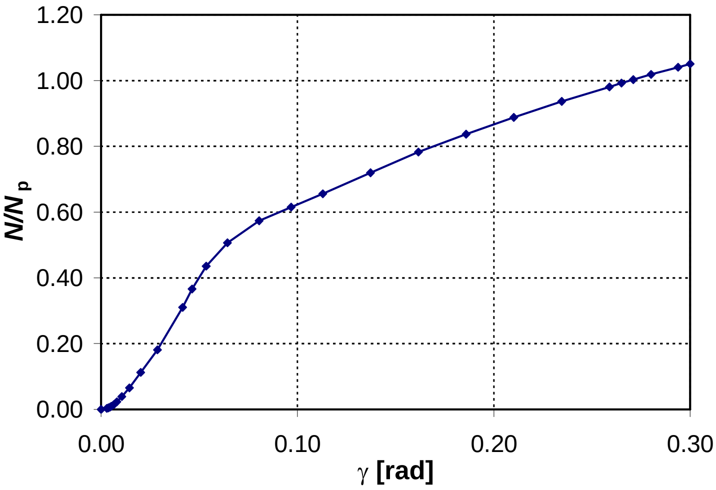

Figure 6.18. Normalized axial force vs. shear deformation angle of HEA100 link (EBs-Test No.2).

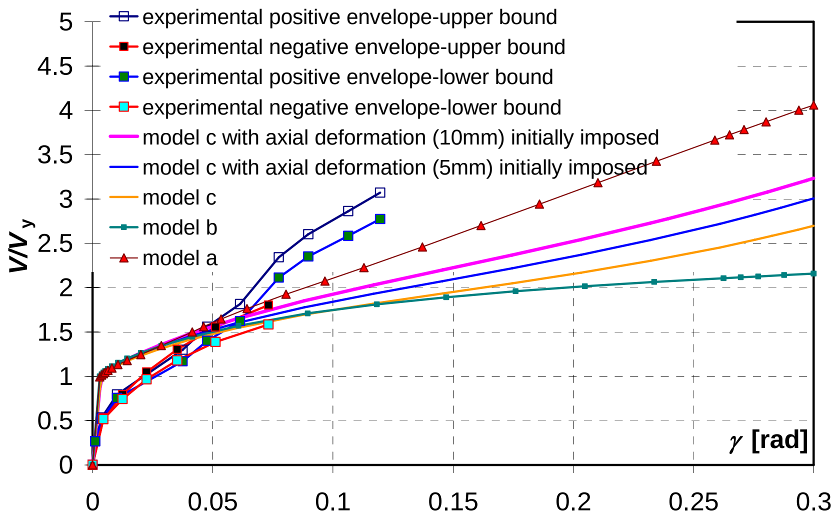

Figure 6.19. Normalized shear force vs. shear deformation angle of HEA100 link for different link end restraining conditions (EBs-Test No.2).

Figure 6.19 shows the relationship between the normalized shear force (V/V_y) and the shear deformation angle, for the three different restraining conditions (a,b and c) compared with the experimental backbone response curves computed a posteriori as explained in Chapter IV. In addition the effect of two different pre-imposed axial lengthening (5 and 10mm, respectively). As it can be noted, under monotonic loading the analyzed link can achieve without local failure large shear over-strength, in particular, up to 4 times the shear yield strength at 0.30 radians. Moreover, the Von Mises stress trends along the link length and the link cross section are worth to be noticed for the most representative models that are the model type a and c. In fact, in those cases the modelling assumptions lead to the larger shear over-strength. In particular, for the model type c only the case of the initial 10mm lengthening has been showed. So, in Figures 6.20 and 6.21 the deformed shapes corresponding to 0.10 radians, 0.20 radians and 0.30 radians are respectively shown with the relevant stress trends per model a and c.

However, the objective of this research is to capture the inelastic response of shear links when they are in a stable range of behaviour under any loading protocol. Since the investigation is limited to short links and experimental evidence consistently indicates that a plastic rotation supply of 0.08 radians is a guaranteed minimum (Okazaki & Engelhardt 2007), the analyses results are discarded for larger values of plastic rotations. In other words, for plastic rotations smaller than or equal to 0.08 radians, neither buckling nor web fracture should affect the link response, thus validating a finite element model not explicitly considering such effects. Therefore, Figure 6.22 summarizes the link shear over-strength (V/V_y) related to the plastic shear deformation angle $\gamma_p=\gamma-\gamma_y$ in the range of [0 rad; 0.8 rad]. Thus emphasizing that, for different link end restraining conditions, link shear over-strength (V/V_y) varies in a range of 1.7÷2.5 at an overall shear plastic deformation of 0.08 radians.

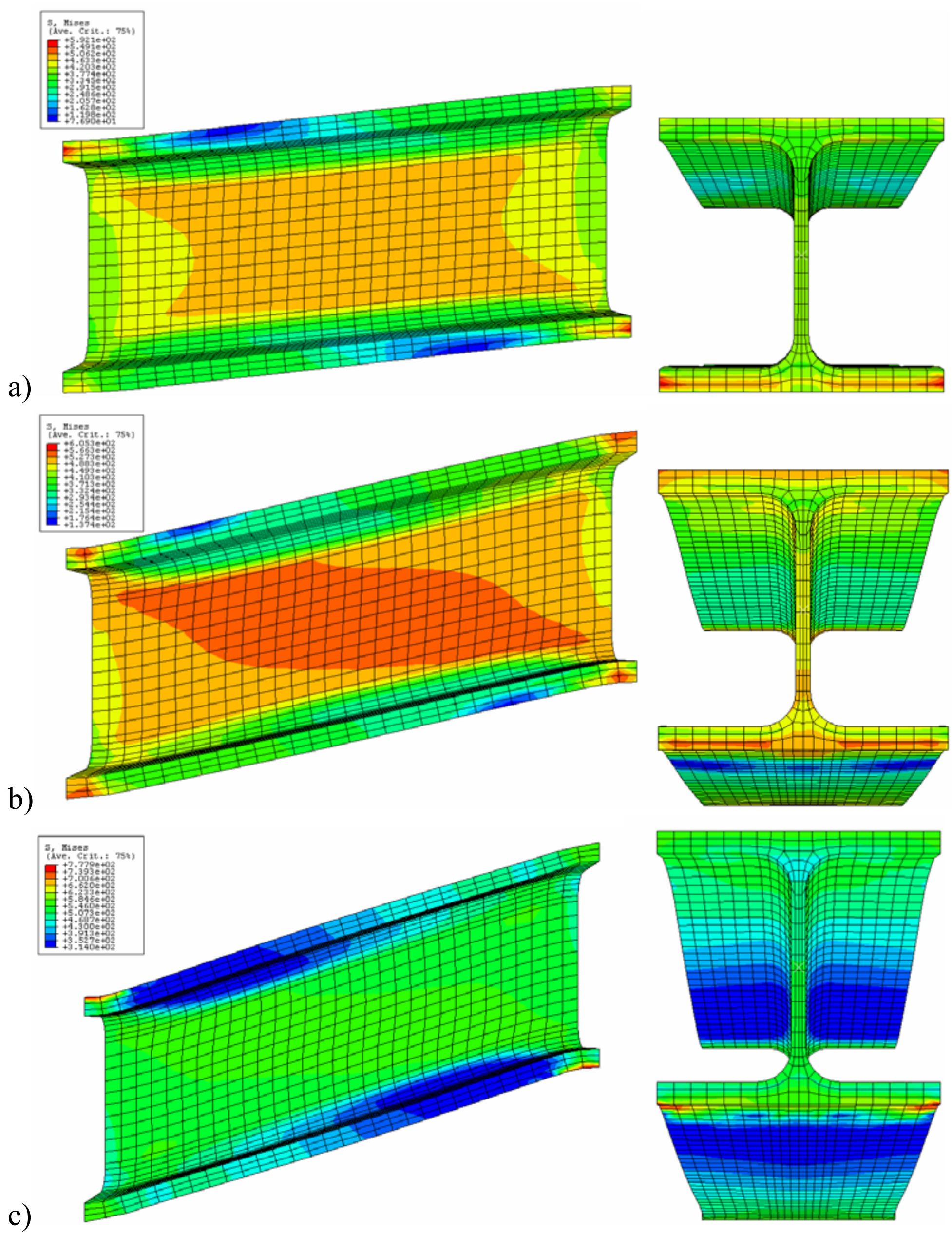

Figure 6.20. Deformed shape with relevant stress trend for model type a (EBs-Test No.2): 0.10 rad (a); 0.20 rad (b); 0.30 rad (c).

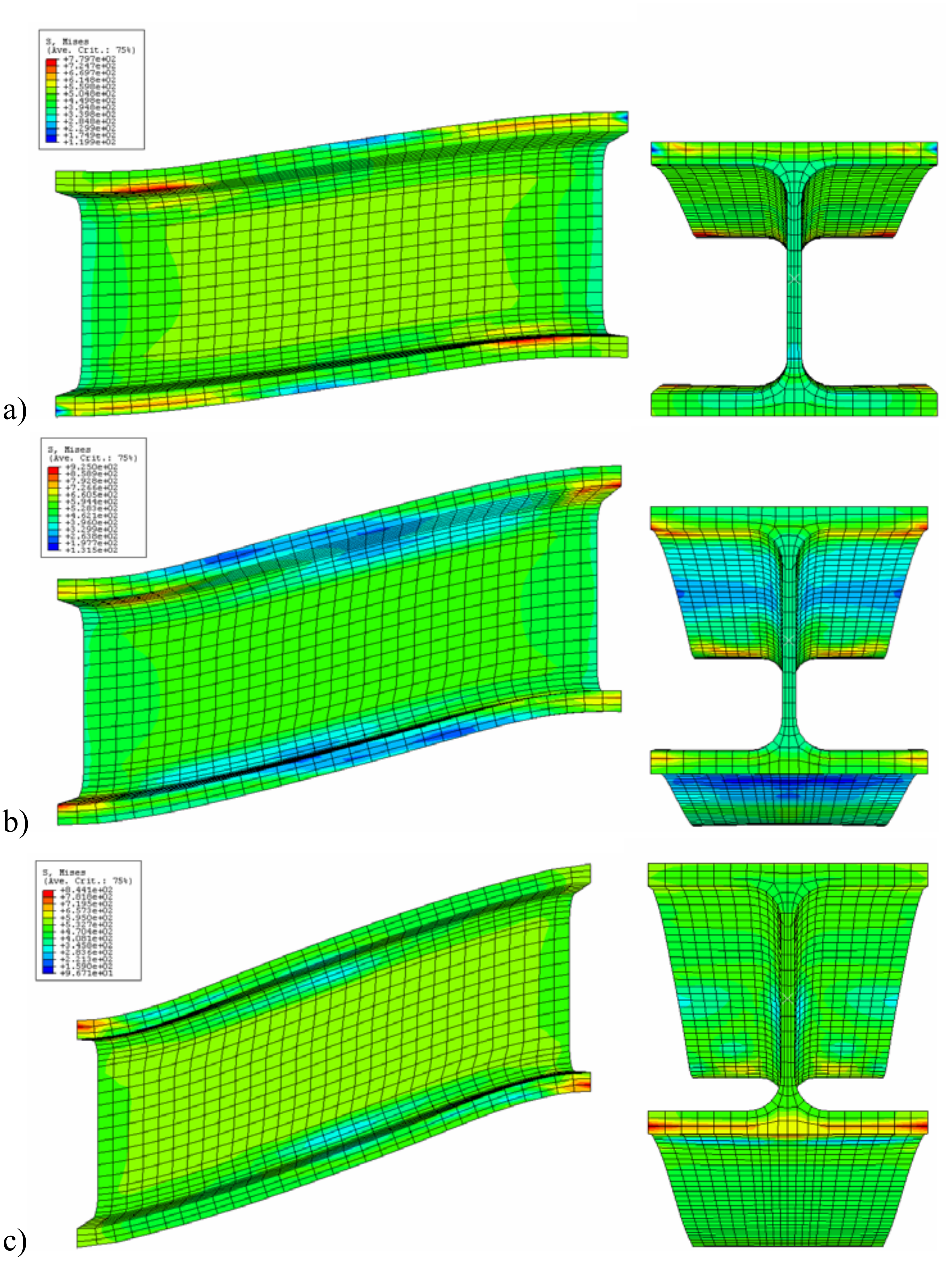

Figure 6.21. Deformed shape with relevant stress trend for model type c (EBs-Test No.2): 0.10 rad (a); 0.20 rad (b); 0.30 rad (c).

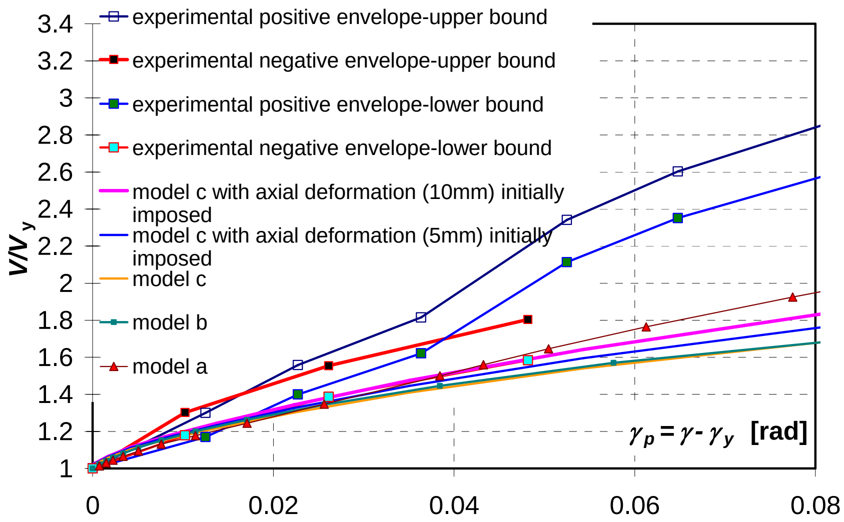

Figure 6.22. Normalized shear force vs. plastic shear deformation angle of HEA100 link for different link end restraining conditions (EBs-Test No.2).

Finally it was simulated the cyclic response of the tested HEA100 link applying the same loading protocol of the experimental test on the RC building (see Figure 4.28b in Chapter IV). To do this it was applied a displacement pattern at the reference point RP-A of the model type-c (Figure 6.15 c) reproducing the experimental loading protocol in terns of shear link rotations. Moreover, in order to evaluate the influence of the initial pre-stressing in the link response, two different models have been analyzed:

1. model type-c without initial pre-stressing;
2. model type-c with an initial imposed axial lengthening of 10mm.

The results are summarized in Figure 6.23, where the normalized link shear force is related to its relevant shear deformation. In particular, it can be easily recognized that the initial tensile pre-stressing permits to achieve shear over-strength of about 3 at a shear deformation of about 0.10 radians. Moreover, notwithstanding the deformability of the link end restraints and without an initial imposed axial deformation, it can be achieved shear over-strength larger than 2 at 0.10 radians, that it is anyway larger than the usual recommended value of 1.5. However, another reason that can brought out this effect can be found in the Baushinger phenomenon, namely in the isotropic and kinematic hardening that is typical of steel material. In fact, in the technical literature (Dusicka et al. 2007) these phenomena can generate an increase of about 20÷30% of the plastic steel monotonic strength. In particular, referring to the American steel C345 (that is similar to the European S355) Dusicka et al. 2007 founded that the maximum cyclic stress was dependent on the strain amplitude with a potential increase of the cyclic stress up to $2f_{ya}$ (i.e. the average steel yielding stress) corresponding to a strain amplitude of 7%. In addition, they discovered that lower is the steel yield stress and larger is the final steel hardening.

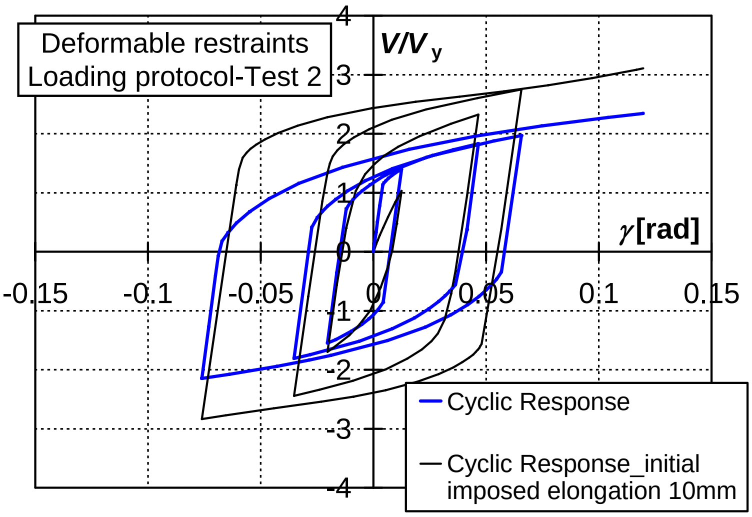

Figure 6.23. Cyclic response of HEA100 link under the experimental loading protocol (EBs-Test No.2).

Finally, in order to better interpret the experimental evidence the envelope curve of a numerical cyclic pushover of the tested building has been compared with the experimental one and with a numerical monotonic pushover curve. The numerical pushover response has been obtained by summing the ordinates of the positive envelope of the cyclic response of the model type-c with pre-stressing (Figure 6.23) with the ordinates of a pushover curve performed on both undamaged and damaged bare RC unit by means of SAP2000 (as shown in Chapter IV) characterized by a floor displacement equal to the link transverse displacement. This approach is justified by the fact that the slab axial deformation is negligible. In addition, the same numerical pushover curve has been obtained in case of monotonic numerical response of the examined link. These response curves have been summarized in Figure 6.24. This plot interestingly shows that the experimental curve manifested a lateral capacity little larger than the numerical cyclic curve and significantly larger than the monotonic curve. However, the difference between the curves is mainly due to the fact that the pinching behaviour of the RC structure has been neglected.

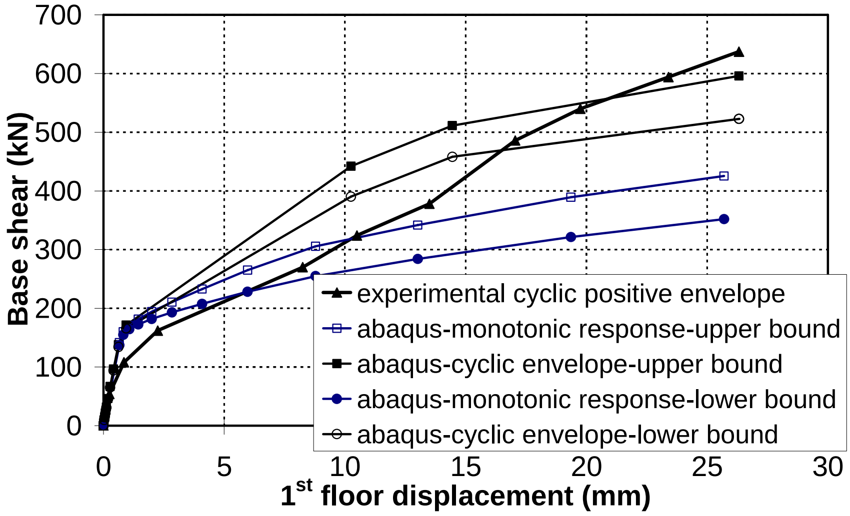

Figure 6.24. Comparison between numerical and experimental cyclic pushover response of HEA100 (EBs-Test No.2).

Modelling and analysis of built-up link (3rd tested EB)

Figures 6.25a,b,c illustrate the geometry of the F.E. model of the link that has been the object of the third test on EBs. The shear link was made of a built-up profile constituted by 90mm x 10mm rectangular plates for flanges and 80mm x 4mm rectangular plate for the web, with a length of 220 mm.

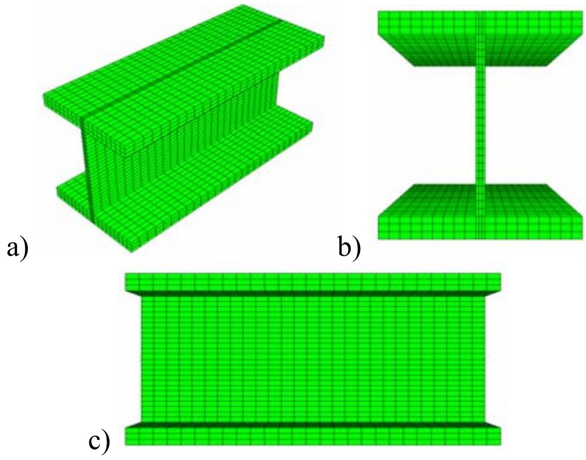

Figure 6.25. Geometric model of built-up link (EBs-Test No.3).

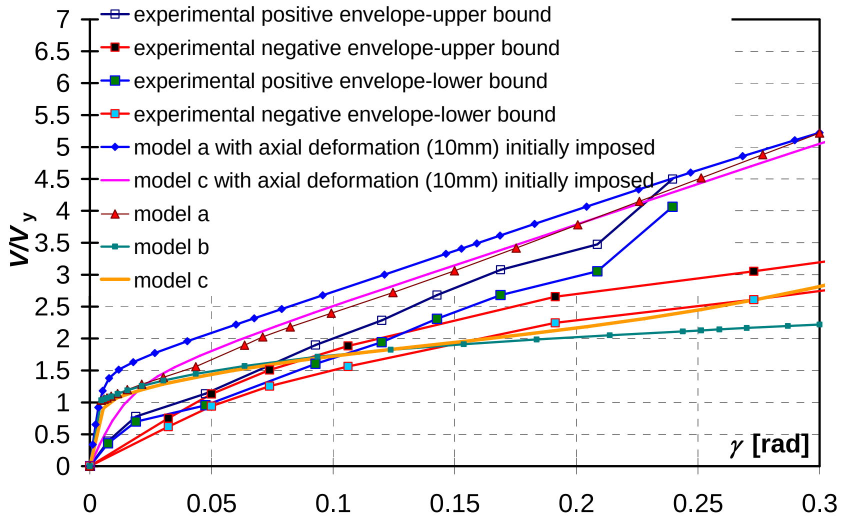

Figure 6.26. Normalized shear force vs. shear deformation angle of built-up link for different link end restraining conditions (EBs-Test No.3).

Similarly to the previous link, the presence of axial restraints significantly influences the overall link response. Once again the relationship between the normalized shear force (V/V_y) and the shear deformation angle has been plotted (Figure 6.26), for the three different restraining conditions (a,b and c) compared with the experimental backbone response curves computed a posteriori as explained in Chapter IV . In this case, only the effect of 10mm pre-imposed axial lengthening has been considered. In particular, in order to clarify in which term a different grade of axial restraint could affect the final over-strength, the 10mm axial deformation has been imposed to the model type a and to the model type c. It is interesting to notice that both models showed the same shear over-strength for large deformations. Moreover, under monotonic loading the analyzed link can achieve without local failure large shear over-strength, in particular, up to 5.2 times the shear yield strength at 0.30 rad.

Figure 6.27 summarizes the link shear over-strength (V/V_y) related to the plastic shear deformation angle $\gamma_p=\gamma-\gamma_y$ in the range of [0 rad; 0.8 rad]. In detail, similarly to the previous case, the link shear over-strength (V/V_y) varies in a range of 1.7÷2.6 at an overall shear plastic deformation of 0.08 radians for different link end restraining conditions.

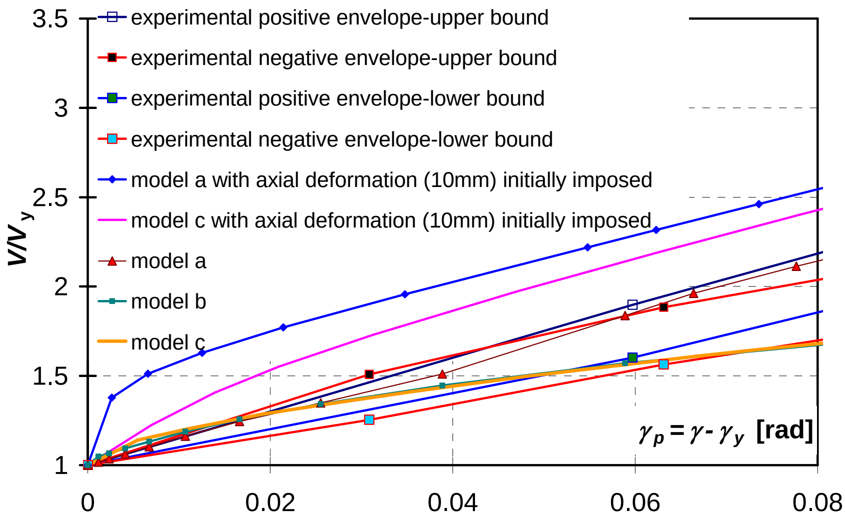

Figure 6.27. Normalized shear force vs. plastic shear deformation angle of HEA100 link for different link end restraining conditions (EBs-Test No.2).

Once more, similarly to the previous case, the deformed shapes corresponding to 0.10 radians, 0.20 radians and 0.30 radians are respectively shown with the relevant Von Mises stress trends per model a and c in Figures 6.28 and 6.29.

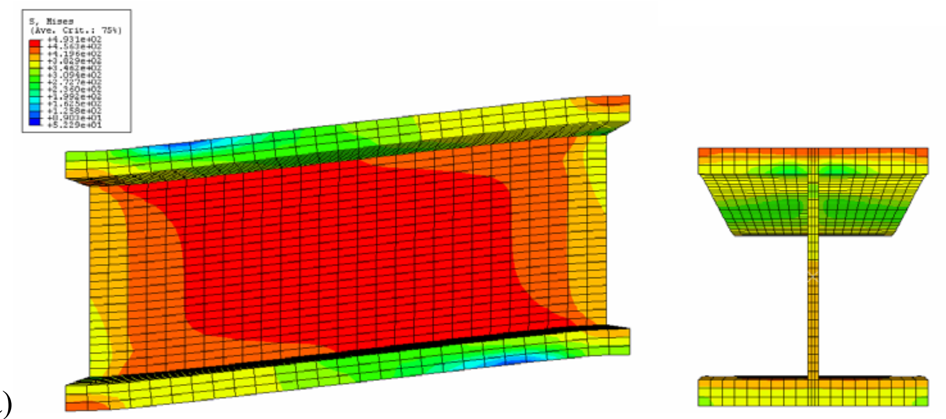

a)

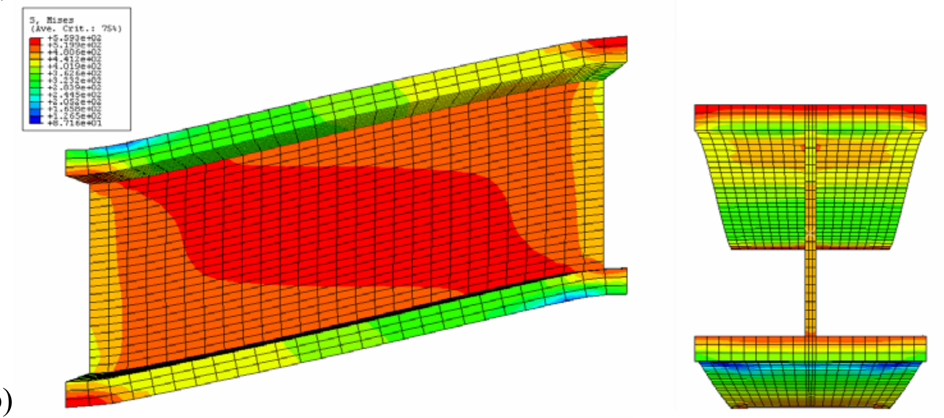

b)

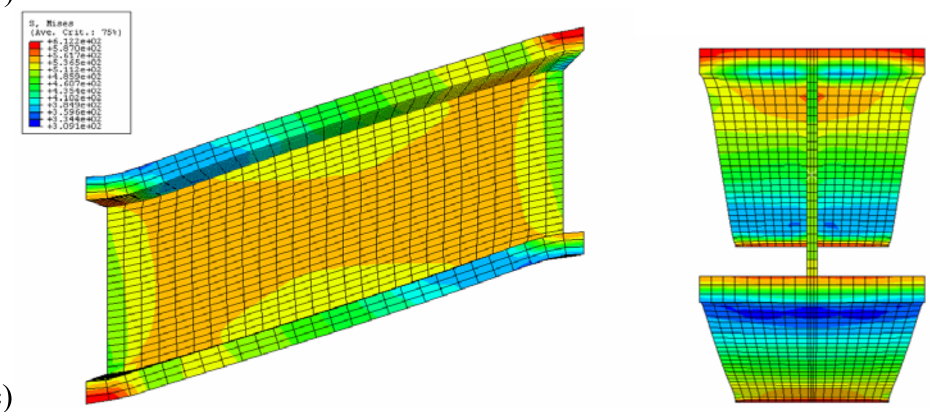

c)

Figure 6.28. Deformed shape with relevant stress trend for model type a (EBs-Test No.3): 0.10 rad (a); 0.20 rad (b); 0.30 rad (c).

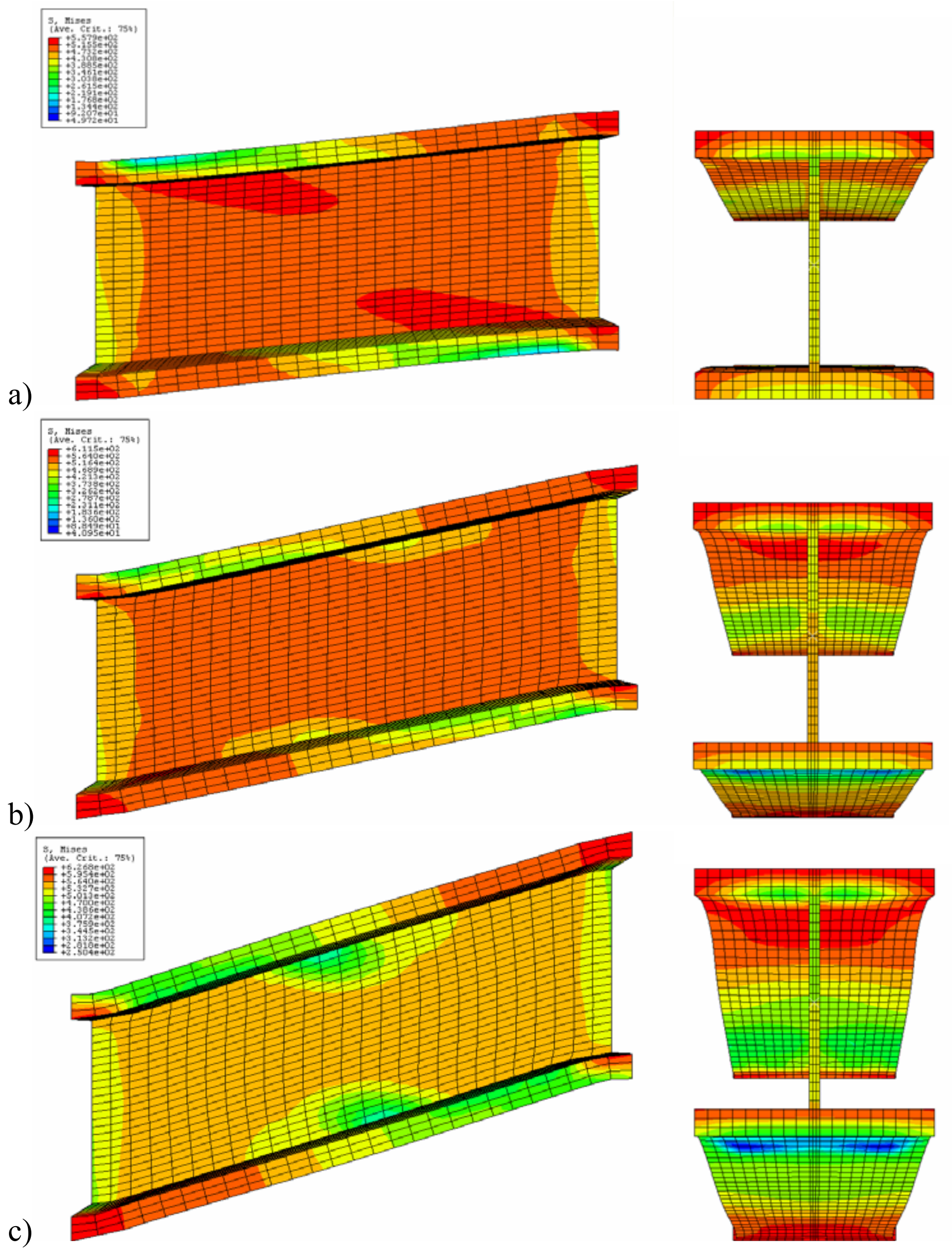

Figure 6.29. Deformed shape with relevant stress trend for model type c (EBs-Test No.3): 0.10 rad (a); 0.20 rad (b); 0.30 rad (c).

Finally it was simulated the cyclic response of the tested built-up link applying the same loading protocol of the experimental test on the RC building (see Figure 4.36b in Chapter IV). To do this it was applied a displacement pattern at the reference point RP-A of the model type-c (Figure 6.15 c) reproducing the experimental loading protocol in terns of shear link rotations. Moreover, in order to evaluate the influence of the initial pre-stressing in the link response, two different models have been analyzed:

3. model type-c without initial pre-stressing;
4. model type-c with an initial imposed axial lengthening of 10mm.

The results are summarized in Figure 6.30, where the normalized link shear force is related to its relevant shear deformation. In particular, it can be easily recognized that the initial tensile pre-stressing permits to achieve shear over-strength of about 2.5 at a shear deformation of about 0.10 radians. Moreover, notwithstanding the deformability of the link end restraints and without an initial imposed axial deformation, it can be achieved shear over-strength larger than 2 at 0.10 radians, that it is anyway larger than the usual recommended value of 1.5.

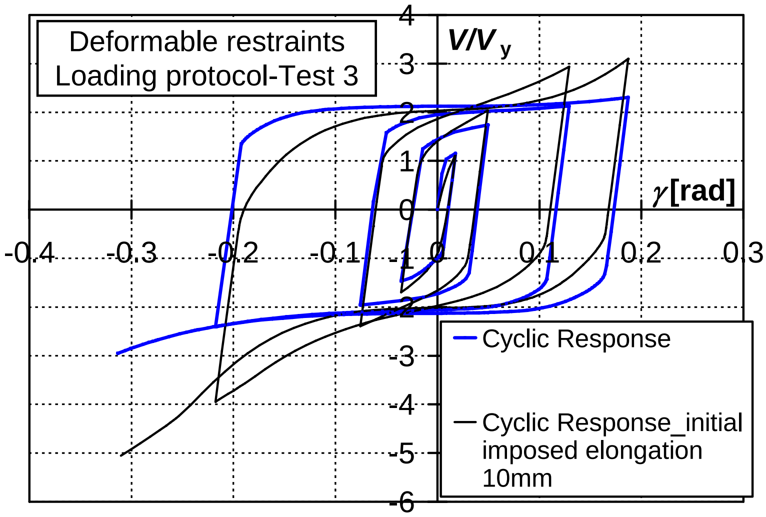

Figure 6.30. Cyclic response of built-up link under the experimental loading protocol (EBs-Test No.3).

Finally, in order to better interpret the experimental evidence the envelope curve of a numerical cyclic pushover of the tested building has been compared with the experimental one and with a numerical monotonic pushover curve. As in the case of the HEA100, the numerical pushover response has been obtained by summing the ordinates of the positive envelope of the cyclic response of the model type-c with pre-stressing (Figure 6.30) with the ordinates of a pushover curve performed on both the undamaged and damaged bare RC unit by means of SAP2000 (as shown in Chapter IV) characterized by a floor displacement equal to the link transverse displacement. This approach is justified by the fact that the slab axial deformation is negligible. In addition, the same numerical pushover curve has been obtained in case of monotonic numerical response of the examined link. These response curves have been summarized in Figure 6.31. This plot interestingly shows that the experimental curve manifested a lateral capacity little larger than the numerical cyclic curve and significantly larger than the monotonic curve. However, the difference between the curves is mainly due to the fact that the pinching behaviour of the RC structure has been neglected.

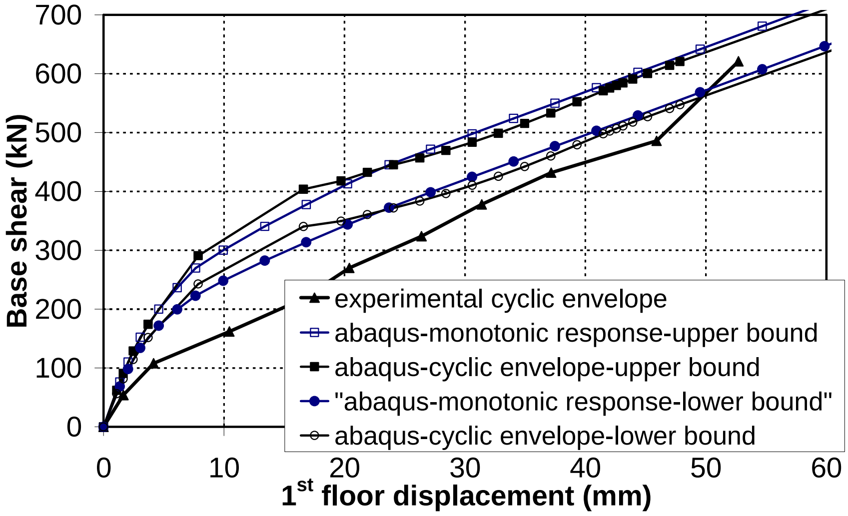

Figure 6.31. Comparison between numerical and experimental cyclic pushover response of built-up (EBs-Test No.3).

Analytical prediction of link shear over-strength

At the light of results of finite element analyses, it can be concluded that the presence of the axial restraint is the main responsible of the anomalous link shear over-strength. In fact, the presence of an axial tensile reaction requires an increase of a second order shear force in order to guarantee the overall rotational balance of the forces acting on the link. Hence, as shown in Figure 6.32, this second order shear is not related to an increase of bending moment, but it is related to global moment due to the tensile axial reaction that is moved from the middle of the gross section by the first order bending moment at both link ends.

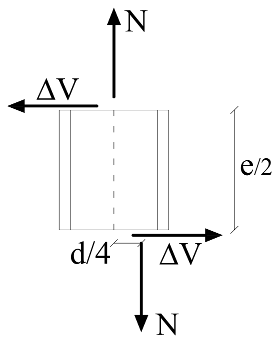

Figure 6.32. Analytical modelling of inelastic link forces.

As noted previously, the axial force in the link starts to develop appreciable values only after web yielding. In the range of interest of the plastic shear deformation angle $\gamma_p=\gamma-\gamma_y$ [0 rad; 0.8 rad], Equation 61 is proposed for simulating the trend of axial force in a link with perfect axial restraints at both ends:

$$\frac{N}{N_p}=\left(\frac{\left(\gamma_p/0.10\right)^2}{1+\left(\gamma_p/0.10\right)^2}\right)^{2/3} \qquad (61)$$

where values of the parameters involved in the Equation 61 have been empirically calibrated against the results of the HE A 100 shape.

From the free body diagram of forces drawn in Figure 6.32 it is possible to calculate the increment of the shear force in the inelastic range ΔV obtained from following equilibrium Equation:

$$\Delta V = \frac{Nd}{2e} \tag{62}$$

Therefore, the link over-strength factor is given by Equation 63:

$$\frac{V}{V_y} = \frac{\alpha V_y + \Delta V}{V_y} = \alpha + \frac{Nd}{2V_y e} \tag{63}$$

The parameter α takes into account the effect of the steel hardening and it is consequently necessary for a good matching of numerical results, now assumed equal to 1.1.

In case of HEA100 the predicted shear over-strength (Figure 6.33) is 2.02, while the numerical one is 1.95 with a scatter in excess of 3.6%. In case of built-up link the predicted shear over-strength (Figure 6.34) is 2.38, while the numerical one is 2.22 with a scatter in excess of 7.5%.

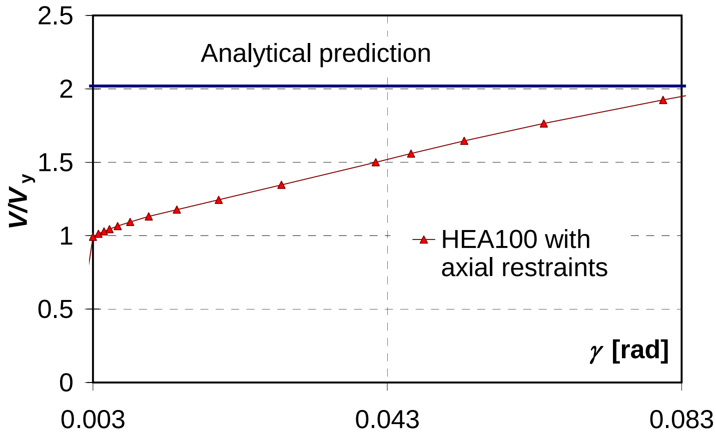

Figure 6.33. Analytical prediction vs. Numerical result (HEA 100).

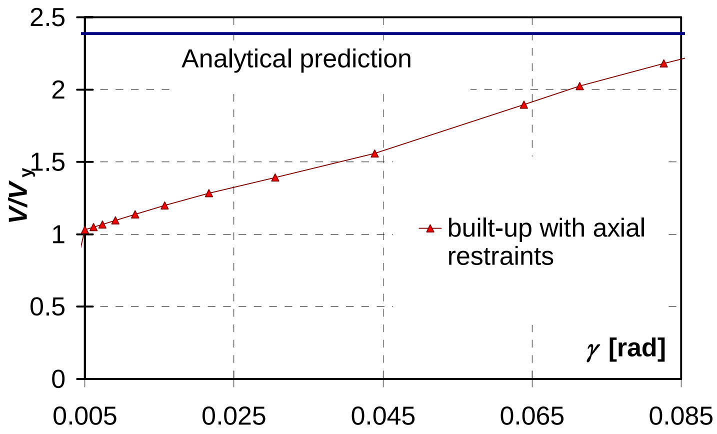

Figure 6.34. Analytical prediction vs. Numerical result (Built-up).

6.3 NUMERICAL MODELLING OF THE RC STRUCTURE EQUIPPED WITH BUCKLING-RESTRAINED BRACES

The bare RC structure has been modelled on the basis of the results dealt with in the Section 6.2.1. In fact, based on the measured elastic-vibration data a numerical model of the building has been implemented in SAP2000, as shown in Figure 6.35.

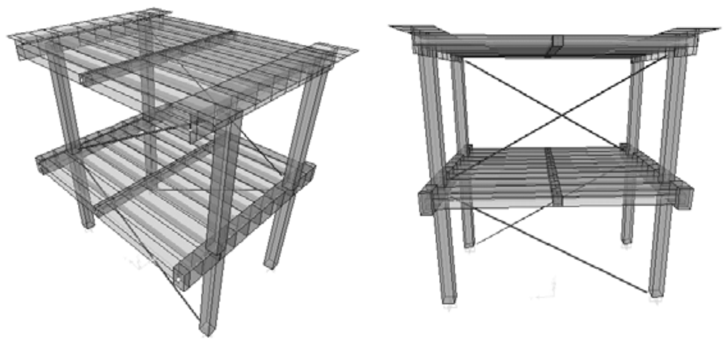

Figure 6.35. Numerical model of the RC unit with BRBs (SAP2000).

Average mechanical properties of structural materials (concrete and steel) have been used. In order to take into account the effect of RC cracking on the lateral stiffness, an effective second moment of area has been assumed for beams and columns. The suggestions of FEMA 356 (2000) were initially adopted to reduce elastic properties of RC members. The experimental evidence showed that the first mode of vibration was mainly translational in the transverse (unbraced) direction; the second mode was mainly translational in the braced direction and, finally, the third mode was essentially torsional.

Figure 6.36 illustrates that good agreement was firstly achieved between experimental and numerical results with reference to the first vibration mode (in the unbraced direction). But significant differences revealed for the second vibration mode (in the braced direction) and also for the third mode (torsion). Hence, in order to correct the second period prediction, the cross-section area of BRBs was increased, considering one single cross-section area composed of the internal core and restraining tube. The reason may be found in the fact that during vibration tests the axial force in the braces did not exceed the friction resistance at the interface between the restraining tubes and the internal core. The calibrated model was finally obtained by adopting the reduction factors of gross second moment of area for RC shown in Table 6.3.

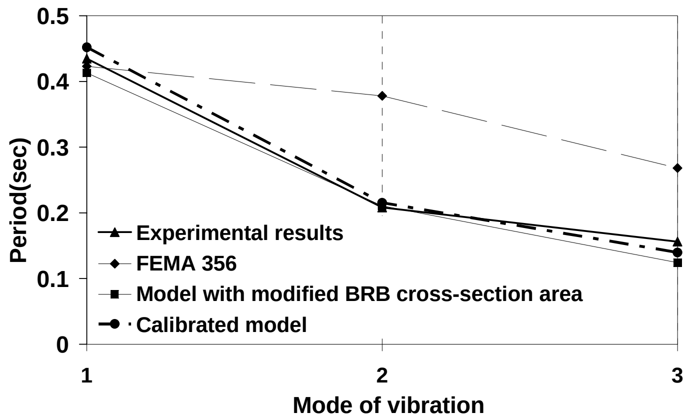

Figure 6.36. RC unit with BRBs: fundamental periods of numerical models vs experimental ones.

Table 6.3. Reduced stiffness for RC members.

		Flexural stiffness	Shear stiffness
beam	FEMA 356	0.50 I_g	0.40 A_v
	Calibrated model	0.40 I_g	0.50 A_v
column	FEMA 356	0.70 I_g	0.40 A_v
	Calibrated model	0.60 I_g	0.50 A_v

Figure 6.37 shows the modal shapes of the braced RC structure as results of the calibrated numerical model.

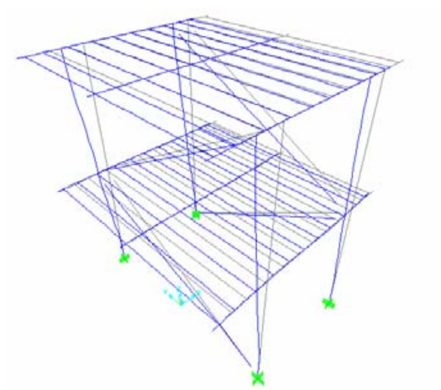

1st mode of vibration (T = 0.4520s)

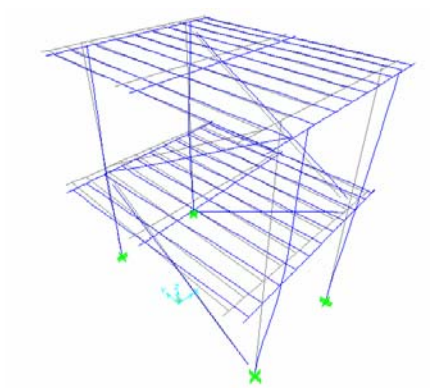

2nd mode of vibration (T = 0.2155s)

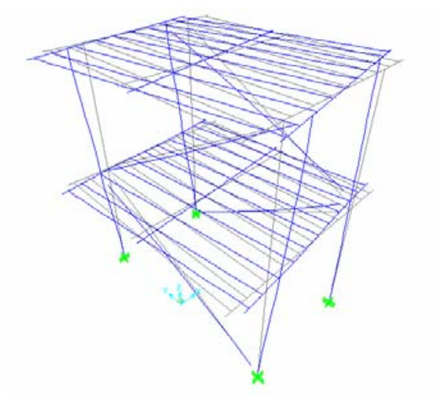

3rd mode of vibration (T = 0.1398s)

Figure 6.37. Modal shapes of braced RC structure.

Once characterized the elastic behaviour of the braced structure, in order to get an effective and reliable numerical model the main topic was to characterize the non linear behaviour of dissipative members (i.e inner cores of BRBs) and the failure modes of non-dissipative ones as well. Since during each pushover test the principal structural subcomponents (i.e. the BRBs) have not been monitored, a simplified approach was pursued in order to minimize the number of parameters to be calibrated. Hence, the tested BRB members were modelled with a truss element using a bilinear force–displacement relationship to simulate hardening. Obviously, the brace core inelastic properties have to be adopted to get a correct prediction of the structure capacity (D'Aniello et al. 2006).

In case of the first test modelling, a preliminary simplified model has been implemented in SAP2000, in order to have an initial esteem of the lateral capacity of the retrofitted RC structure. The main assumptions of this model were:

- elastic perfectly plastic behaviour of BRBs;
- no differences in tension and compression axial strength of BRBs;
- no cracking in the RC structure.

This initial model confirmed the design target i.e. BRBs yielded and started dissipating energy far before the formation of plastic hinges in columns and beams of the RC frame (Figure 6.39, "preliminary model").

Then, since the first test has shown significant over-strength, the studied structure has been modelled to consider this important aspect. Because the failure mode of tested BRBs in compression has been governed by the flexural hinging of terminal plates and the flexural failure of end closing plates (Figure 4.41, Chapter IV), the force-deformation relationship of braces was surely affected and distorted. However, a simplified approach has been followed for schematizing the force-deformation relationship. In fact, the simplified model differs from the preliminary one in the following aspects:

1) axial plastic hinges of BRBs are characterized by a bi-linear force-deformation relationship;

2) a difference of 10% in tension and compression axial strength of BRB members has been assumed;

3) cracking in the RC structure has been taken into account.

In particular, the post-elastic stiffness of the force-deformation relationship of axial plastic hinges of BRBs was assumed equal to 3% of the elastic one (Tsai et al. 2004a,b).

This simplified approach revealed a good agreement with experimental results within the elastic field of structural response, but it underestimated the inelastic capacity of the tested structure (Figure 6.39, "simplified model").

Finally, in order to calibrate the numerical response to the experimental one, a third model has been implemented. The improved model is based upon the main assumptions of the previous one. In fact, it differs only in the value of the post-elastic stiffness of the force-deformation relationship of axial plastic hinges of BRBs. Thus, with a trial-and-error process, the strain hardening stiffness of the truss model was calibrated on the experimental pushover curve. It was finally fixed as 5% of the initial brace stiffness. This modelling approach adequately predicted the experimental global response, as shown in Figure 6.39. Moreover, this numerical model confirmed the magnitude of BRB local ductility at peak response. In fact, the maximum computed brace ductility μ (at the first floor) was equal to 5.02 (close to the value established on the experimental basis).

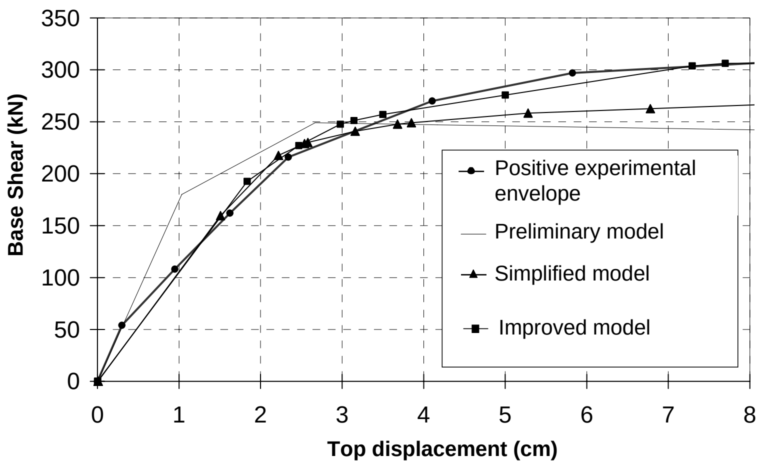

Figure 6.39. Numerical response curves vs. experimental backbone curve (BRBs Test No.1).

The preliminary model and the simplified model of the second BRB structure were substantially equal to those adopted for simulating test No.1. In fact, the modelling hypotheses were the same as those of the previous case, while the elastic stiffness and yielding strength of the second type of tested BRBs did not appreciably differ from those of the first type.

Then, because during the second test the local buckling failure of one end plate at the first story occurred (Figure 4.49, Chapter IV), the structure has been modelled to take into account this event. The calibrated model was defined considering the tensile brace at the first floor with an initial lateral deflection equal to the value measured during the test (about 85mm), as shown in Figures 6.40a,b.

Moreover, the test put in evidence the local buckling of the internal core in compression notwithstanding the restraining action of tube walls. This phenomenon influenced the axial response of BRB in compression. So, if the post-elastic stiffness of BRB in tension was assumed equal to 2.5% of the elastic one (Black et al. 2002, Tsai et al. 2004a), the post yield branch in compression was derived by calibrating the response curve with a trial-and-error process and finally assumed equal to 9% of the elastic axial stiffness.

As shown in Figure 6.41, this model adequately predicted the initial elastic stiffness and the final strength and stiffness. Once again, the improved model confirmed the magnitude of BRB local ductility at peak response. In fact, the maximum computed brace ductility μ (at the first floor) is equal to 14.33 (close to the value coming from test results).

Differences between the numerical and experimental response curves in the post-elastic range are mainly due to the difficulties in predicting the response of the RC structure, which was significantly damaged in the first test (on BRB system No.1), as well as to the difficulties in interpreting and modelling the several local failure mechanisms occurred in the bracing system.

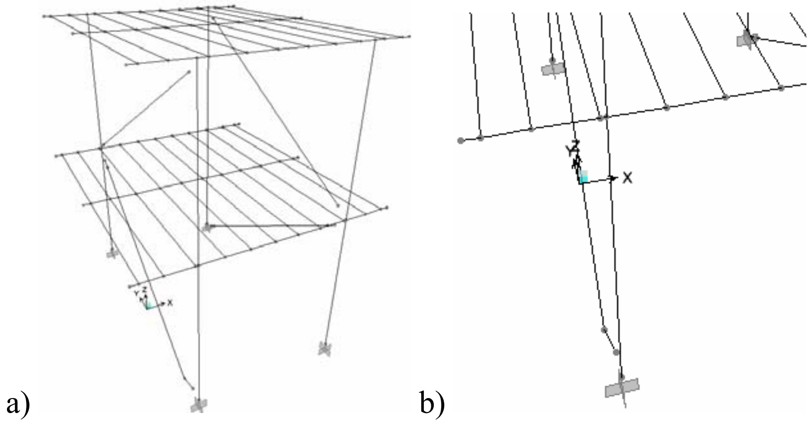

Figure 6.40. Numerical model (a) calibrated on test No.2 and particular (b) of modelled brace at 1st floor.

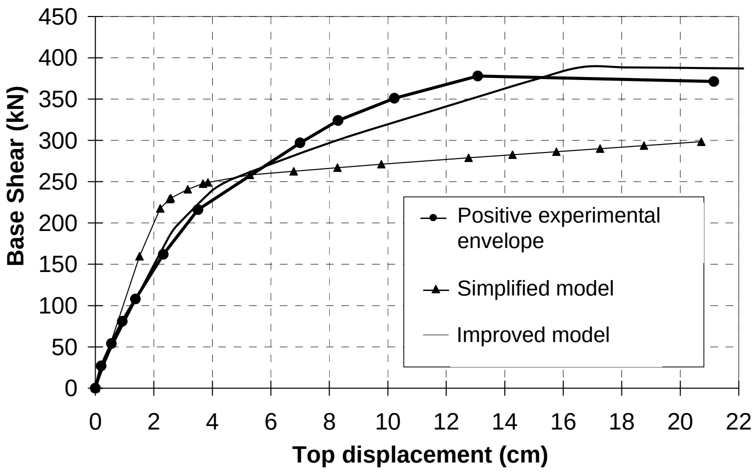

Figure 6.41. Numerical response curve vs. experimental backbone curve (BRBs Test No.2).

6.4 NON LINEAR DYNAMIC ANALYSES OF RETROFITTED RC STRUCTURAL UNITS

6.4.1 Seismic hazard assessment

The investigated RC structures are located in the ex-industrial area of the Bagnoli district of Naples (Italy), where the expected PGA is about 0.25g.

The 2-storey reinforced concrete building structure was designed and constructed for resisting mainly vertical loads, according to old structural codes, without considering the seismic action. As a consequence, it was characterized by significant lacks in local details and in its structural concept. However, it was well designed and constructed for its time, and has been carefully maintained over its life. Hence, the question is in which terms the structure can overcome seismic events as it is and how the presence of EBs or the presence of BRBs can improve the overall structural performance.

Thus, a set of 8 accelerograms, compatible with the Italian spectrum for PGA of 0.25g and soil type C, has been used. In Figure 6.42 the response spectra of these accelerograms are compared to the Italian elastic response spectrum of Italian code (OPCM3431). Moreover, the El Centro North-South (NS) and the East-West (EW) acceleration records have been adopted. In particular, these accelerograms have been scaled with the factor (0.718) in order to make them compatible with the Italian elastic response spectrum.

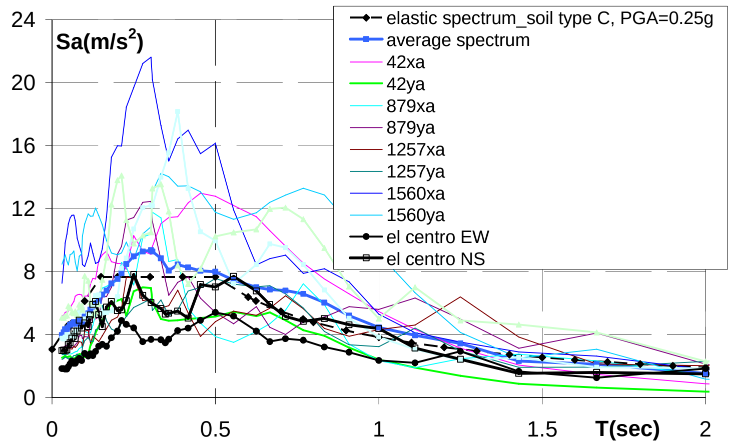

Figure 6.42. Comparison of response spectra of adopted accelerograms with elastic spectrum of Italian code.

6.4.2 Basic modelling assumptions

Differently from the 3D numerical models defined in the previous Sections 6.2.2 and 6.3.1, 2D models have been adopted. In fact, a 2D model reduces the computational time and it is easier to be defined and managed in post-processing phase. Hence, the modelling effort was directed to reproduce with a 2D model the same response of the whole 3D model of the structure. However, the first step has been the characterization of nonlinear properties of structural elements in order to properly carry out a set of non-linear dynamic time history analyses. Hence, the non-linear hysteretic properties have been reproduced by introducing into the model the so-called "non-linear links" available in SAP2000. In case of RC members, the inelastic behaviour has been lumped in zero-length "non-linear links" placed at both element ends, adopting the hysteretic Takeda-Pivot model to simulate their inelastic cyclic response. Shear links of EBs and BRBs were modelled using "non-linear link" elements too. In particular, in case of BRBs the Bouc-Wen model (see Chapter II) with "*n*"=1 has been assumed for all force-displacement hysteresis relationships with 2.5% of post-yield to elastic stiffness ratio. Moreover, the tension strength was calculated from the cross-sectional area assuming no material over-strength.

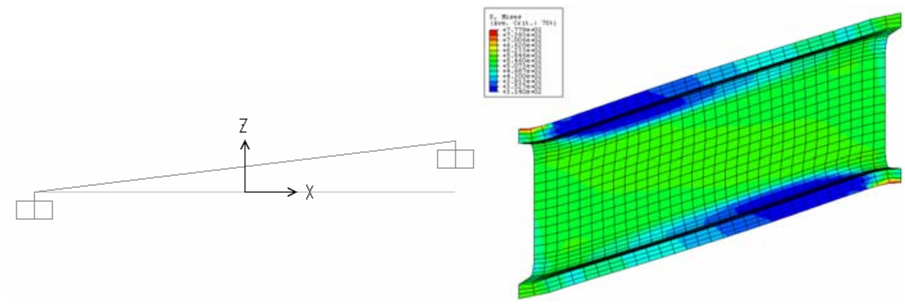

Figure 6.43. Numerical model of Y-inverted steel link: SAP2000 (a); ABAQUS 6.5 (b).

EBs were modelled using "non-linear link" elements too, but in this case, a preliminary study has been performed in order to correctly predict their inelastic response. To simulate the hysteretic link behaviour, the Bouc-Wen model has been adopted. In particular, the shear force vs. deformation relationship in the model implemented in SAP2000 has been calibrated on the basis of the results of the finite element analyses carried out by means of the commercial software ABAQUS 6.5. Figure 6.43 shows the displacement shapes of link modelled in SAP2000 (Figure 6.43a) and in ABAQUS (Figure 6.43b). In Figure 6.44 this aspect is clearly shown comparing the hysteretic Bouc-Wen model (characterized by "*n*"=2) with the F.E. monotonic link response.

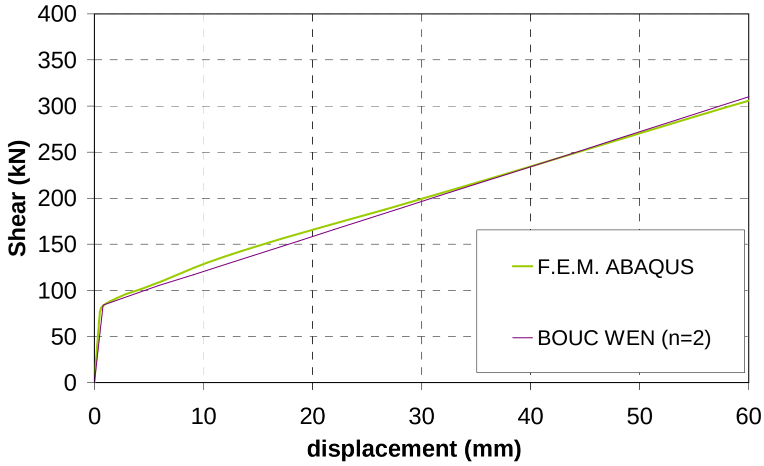

Figure 6.44. Calibration of Bouc-Wen model with F.E.M monotonic response (ABAQUS 6.5) to simulate the inelastic behaviour of EBs.

As above mentioned, it was investigated how simulating the influence of floor joists into a 2D model. Hence, assuming the RC unit equipped with BRBs as example, several models have been developed in order to test which is the minimum number of floor joists that effectively influence the lateral response of the structure. Because of the structural symmetry, it was initially possible to model half part of the structure that gives the same response of the model of the whole structure. Starting from this simplified approach, several models have been analyzed reducing the number of floor joists. Figure 6.45 clearly shows that at least two floor joists needs to be considered for predicting the lateral response. Moreover, all numerical models showed that all floor joists remain elastic, with a formation of weak column-strong beam mechanism under lateral loads. This consideration led to develop a simplified

2D model, characterized by an elastic beam with a flexural stiffness equivalent to two joists.

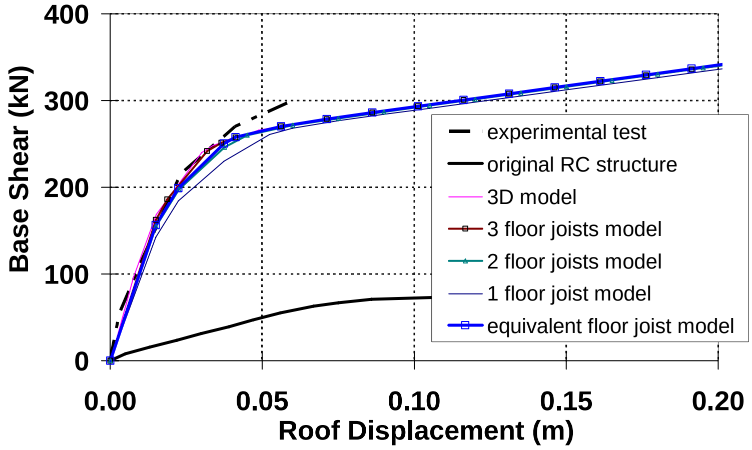

Figure 6.45. Comparison of simplified model reducing the number of floor joists.

Similarly, Figure 6.46 shows the comparison of numerical pushover curve of 2D model of RC with EBs with the three relevant experimental response curves. As it can be seen, the numerical initial stiffness matched quite well the experimental one, while the numerical lateral strength is intentionally underestimated in order to increase the seismic demand.

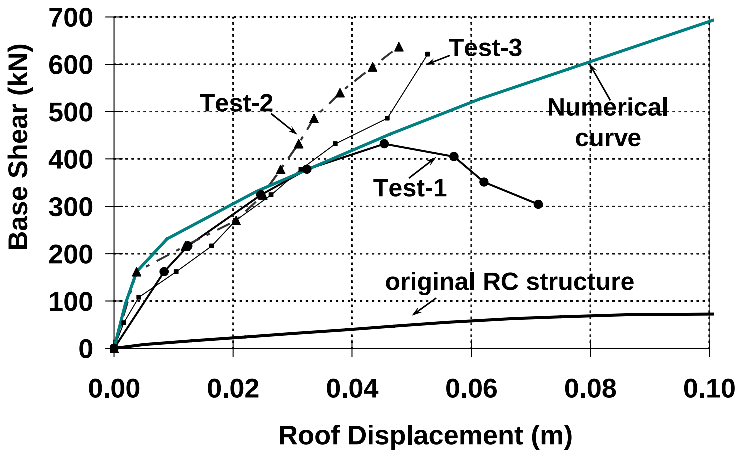

Figure 6.46. Comparison of 2D model with experimental response of EBs.

Furthermore, the masses were lumped in the floor centroid. The effective seismic weight of each floor included the total dead load (assuming an additional dead load of $0.5\ \mathrm{kN/m^2}$) and 15% of the live load ($2.5\ \mathrm{kN/m^2}$ was assumed).

6.4.3 Analysis results of the real unbraced structure

All inelastic analyses clearly showed that only the columns are damaged. In particular, referring to Figure 6.47 Table 6.4 summarizes the plastic rotation demands. Moreover, maximum interstory drift ratios for the first and the second floor are given in Tables 6.5 and 6.6, respectively.

The assessment of the structural elements is made comparing the seismic demands (plastic rotations) with the capacities for the selected performance level. According to FEMA 356 and on the basis of the column properties, the maximum plastic rotation capacity at both column ends for the performance level of collapse prevention (CP) should be taken as 0.006 (see Table 6-8 in that document). Note that, for the performance levels of immediate occupancy (IO) and life safety (LF) a plastic rotation less than 0.005 should be taken.

As shown in Table 6.4, the plastic rotation demands in columns were higher than 0.006, indicating that the columns could experience severe damage. Since in this structure the columns are the main elements able to resist lateral loads, a total collapse of the structure may be expected. Also, note that the plastic rotation demands under 42xa record is higher than 0.02 at the base of the column of the first floor.

6.4.4 Analysis results of the structure equipped with EBs

All inelastic analyses clearly showed that the whole structure remains in elastic field. This is mainly due to the high lateral stiffness of the system that significantly reduces the interstory drift ratios. This effect is clearly shown in Tables 6.5 and 6.6 summarize, where the maximum interstory drift ratios for the first and the second floor are respectively compared with those of unbraced original RC structure.

6.4.5 Analysis results of the structure equipped with BRBs

The BRBs enhance the strength, stiffness and ductility of the structure. As can be seen from Tables 6.4 through 6.6, and from Figures 6.48 to 6.57, a significant decrease of seismic demands (floor displacements, interstory drifts and plastic rotations) was achieved. The plastic engagement of BRBs is summarized in Table 6.7, where the ductility demand is reported per accelerogram record, where it can be noticed that the maximum ductility demand is about 3.61 in case of 1550ya record. Moreover, the BRB inelastic response is plotted in Figures 6.58 to 6.67 in terms of hysteretic response and axial demand vs. time per accelerogram record.

Analyzing the effect on RC members, it was noticed that the presence of BRBs significantly reduces the bending moments, a slight increase in axial force demands in the first storey columns has been observed. However, this effect does not reduce the capacity of RC columns.

6.4.6 Performance comparison

Both the bracing systems increase the strength and stiffness of the structure and they can provide a supplementary reserve of dissipation in case of more severe seismic events, absorbing a large portion of the earthquake-induced energy through link shear yielding.

In particular, because of the large stiffness and strength given by EB system, the braced structure behaves in elastic field. Another important advantage obtained when EBs were used was their very low contribution to axial force demands in the columns, and hence foundation strengthening is not required in this case.

The comparison between the response of the original RC structure and the one of the RC frame equipped with BRBs shows a significant improvement in lateral capacity, too. The main results are the significant reduction in plastic demand in RC members and a reduction of story displacements, interstory drifts, moments and shear forces. The BRBs absorb a large portion of the earthquake-induced energy through yielding in both compression and tension cycles, leaving the main structural system (columns and beams) mostly in the elastic range, thus minimizing damage in these structural members.

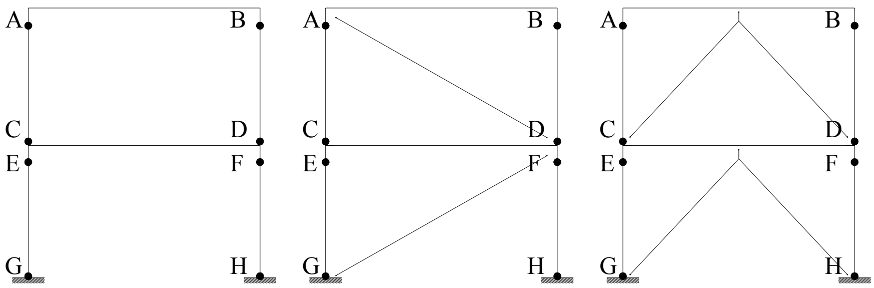

Figure 6.47. Critical plastic regions.

Table 6.4. Time history analysis results of the 2-D models: maximum plastic rotation demands

Node (Fig. 6.47)	unbraced RC structure	RC structure equipped with EBs	RC structure equipped with BRBs	
	Plastic Rotation $\Phi_p=(\Phi_r-\Phi_y)$ [rad]	Plastic Rotation $\Phi_p=(\Phi_r-\Phi_y)$ [rad]	Plastic Rotation $\Phi_p=(\Phi_r-\Phi_y)$ [rad]	Reduction of plastic demand $\Phi_{RC}-\Phi_{RC+BRB})/\Phi_{RC}$ [%]
A	0.010853	0 (=elastic behaviour)	0.001066	90.18
B	0.010746	0 (=elastic behaviour)	0.003006	72.03
C	0.00791	0 (=elastic behaviour)	0.000752	90.49
D	0.007989	0 (=elastic behaviour)	0.000638	92.01
E	0.005054	0 (=elastic behaviour)	0.00247	51.13
F	0.005004	0 (=elastic behaviour)	0.000958	80.86
G	0.021944	0 (=elastic behaviour)	0.008584	60.88
H	0.022163	0 (=elastic behaviour)	0.007694	65.29

Table 6.5. Time history analysis results of the 2-D models: 1st floor interstory drift ratios

Accelerogram	unbraced RC structure		RC structure equipped with EBs		RC structure equipped with BRBs	
	Max	Min	Max	Min	Max	Min
42xa	1.623	-2.011	0.058	-0.065	0.269	-0.212
42ya	0.767	-0.918	0.018	-0.030	0.712	-0.67
879xa	0.596	-0.662	0.038	-0.032	0.404	-0.354
879ya	0.883	-0.783	0.037	-0.043	0.343	-0.253
1257xa	0.756	-0.936	0.030	-0.029	0.3	-0.151
1257ya	1.196	-0.94	0.029	-0.028	0.323	-0.246
1560xa	1.494	-1.59	0.064	-0.083	0.618	-0.719
1560ya	1.911	-1.787	0.064	-0.099	0.499	-0.905
El Centro NS	0.968	-1.015	0.053	-0.035	0.289	-0.220
El Centro EW	0.667	-0.597	0.023	-0.023	0.211	-0.237

Table 6.6. Time history analysis results of the 2-D models: roof interstory drift ratios

Accelerogram	unbraced RC structure		RC structure equipped with EBs		RC structure equipped with BRBs	
	Max	Min	Max	Min	Max	Min
42xa	2.065	-2.603	0.041	-0.047	0.009	0.007
42ya	0.994	-1.168	0.014	-0.021	0.025	0.028
879xa	0.71	-0.885	0.029	-0.024	0.435	0.377
879ya	1.159	-0.995	0.026	-0.032	0.332	0.251
1257xa	0.995	-1.165	0.023	-0.024	0.296	0.135
1257ya	1.51	-1.194	0.023	-0.023	0.327	0.236
1560xa	2.062	-2.132	0.048	-0.064	0.64	0.907
1560ya	2.55	-2.403	0.047	-0.070	0.509	1.183
El Centro NS	1.26	-1.48	0.044	-0.029	0.293	0.223
El Centro EW	0.866	-0.794	0.017	-0.017	0.192	0.204

Table 6.7. Time history analysis results of the 2-D models: BRB ductility demand

Accelerogram	1^{st} floor	2^{nd} floor
	Δ_p/Δ_y	Δ_p/Δ_y
42xa	0.061	0.015
42ya	1.79	0.005
879xa	0.586	0.746
879ya	0.326	0.321
1257xa	0.178	0.165
1257ya	0.268	0.279
1560xa	1.82	2.70
1560ya	2.50	3.61
El Centro NS	0.113	0.136
El Centro EW	0 (=elastic behaviour)	0 (=elastic behaviour)

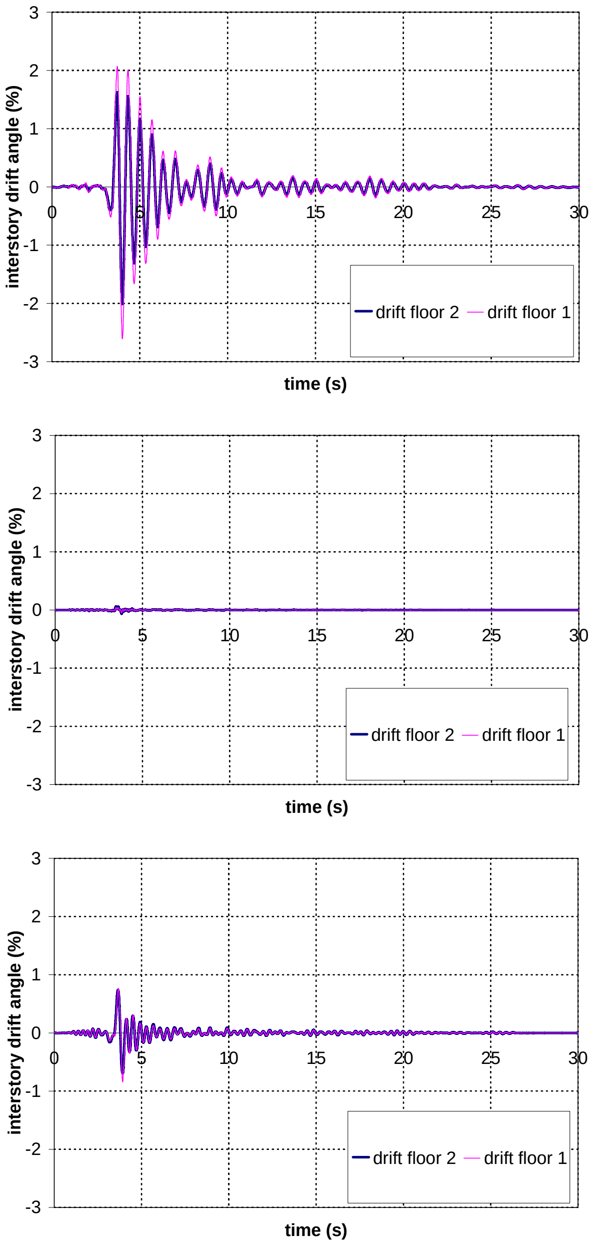

a)

b)

c)

Figure 6.48. Interstory drift vs. Time under 42xa record: original RC structure (a); RC structure equipped with EBs (b); RC structure equipped with BRBs (c).

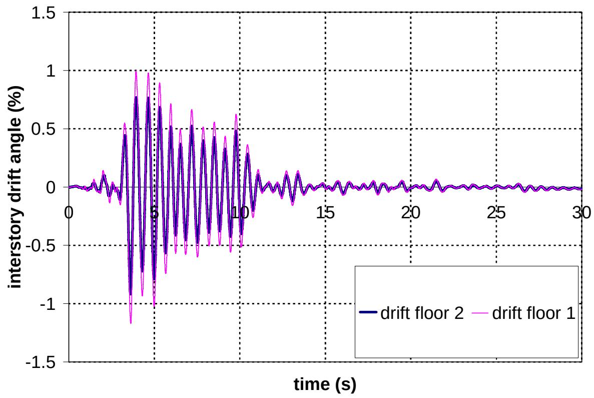

a)

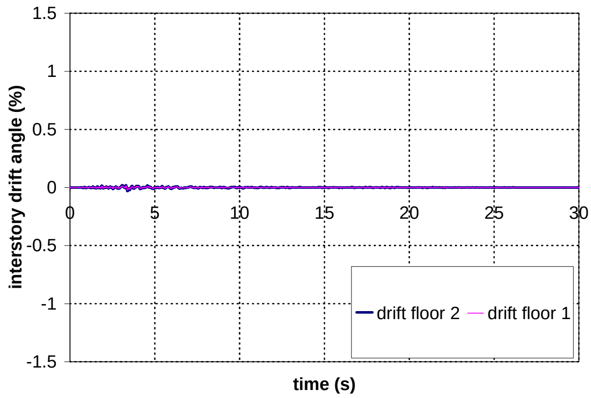

b)

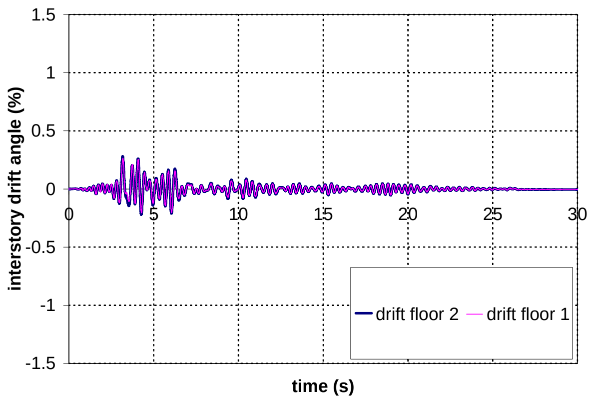

c)

Figure 6.49. Interstory drift vs. Time under 42ya record: original RC structure (a); RC structure equipped with EBs (b); RC structure equipped with BRBs (c).

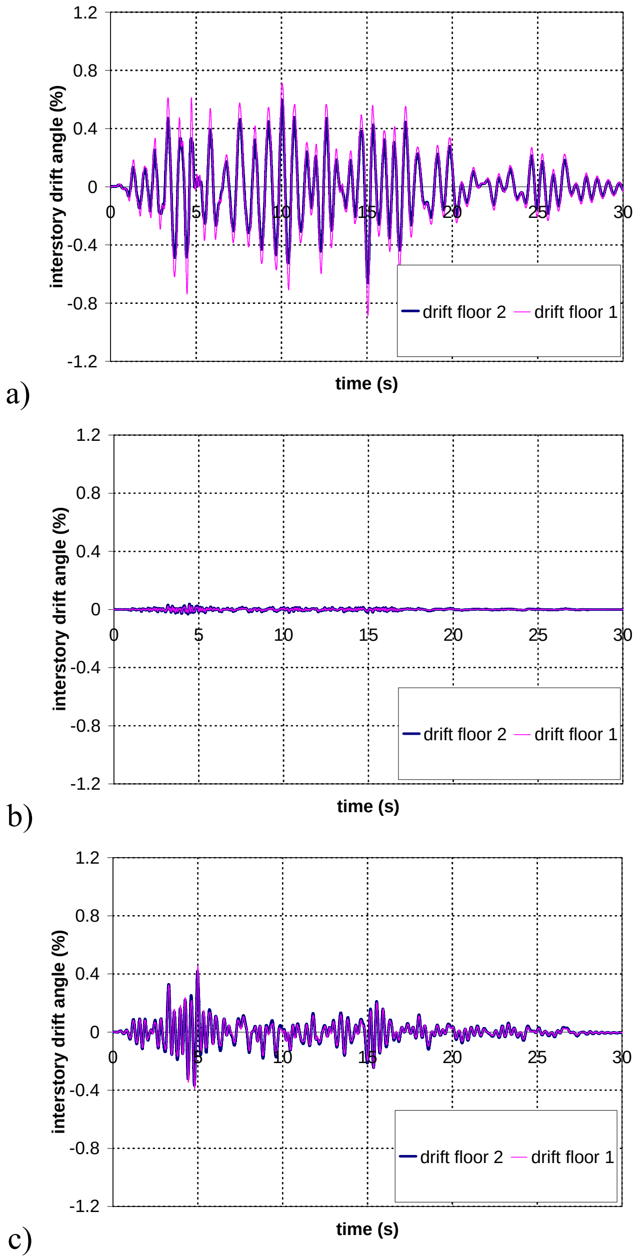

Figure 6.50. Interstory drift vs. Time under 879xa record: original RC structure (a); RC structure equipped with EBs (b); RC structure equipped with BRBs (c).

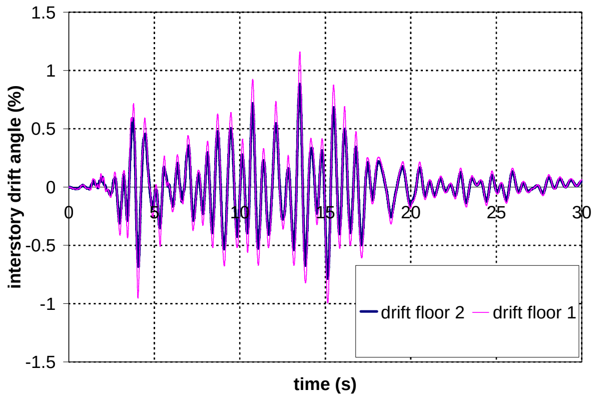

a)

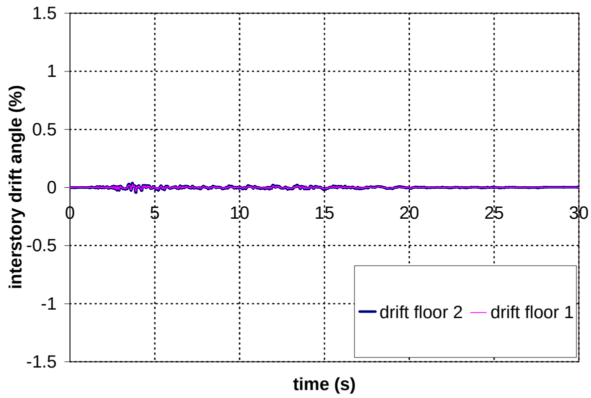

b)

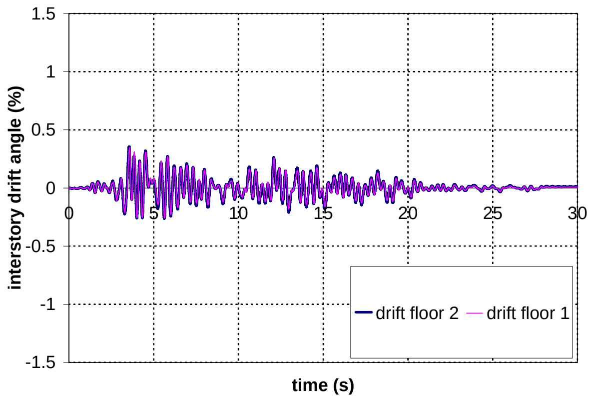

c)

Figure 6.51. Interstory drift vs. Time under 879ya record: original RC structure (a); RC structure equipped with EBs (b); RC structure equipped with BRBs (c).

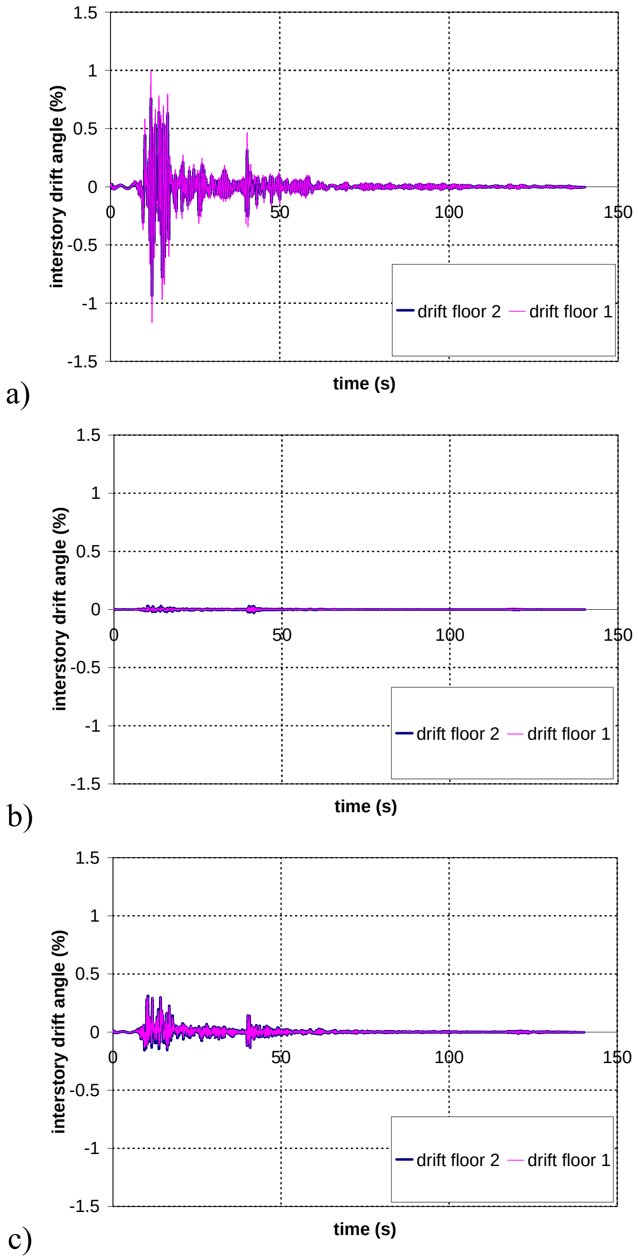

Figure 6.52. Interstory drift vs. Time under 1257xa record: original RC structure (a); RC structure equipped with EBs (b); RC structure equipped with BRBs (c).

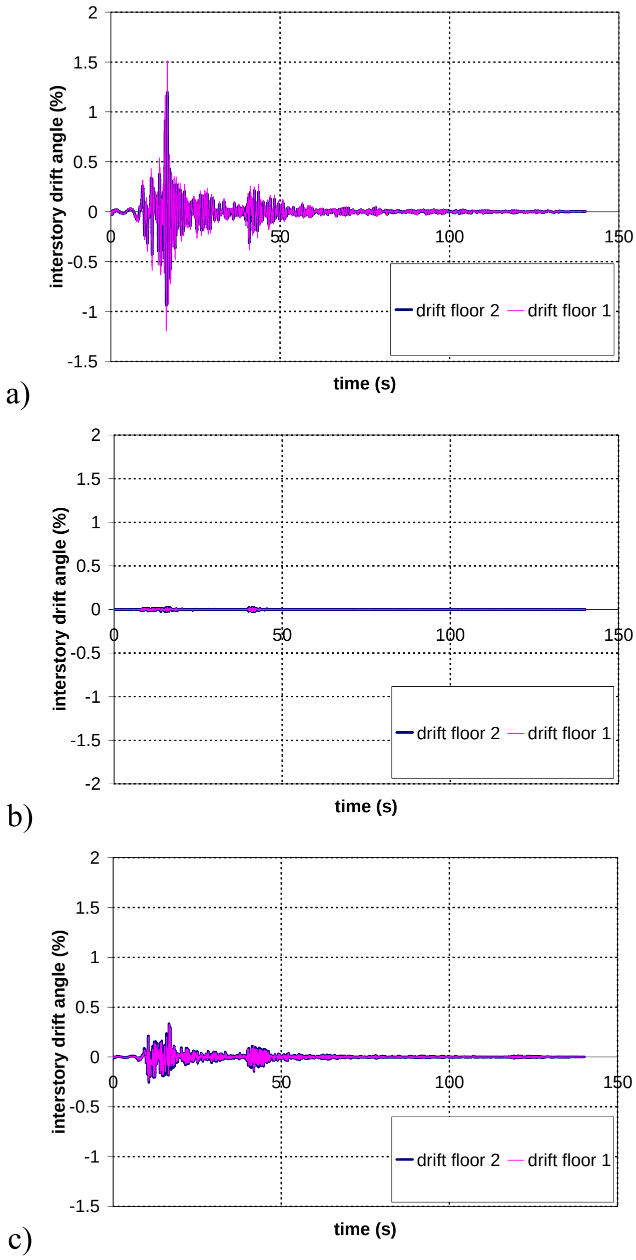

Figure 6.53. Interstory drift vs. Time under 1257ya record: original RC structure (a); RC structure equipped with EBs (b); RC structure equipped with BRBs (c).

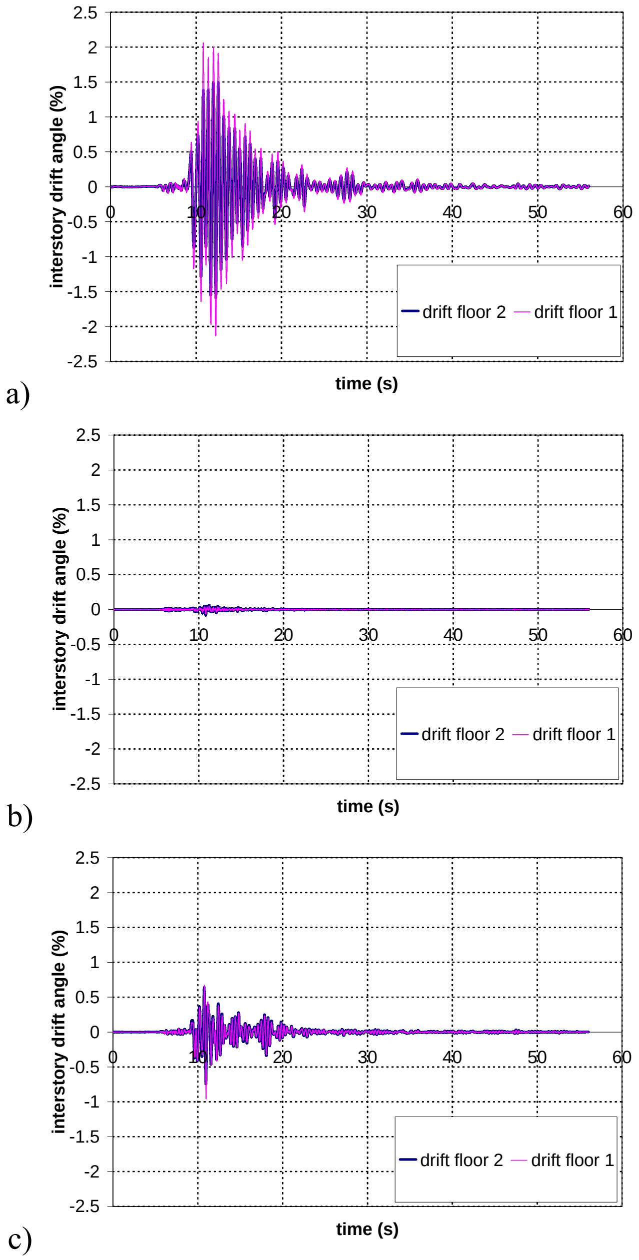

Figure 6.54. Interstory drift vs. Time under 1560xa record: original RC structure (a); RC structure equipped with EBs (b); RC structure equipped with BRBs (c).

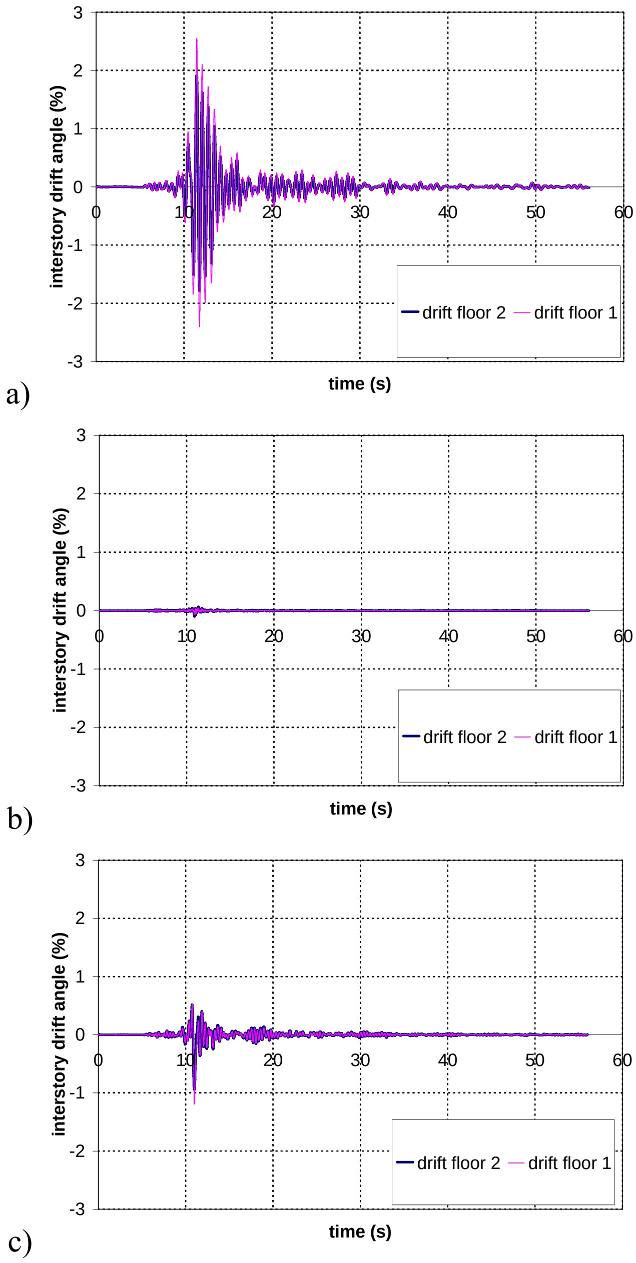

Figure 6.55. Interstory drift vs. Time under 1560ya record: original RC structure (a); RC structure equipped with EBs (b); RC structure equipped with BRBs (c).

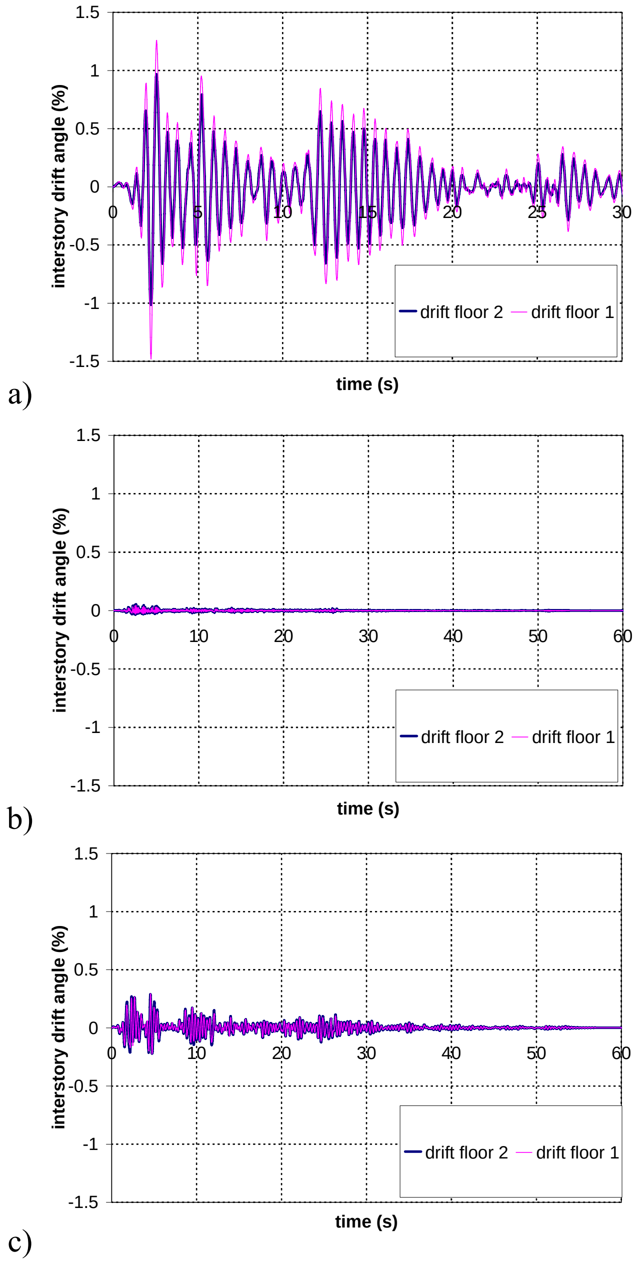

Figure 6.56. Interstory drift vs. Time under El Centro NS record: original RC structure (a); RC structure equipped with EBs (b); RC structure equipped with BRBs (c).

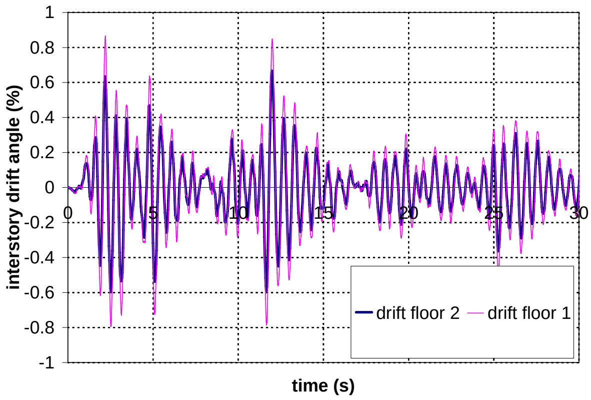

a)

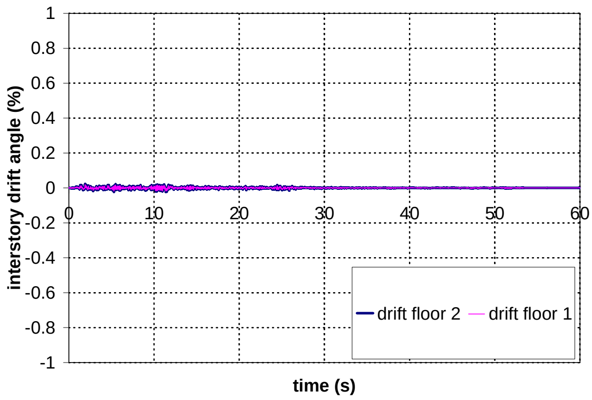

b)

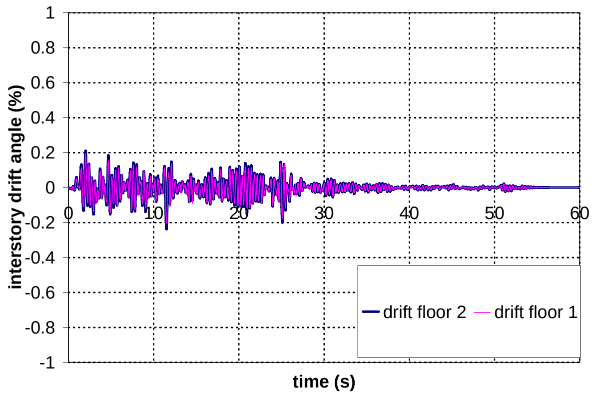

c)

Figure 6.57. Interstory drift vs. Time under El Centro EW record: original RC structure (a); RC structure equipped with EBs (b); RC structure equipped with BRBs (c).

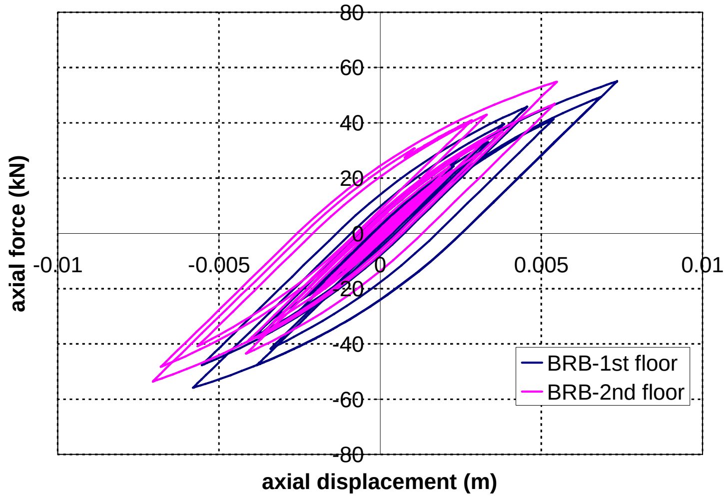

a)

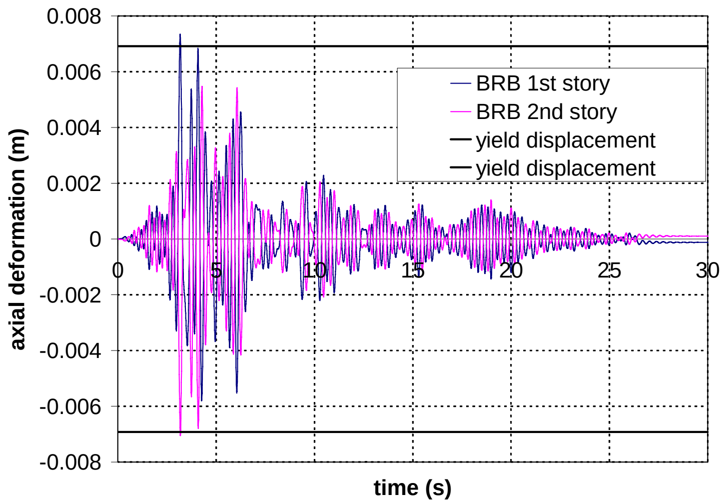

b)

Figure 6.58. BRBs response for accelerogram 42xa: hysteretic engagement (a); axial deformation vs. time (b).

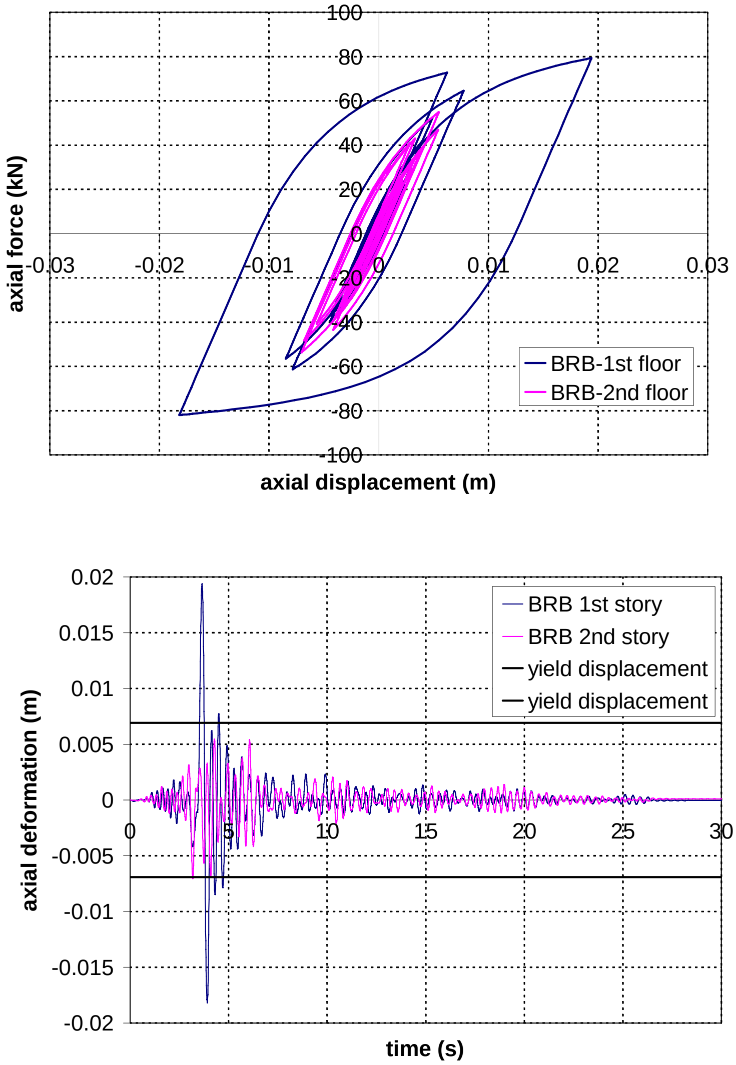

a)

b)

Figure 6.59. BRBs response for accelerogram 42ya: hysteretic engagement (a); axial deformation vs. time (b).

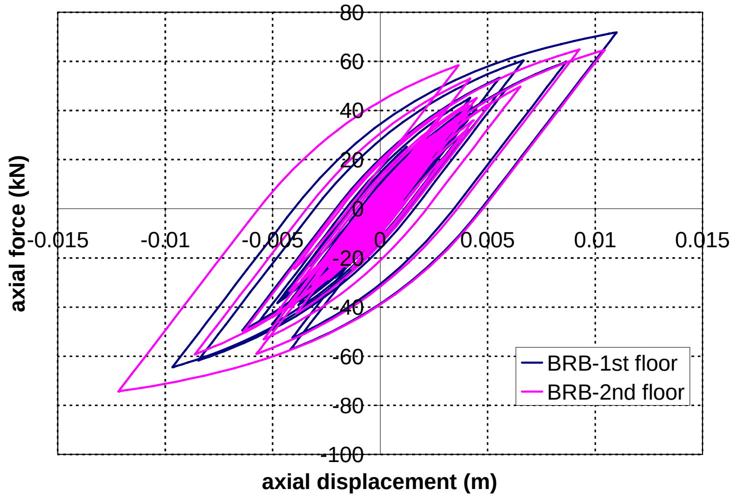

a)

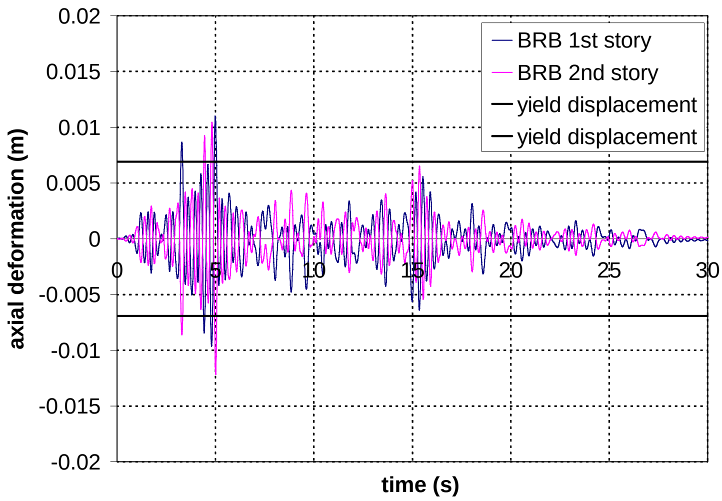

b)

Figure 6.60. BRBs response for accelerogram 879xa: hysteretic engagement (a); axial deformation vs. time (b).

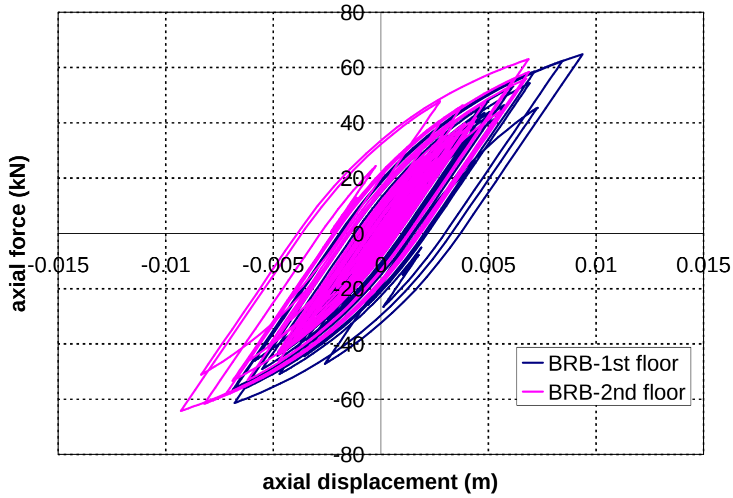

a)

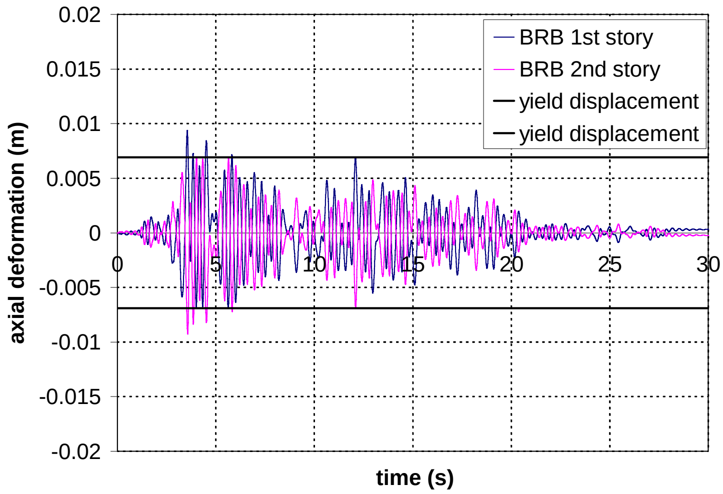

b)

Figure 6.61. BRBs response for accelerogram 879ya: hysteretic engagement (a); axial deformation vs. time (b).

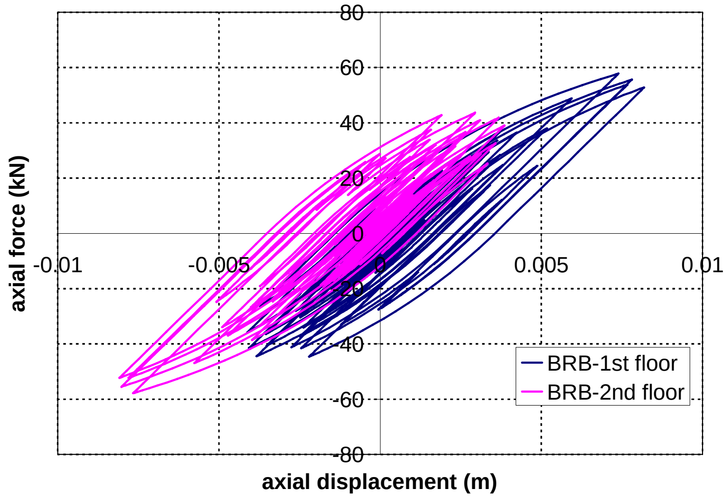

a)

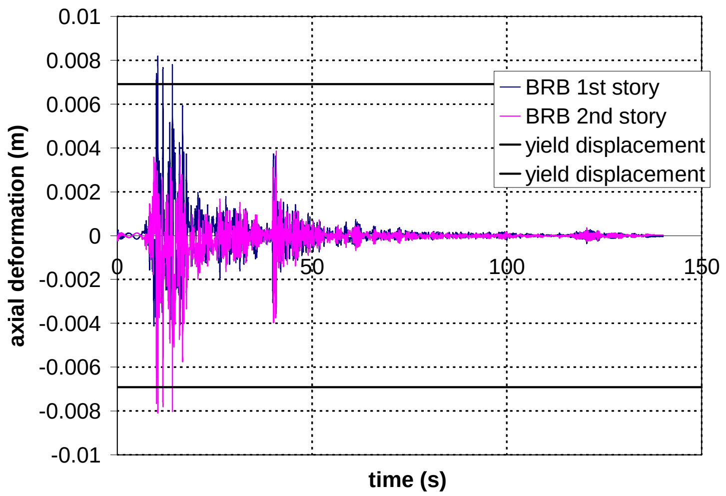

b)

Figure 6.62. BRBs response for accelerogram 1257xa: hysteretic engagement (a); axial deformation vs. time (b).

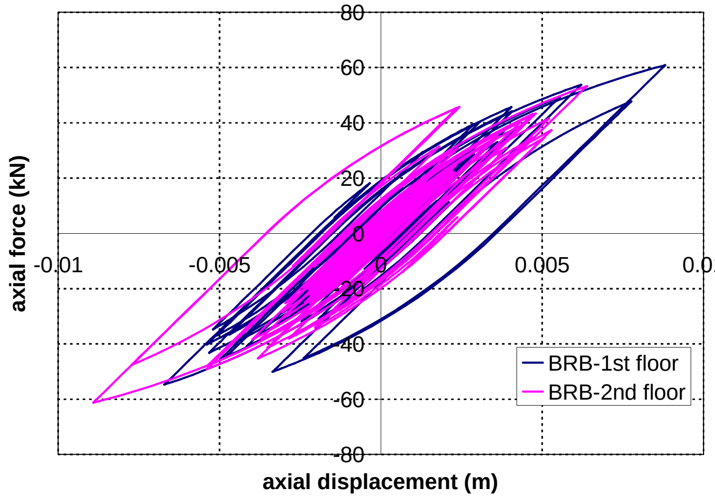

a)

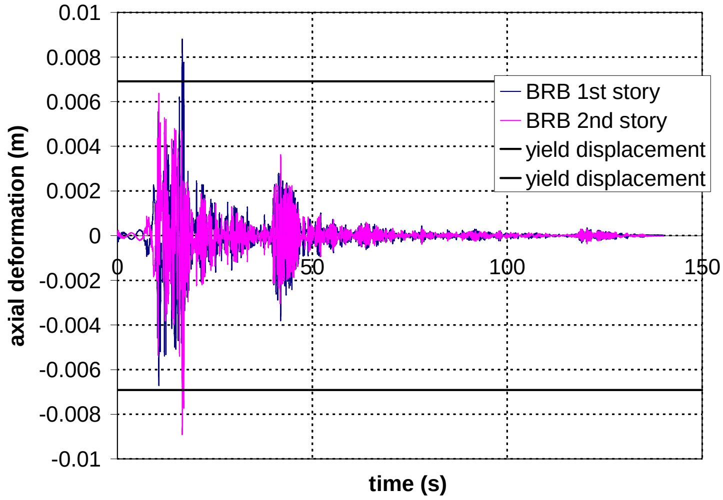

b)

Figure 6.63. BRBs response for accelerogram 1257ya: hysteretic engagement (a); axial deformation vs. time (b).

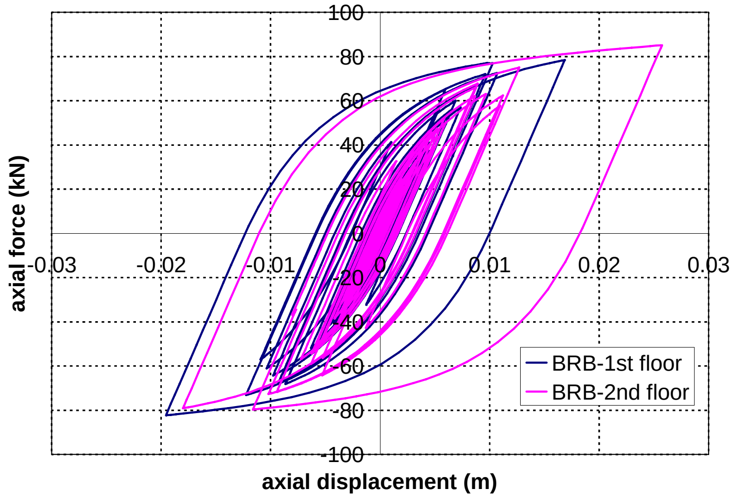

a)

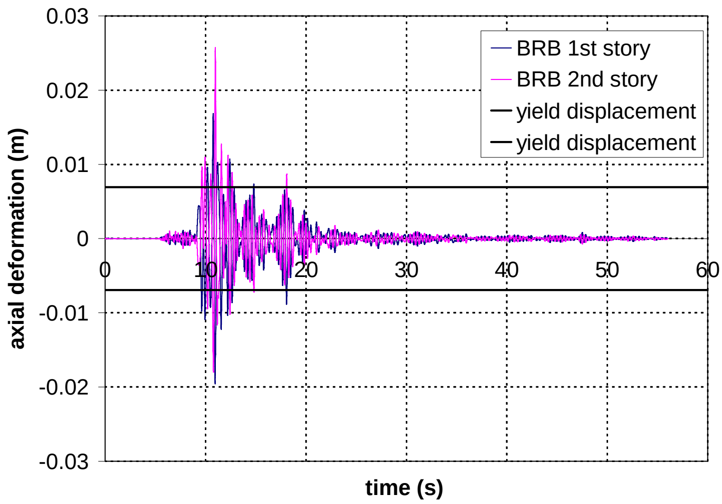

b)

Figure 6.64. BRBs response for accelerogram 1560xa: hysteretic engagement (a); axial deformation vs. time (b).

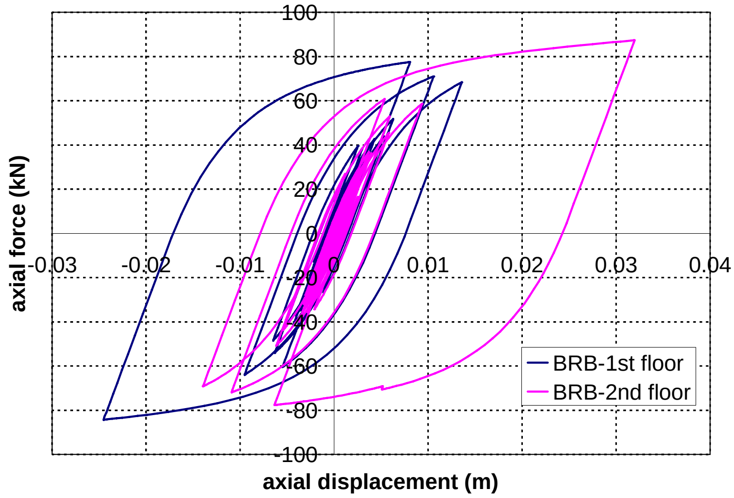

a)

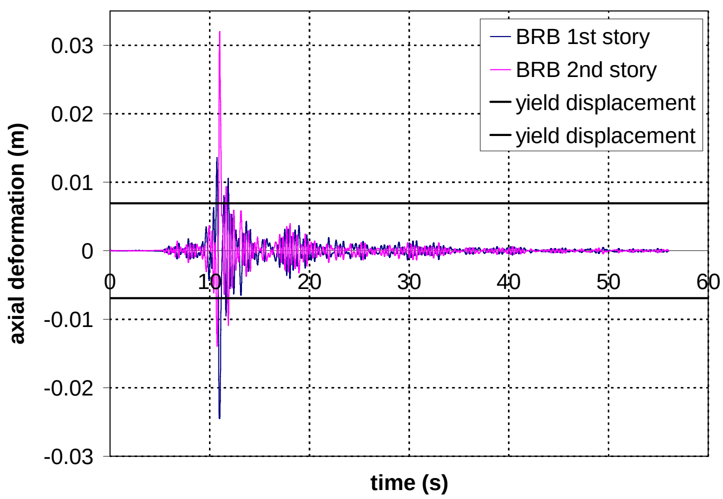

b)

Figure 6.65. BRBs response for accelerogram 1560ya: hysteretic engagement (a); axial deformation vs. time (b).

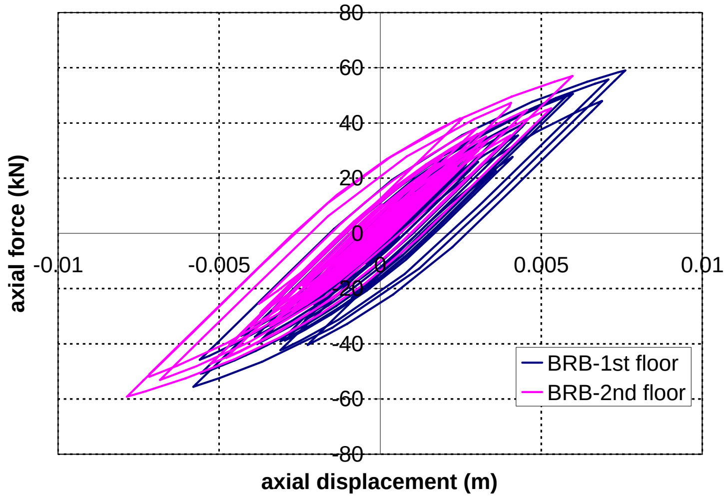

a)

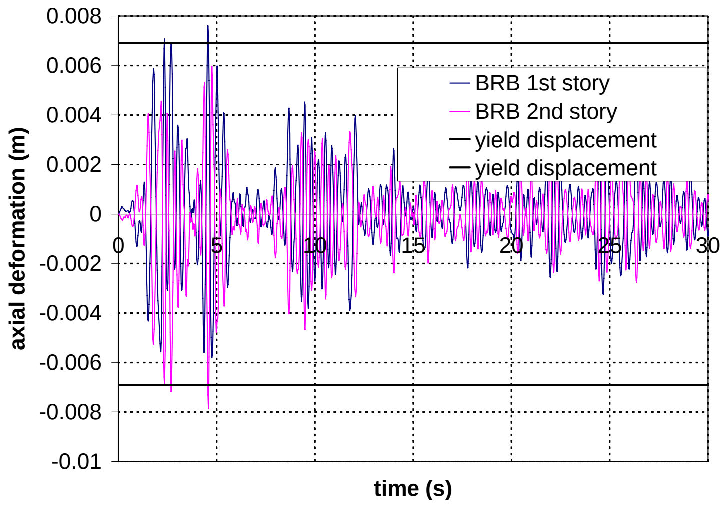

b)

Figure 6.66. BRBs response for accelerogram El Centro NS: hysteretic engagement (a); axial deformation vs. time (b).

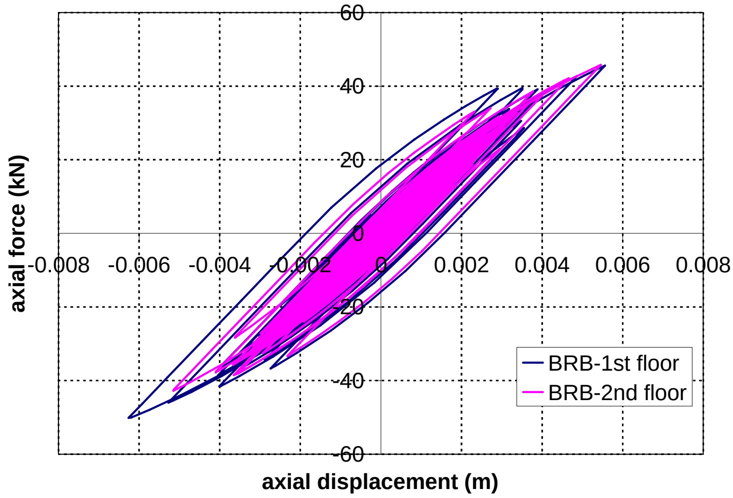

a)

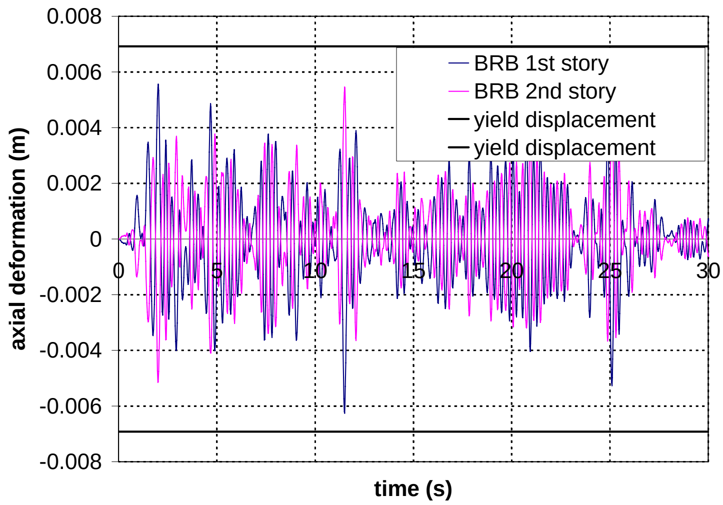

b)

Figure 6.67. BRBs response for accelerogram El Centro EW: hysteretic engagement (a); axial deformation vs. time (b).

Chapter VII
Numerical modelling of the tested masonry infilled RC structure equipped with BRBs

7.1 GENERAL

The numerical modelling of the tested two story RC building has been a very complex study, because of the large number of aspects to be taken into account, such as the presence of non structural elements as the perimetric facing walls and partition walls, the influence of staircase and the level of damage reached in the RC members after each performed experimental test. In particular, three different steps of the structural performance related to their relevant performed test are of interest and consequently they have been modelled:

1. the structural response of the original undamaged and unbraced masonry infilled RC building (corresponding to the first test carried out on the building as it was);
2. the lateral response of the RC structure severely damaged after testing (corresponding to the final state of the RC structure after the second experimental test, where the building was strengthened by means of the use of C-FRP bars put into the mortar joints of the facing walls) and locally repaired, that has been assumed as the initial design state of an hypothetic RC building to be seismic retrofitted by means of BRBs;

3. the lateral response of the masonry infilled RC building retrofitted with BRBs (corresponding to the response shown after the third test, where the RC structure was equipped with the studied special “only-steel” BRB).

7.2 NUMERICAL MODELLING OF THE PRIMAL MASONRY INFILLED RC BUILDING AS IT WAS

7.2.1 Elastic response of the primal masonry infilled RC structure

The first step to model the RC structure as it was consisted in the schematization of its elastic behaviour, which is the calibration of its lateral stiffness. This purpose was obtained thanks to the knowledge of dynamic properties of the building under examination. Hence, some dynamic tests have been carried out in cooperation with "STRAGO s.r.l." which furnished acceleration transducers, the acquisition system, the vibrodyne and the software for data processing.

In order to plan the experimental dynamic tests, a preliminary numerical model of the structure (as shown in Figure 7.1) has been developed by using the well-known commercial software SAP2000.Through this study, an initial assessment of the natural frequencies of the system and the relevant vibration modes have been obtained. In such a way, it was possible to subsequently fix a suitable range of sampling frequencies of signals, as well as to establish an optimal position of the measuring points. The preliminary model has been developed assuming the following hypotheses:

1. Inertia has been lumped in the centroid of masses at each floor, where the presence of the rigid diaphragm has been simulated allowing to have only three dynamic degrees of freedom at each floor, i.e. two translations and one torsional rotation.
2. Moreover, the presence of perimetric and partition walls has not been purposely taken into account in this model, in order to understand how these elements, usually considered as non-structural, can influence the global response.

The results of this numerical analysis are presented in Table 7.1 and Table 7.2 in terms of masses, periods and modal participating masses. The modes of vibration are shown in Figure 7.2.

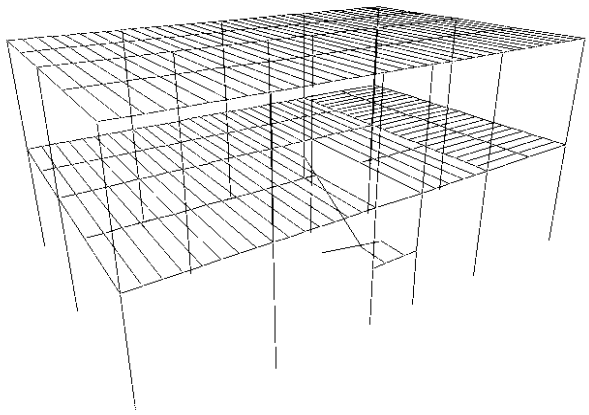

Figure 7.1. Numerical model of existing structure.

Table 7.1. Dynamic masses lumped at centroid of floors.

	Translational mass	Rotational mass
	kNs^2/m	kNm^2
1°floor	196.864	10763.548
2°floor	146.894	7182.155

Table 7.2. Dynamic properties of the model: periods, frequencies and modal participating masses.

	Period Sec	Frequency Hz	M_x %	M_y %	$SumM_x$ %	$SumM_y$ %
Mode 1	0.814	1.23	42.4	27.1	42.4	27.1
Mode 2	0.783	1.28	28.	57.4	70.5	84.5
Mode 3	0.652	1.53	21.4	1.8	91.9	86.3

From the data reported in Table 7.2, it is evident that there is an important coupling between torsional and translational vibration modes. Consequently, the participating mass associated to the first vibration mode is only 42.4%. In order to highlight this aspect, the orthonormalized modal shapes are plotted in Figure 7.2. As far as the first mode is concerned, referring to relative floor rotation, the torsional effects at the first story are stronger than those at the second story, because of the presence of the staircase structure and one stiff beam only at the first floor, as previously mentioned. For the second mode, the torsional-translational coupling is less important even if it is not possible to identify the direction of translation. The third mode shows that the torsional component is prevailing.

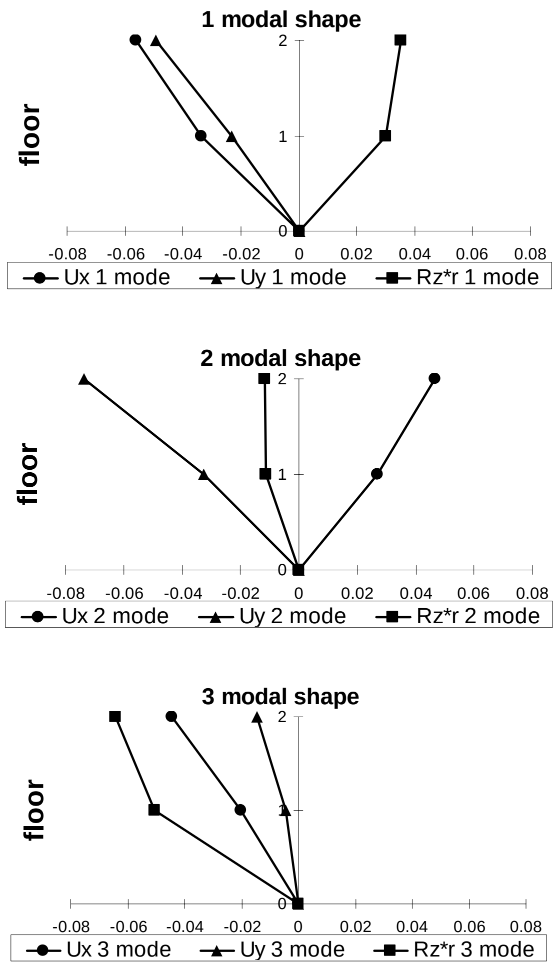

Figure 7.2. Preliminary model: the first three modal shapes.

After the preliminary study, an experimental dynamic test was carried out on the basis of the data deduced by the simplified model. The structural response has been measured using 16 accelerometers (Figure 7.3), having the following technical characteristics:

- Type of accelerometer: Force balance

- Bandwidth: DC – 200 Hz
- Full scale range: ± 1g
- Sensitivity: 10V/g
- Linearity: < 1000μg/g
- Hysteresis: <0.1% of full scale
- Cross-axis sensitivity:<1% (including misalignment)

Figure 7.3. The adopted accelerometer.

Transducers have been fixed to the roof structure by means of an aluminum base and fastening screws. The position of the accelerometers has been chosen in such a way to correctly record the foreseen modes of vibration of the structure (Ren et al. 2004). Six accelerometers were fixed on the first floor, while the remaining were placed on the second floor, where the vibrodyne was also positioned (see Figure 7.4).

In order to have a good sample of the acceleration signals induced by the sinusoidal force of the vibrodyne and also to control the measures taken at other data acquisition channels, two "reference" sensors (number 14 and 15 in Figure 7.4) were placed near the vibrodyne.

The plan disposition of accelerometers on the two floors is shown in Figure 7.4, along with the position and orientation of the vibrodyne. Arrows define the positive direction of each measure.

The analogical signals were acquired by a digital recorder (National Instruments, model PXI-1042) with two cards of acquisition (NI 4472) having 8 architecture parallel channels with the precision of 24 bit and frequency of sampling equal to 102.4Ksamples/sec (Figure 7.5).The whole process of acquisition is driven by a software written in the programming language Labview 7.0. This software allows the acquisition of all signals and the real time visualization of the accelerograms and the Fourier Spectra to be carried out.

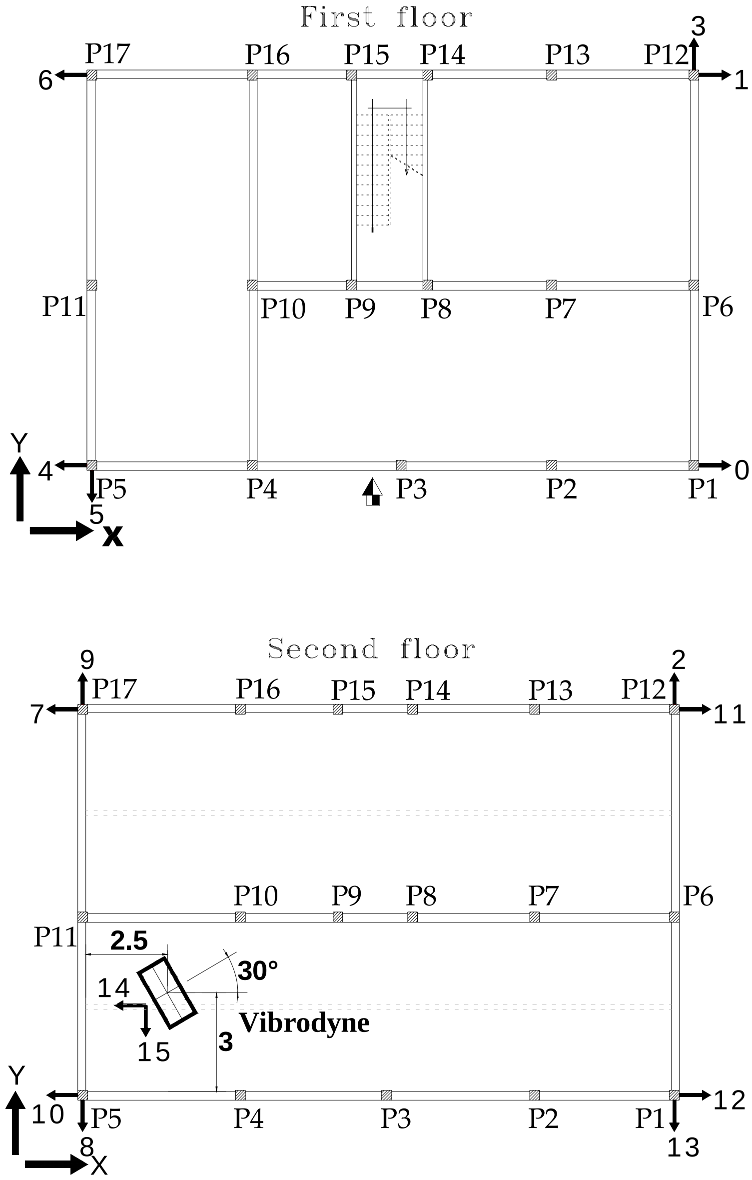

Figure 7.4. The position of vibrodyne.

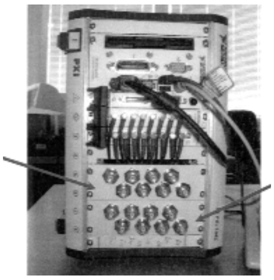

Figure 7.5. The acquisition system PXI–1042.

Finally the excitation system consisted in a vibrodyne (Figure 7.6) characterized by the following characteristics:

1. dimensions 200cmx100cmx100cm (length, height, depth)
2. structural weight of frame: 500Kg
3. maximum number of masses placed in each counterrotating flat basket: 4x33Kg and 3x27Kg
4. flat basket diameter: 90cm
5. power input: 2kw

The vibrodyne was tilted of 30° on the longitudinal (X) side of the building (as shown in Figure 7.4), so that to significantly excite the fundamental flexural shapes in both principal directions of the building. The choice of this position has been guided by the aim to prevent cracks in masonry infill walls in the Y direction. In fact, a pushover test up to collapse of the building was planned to be carried out in this direction after the dynamic test presented in this paper. Hence, the need to maintain the integrity of both structural and non–structural elements mainly resisting in the transversal direction.

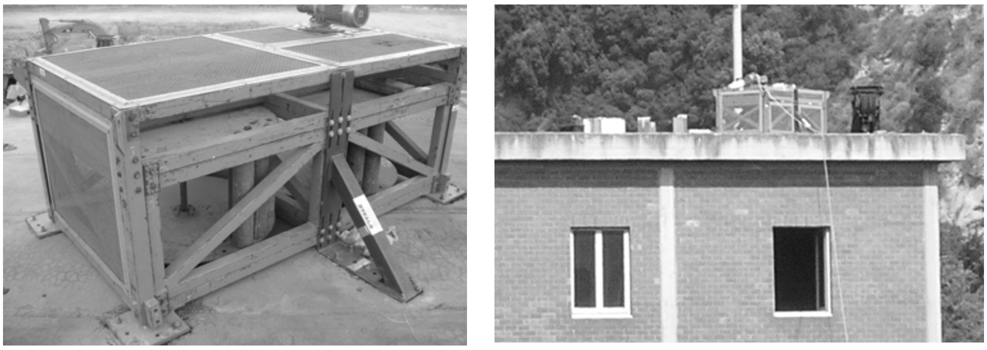

Figure 7.6. The vibrodyne placed on the roof of the building.

The response of the sensors has been acquired in a range of frequencies from 20 through 68 Hz. Each acquisition has been performed for a time duration of 10 seconds and then the values of Fourier spectra of all the channels on that frequency have been memorized. The sampling process has been conducted as follows:

1. a first excursion in the frequency domain from 20 Hz through 60 Hz as measured at the inverter (i.e. 0.7 Hz through 2.3 Hz of frequency of force at vibrodyne) with a footstep of 2 Hz.
2. a second excursion in the frequency domain from 60 Hz through 68 Hz as measured at the inverter (i.e. 2.3 Hz through 2.64 Hz of frequency of force at vibrodyne) with a footstep of 4 Hz.

Because the theoretical frequencies are close each other, it has been required to investigate more in detail through the range of theoretical frequencies (De Sortis et al. 2005; Ren et al. 2004). For this reason the adopted footstep in excursion of frequencies for the inverter has been chosen smaller in first range of frequency (20÷60 Hz), where the natural frequencies are expected to be included.

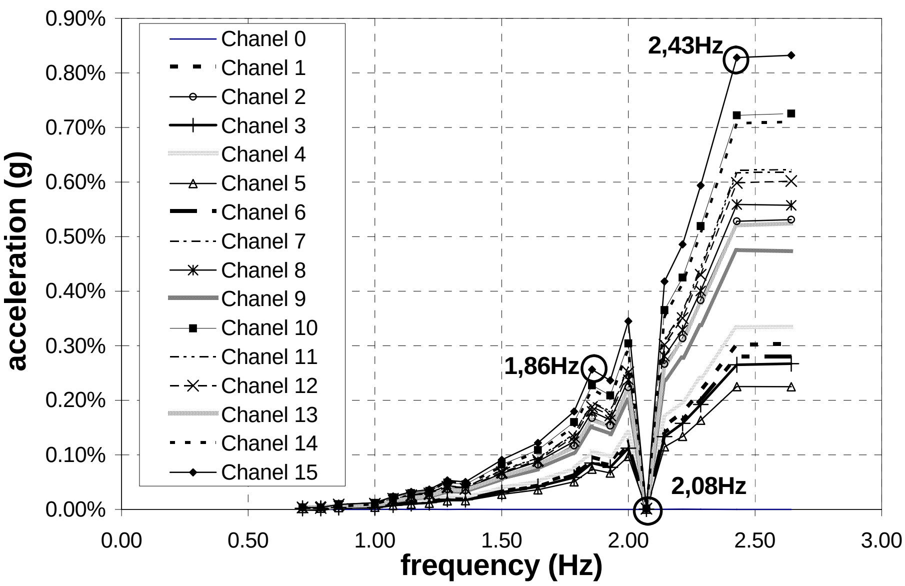

Figure 7.7. Acceleration versus frequency relationship.

Because the vibrodyne produces a centrifugal force, firstly the acceleration versus frequency relationship has been plotted. This diagram (shown in Figure 7.7) is characterized by a parabolic trend, except in correspondence of values of natural frequencies of the structure, when resonance conditions occur.

The peak values of Fourier Spectra are amplified under conditions of resonance, so it is possible to recognize the natural frequencies in correspondence of such peaks (Richardson 1986, Richardson 1999).

An example of the measured acceleration time histories is shown in Figure 7.8, together with the corresponding FFT transfer function.

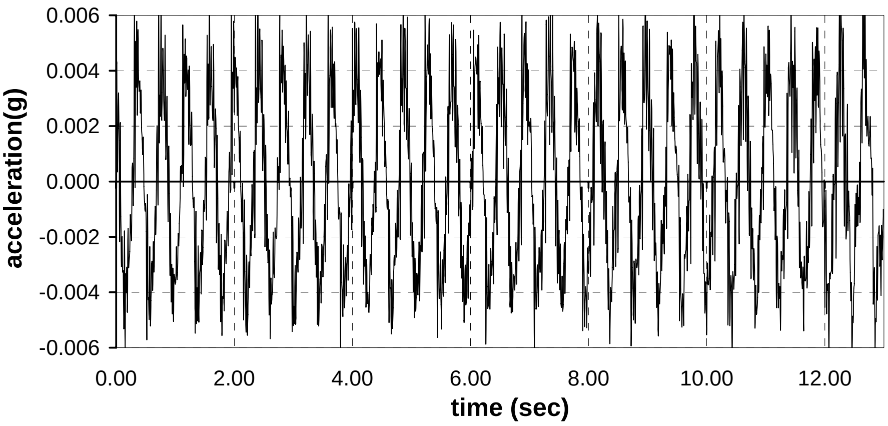

a)

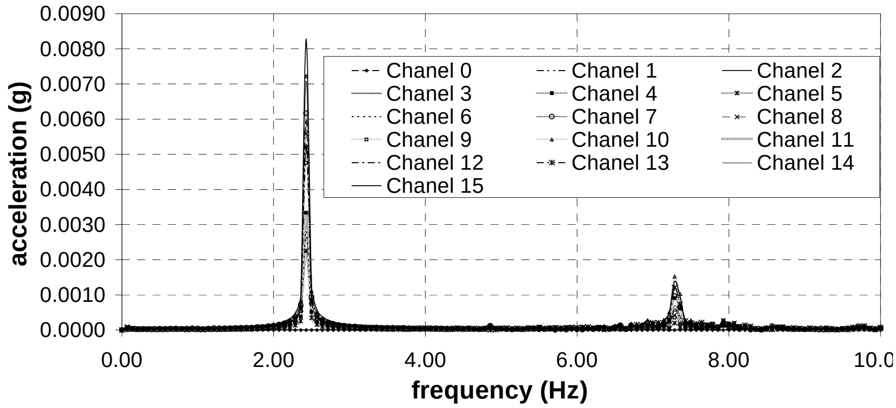

b)

Figure 7.8. An example of measured data and corresponding spectrum: time history at 2,43Hz frequency, channel 8 (a); FFT of signal at 2.43 Hz frequency (b)..

The evaluation of modal damping ξ has been carried out by means of half-power band width method (Chopra, 2000).

The periods, frequencies and modal damping are presented for first three natural modes of vibration in Table 7.3.

Table 7.3. Measured dynamic properties.

	Period	Frequency	Prevalent verse of the modal shape	ξ
	Sec	Hz		%
Mode 1	0.537	1,86	Flexural in X (ref. Figure 7.4)	1,15
Mode 2	0.481	2,08	Flexural in Y (ref. Figure 7.4)	2,96
Mode 3	0.412	2,43	Torsional around Z (ref. Figure 7.4)	1,38

As it was expected, the experimental periods and the fundamental modal shapes are sensitively different with respect to those deduced by the preliminary model, as shown in Table 7.4. In particular, contrary to the experimental results the numerical modal shape of the bare RC structure, obtained neglecting the presence of infill walls as above mentioned, show a significant torsional coupling without a prevailing flexural direction. This difference is due to the fact that the contribution offered by masonry infill walls to the system stiffness has not been considered in the numerical model. As expected these "non–structural" elements significantly increase the lateral stiffness, hence the measured periods are smaller than the theoretical ones.

Table 7.4. Preliminary theoretical vs. experimental periods.

	Period (sec)		
	Numerical model	Experimental Test	Variation (%)
Mode 1	0.814	0.537	34.0
Mode 2	0.783	0.481	38.6
Mode 3	0.652	0.412	36.8

As a consequence, in order to calibrate the elastic lateral stiffness of the structure under examination it has been necessary to take into account the presence of both partition walls and infill facing walls placed in the direction of interest, i.e. the direction of pushover test. Once again the calibrated model of the structure under investigation has been carried out by means of the well know non-linear finite element program SAP 2000 version 9.1.6. Beams and columns have been modelled as frame elements. A fixed restrained at columns' bases has been assumed. The first and second floors have been modelled considering all floor joists.

The staircase has been modelled as a frame element with a rectangular cross section, in which the steps have been considered as an additional load.

Referring to the lab tests performed, the materials properties of structural elements have been assumed equal to the ones experimentally evaluated on material specimens sampled by similar and coeval RC buildings in the same area (in particular, the concrete compression strength was confirmed by schlerometric measurements in situ). Moreover, in case of secondary elements, such as masonry infill walls several lab tests have been performed to determine both the compression strength and the elastic modulus. The average values of the material mechanical properties of structural elements are summarized in Table 7.5, while the material properties of the masonry infill walls are summarized in Table 7.6.

Table 7.5. Material properties of structural members.

material	E (MPa)	f_{cm} (MPa)	f_{ym} (MPa)
Concrete	30000	28.5	
Steel rebars	210000		480

Table 7.6. Material properties of masonry infill walls.

Material	$E=750f_{wv}$ (MPa)	f_{bm} (MPa)	f_m (MPa)	f_{wv} (MPa)	f_{vko} (MPa)	f_{wt} (MPa)
semi-hollow tile wall	6412.5	17.11	2.5	8.55	0.214	0.485
semi-hollow light concrete wall	1357.5	3.06	2.5	1.81	0.045	0.223

Where, E is the elastic modulus, f_{cm} is the average compression strength of concrete, f_{ym} is the average steel yield strength, f_{bm} is the average compression strength of bricks, f_m is the average compression strength of mortar, f_{wv} is the average compression strength of masonry (Paulay & Priestley 1992), f_{vko} is the average pure shear strength of masonry without any applied vertical loads, f_{wt} is the average tensile strength of masonry.

The main modelling hypothesis to schematize the RC members characterizing the elastic response of the primal masonry infilled RC structure was to assume no reduction in columns gross moment of inertia.

In addition, the presence of masonry infill walls and partition walls was taken into account. In particular, the presence of this type of resisting elements can be dealt with introducing an equivalent strut into the RC frame as shown in Figures 3 and 4 in accordance with the numerical modelling results on masonry infill reinforced concrete structure proposed by Al-Chaar (2002).

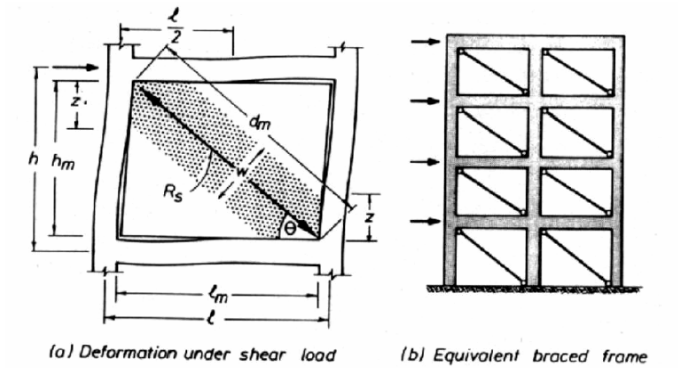

Figure 7.9. Equivalent strut mechanism.

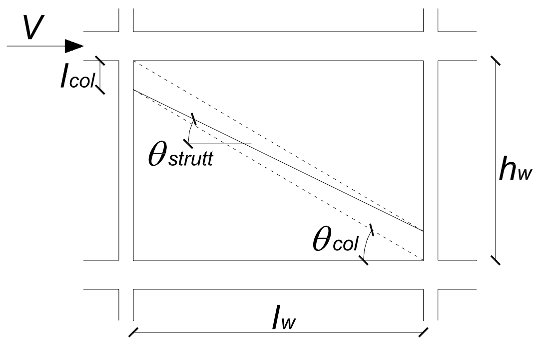

Figure 7.10. Equivalent strut geometry.

In particular, Figure 7.10 shows the geometry of the equivalent strut according to Al-Chaar model that refers to FEMA 356. Hence, the width "*a*" of the equivalent strut was estimated as follows:

$$a = 0.175 \cdot D \cdot (\lambda_1 \cdot H)^{-0.4} \quad (64)$$

where D is the length of the frame diagonal (i.e. $D = \sqrt{l_w^2 + h_w^2}$, ref. Figure 7.10), while $\lambda_1 \cdot H$ is the relative stiffness between the RC frame and the masonry infill wall, given by the following expression with the lengths are expressed in *inch*:

$$\lambda_1 \cdot H = H \cdot \sqrt[4]{\frac{E_m \cdot t \cdot sen2\theta}{4 \cdot E_c \cdot I_{col} \cdot h}} \quad (65)$$

Once defined the width of the equivalent strut, it was assumed a conventional eccentricity of the diagonal strut related to the transverse dimension of the strut, according to the following Equation:

$$l_{col} = \frac{a}{\cos\theta_{col}} \quad (67)$$

where:

$$tg\theta_{col} = \frac{h - \dfrac{a}{\cos\theta_{col}}}{l} \quad (68)$$

Moreover, according to Al-Chaar model, the presence of the openings has been taken into account reducing the area and the strength of the equivalent diagonal strut by means of reduction coefficients. Namely, the reduced area of the equivalent strut was assumed equal to:

$$a_{red} = a \cdot R_1 \cdot R_2 \quad (69)$$

where R_1 takes into account the presence of the openings into the wall and R_2 takes into account the presence of a possible state of damage of the masonry panel. In particular, in this case since the structure was initially undamaged it was assumed R_2=1, while R_1 has been calculated as follows:

$$R_1 = 0,6\left(\frac{A_{open}}{A_{panel}}\right)^2 - 1,6\left(\frac{A_{open}}{A_{panel}}\right) + 1 \quad (70)$$

where A_{open} is the area of the openings and A_{panel} is the masonry panel area equal to $l \bullet h$.

Finally the numerical model calibrated on the basis of the elastic dynamic properties is shown in Figure 7.11.

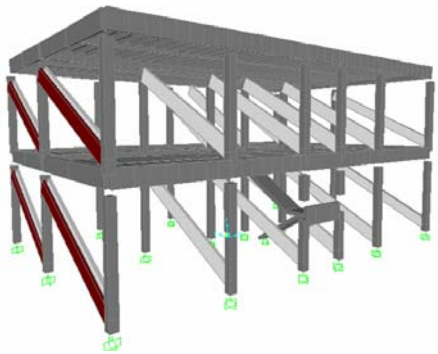

Figure 7.11. Numerical model geometry (SAP2000).

Contrary to the previous case, the fundamental modal shape related to the direction of the experimental pushover reveals to be very regular, namely it is mainly flexural in Y direction, as clearly summarized in Figures 7.12a,b and c.

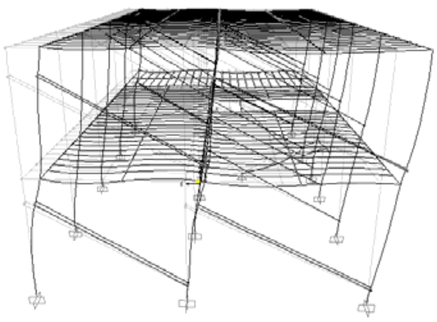

a)

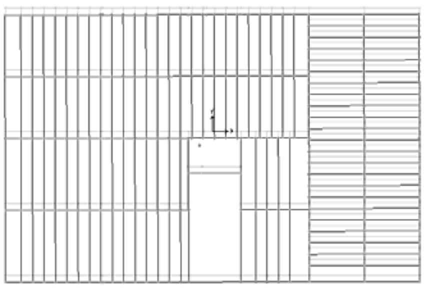

b)

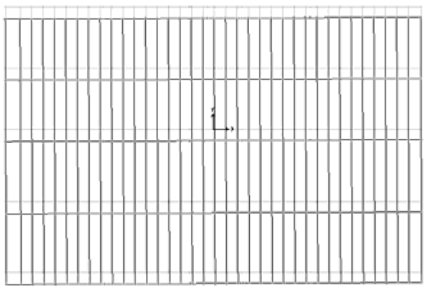

c)

Figure 7.12. Numerical modal shape of the calibrated model: 3D view (a); first floor view (b); roof view (c).

The so defined model adequately interprets the actual dynamic response of the building under examination. In fact, as Table 7.7 clearly highlights, the numerical fundamental period differs less than 2% respect to the measured value.

Table 7.7. Theoretical vs. experimental periods.

Period (sec)			
Numerical model: bare structure	Numerical model: masonry infilled structure	Experimental Test	Variation (%)
0.783	0.473	0.481	1.62

In addition, in order to underline the role of the masonry infill walls in the lateral response of the structure it is interesting to compare the orthonormalized modal shape of the bare RC structure with the one of the infilled RC frame. So, as shown in Figure 7.13 neglecting the masonry infill walls let to incorrectly schematize the dynamic response of such type of structures. In fact, the presence of the masonry infill walls act as a sort of bracing system regularizing the lateral dynamic behaviour.

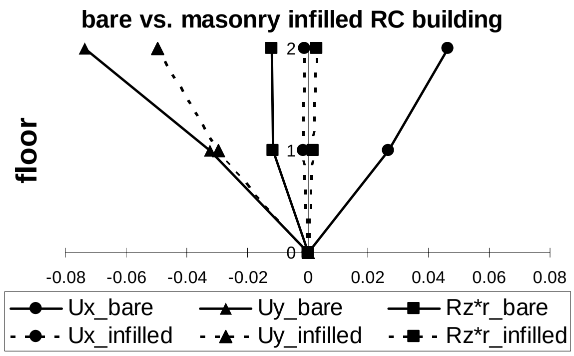

Figure 7.13. Bare vs. masonry infilled RC building dynamic response.

7.2.2 Inelastic response of the primal masonry infilled RC structure

Starting from the model defined in the previous Section, it needed to characterize its nonlinear properties. Therefore, the main modelling hypotheses assumed to schematize the non-linear behaviour of RC members were:

1. elastic-perfectly plastic flexural hinges for RC members, computed according to standard models (Eurocode 2, 2004);
2. fixed end-rotations have been neglected and no limit (infinite ductility) has been placed on the inelastic hinge rotation capacity;
3. elastic-perfectly plastic shear hinges for RC columns, computed according to standard models (Eurocode 2, 2004);

Moreover, the capacity of masonry infill walls and partition walls was taken into account. In particular, referring to Al-Chaar (2002) results, the force-deformation relationship of each modelled equivalent strut was lumped at the middle of the diagonal strut and it assumed according to suggestions of FEMA356 (ref. Table 7-9 of the relevant document), as schematically shown in Figure 7.14.

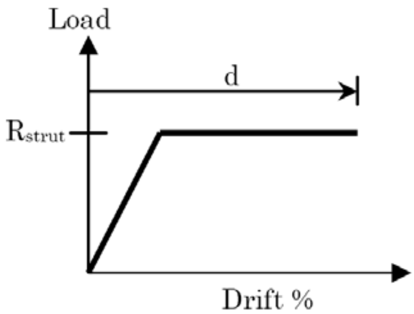

Figure 7.14. Force-deformation relationship of each modelled equivalent strut.

In particular, referring to Figure 7.14, R_{strut} is the axial strength of each equivalent strut and it is a function of the mechanical properties of the materials and of openings' dimension. It was assumed in accordance with the FEMA 356 as:

$$R_{strutt} = \min\left\{R_c, R_{shear}/\cos\theta_{strut}\right\} \tag{71}$$

In particular, R_c is the crushing strength calculated as:

$$R_c = a_{red} \cdot t \cdot f_{wv} \tag{72}$$

where the reduced area of the equivalent strut is given by Equation 69, f_{wv} is the average compression strength of masonry given by Table 7.6 and t is the wall thickness.

Moreover, R_{shear} is the expected masonry bed-joint shear strength.

$$R_c = a_{red} \cdot t \cdot f_v \tag{73}$$

where f_v is the shear strength of the masonry wall.

Finally, the 3D model, as shown in Figure 7.11, was investigated under nonlinear pushover analysis. In particular, the load pattern was applied to reproduce the applied load during the full scale test on the building under study. In fact, the lateral force system simulates an inverted triangular load distribution.

The numerical results are summarized in Figure 7.15 in terms of capacity response curve (base shear vs. roof displacement); moreover, the comparison with experimental results is also illustrated. A quite good agreement is reached in terms of initial stiffness, collapse mechanism and maximum strength, if P-Δ effects are taken into account. In particular, numerical results have showed the formation of column-type collapse mechanism with the formation of plastic hinges at both the ends of columns of the first floor and in correspondence of the staircase and the diagonal cracks in the infill due to the shear force too (Figure 7.16).

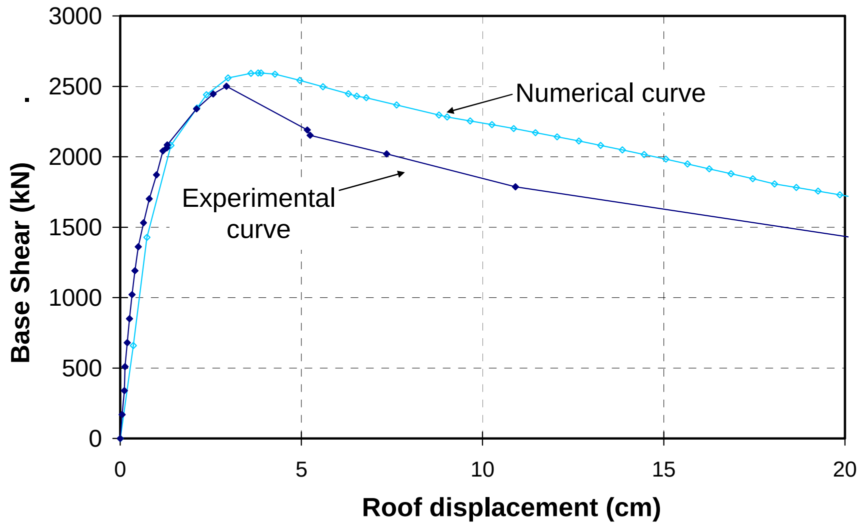

Figure 7.15. Comparison between numerical and experimental results.

a)

b)

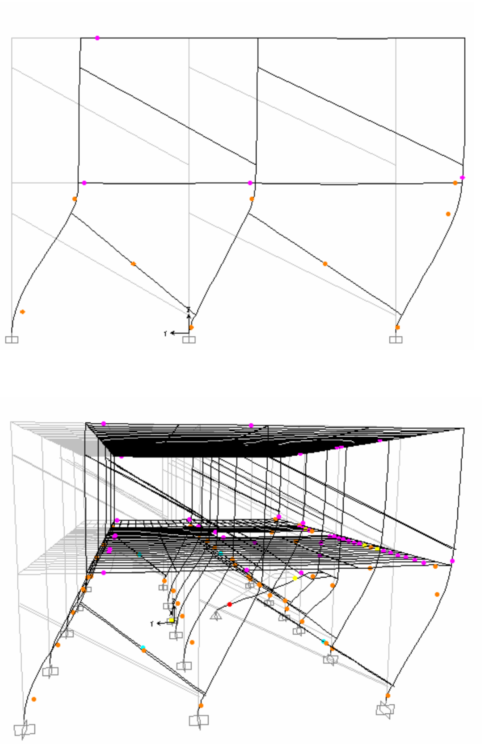

Figure 7.16. Column-type collapse mechanism: plan view (a), 3D view (b).

7.3 NUMERICAL MODELLING OF THE DAMAGED RC STRUCTURE BEFORE THE INTRODUCTION OF BRBs

Modelling the lateral response of the RC structure severely damaged and locally repaired after the second experimental test (where the building was strengthened by means of the use of C-FRP bars put into the mortar joints of the facing walls) is a crucial phase of the modelling study. In fact this physical condition has been assumed as the initial design state of the hypothetic RC building that has been seismic retrofitted by means of BRBs.

Obviously, modelling starting point of this structural state should be traced back to the results described in the previous Section. In fact, it needed to upgrade the model of primal masonry infilled RC structure schematizing the updated state of the damaged structure. This task was reached calibrating the numerical model on the basis of the experimental lateral capacity response (defined as shown in Section 5.4.2, Chapter V, and reminded in Figure 7.17) by taking into account the actual final damage pattern after testing.

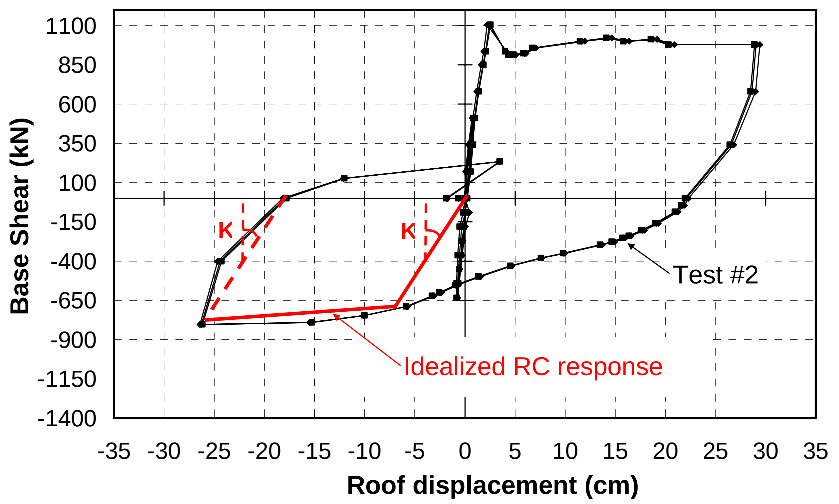

Figure 7.17. Definition of the experimental lateral capacity response representative of the final damaged state of the RC structure after the second Test.

Hence, referring to the damage assessment and the subsequent partial repairing fully shown in Chapter V, the modelling effort was turned to numerically replicate the expected final structural state. This implied to adopt the following modelling assumptions:

1. *neglecting the presence of the staircase*: in fact, after the two experimental pushover test on the unbraced building the staircase structure practically failed and it was not repaired;
2. *taking into account the cracking in the RC structure*: in fact, after testing it was noted a significant spread cracking into columns. This phenomenon was schematized reducing both the gross moment of inertia and the shear area of columns up to 40% of the initial values;
3. *placing the plastic hinges in their actual position as what highlighted by the structural surrey*: in fact, because of the presence of infill walls

the position of plastic hinge was moved in some perimetric columns from their base to their middle length;

4. *reducing the flexural and shear capacity of the damaged internal columns*: in fact after testing only the columns placed on the two perimetric side of the building in the push direction have been repaired, as shown in Figure 7.18. Therefore it needed to calculate the residual flexural capacity of the not repaired columns. Starting from the observation of the actual state of those columns, as highlighted by Figure 7.19a, this modelling issue has been treated assuming, as shown in Figure 7.19b, that at both column ends the gross section is composed by a central concrete core and by the steel longitudinal rebars. The first transmitting the shear forces and the resultant of compression axial forces, the latter able to transfer only the tensile forces. Hence, the flexural and axial capacity of damaged columns has been schematized as a sort of strut and tie system composed by inelastic spring representing a reduce column gross section. In particular, the inner concrete core has been defined thanks to the data measured coming from the geometrical survey performed after the second testing, resulting that the spalled concrete was on the average about two times the original cover of longitudinal steel rebars.

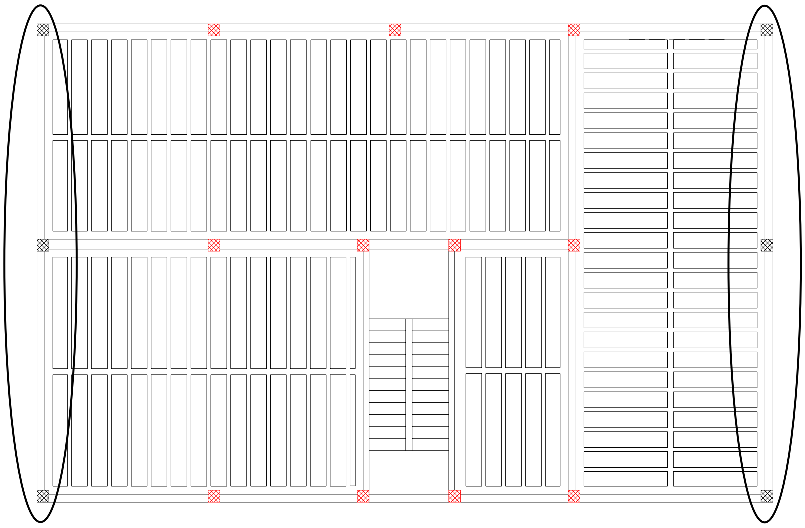

Figure 7.18. Position of the repaired columns (the red columns were not repaired).

a)

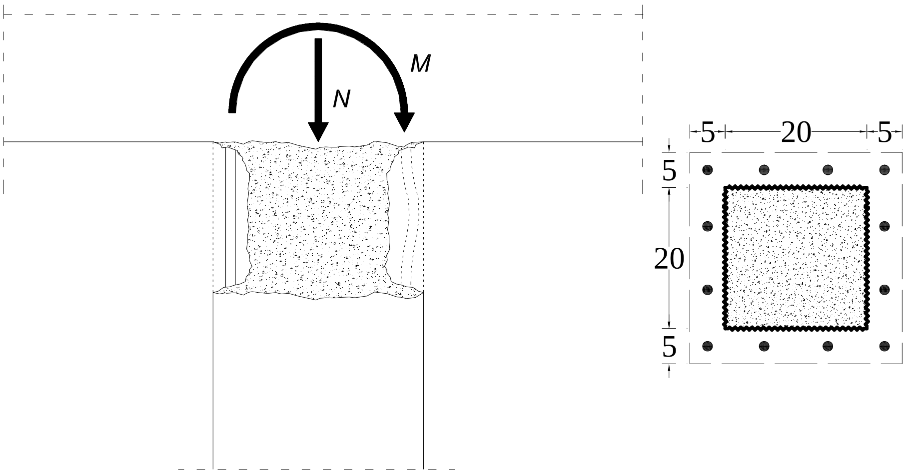

b)

Figure 7.19. Modelling assumptions for the damaged RC columns: actual state after testing (a), equivalent strut and tie scheme (b).

Finally, the numerical response of the calibrated model reproducing the lateral response of the RC structure severely damaged and locally repaired after the second experimental test is shown in Figure 7.20, where it was compared with the idealized response coming from the analysis of results of second test. This direct comparison clearly shows that the above listed hypotheses let to adequately reproduce the expected physical state of the building under examination.

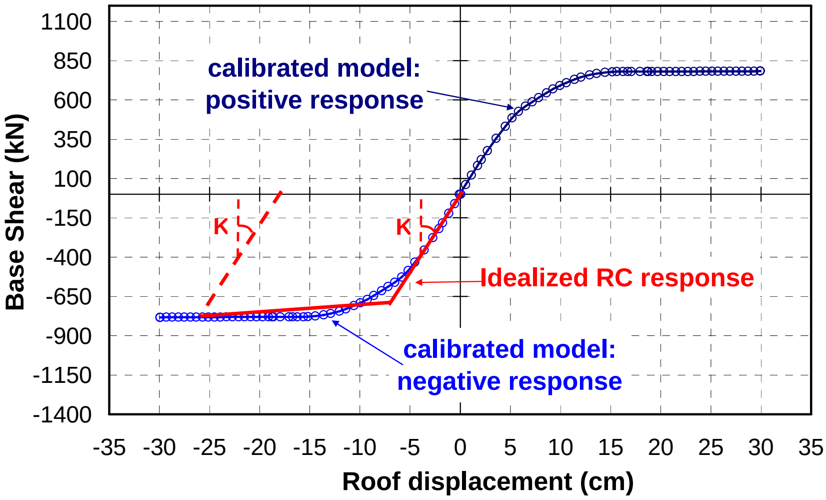

Figure 7.20. Comparison between numerical and idealized response curves.

7.4 NUMERICAL MODELLING OF THE MASONRY INFILLED RC BUILDING EQUIPPED WITH BRBs

This modelling phase is the most significant, because it is directly related to the experimental activity carried out on the studied innovative "only-steel" BRB prototype. So, as it can be easily recognized the starting point to simulate the lateral response of the masonry infilled RC building retrofitted with BRBs is the numerical model defined in the previous Section. In fact, in addition to the modelling hypotheses listed and commented on in Section 7.3, the updated model (shown in Figure 7.21) takes into account the presence of the rebuilt masonry infill facing walls and the presence of the diagonal BRBs, as well.

Once again, the masonry infill walls have been schematized as two equivalent diagonal struts by means of the Al-Chaar model (2002) as explained in detail in Section 7.2. In particular, in this case both the facing walls were made of semi-hollow light concrete bricks (i.e. concrete and lapillo blocks), whose mechanical properties are summarized in Table 7.6.

BRBs have been modelled as a truss element by means of the so-called "non-linear links" available in SAP2000, similarly to how explained in

Section 6.4.2. In fact, their non-linear hysteretic properties have been reproduced adopting the Bouc-Wen model, but some hypotheses have been assumed for properly calibrate the parameter "*n*" and the relevant post-yield to elastic stiffness ratio "*K*". Initially, according to what usually suggested for unbonded BRB (Black et al. 2002, Tsai et al. 2004a) it was assumed "*n*"=1 and "*K*"=0.025. As shown in Figure 7.22, this assumption led to underestimate the hardening developed by the tested BRB, namely in an underestimate of the overall lateral capacity exhibited by the numerical model. Thus, with a trial-and-error process, it was increased the post-yielding ratio from 0.025 to 0.05, which is similar to the value previously adopted for the BRB prototype 1 (see Chapter 6, Section 6.3.1). This assumption led to have a numerical response fitting better the experimental capacity curve. However, another hypothesis on the force-deformation relationship for the tested BRB prototype 3 has been analyzed in order to have a numerical response closer to the experimental one. In fact, it has been finally assumed "*n*"=0.5 and "*K*"=0.05 for the Bouc-Wen model. This modelling approach seems to be the more appropriate, allowing to adequately predict the experimental global response and, in addition, the collapse mechanism, as shown in Figures 7.22 and 7.23, respectively.

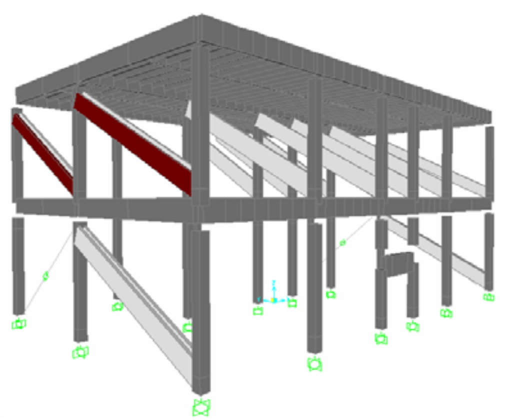

Figure 7.21. Calibrated numerical model of the masonry infilled RC structure equipped with BRBs prototype 3 (SAP2000).

It is worth to notice that the deviations of numerical results from the experimental response curve (Figure 7.22) are mainly due to the difficulties to properly model the damages induced by previous tests on RC structure.

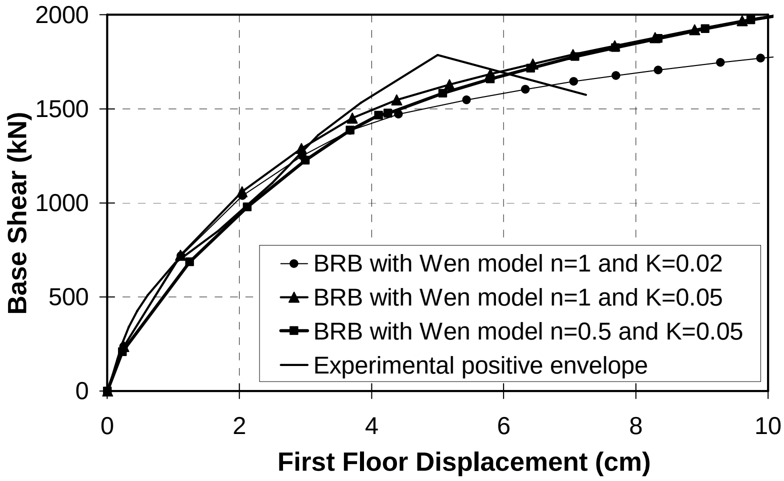

a)

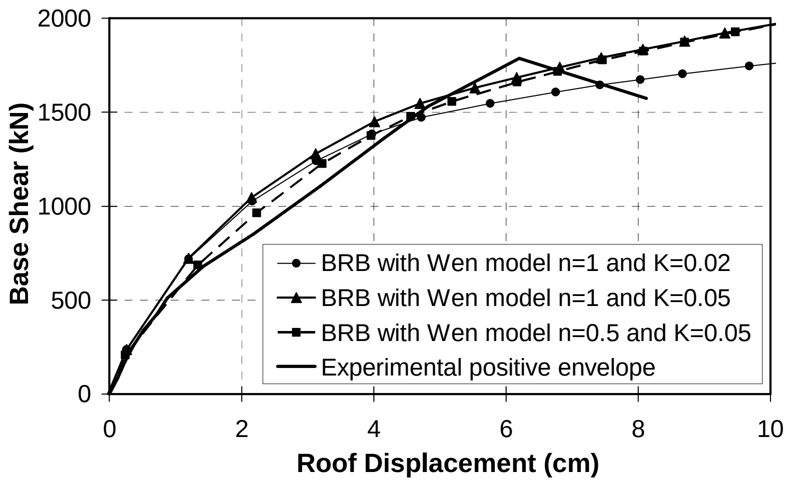

b)

Figure 7.22. Experimental vs. numerical response curves for different BRB modelling assumptions: base shear vs. first floor displacement curves (a); base shear vs. roof displacement curves (b).

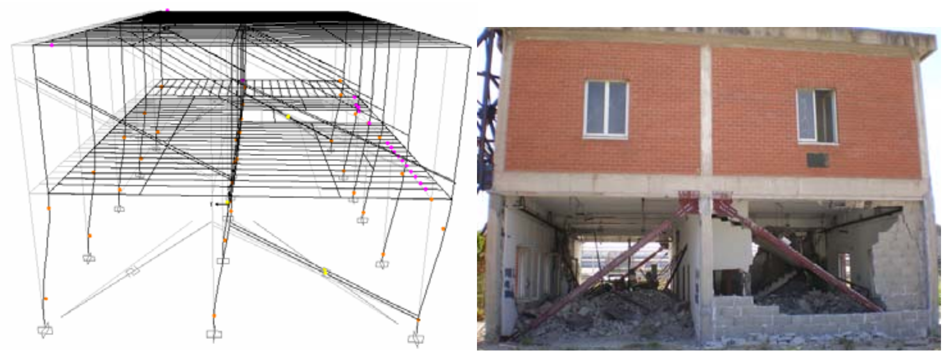

Figure 7.23. Numerical vs. experimental collapse mechanism.

Moreover, in order to quantitatively evaluate the contribution of masonry infill walls on the overall lateral response, another numerical model has been analyzed. To do this, the new model (shown in Figure 7.24) has been developed neglecting the presence of masonry infill walls at the first level, while it is identical to the calibrated one in all the other modelling hypotheses.

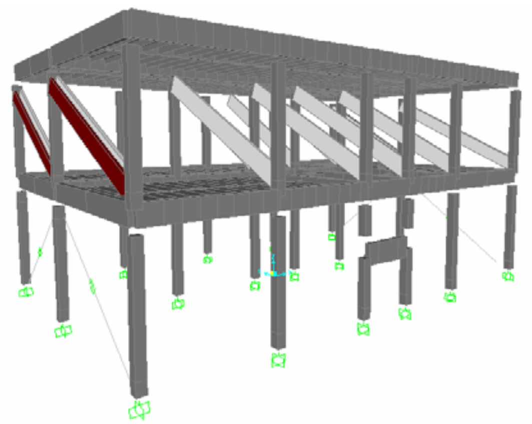

Figure 7.24. Numerical model neglecting the presence of the masonry infill walls at the first level (SAP2000).

Hence, in Figure 7.25 the experimental response is compared with the numerical one given by calibrated model with and without masonry infill walls. It can be concluded that in this case the presence of the bracing system minimizes the influence of infill walls on the global response. In fact, numerical model highlighted that masonry infill walls contribute of about 10% to the lateral capacity.

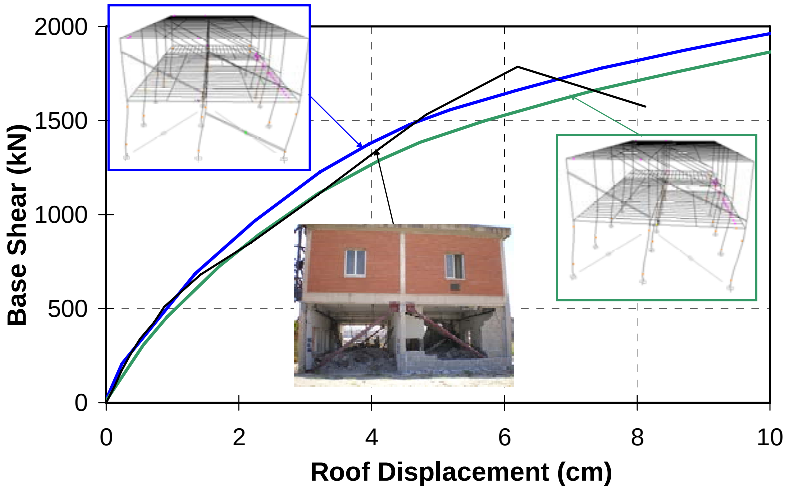

Figure 7.25. Experimental vs. numerical response curves neglecting or not the masonry infill walls at the first level.

Chapter VIII
Conclusive remarks

The research activity presented in this PhD thesis has been finalised to the study of steel dissipative bracing systems for the seismic retrofitting of existing RC structures.

The main reasons having aimed this study were due to the fact that steel dissipative bracing systems are a simple and effective seismic retrofit system. They behave as sacrificial ductile fuses, performing as overall displacements reducers and limiting the inter-story displacements enough to avoiding/reducing the structural damage. In fact, among the possible solutions to retrofit an existing structure, bracing systems are a simple and effective retrofit system, especially when story drifts need to be limited. The idea is to design systems that are strong enough to resist the seismic forces and light enough to keep the existing structural elements far from needing further reinforcement. Furthermore, if these systems could be installed quickly and eliminate the need to disrupt the occupants of existing structures, they would be even more desirable (in the context of a hospital retrofit for example).

However, steel dissipative bracing systems cannot be considered the panacea for the seismic protection issue, but they could be a viable feasible reliable and effective solution.

As explained in detail in their relevant Chapter of this little pamphlet, the study has been focused on the structural performance of two different steel dissipative bracing systems for seismic retrofitting of existing structures, providing high elastic stiffness, stable inelastic response and excellent ductility and energy dissipation capacity:

- Eccentric Braces (EBs)
- Buckling-Restrained Braces (BRBs)

Therefore, after a wide review of the scientific literature about these metal systems, the attention has been focused on the experimentation of these systems as sacrificial devices applied to existing RC structures. In particular, three RC structures have been adopted as specimens for physical and numerical testing:

1. two bare RC unit consisting in a two story-one bay frame obtained by the sub-structuring of a real RC building;
2. a real masonry infilled RC building

Hence, two different set of experimental tests have been performed with different purposes, the first on the two RC units and the second set on the real masonry infilled RC building.

Tests carried out on the two above mentioned RC units led to characterize the behaviour of the device component of both systems and to directly compare their performance highlighting their relative advantages and disadvantages, as well. In this way it was possible to investigate the local performance of both systems (EBs and BRBs) being a cue for thought about two different design issues. The first is directly related to EBs, in fact the current study deepened the link shear over-strength phenomenon, whose knowledge is fundamental for sizing the elements that must remain elastic, according to capacity design principles. In particular, in case of detachable EBs, link end-connections exhibit a key role in determining the system ductility, especially if bolted connections are selected for removable links. Experimental test results clearly highlighted this aspect, emphasizing large over-strength of short links with respect to the first yielding shear and the consequent danger of connection failure. The second issue is related to clarify and deepen the design aspect of BRBs, in order to develop a special "only-steel" detachable BRB for improving the seismic response of existing buildings. In this sense, the performed experimental activity has been a useful tool, giving precious information on several aspects as: 1) design of the inner clearance; 2) the core length. In fact, both the clearance width and the core length affect the strain concentration at the core free length. In particular, the greater is the core length and the greater will be the resultant friction resistance between the restraining unit and the core. Consequently, the greater it will be the possibility to have damage concentration at the core ends, where the friction action is lower.

However, testing results coming from the first experimental set have shown the effectiveness and reliability of both examined metal systems in order to improve the original capacity of the RC structure in terms of strength, stiffness and ductility. They also are deemed to be very precious in helping the improvement of the knowledge about the seismic response of RC framed buildings, with and without repairing/reinforcing interventions. In Figure 8.1 the lateral-load response of the all tests on the two tested bracing systems (EBs and BRBs) is compared in terms of envelope curve corresponding to the positive loading direction. Besides, the behaviour is also compared with the results of a previous pushover test, which was carried out on a bare RC structure very similar to the one tested with the bracing systems. All tests showed a significant increase of lateral stiffness and strength respect of the one of the original unbraced RC structure. In particular, in case of EBs it was observed an increase of the lateral capacity from 5.65 to 8.34 times respect to the capacity of the original unbraced RC structure, while in case of BRBs from 4.08 to 4.95 times.

Moreover, instead of EBs, BRBs are characterized by lower over-strength capacity (at the most equal to the material axial over-strength), but they can provide for the structure a larger displacement capacity than EBs. In fact, referring to the studied cases, short shear links should develop shear deformation angles larger than 0.60 radians in order to provide the same displacement capacity of the tested BRB type-2. This large shear deformation is not reasonable, since no shear link is able to provide it. This implies that BRBs let to control stiffness, strength and ductility better than EBs. Moreover, respect to EBs, BRBs revealed to provide a more complete structural performance, since they can improve not only the lateral stiffness and strength capacity but also, if it necessary, the displacement capacity of the structure. In fact, test results on two different types of “only steel” BRBs showed good ductility of this system.

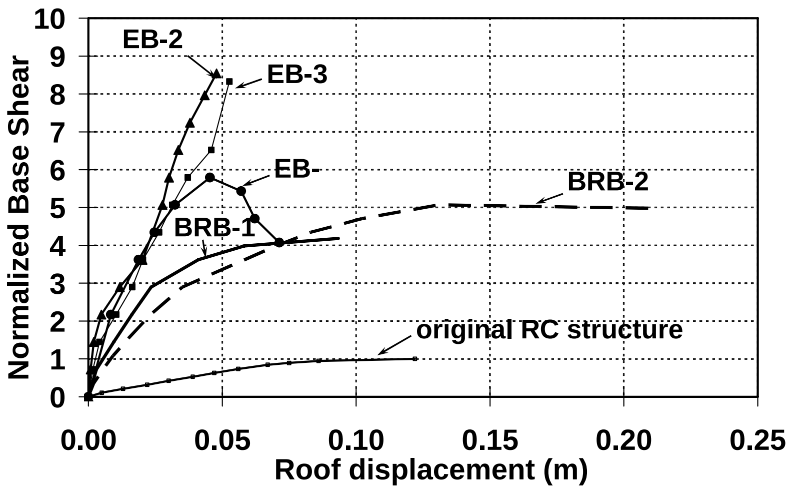

Figure 8.1. Comparison of response curves of tested bracing systems.

In addition to their intrinsic value, the experimental data coming from the first set of tests have been advantageously used for setting up analytical models for reinforced structures which can be conveniently exploited for a better understanding of the complex phenomena influencing the actual response of RC building structures.

The tests on EBs showed anomalously large values of shear over-strength. The numerical investigation highlighted the main responsible of this phenomenon:

(i) large cross section flange over web area;

(ii) the presence of axial restraints to the links.

In particular, numerical analyses emphasized the second aspect. In fact, in classic eccentric bracing of steel buildings shear links belong to the floor beams and they are placed either in a symmetric configuration at the middle of the beam or adjacent to the column. In the first case, the axial force in the link is theoretically zero; in the second case, it is usually deemed to be minimal, and therefore negligible, with respect to shear and moment actions. A few studies have been conducted on links subjected to both shear and axial forces (Kasai & Popov 1986), highlighting that a compression axial force is detrimental to the local buckling behaviour. In fact, there may be cases where the axial force in the link is non-negligible. One example is the case of vertical links in inverted Y-shaped assemblage, which is a suitable configuration in case of seismic upgrading of existing reinforced concrete structures. There are two sources of axial force in the link: (a) vertical loads directly applied after mounting of the link; (b) the axial restraint given by the stiffness of the braces and floor beam, in the vertical direction. Vertical loads acting on the floor introduce compression axial forces in the link. Contrary, the axial restraints produce a tension axial force, because of second order geometric effects.

Finite element numerical simulations of the shear response of the tested links have been performed in this research activity analyzing different boundary conditions at each link end. They showed that axial forces develop and appreciably contribute to the link post-yield stiffness. Tension forces are able to delay local buckling and to increase peak inelastic shear strength. Since capacity design requires consideration of the maximum forces that could develop in the dissipative elements, considering the significant danger coming from unexpected failures in link end connections, the case of tension axial force in the link is deemed to be worthy of consideration. Moreover, an analytical approach has been proposed, allowing prediction of the shear force vs. shear angle response. The basic idea of the proposed analytical model is that the presence of an axial tensile reaction requires an increase of a second order shear force in order to guarantee the overall rotational balance of the forces acting on the link. As a consequence, the second order shear is not related to an increase of bending moment, but it is related to global moment due to the tensile axial reaction that is moved from the middle of the gross section by the first order bending moment at both link ends. So, the increment of the shear force in the inelastic range (ΔV) is obtained from equilibrium a free body diagram of forces (see Chapter VI). Comparing the analytical prediction with numerical results, the method revealed almost satisfactory in predicting the shear response. Further work is required for a better understanding of the interaction of stiffening effects due to axial tension forces and gradual yielding of flanges. Hence, the numerical investigation on link with axial restraints is still in progress. The goal is to develop a simple formula able to predict the link over-strength, thus becoming a powerful design tool.

Starting from the background matured by the tests carried out on the two RC units, the second experimental phase has been directed to the analysis of a real masonry infilled RC building to be seismic retrofitted. Because of its advantages, the choice turned on BRBs, hence, the idea to develop (and to improve in future) an innovative “only-steel” detachable BRB for seismic retrofitting of existing RC structure. This BRB specimen (called prototype 3 in the relevant Section of this volume) was an upgrading of the two typologies previously tested on the RC unit. In this case, the BRB system was designed such that to be hidden between two facings of masonry infill panels. This device has been designed to be mounted onto a real two-story RC building.

The RC structure equipped with BRB was built at the beginning of ‘80s within the steel mill ILVA in Bagnoli (Naples, Italy) and it was destined to demolition by competent Authority. This RC structure has been initially tested in initial original conditions (Della Corte et al 2006). It was pushed by lateral loading up to severe damage of both structural frame members and infill walls. Lateral loads have been applied according to an inverted triangular distribution. The test showed the formation of a weak story at the first floor. After these tests, the structure has been repaired and the above mentioned BRB prototype has been designed. The BRBs has been placed at the perimeter. In particular, in one bay the external facing wall has been reconstructed, in such a way to directly evaluate the interaction between the brace and the wall. Test results showed a good response of the brace up to a calculated brace strain of about 1.2%, corresponding to an interstory drift of about 1.1%. For larger strains, local buckling of the unrestrained non-yielding end-plate occurred. However, three contributory factors sparked off the undesired local buckling of end unrestrained portions of tested BRBs:

(i) The actual yield stress for the steel of the core plate was appreciably larger than the expected value. In fact, all devices have been designed with a steel grade S275, while the measured yielding stress of steel constituting the core corresponds to grade S355 (with an average yield stress of 378MPa).

(ii) Improper, unintentional, fabrication of the welds connecting the unrestrained portion of non-yielding plate and the stiffening steel bars, with consequent failure of the welds (Figure 8.2). The fillet welds were designed to be continuous for the overall length of the stiffeners. Regrettably, these welds were interrupted; they have been spot welded with alternate stretches with a large pitch between each spot weld.

(iii) the inner clearance between yielding core and restraining sleeve has not been complied with. In fact, the design clearance has been fixed to be 1mm per core side. But, having detached the devices after the test, a clearance lower than 0.5mm per core side has been measured. This aspect probably contributed to impair the formation of the plastic higher buckling modes and, consequently, limited the shortening capacity of tested devices.

Figure 8.2. Failure of welds between stiffeners and inner plate.

Notwithstanding the lateral response of the braced structure was impaired by buckling of the unrestrained non-yielding segment, the global response was satisfactory. Moreover, it is important to underline that the system ductility was finally quite large. In fact, even if the overall maximum displacement was limited by the local failure of BRB unrestrained end-portions (corresponding to a maximum interstory drift of 1.11%) the measured global ductility was significantly large corresponding to the local brace buckling was $\mu=\theta_b/\theta_y$=1.11%/0.18%≈6 (Figure 8.3). Both these results reveal that notwithstanding the lack of accuracy in the manufacturing process of local details and the use of a higher steel grade than designed one, this system is robust enough to be able to provide high global ductility, improving strength and stiffness. However, the design goal was not entirely achieved because the designed ductility to be attained was μ=8. In spite of this aspect, the achieved experimental results give rise to the need to investigate in which terms a hysteretic steel device like a BRB performs after its range of design functioning.

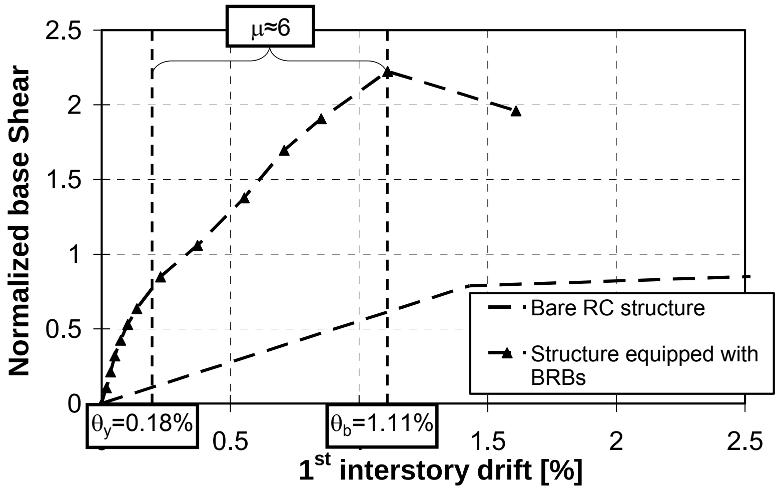

Figure 8.3. Overall ductility measurement.

As done for the first set of experimental tests, in this case a numerical study has been carried out in order to better understand the complex phenomena influencing the actual response of masonry infilled RC structures. In fact, the experimental activity highlighted that this type of buildings can be strongly affected by the presence of the walls and their interaction with infilling frames, when they are in tight contact. This effect can produce large differences with theoretical models prediction based solely on the frame contribution. Results of the experimental dynamic identification of the investigated building show that neglecting the infill-walls contribution led to an overestimation of the natural periods of vibration ranging from 34% to 39% depending on the vibration mode. However, the numerical modelling of the tested masonry infilled RC building has been a very complex study, because of the large number of aspects to be taken into account. In particular, three different structural conditions related to their relevant performed test have been analyzed:

1. the structural response of the original undamaged and unbraced masonry infilled RC building;

2. the lateral response of the RC structure severely damaged after testing and locally repaired, that has been assumed as the initial design state of an hypothetic RC building to be seismic retrofitted by means of BRBs;
3. the lateral response of the masonry infilled RC building retrofitted with BRBs.

Results of the static inelastic tests show that the strength of the building was increased up to 2.5 times the strength that could be expected on the basis of the bare RC frame (i.e. neglecting the wall contribution). The numerical models confirmed that the introduction of steel braces minimize the influence of non-structural elements on lateral capacity of the retrofitted building.

Anyway, the main value of this second set of experimental tests consisted in having highlighted that the actual weak points that could affect the response of “only-steel” BRB devices are essentially due to technological inaccuracy.

At the light of these experiences, another full-scale test on the same RC building equipped with a new BRB prototype (henceforth called prototype 4) is in planning. In fact, this device is already under manufacturing during the presentation of the current pamphlet of my PhD thesis. Obviously, the aim is to improve the performance of the last tested “only-steel” BRB prototype, simplifying some local details and modifying some geometrical proportion in order to improve the “robustness” of the device. To achieve this goal, some adjustments should be carried out. In particular, in addition to more severe quality check on the material and the constructional tolerances, two local details were modified.

As shown in Figure 8.4a, the new prototype is characterized by a shorter unrestrained end-portion, passing from 180mm to 50mm per both ends, extending the restraining sleeve by adding a new stump of sleeve full welded to the original one. The idea to reduce the free stroke length of yielding core descended to the fact that it is unnecessary design a device able to provide systems deformation ductility considerably in excess respect to the maximum displacement demand. Moreover, instead of two rectangular plates (21mmx10mm) fillet welded per side of inner plate, the detail of longitudinal stiffener has been simplified, being made of a single rectangular steel bar (52mmx30mm) full welded to the tapered core, as shown in Figures 8.4a,b.

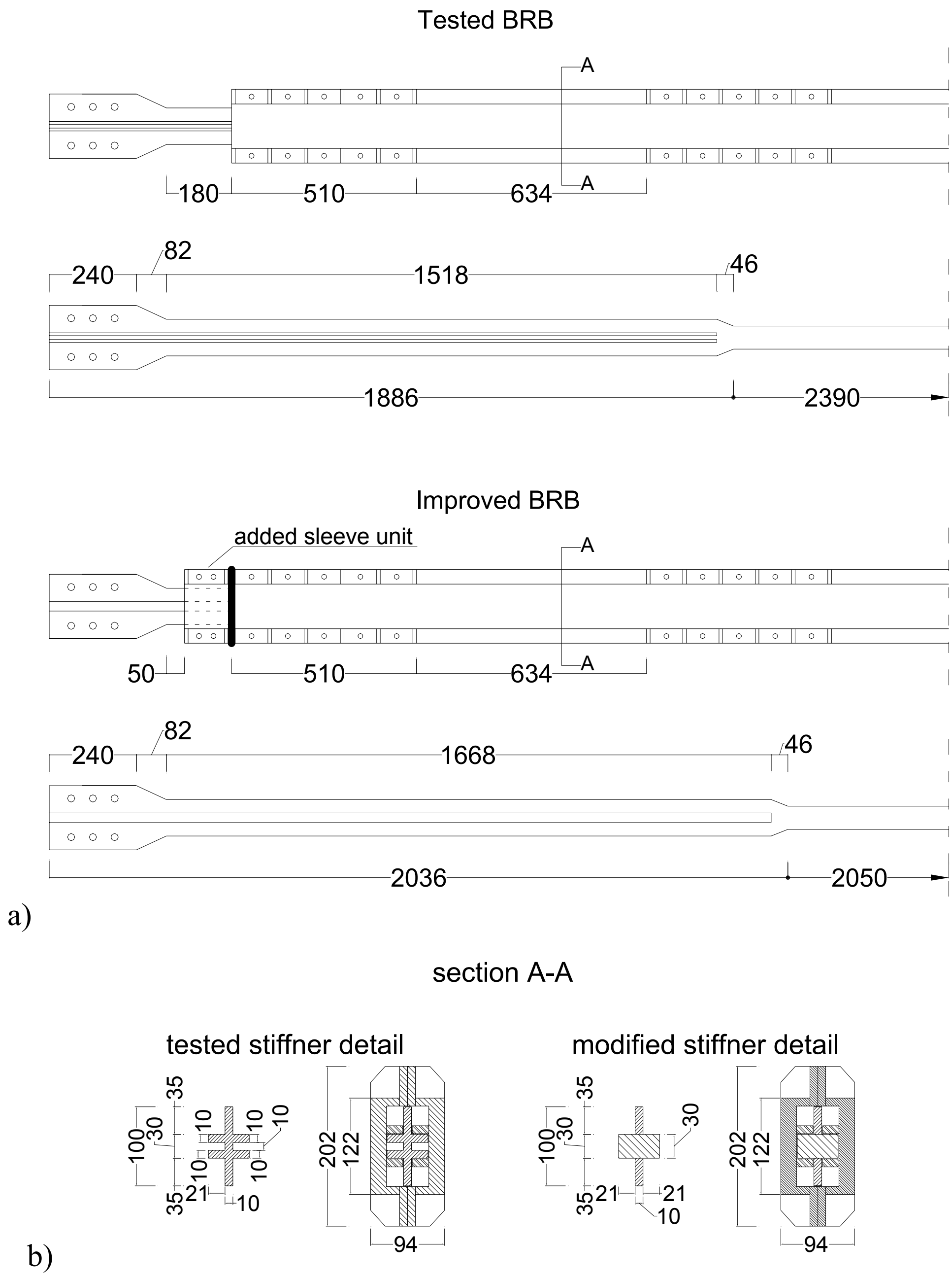

Figure 8.4. New BRB prototype 4 vs. tested prototype 3.

References

Akiyama, H., (1985). Earthquake-Resistant Limit-State Design for Buildings. University of Tokyo Press.

Aiken, I.D., Whittaker, A.S., (1993). Development and application of passive energy dissipation techniques in the U.S.A.. *Proc. of the International Post-SmiRT Conference Seminar on Isolation, Energy Dissipation and Control of Vibration of Structures*, Capri, (Italy), August 23 to 25.

Al-Chaar G., (2002). "Evaluating Strength and Stiffness of Unreinforced Masonry Infill Structures", US Army Corps of Engineers – Engineer Research and Development Center.

American Institute of Steel Construction, Inc. (AISC) (1999). Load and Resistance Factor Design Specification. *American Institute of Steel Construction Inc*., Chicago.

American Institute of Steel Construction, Inc. (AISC) (2001). "Recommended Provisions for Buckling-Restrained Braced Frames," American Institute of Steel Construction/Structural Engineers Association of California Task Groupr.

American Institute of Steel Construction, Inc. (AISC) (2002). Seismic provisions for structural steel buildings. Standard ANSI/AISC 341-02. Chicago (IL, USA).

American Institute of Steel Construction, Inc. (AISC) (2005). Seismic provisions for structural steel buildings. Standard ANSI/AISC 341-05. Chicago (IL, USA).

Applied Technology Council, (1996). ATC-40: Seismic evaluation and retrofit of concrete buildings. November.

Barecchia, E., Della Corte, G. & Mazzolani, F. M., 2005. Numerical-experimental analysis of shear links for steel eccentric braced frames. Proocedings of the XX C.T.A. congress, (First International Workshop on Advanced in Steel Con-structions), Ischia, 26-28 September, pp.49-56.

Barecchia E., D'Aniello M., Della Corte G., Mazzolani F.M. (2006) "Eccentric bracing in seismic retrofitting: from full scale tests to numerical FEM analysis". International Conference On Metal Structures 2006 "Steel - A New And Traditional Material For Building" Poiana Braşov September 20-22.

Barecchia E., Della Corte G., Mazzolani F..M., (2006). Plastic over-strength of short and intermediate links. Proceedings of the STESSA Conference, Yokohama, Japan.

Barecchia E, D'Aniello M., Della Corte G., Mazzolani F.M., (2006). "Steel Eccentric Braces". Chapter of the volume: "Seismic upgrading of RC buildings by advanced techniques. – The ILVA-IDEM Research Project." Monza (Milan, Italy): Polimetrica

Black C., Makris N., Aiken I., (2002). Component testing, stability analysis and characterization of buckling restrained braces. PEER Report 2002/08, Pacific Earthquake Engineering Research Center, University of California at Berkeley.

Bracci J. M., Reinhorn A. M., Mander J. B. (1995). Seismic Resistance of Reinforced Concrete Frame Structures Designed for Gravity Loads: Perfomance of Structural System. ACI Structural Journal Technical Paper, Title no.92-S58, September – October.

Buda G., Buonsanti M., Santini A. (2004). "Valutazione sperimentale delle caratteristiche dinamiche delle torri-faro dell'aeroporto dello stretto", Ingegneria sismica, vol.3, 19–29

Byfield, M.P., Davies, J.M. & Dhanalakshmi, M., (2005). Calculation of the strain hardening behaviour of steel structures based on mill tests. Journal of Constructional Steel Research, 61, 133-150.

Calderoni B, Lenza P, Rossi P.P. (2000). Prescrizioni normative e sicurezza sismica. Ingegneria sismica.

Carden L., Itani A., Buckle I. & Aiken I., (2004). Buckling Restrained Braces for Ductile end cross frames in steel plate girder bridges. Proceedings of the 13th World Conference on Earthquake Engineering, Canada.

Chen, C.C., Lu, L.W., (1990). Development and experimental investigation of a ductile CBF system. *Proceedings of the 4th National Conference on Earthquake Engineering*, Palm Springs, California, Vol.2, p.p. 575-584.

Chen C.H., (2002). Recent advances of seismic design of steel building in Taiwan. International training programs for seismic design of building structures, Taiwan

Chen C.H., Hsiao P.C., Lai J.-W., Lin, S.L., Weng, Y.T. & Tsai, K.C., (2004). Pseudo-dynamic test of a full-scale CFT/BRB frame: Part2- Construction and testing. Proceedings of the 13th World Conference on Earthquake Engineering, Canada.

Chopra, A. (2000). Dynamics of structures: Theory and Applications to Earthquake Engineering, Prentice Hall

Ciampi, V., (1993). Development of passive energy dissipation techniques for buildings. *Proc. of the International Post-SmiRT Conference Seminar on Isolation, Energy Dissipation and Control of Vibration of Structures*, Capri, (Italy), August 23 to 25.

Clark, W., Kasai, K., Aiken, I.D., Kimura, I., (2000). Evaluation of design methodologies for structures incorporating steel unbonded braces for energy dissipation. *Proceedings of the 12th World Conference on Earthquake Engineering*, Auckland, New Zealand , Paper No. 2240, CD-ROM.

D'Aniello M., Della Corte G.,Mazzolani F.M., (2005). "Seismic Upgrading of RC buildings using Eccentric Braces: full-scale experimental tests". XX C.T.A. Conference – First Int. Workshop on ADVANCES IN STEEL CONSTRUCTIONS, Ischia (Italy), 26-28 September.

Della Corte G., D'Aniello M., Mazzolani F.M., (2005). "Seismic Upgrading of RC buildings using Buckling Restrained Braces: full-scale experimental tests". XX C.T.A. Conference – First Int. Workshop on ADVANCES IN STEEL CONSTRUCTIONS, Ischia (Italy), 26-28 September.

D'Aniello M., Della Corte G., Mazzolani F.M, (2006). "Eccentric Bracing As Solution For Seismic Upgrading Of Existing RC Structures". WP6 data sheet of PROHITECH project. Doc. No. 01.06.02.01.

D'Aniello M., Della Corte G., Mazzolani F.M, (2006). "Buckling Restrained

Braces As Solution For Seismic Upgrading Of Existing RC Structures”. WP6 data sheet of PROHITECH project. Doc. No. 01.06.03.01.

D’Aniello, M., Della Corte, G. & Mazzolani, F.M., (2006). Seismic Upgrading of RC Buildings by Steel Eccentric Braces: Experimental Results vs Numerical Modeling. Proceedings of the STESSA Conference, Yokohama, Japan, 14-17 August.

D’Aniello M., Della Corte G., Mazzolani F.M., (2006). “Seismic Upgrading of RC Buildings by Buckling Restrained Braces: Experimental Results vs. Numerical Modeling”. STESSA 2006. Conference – Steel Structures in Seismic Area. Japan, 14-17 August.

D’Aniello M., (2006), “Seismic upgrading of RC structure by steel Eccentric Bracing: an experimental and numerical study”. Pollack Periodica, No.2 October 2006.

D’Aniello M., Della Corte G., Mazzolani F.M., (2006). “Steel Buckling Restrained Braces”. Chapter of the volume: “Seismic upgrading of RC buildings by advanced techniques. – The ILVA-IDEM Research Project.” Monza (Milan, Italy): Polimetrica

D’Aniello M., Della Corte G., Mazzolani F.M, (2006). “Design Methods for Eccentric Braces”. WP9 data sheet of PROHITECH project.

D’Aniello M., Della Corte G., Mazzolani F.M, (2006). “Design Methods for Buckling Restrained Braces”. WP9 data sheet of PROHITECH project.

D’Aniello M., Della Corte G., Mazzolani F.M., (2007). “Steel Buckling Restrained Braces For Seismic Upgrading of RC Buildings”. WORKSHOP RELUIS-Materiali e approcci innovativi per il progetto in zona sismica e la mitigazione della vulnerabilità delle strutture. SALERNO, ITALY February 12-13.

D’Aniello M., Della Corte G., Mazzolani F.M., (2007). “Dissipative Bracing Systems For Seismic Upgrading of RC Structures: Full Scale Tests”. Modern Building Materials, Structures and Techniques. Vilnius Gediminas Technical University (VGTU), May 16 -18.

D’Aniello M., Della Corte G., Mazzolani F.M., (2007). “A special type of buckling-restrained brace for seismic retrofitting of RC buildings: design and testing”. XXI C.T.A. Conference, Catania (Italy) 1-3 October.

D’Aniello M., Della Corte G., Mazzolani F.M, (2007). “Numerical analysis of a real RC building and comparison with experimental results”. WP8 data sheet of PROHITECH project.

Dusicka P., Itani A. M. & Buckle I. G., (2004a). Evaluation of Conventional and Speciality Steels in Shear Link Hysteretic Energy Dissipators. Proceedings of the 13th World Conference on Earthquake Engineering, (CD-ROM, paper n. 522), Vancouver, Canada.

Dasgupta P., Goel S., Parra-Montesinos G. & Tsai K.-C., (2004). Performance-Based Seismic Design and Behaviour of a Composite Buckling Restrained Braced Frame. Proceedings of the 13th World Conference on Earthquake Engineering, Canada.

Della Corte, G. & Mazzolani, F.M., (2006). Full scale tests of advanced seismic upgrading techniques for RC Buildings. Proceedings of the 2nd fib Congress, Naples, Italy, 5-8 June.

Della Corte G., D’Aniello M., Mazzolani F.M., (2007). “Inelastic response of shear links with axial restraints: numerical vs. analytical results” 5th International Conference on Advances in Steel Structures, Singapore, 5 – 7 December.

De Sortis A., Antonacci E., Vestroni F. (2005). "Dynamic identification of a masonry building using forced vibration tests”, Engineering Structures vol.27 155–165.

Dusicka, P. Itani A. M. & Buckle I. G., (2004b). Finite Element Investigation of Steel Built-Up Shear Links Subjected to Inelastic Deformations. ANCER: Annual Meeting: Net-working of Young Earthquake Engineering Researchers and Professionals.

Dusicka P., Itani A.M., Buckle I. (2007). Cyclic response of plate steels under large inelastic strains. Journal of Constructional Steel Research 63, 156–164

Ehsani, M. R. and Wight, J. K., (1985). “Effect of Transverse Beams and Slab on Behavior of Reinforced Beam-to-Column Connections,” JACI 82, No. 2, 188—195, Mar.-Apr..

Engelhardt M.D, Popov E.P,, (1989). On Design of Eccentrically Braced Frames. Earthquake Spectra, vol.5, No.3, 495-511.

Engelhardt M.D, Popov E.P,, (1992). Experimental performance of long links in eccentrically braced frames. Journal of Structural Engineering, Vol.188, No.11:3067-3088.

Eurocode 3, (2003). Design of steel structures - Part 1-8:Design of joints.

Eurocode 8, (2003). Design of structures for earthquake resistance–Part 1: General rules, seismic actions and rules for buildings.

Fahnestock L.A., Sause R. & Ricles J.M., (2003). Analytical and experimental studies on buckling restrained braced composite frames. Proceedings of the International workshop on Steel and Concrete Composite Construction (IWSCCC-2003), October, 8-9, Taipei, pp. 177-188.

FEMA-273, (1996). NEHRP Guidelines for the seismic rehabilitation of buildings. Washington, D.C.

FEMA 356 (2000). Prestandard and commentary for the Seismic Rehabilitation of Buildings. Building seismic safety Council for the Federal Emergency Management Agency, Washington.

Field C., Ko E., (2004). Connection Performance of Buckling Restrained Braced Frames. Proceedings of the 13th World Conference on Earthquake Engineering, Canada.

Foutch D.A., (1989). Seismic Behavior of Eccentrically Braced Steel Building. Journal of Structural Engineering, vol.115, No. 8, 1857-1876.

Gerard, G., (1948). Critical Shear Stress of Plates above the Proportional Limit. Journal of Applied Mechanics Engineering, vol.15, No. 1, 7-12

Gerard, G., (1962). Introduction to Structural Stability Theory. McGraw-Hill Book Company, Inc. New York

Ghobarah A., Elfath A.H., (2001). Rehabilitation of a reinforced concrete frame using eccentric steel bracing. Engineering Structures, vol. 23, 745–755

Ghobarah, A., (2001). Performance-based design in earthquake engineering: state of development. *Engineering Structures,* n. 23, 878-884.

Gioncu V. and Mazzolani F.M., (2002). Ductility of seismic resistant steel structures. *Ed. SPON PRESS*, London

Hanson, N. W. and Conner, H. W., (1967). “Seismic Resistance of Reinforced Concrete Beam—Column Joints,” JSTR 93, 5T5, 533—560, Oct..Bruneau E., Uang C.M. and Whittaker A., (1998). Ductile Design of Steel Structures. McGraw-Hill, U.S.A.

Hjelmstad K.D., Popov E.P., (1983). Cyclic Behavior and Design of Link Beams. Journal of Structural Engineering, vol.109, No. 10, 2387-2403,.

Kasai K., Popov E.P,. (1986a). General Behavior of WF Steel Shear Link Beams. Journal of Structural Engineering, vol.112, No. 2, 362-382, 1986

Kasai K., Popov E.P., (1986b). Cyclic Web Buckling Control for Shear Link Beams. Journal of Structural Engineering, vol.112, No. 3, 505-523.

Krawinkler Krawinkler H., Bertero V. V. and Popov E. P., (1975). Shear Behavior of Steel Frames Joints, Journal of the Structural Division ASCE, vol. 101, 2317-2336 No. ST11, November.

Krawinkler, H. (1996). A few basic concepts for performance based seismic design. *Proc. of 11th World Conference on Earthquake Engineering*. Acapulco, Mexico.

Inoue K, Sawaizumi S, Higashibata Y., (2001). Stiffening requirements for unbonded braces encased in concrete panels. Journal of Structural Engineering, ASCE;127(6):712–9.

Itani A, Douglas B.M. & ElFass S., (1998). Cyclic behavior of shear links in retrofitted Richmond-SanRafael Bridge towers. Proceedings of the First World Congress on Structural Engineering – San Francisco, Paper No. T155-3, Elsevier Science Ltd.

Iwata M., Kato, T. & Wada, A., (2000). “Buckling-restrained braces as hysteretic dampers,” Proceedings of Third International Conference on Behavior of Steel Structures in Seismic Areas (STESSA 2000), Montreal, Canada, pp.33-38.

Iwata, M., Huang, H., Kawai, H., Wada, A., (1995). Study on the Damage Tolerant Structures. *Journal of Architecture and Building Science*, AIJ, Vol. 110, No. 132, pp. 82-88.

Izumi, M., et al. (1992). Low cycle fatigue tests on shear yielding type low-yield stress steel hysteretic damper for response control, part 1 and 2. *Proc. Annu. Meeting of the Arch. Inst. Of Japan*, Tokyo, Japan, 1333-1336.

Lin, S.L., Weng, Y.T., Tsai, K.C., Hsiao P.C., Chen C.H. & Lai J.-W., (2004). Pseudo-dynamic test of a full-scale CFT/BRB frame: Part3-Analisys and Performance Evaluation. Proceedings of the 13th World Conference on Earthquake Engineering, Canada.

Mc Daniel, C. C., Uang, C. & Seible, F., (2003). Cyclic Testing of Built-Up Steel Shear Links for the new Bay Bridge. Journal of Structural Engineering, vol. 129, No 6.

Malley J.O., Popov E.P., (1984). Shear Links in Eccentrically Braced Frames. Journal of Structural Engineering, vol.110, No. 9, 2275-2295.

Mazzolani F.M. editor, (2000). Moment resistant connections of steel frames in seismic areas: design and reliability. *E & FN SPON*, London.

Mazzolani, F.M., Calderoni, B., Della Corte, G., De Matteis G., Faggiano B., Landolfo, R., Panico, S., (2003). Full-scale testing of different seismic upgrading techniques on an existing RC building. *Proc. of the Fourth International Conference on the behaviour of steel structures in seismic areas* (STESSA 2003), Mazzolani F.M. Editor, A.A. Balkema, Rotterdam, The Netherlands.

Mazzolani F. M.,Calderoni B., Spina D., Valente C. (2004). “Identificazione strutturale dell'edificio esistente: il progetto ILVA-IDEM”, XI Congresso Nazionale “L’ingegneria Sismica in Italia”, Genova 25-29 gennaio 2004

Mazzolani F.M., Della Corte G. & Faggiano B., (2004). Seismic Upgrading of RC Buildings by means of Advanced Techinques: the ILVA-IDEM Project, Proceedings of the 13th World Conference on Earthquake Engineering, B.C. Canada.

Mazzolani F. M., Dolce M., Landolfo R., Nicoletti M. (2004). “Seismic upgrading of RC buildings by means of innovative techniques: the ILVA-IDEM project”, XI Congresso Nazionale “L’ingegneria Sismica in Italia”, Genova 25-29 gennaio.

Mazzolani F.M., D'Aniello M., Della Corte G., (2005). "Modal testing and dynamic identification of a two-story RC building". International Conference on Earthquake Engineering to mark 40 years of IZIIS – Skopje-Ohrid (Republic of Macedonia), 27-31 August.

Mazzolani F.M., Della Corte G., Barecchia E., D'Aniello M., (2007). "Experimental tests on seismic upgrading techniques for RC buildings". Workshop-Urban habitat constructions under catastrophic events, COST C26. Prague (CZ) 30-31 March.

Mayes R.L., Goings C., Naguib W., Harris S., Lovejoy J., Fanucci J.P., Bystricky P., & Hayes J.R., (2004). Comparative Performance of Buckling Restrained Braces and Moment Frames. Proceedings of the 13th World Conference on Earthquake Engineering, Canada.

Meinheit, D. F. and Jirsa, J. 0., (1982). "Shear Strength of R/C Beam—Column Connections," JSTR 107, 5Th, 2227—2244, Nov..

Merrit S., Uang C.M. & Benzoni G., (2003). Subassemblage testing of corebrace buckling-restrained braces. Report No. TR-2003/01, Department of Structural Engineering, University of California, San Diego, La Jolla, California 92093-0085, February.

Mochizuki S., Murata Y., Andou N. & Takahashi S., (1979). Experimental study on buckling of unbonded braces under axial forces: Parts 1 and 2. Summaries of technical papers of annual meeting. Architectural Institute of Japan;. p. 1623–6

Mochizuki S., Murata Y., Andou N. & Takahashi S., (1980). Experimental study on buckling of unbonded braces under axial forces: Part 3. Summaries of technical papers of annual meeting. Architectural Institute of Japan; p. 1913–4

Mochizuki S., Murata Y., Andou N. & Takahashi S., (1982). Experimental study on buckling of unbonded braces under axial forces: Part 4. Summaries of technical papers of annual meeting. Architectural Institute of Japan; p. 2263–4

Nader M., Lopez-Jara J. & Mibelli, C., (2002). Seismic Design Strategy of the New San Francisco-Oakland Bay Bridge Self-Anchored Suspension Span, Proceedings of the Third National Seismic Conference & Workshop on Bridges & Highways, MCEER Publications, State University of New York, Buffalo, NY.

Nakashima, M., Saburi, K., Tsuji, B., (1996). Energy Input and dissipation behaviour of structures with hysteretic dampers. *Earthquake Eng. Struct. Dynamics*, 25: 483-96.

Nishimoto, K., Nakata, Y., Kimura, I., Aiken, I., Yamada, S. & Wada, A., (2004). Sub-assembly testing of large buckling restrained unbonded braces. Proceedings of the 13th World Conference on Earthquake Engineering, Canada.

Okazaki T., Engelhardt M.D., Nakashima M., Suita K. (2004). Experimental study on link-to-column connections in steel eccentrically braced frames. Proceedings of the 13th World Conference on Earthquake Engineering, Vancouver, Canada, CD-ROM: paper no. 275.

Okakazi T., Arce G., Ryu H., Engelhardt M.D., (2004). Recent Research on Link Performance in Steel Eccentrically Braced Frames, Proceedings of the 13th World Conference on Earthquake Engineering, B.C. Canada.

Okazaki T., Engelhardt M.D. (2007). Cyclic loading behavior of EBF links constructed of ASTM A992 steel. Journal of constructional Steel Research, 63, 751-765.

Okazaki,T., Engelhard, M.D. (2007). Cyclic loading behavior of EBF links constructed of ASTM A992 steel. Journal of Constructional Steel Research 63, 751–765

Paulay, T., Park, R., and Priestley, M. J. N., (1978). "Reinforced Concrete Beam—Column Joints under Seismic Actions," JA CI Proc. 75, No. 11, 585— 593, Nov..

Park, R., (1986). "Ductile Design Approach for Reinforced Concrete Frames," EERI Earthquake Spectra 2, No. 3, 565—619, May.

Popov E.P., Engelhardt M.D., (1988). Seismic Eccentrically Braced Frames. Journal of Construction and Steel Research, (10) 321-354.

Popov E.P., Malley J.O., (1983) Design of links and beam-to-column connections for eccentrically braced steel frames. Report No. EERC 83-03.

Berkeley (CA): Earthquake Engineering Research Center, University of California.

Priestley, M.J.N., (1997). Displacement-based seismic assessment of reinforced concrete buildings. *Journal of Earthquake Engineering*; 1(1): 157-92.

Rai, D. and Wallace, B.J., (1998). Aluminium shear links for enhanced seismic resistance. *Earthquake Engineering and Structural Dynamics* 27, 315-342.

Ramadan T, Ghobarah A., (1995). Analytical model for shear–link behavior. J Struct Engng, ASCE, 121(11):1574–80.

Richards, P. & Uang, C, (2004). Development of Testing protocol for Links in Eccentrically Braced Frames. Proceedings of the 13th World Conference on Earthquake Engineering, (CD-ROM, paper n. 2795), Vancouver, Canada.

Richardson M.H. (1986). "Global frequency & damping estimates from frequency response measurements", 4rd IMAC Conference, Los Angeles, CA February.

Richardson M.H. (1999). "Structural Dynamics Measurements", Spectral Dynamics – April 11-16.

Ricles J.M., Popov E.P. (1987). Dynamic analysis of seismically resistant eccentrically braced frames. Earthquake Engineering Research Center, University of California, Berkeley.

Ricles J.M., Popov E.P., (1994). Inelastic Link Element for EBF Seismic Analysis. Journal of Structural Engineering, vol.120, No. 2, 441-463.

Roeder C.W., Popov E.P., (1978). Eccentrically Braced Steel Frames for Earthquakes, Journal of Structural Engineering, American Society of Civil Engineers, Volume 104, Number 3.

Ren Wei-Xin, Zong Zhou-Hong, (2004). "Output-only modal parameter identification of civil engineering structures", Structural Engineering and Mechanics, Vol. 17, No. 3-4

Sabelli R., Mahin S. & Chang C., (2003). Seismic demands on steel braced frame buildings with buckling-restrained braces. Engineering Structures, Vol. 25 (5).

Sabelli R., Aiken I., (2004). U.S. building-code provisions for buckling-restrained braced frames: basis and development. Proceedings of the 13th World Conference on Earthquake Engineering, Vancouver, Canada, CD-ROM: paper no. 1828.

Sabelli R., Lopez W., (2005). Design of Buckling Restrained Braced frames.

SAC (1997), ”Protocol for Fabrication, Inspection, Testing, and Documentation of Beam-Column Connection Tests and Other Experimental Specimens. Appendix E: Loading Protocol for Stepwise Increasing Cyclic Tests”, SAC Background Document SAC/BD-97/02.

Saritas A., Filippou F.C. (2004). Modelling of shear-yielding members for seismic energy dissipation. Proceedings of the 13th World Conference on Earthquake Engineering, Vancouver, Canada, CD-ROM: paper no. 1799.

Sarraf M., Bruneau, M., (2004). Performance tests of innovative ductile steel retrofitted deck-truss bridges. Proceedings of the 13th World Conference on Earthquake Engineering, Canada.

SEAOC (Structural Engineers Association of California) Blue Book, (1990). Recommended lateral force requirements and commentary. Sacramento, California, U.S.A.

SEAOC, (1995). Performance-Based Seismic Engineering. California.

Stratan, A., and Dubina, D. (2002). "Seismic performance of eccentric braced frames with removable low yield steel link", Proceedings of International Conference Earthquake Loss Estimation and Risk Reduction, 24-26 October 2002, Bucureşti, România, 117-127.

Timoshenko, S.P., Gere, J.M., (1961). Theory of Elastic Stability, 2nd Ed., McGraw-Hill Book Company. Inc,New York.

Tsai K.C., Huang Y.C., (2002). Experimental responses of large scale BRB frames. Report No. CEER/R91-03, Center for Earthquake Engineering Research.

Tsai, K.C., Lai, J.W., Hwang, Y.C., Lin, S.L. & Weng, Y.T., (2004,a). Research and application of double-core buckling restrained braces in Taiwan. Proceedings of the 13th World Conference on Earthquake Engineering, Canada.

Tsai, K.C., Weng, Y.T., Lin, S.L. & Goel, S., (2004,b). Pseudo-dynamic test of a full-scale CFT/BRB frame: Part1-Performance Based Design. Proceedings of the 13th World Conference on Earthquake Engineering, Canada.

Tremblay R., Poncet L., Bolduc P., Neville R. & De Vall R., (2004). Testing and Design of Buckling Restrained Braces for Canadian Application. Proceedings of the 13th World Conference on Earthquake Engineering, Canada.

Vulcano, A., (1991). Use of steel braces with damping devices for earthquake retrofit of existing framed structure, *Costruzioni Metalliche*, No. 4.

Wada, A., Connor, J.J., Kawai, H., Iwata, M., Watanabe, A., (1992). Damage Tolerant Structures. *Fifth US-Japan Workshop on the Improvement of Building Structural Design and Construction Practices*, ATC-15, California, USA.

Wada, A., Iwata, M., Huang, Y.H., (1997). Seismic design trend of tall buildings after the Kobe earthquake. *Proc. of the International Post-SmiRT Conference Seminar on Isolation, Energy Dissipation and Control of Vibration of Structures*, Taormina, (Italy), August 25 to 27.

Wada A., Nakashima M., (2004). From infancy to maturity of buckling restrained braces research. Proceedings of the 13th World Conference on Earthquake Engineering, Vancouver, Canada, CD-ROM: paper no. 1732.

Wakabayashi M., Nakamura T., Katagihara A., Yogoyama H. & Morisono T., (1973). Experimental study on the elastoplastic behavior of braces enclosed by precast concrete panels under horizontal cyclic loading—Parts 1 & 2. Summaries of technical papers of annual meeting, vol. 10. Architectural Institute of Japan, Structural Engineering Section; p. 1041–4

Wakabayashi M., Nakamura T., Katagihara A., Yogoyama H. & Morisono T., (1973). Experimental study on the elastoplastic behavior of braces enclosed by precast concrete panels under horizontal cyclic loading—Parts 1 & 2. Summaries of technical papers of annual meeting, vol. 6. Kinki Branch of the Architectural Institute of Japan; p. 121–8

Watanabe A., Hitomi Y., Saeki E., Wada A. & Fujimoto M., (1988). Properties of brace encased in buckling-restraining concrete and steel tube. In: Proc. of ninth world conf. on earthquake eng, vol. IV. p. 719–24.

Xie Q., (2005). State of the art of buckling-restrained braces in Asia. Journal of Constructional Steel Research vol. 61 p. 727–748.